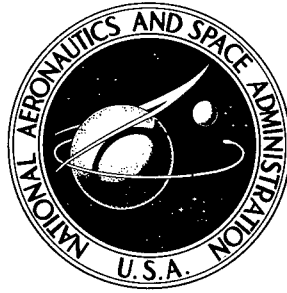


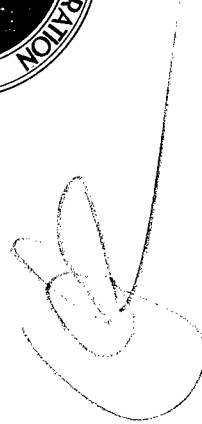
B058117

NASA TECHNICAL NOTE



NASA TN D-2468

NASA TN D-2468



PROPERTY OF:

DISTRIBUTION STATEMENT A
Approved for Public Release
Distribution Unlimited

AMPTAC LIBRARY

THE MICROMETEOROID SATELLITE EXPLORER XIII (1961 CHI)

COLLECTED PAPERS ON
DESIGN AND PERFORMANCE

by Charles T. D'Aiutolo, Coordinator

Langley Research Center

Langley Station, Hampton, Va.

20011217 068

58117

THE MICROMETEOROID SATELLITE EXPLORER XIII (1961 CHI)

COLLECTED PAPERS ON DESIGN AND PERFORMANCE

Charles T. D'Aiutolo, Coordinator

Langley Research Center
Langley Station, Hampton, Va.

NATIONAL AERONAUTICS AND SPACE ADMINISTRATION

For sale by the Office of Technical Services, Department of Commerce,
Washington, D.C. 20230 -- Price \$3.50

Reproduced From
Best Available Copy

FOREWORD

The Micrometeoroid Satellite, Explorer XIII (1961 Chi) was a cooperative effort between three NASA Centers - Langley, Lewis, and Goddard. This report contains contributions from the Langley Research Center and the Goddard Space Flight Center. The coordinator, who was formerly a Langley employee but is presently with NASA Headquarters, gratefully acknowledges the efforts of not only the authors who have contributed to this report but to all others associated with the Explorer XIII.

CONTENTS

	Page
FOREWORD	i
SUMMARY	1
CHAPTER I - INTRODUCTION	3
By Charles T. D'Aiutolo, NASA Headquarters	
REFERENCES	5
CHAPTER II - SPACECRAFT	7
By Charles T. D'Aiutolo, NASA Headquarters	
SECTION I - DESCRIPTION	7
SECTION II - LAUNCH OPERATIONS	15
SECTION III - ASCENT PERFORMANCE	19
SECTION IV - ORBITAL PERFORMANCE	21
SECTION V - DATA ACQUISITION	22
SECTION VI - REFERENCES	24
TABLES	25
CHAPTER III - MECHANICAL DESIGN AND INTEGRATION	29
By Hugh C. Halliday, Langley Research Center	
SECTION I - INTRODUCTION	29
SECTION II - DESIGN DETAILS	29
SECTION III - SURFACE TREATMENT	32
SECTION IV - FIT CHECK	33
SECTION V - BALANCING AND FINAL ASSEMBLY	33
SECTION VI - REFERENCES	34
CHAPTER IV - TELEMETRY DESIGN	35
By Walt C. Long, Langley Research Center	
SECTION I - INTRODUCTION	35
SECTION II - SYSTEMS DESCRIPTION	35
SECTION III - ANTENNA SYSTEMS	47
SECTION IV - CHANNEL ALLOCATIONS	50
SECTION V - GROUND COMPATIBILITY TESTS	53
SECTION VI - OPERATIONAL RESULTS	61
SECTION VII - REFERENCES	63
TABLES	66
CIRCUIT DIAGRAMS	70
CHAPTER V - POWER-SUPPLY SYSTEMS AND TEST SOLAR CELLS	79
By John L. Patterson, Langley Research Center	
SECTION I - INTRODUCTION	79
SECTION II - POWER-SUPPLY SOLAR CELLS	79
SECTION III - BATTERIES	88
SECTION IV - COMPLETE POWER-SUPPLY SYSTEM	93
SECTION V - SOLAR-CELL TEST GROUPS	96
SECTION VI - FLIGHT RESULTS	98

	Page
SECTION VII - APPENDIX A	99
SECTION VIII - APPENDIX B	100
SECTION IX - REFERENCES	100
CHAPTER VI - THERMAL DESIGN	101
By Earl C. Hastings, Jr., Richard E. Turner, and G. Louis Smith, Langley Research Center	
SECTION I - INTRODUCTION	101
SECTION II - SYMBOLS	101
SECTION III - ANALYTICAL METHODS	103
SECTION IV - RESULTS AND DISCUSSION	103
SECTION V - CONCLUDING REMARKS	117
SECTION VI - REFERENCES	117
CHAPTER VII - TEST PROGRAM	119
By W. S. Haywood and Hugh C. Halliday, Langley Research Center	
SECTION I - INTRODUCTION	119
SECTION II - ENVIRONMENTAL TEST SPECIFICATIONS	119
SECTION III - FUNCTIONAL AND DESIGN TESTS	124
SECTION IV - FLIGHT QUALIFICATION TESTS	128
SECTION V - FLIGHT ACCEPTANCE TESTS	135
CHAPTER VIII - DATA REDUCTION	145
By Sheldon Kopelson, Langley Research Center	
SECTION I - INTRODUCTION	145
SECTION II - DATA READOUT SYSTEM	145
SECTION III - DATA PROCESSING OPERATIONS	152
SECTION IV - PERFORMANCE EVALUATION	152
TABLE	156
CHAPTER IX - PRESSURIZED-CELL EXPERIMENT	157
By Charles A. Gurtler, Langley Research Center	
SECTION I - INTRODUCTION	157
SECTION II - DESCRIPTION	158
SECTION III - ENVIRONMENTAL TESTING	163
SECTION IV - CALIBRATION	165
SECTION V - FLIGHT RESULTS	165
CHAPTER X - COPPER-WIRE-CARD DETECTORS	167
By Luc Secretan, Goddard Space Flight Center	
SECTION I - DESCRIPTION	167
SECTION II - RESULTS	170
CHAPTER XI - CADMIUM-SULFIDE EXPERIMENT	171
By Luc Secretan, Goddard Space Flight Center	
SECTION I - DESCRIPTION	171
SECTION II - RESULTS	172

	Page
CHAPTER XII - IMPACT-DETECTION EXPERIMENT	175
By Alfred G. Beswick, Langley Research Center	
SECTION I - INTRODUCTION	175
SECTION II - IMPACT-DETECTION-SYSTEMS OPERATION	175
SECTION III - DESCRIPTION OF INSTRUMENTATION	178
SECTION IV - CALIBRATION	183
SECTION V - RESULTS AND CONCLUSIONS	194
SECTION VI - REFERENCE	196
TABLES	197

THE MICROMETEOROID SATELLITE EXPLORER XIII (1961 CHI)

COLLECTED PAPERS ON DESIGN AND PERFORMANCE

Charles T. D'Aiutolo, Coordinator

SUMMARY

The NASA Micrometeoroid Satellite Explorer XIII (1961 Chi) was developed to obtain a measure of the micrometeoroid penetration hazard to spacecraft by recording penetrations of thin materials. In addition to providing engineering data on this problem, the satellite was designed to measure the space density of cosmic dust for particle masses of 3×10^{-7} grams or greater, 3×10^{-8} grams or greater, and 3×10^{-9} grams or greater. Further, the satellite was designed to obtain data useful in the design of solar-cell power supplies for spacecraft.

The Explorer XIII was launched due east from the NASA Wallops Station, Wallops Island, Virginia on August 25, 1961 at 18:29:44 hours and injected into a near-earth orbit by means of a Scout launch vehicle. Due to a large injection-angle error, the orbital lifetime of the spacecraft was only $2\frac{1}{2}$ days. Despite the very short life of the Explorer XIII, several successful interrogations of the telemeter systems were made and significant data were obtained on the meteoroid environment.

The satellite exposed three materials to the meteoroid environment: beryllium copper from 0.001 to 0.005 inch thick, type 304 stainless steel 0.003 and 0.006 inch thick, and copper wire 0.002 and 0.003 inch in diameter.

Several hundred micrometeoroid impacts were measured by the impact detectors during the useful life of the Explorer XIII; however, no penetrations were recorded in any of the material samples. *end*

The satellite instrumentation performed as expected with the exception of the cadmium-sulfide cell detector which became inoperative during ascent. Temperatures measured on the satellite at various locations were generally higher than predicted which, as shown by the post-flight analysis, could be explained by aerodynamic heating during the low-perigee passages.

This report includes a description of the spacecraft, experiments, and launch vehicle, as well as a discussion of flight data during ascent to orbit, orbital performance, and data acquisition and reduction. Telemeter and power-supply systems are given extensive coverage and operational results are presented. The thermal design is discussed and actual thermal-performance data in flight are presented. A section is devoted to subsystem, flight qualification, and flight-acceptance testing. Separate sections describe the aim and results of the experiments, discuss the design, development, construction, and performance of the apparatus used. *end*

CHAPTER I

INTRODUCTION

By Charles T. D'Aiutolo
NASA Headquarters

One of the hazards of the space environment is the possibility of damage to space vehicles by collision with micrometeoroids. The probability of damage depends upon the frequency, velocity, and mass of micrometeoroids in space as well as the depth of penetration by a particle impacting the space vehicle.

A number of direct measurements on the meteoroid environment have been made by satellites and sounding rockets (see, for example, ref. I-1). These measurements have established the flux rates of meteoroids with small penetrating capabilities in spacecraft materials. Extensive ground observations of meteors by radar and photographic techniques have established the flux rates of meteors (see ref. I-2); however, the rate of occurrence of meteors is such that the probability of collision of the spacecraft with a solid particle having the dimensions of meteor-producing particles is rather remote.

Hypervelocity impact investigations in the laboratory have defined, in a preliminary manner, the penetration physics and damage in various materials resulting from particle impacts simulating meteoroids (see, for example, refs. I-3 and I-4). These experiments have two shortcomings: the impact velocities have been below minimum meteoroid velocities, and projectile masses have been several orders of magnitude greater than meteoroid masses likely to be encountered by a small spacecraft during a mission. A compilation of data obtained from all these investigations indicates that meteoroids can present a serious hazard to spacecraft. However, the information available is far from adequate for use in designing efficient and reliable space vehicles.

In order to provide a more accurate estimate of the probability of penetration in spacecraft structures by meteoroids, a straightforward experiment is required which will allow a direct measure of the penetration hazard. This basically was the approach taken by the micrometeoroid satellite.

The design objectives of the micrometeoroid satellite were:

To obtain a direct measure of the micrometeoroid penetration hazard in structural skin samples;

To measure the impact frequency of micrometeoroids having momenta in the range of 10^0 gm-cm/sec or larger, 10^{-1} gm-cm/sec or larger, and 10^{-2} gm-cm/sec or larger;

To correlate these measurements with data obtained from other satellite and sounding rocket investigations; and

To obtain data useful in the design of solar cells for spacecraft power supplies by a comparison of measurements obtained from protected and unprotected test solar cells.

The satellite was a cooperative effort between the NASA Research Centers. Langley Research Center had the responsibilities for payload integration as well as the overall system. Langley and Lewis Research Centers and the Goddard Space Flight Center designed and fabricated various types of penetration detectors, and Langley designed impact detectors. Telemetry was the responsibility of Langley, while data acquisition was accomplished by the Minitrack Receiving Station Network of the Goddard Space Flight Center. The data were reduced at Langley and data analysis was made at the cognizant research centers.

The micrometeoroid satellite was launched on August 25, 1961 at 18:29:44 hours due east from the NASA Wallops Station and injected into a near-earth orbit by means of a Scout vehicle. Upon completion of its first orbit, the satellite was designated Explorer XIII. Due to an injection-angle error of the Scout launch vehicle, the satellite was placed into an orbit whose lifetime was only about $2\frac{1}{2}$ days instead of the design lifetime of at least 1 year.

Although the Explorer XIII had a short life, significant data were obtained on the micrometeoroid environment.

This report includes a description of the spacecraft, experiments, launch vehicle, as well as a discussion of flight data during ascent to orbit, orbital performance, and acquisition and reduction of data. Telemeter and power-supply systems are given extensive coverage in separate chapters wherein operation results are presented. Prelaunch thermal design studies and tests are discussed in another chapter and flight thermal performance is presented for comparison. In order to insure high reliability, the satellite was subjected to comprehensive and rigorous testing with respect to functions and environmental conditions. A chapter is devoted to subsystem, flight-qualification, and flight-acceptance testing. Test specifications as well as results are presented. Since data obtained from the satellite required rather extensive reduction procedures before analysis could be undertaken, data reduction is given extensive coverage. Each experiment is presented in a separate chapter which describes the aims of the experiment, discusses the design, construction, and performance of the apparatus used, and reports the results of the findings.

Presented herein is the description of and results from the initial S-55 series of micrometeoroid satellites. (A detailed description of the development of one of the several experiments on this initial S-55 satellite and the conclusions drawn from the satellite's brief lifetime in orbit is given in ref. I-5.) Subsequently, another S-55 satellite was successfully launched and injected into orbit and designated the Explorer XVI. Preliminary results from this satellite are found in references I-6 to I-9.

REFERENCES

- I-1. Alexander, W. M., McCracken, C. W., Secretan, L., and Berg, O. E.: Review of Direct Measurements of Interplanetary Dust From Satellites and Probes. A paper presented at the COSPAR meeting May 1962. (To be published in Proc. Third Int. Space Sci. Symposium by North Holland Pub. Co.)
- I-2. Hawkins, Gerald S., and Upton, Edward K. L.: The Influx Rate of Meteors in the Earth's Atmosphere. The Astrophysical Jour., vol. 128, no. 3, Nov. 1958, pp. 727-735.
- I-3. Herrmann, W., and Jones, A. H.: Correlation of Hypervelocity Impact Data. Proc. 5th Symp. on Hypervelocity Impact by the Tri-Service Committee, April 1962, vol. I, pt. 2, pp. 384-438.
- I-4. Herrmann, Walter, and Jones, Arfon H.: Survey of Hypervelocity Impact Information. A.S.R.L. Rep. No. 99-1 (Contract AF 19(604)-7400), M.I.T., Sept. 1961; Addendum, Oct. 1961.
- I-5. Staff of the Lewis Research Center: Micrometeoroid Satellite (Explorer XIII) Stainless-Steel Penetration Rate Experiment. NASA TN D-1986, 1963.
- I-6. Hastings, Earl C., Jr. (Compiler): The Explorer XVI Micrometeoroid Satellite - Description and Preliminary Results for the Period December 16, 1962, Through January 13, 1963. NASA TM X-810, 1963.
- I-7. Hastings, Earl C., Jr. (Compiler): The Explorer XVI Micrometeoroid Satellite - Supplement I, Preliminary Results for the Period January 14, 1963, Through March 2, 1963. NASA TM X-824, 1963.
- I-8. Hastings, Earl C., Jr. (Compiler): The Explorer XVI Micrometeoroid Satellite - Supplement II, Preliminary Results for the Period March 3, 1963, Through May 26, 1963. NASA TM X-899, 1963.
- I-9. Hastings, Earl C., Jr. (Compiler): The Explorer XVI Micrometeoroid Satellite - Supplement III, Preliminary Results for the Period May 27, 1963, Through July 22, 1963. NASA TM X-949, 1964.

CHAPTER II

SPACECRAFT

By Charles T. D'Aiutolo
NASA Headquarters

SECTION I - DESCRIPTION

The micrometeoroid satellite Explorer XIII was the payload of Scout vehicle ST-6, and contained five experiments to obtain information regarding micrometeoroids. These experiments consisted of the following detectors: pressurized cells, steel-covered grids, copper-wire cards, cadmium-sulfide cells, and impact detectors. In addition, a series of temperature measurements were made at selected places throughout the satellite. Voltage measurements were made on test solar cells to measure degradation of the cells.

Configuration.- The satellite was cylindrical in shape; about 23 inches in diameter and about 76 inches in length. The general arrangement of the spacecraft is shown in figure II-1, and exploded views are shown in figure II-2. The satellite was installed around the fourth stage of the Scout vehicle (X-248 rocket motor). The Langley pressurized-cell experiment was mounted around the periphery of the rocket motor; the Lewis steel-covered-grid experiment and the Goddard copper-wire-card experiment were located on the fourth-stage support structure. A shell was mounted on the fore-end of the spacecraft just forward

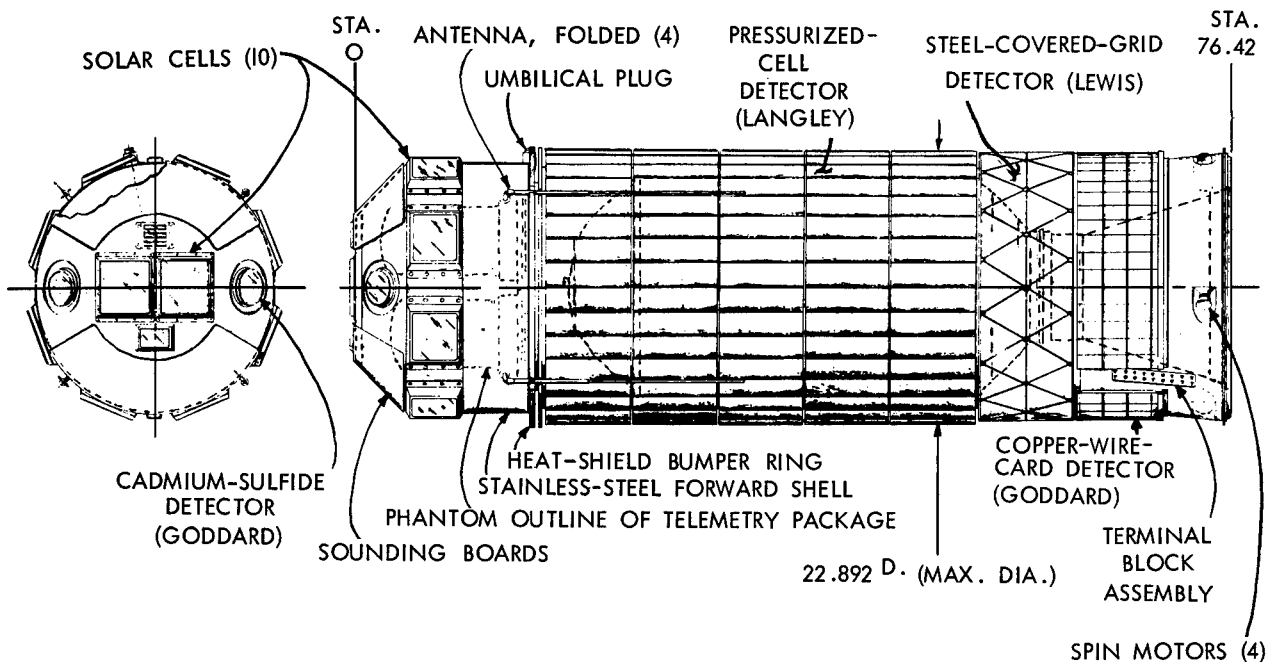
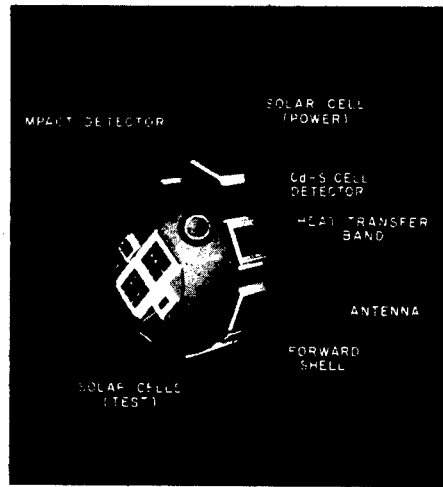
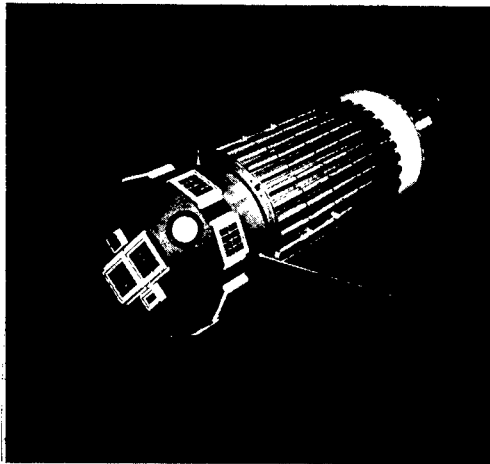


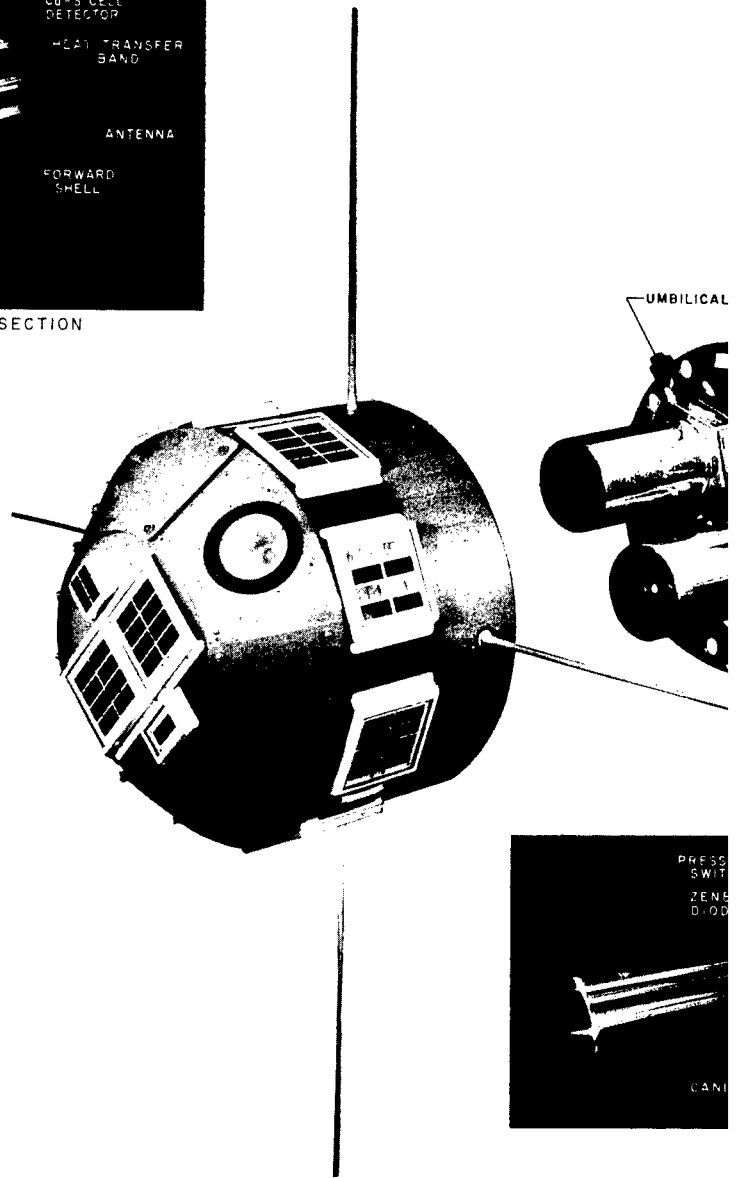
Figure II-1.- General arrangement of Explorer XIII.

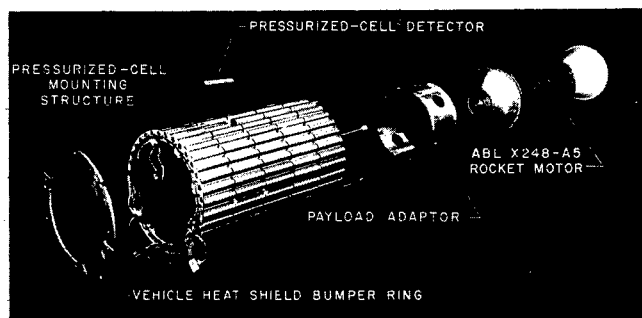


FORWARD SECTION

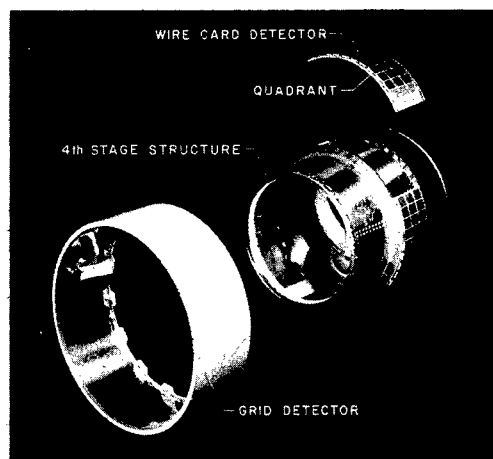
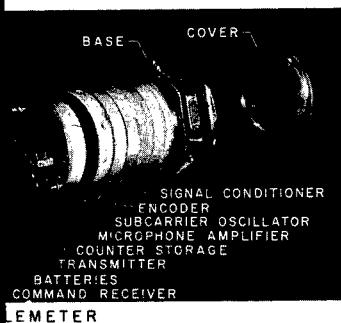
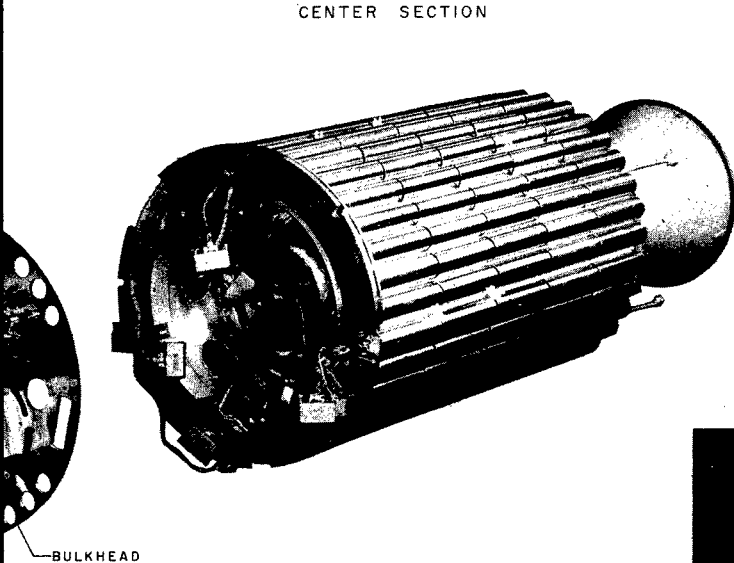


ASSEMBLED SPACECRAFT





CENTER SECTION



AFT SECTION

Figure II-2.- Exploded view of Explorer XIII.

L-64-3017

of the pressurized-cell experiment. On this shell were mounted the erectile antennas, the solar cells, the cadmium-sulfide cells, and "sounding boards" to which were mounted impact detectors to determine collisions with micrometeoroids. The "sounding boards" were acoustically isolated from the rest of the satellite structure. Within the shell and upon a thermally isolating bulkhead, were mounted the telemeters and the radio beacon. Detectors from each experiment were divided equally between the two telemeters. It should be noted that the motor casing is used as a structural member for the satellite and thus went into orbit as part of the satellite. A cutaway drawing of the satellite is presented in figure II-3 and shows the instrumentation telemeters and mounting details of solar cells and experiments as well as other features. A brief description of the experiments follows. More detailed descriptions are presented in later chapters and in reference III-1.

Langley Pressurized-Cell Detector.- The Langley pressurized-cell detectors are the primary sensors of the satellite and occupy the major portion of the sensitive area. A total of 160 cells of various thicknesses were mounted around the periphery of the spacecraft in five circular rows. Each row contained 32 cells. The cells were fabricated from beryllium-copper. Details of the pressurized-cell experiment are shown in figure II-4 and discussed in more detail in chapter IX. Five different thicknesses were incorporated: 0.001, 0.0015, 0.002, 0.0025, and 0.005 inch. The cells were pressurized with helium so that a puncture by a micrometeoroid would allow the helium to leak out. By means of a pressure-activated switch located on each cell, the pressure loss could be detected and telemetered. Helium gas was used in the cells and was pressurized to about 10 psi over atmospheric pressure so that the pressure switch would be closed on the ground, thereby providing a check prior to launch; the switch would open if the pressure in the cell dropped to about 5 psi. No attempt was made to monitor pressure leak rate. The penetration area of each detector is about 21.8 sq in. (140 cm²) so that 24.2 sq ft (2.25 m²) of area were exposed for this experiment. However, because of the semicircular cross section of the pressurized cells (see fig. II-4) the effective area for micrometeoroid capture was smaller than the exposed area. This effective area was considered to be π times the diameter of the outer surface (23 inches, see fig. II-1), multiplied by the detector sensing length of the column of five detectors (35.6 inches) with a correction for the open area between detectors. This definition of area gives a total value of 17 square feet (1.58 square meters).

Shown in the following table are the number of beryllium-copper cells of each thickness as well as the exposed area of each thickness:

Thickness, in.	Number of cells	Total exposed area in -	
		Sq ft	Sq m
0.0010	60	6.350	0.58
.0015	40	4.250	.40
.0020	20	2.125	.20
.0025	20	2.125	.20
.0050	20	2.125	.20

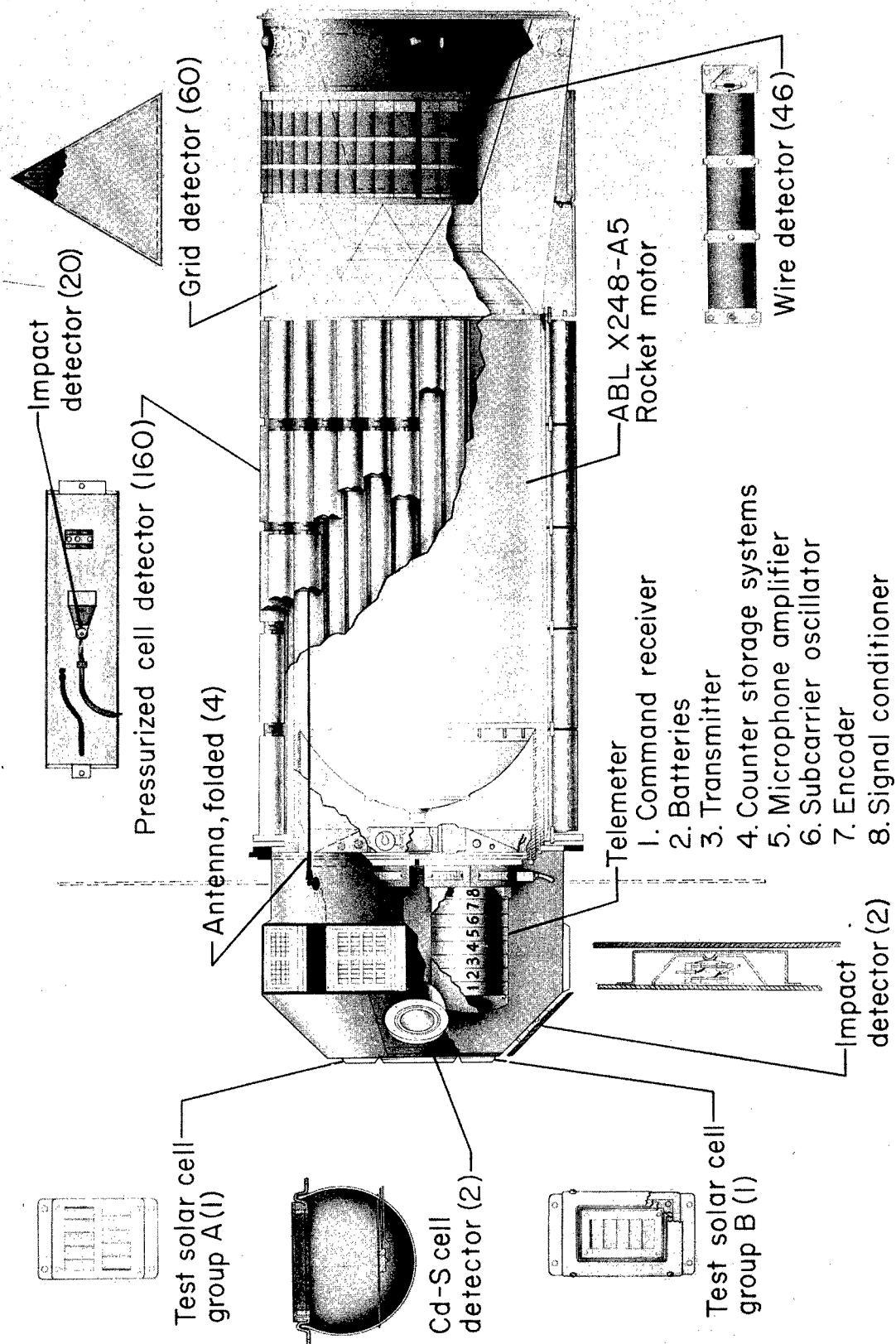


Figure II-3.- Cutaway view of the micrometeoroid satellite.
L-64-3076

Lewis Steel-Covered-Grid Detectors.- The Lewis steel-covered-grid detectors were units developed by the Lewis Research Center. A drawing of this detector is presented in figure II-5. Each detector consisted of a printed circuit about 60 microinches thick attached to 0.00025-inch-thick insulation. This circuit was mounted on the underside of type 304 stainless-steel skin samples. The samples were 0.003 and 0.006 inch thick. Each sample is an equilateral triangle whose sides are 4.57 inches long. The satellite incorporated 60 of these detectors. The thicknesses and areas are listed in the following table:

Thickness, in.	Number of sensors	Total exposed area in -	
		Sq ft	Sq m
0.003	50	3.00	0.28
.006	10	.75	.07

A detailed description of this experiment is given in reference II-1.

Goddard Copper-Wire-Card Detectors.- These copper-wire-card detectors were developed by the Goddard Space Flight Center and were similar to the detectors flown on the Explorer I as well as other satellites. A drawing of the

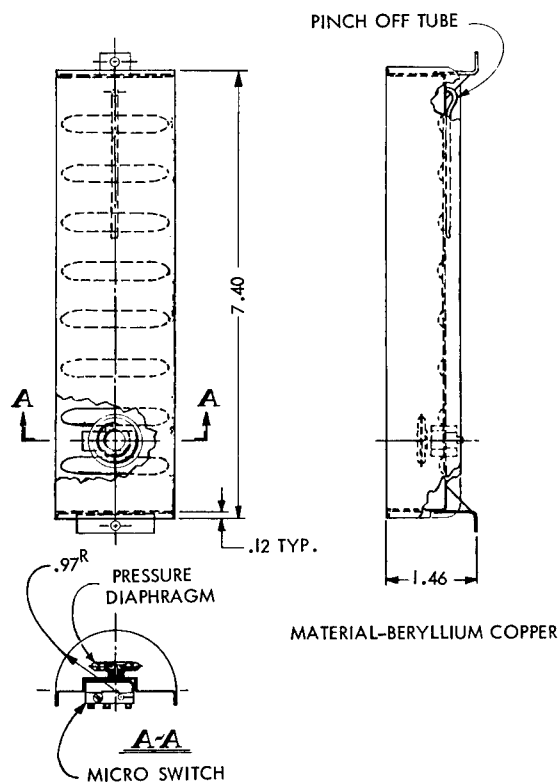


Figure II-4.- Pressurized-cell detector.
All dimensions in inches.

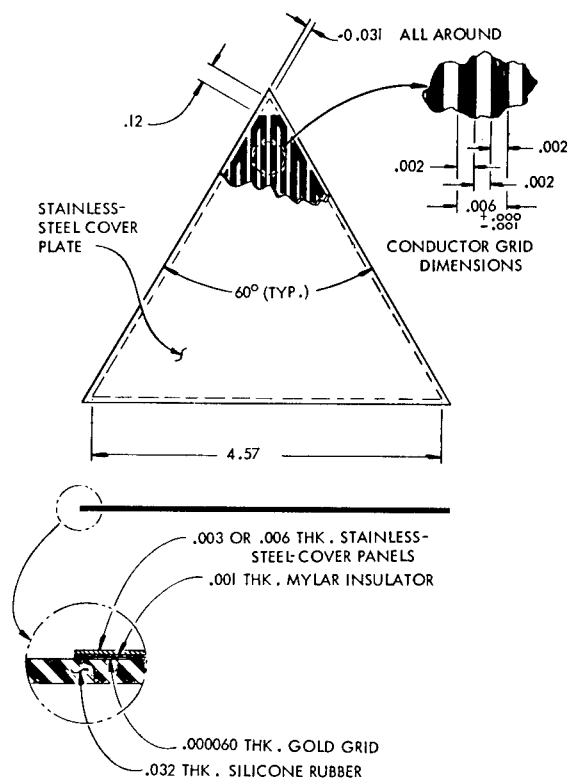


Figure II-5.- Steel-covered-grid detector.
All dimensions in inches.

copper-wire-card detector is shown in figure II-6 and is discussed in detail in chapter X. Each detector consisted of a winding of fine wire mounted to a card

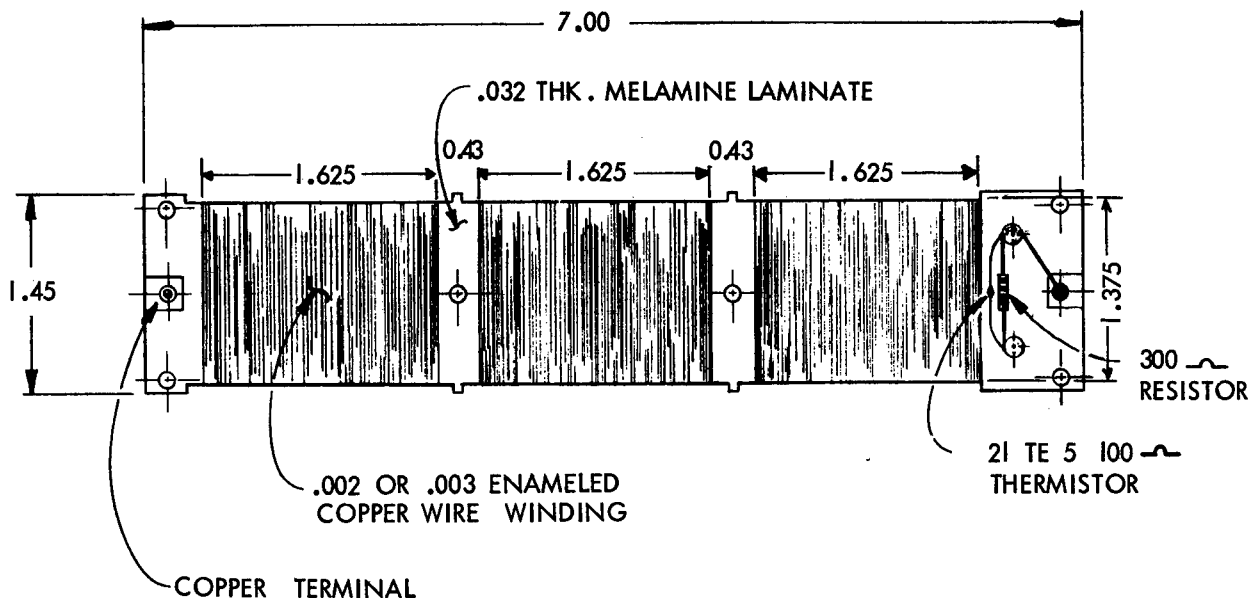


Figure II-6.- Copper-wire-card detector. All dimensions in inches.

rectangular in shape whose dimensions were 1.45 by 7.00 inches. This experiment incorporated two wire sizes of 0.002- and 0.003-inch diameter. Thicknesses and areas are shown in the following table:

Thickness, in.	Number of sensors	Total exposed area in -	
		Sq ft	Sq m
0.002	14	0.98	0.09
.003	32	2.27	.21

Goddard Cadmium-Sulfide Cells.- The cadmium-sulfide-cell detectors were also developed by the Goddard Space Flight Center. A drawing of this detector is shown in figure II-7 and discussed in detail in chapter XI. Basically, the detector consisted of a Cd-S cell mounted in an aluminum-coated glass flask. The exposed surface, whose diameter was about 2.6 inches (6.1 cm) (actual useful diameter about 2.00 inches (5.08 cm)), was covered with a sheet of 0.00025-inch film coated with evaporated aluminum on both sides. Extremely small particles could penetrate the aluminized film and allow light to enter the cell. The geometry of the flask was designed to focus the light onto the Cd-S cell; the cell resistance changed as a function of illumination. Two of these units were incorporated on the spacecraft, and were mounted in the forward shell, 180° apart. (See fig. II-1.)

Langley Impact Detectors.- The impact detectors were a Langley experiment and three levels of sensitivity were employed. Two acoustically isolated "sounding boards" on the forward shell were used for the highest and lowest levels, and twenty 0.005-inch pressurized cells were instrumented with transducers for the intermediate sensitivity level. Figures II-8 and II-9 are drawings of the impact detectors on the sounding boards and pressurized cells. This experiment is discussed in more detail in chapter XII. The following table lists the area and design sensitivities of the impact detectors.

Component	Total exposed area in -		Design sensitivity, dyne-sec
	Sq ft	Sq m	
Sounding boards	1.53	0.14	{ 1 .01 .1
0.005-inch pressurized cells	2.30	.21	

Detector Correlation.- From the preceding discussion of the various penetration and impact experiments, it may be seen that each of the detectors complemented each other, thereby allowing a correlation to be made between the individual detectors.

The total exposed area of all penetration and impact detectors on the Explorer XIII was about an order of magnitude greater than other micrometeoroid experiments flown on earlier satellites.

Silicon Solar Cells.- These detectors were planned to determine the adverse effects of space environments on the silicon solar cells. There were five groups of five shingled solar cells; one group had 0.062 inch of fused silica mounted 0.062 inch above the cells, two groups had 0.006 inch of glass bonded directly to the solar cells with an epoxy cement, and the remaining two groups were unprotected. Three of the test solar cell groups were mounted to the front face of the forward shell. The remaining two test solar cell groups were mounted 180° apart on the cylindrical section of the forward shell.

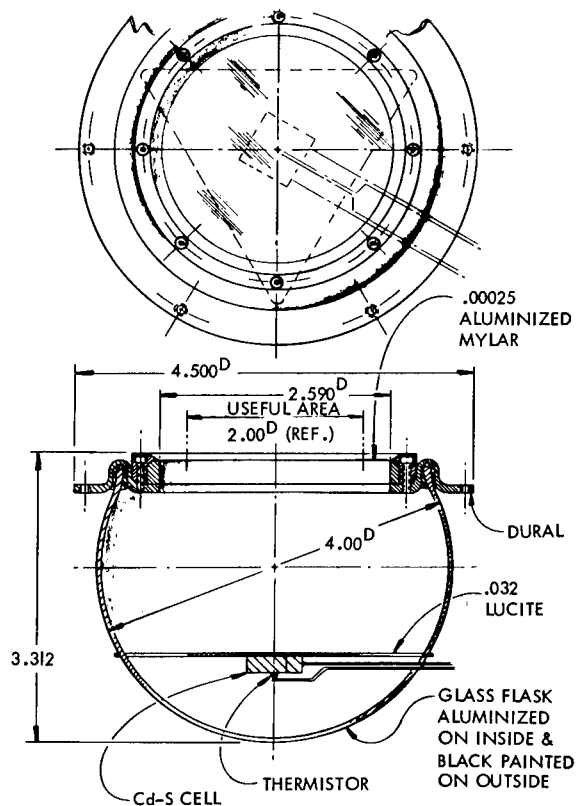


Figure II-7.- Cadmium-sulfide cell detector. All dimensions in inches.

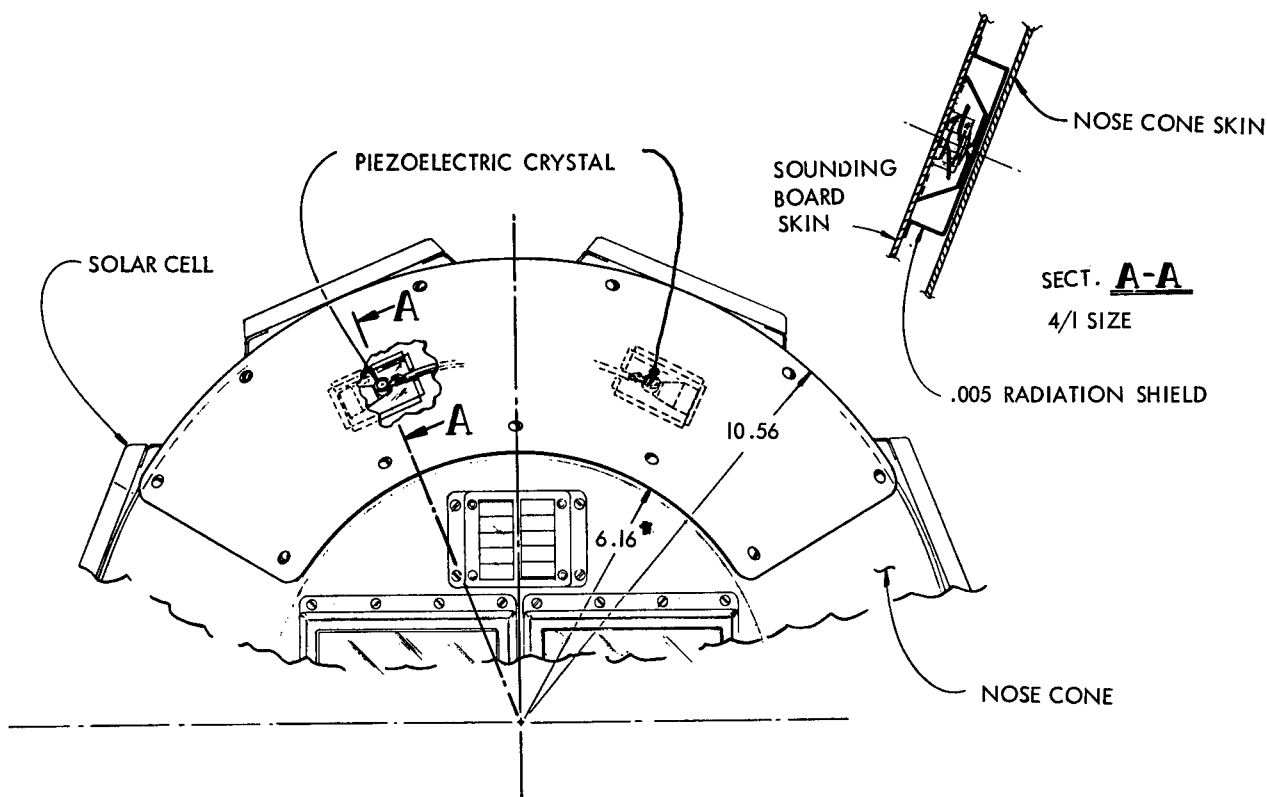


Figure II-8.- Sounding-board impact detectors. All dimensions in inches.

Sketches of the solar cell groups are shown in figures II-10 and II-11. Further description of this experiment appears in chapter V, section V.

Satellite Weight Breakdown.- The weight breakdown of the micrometeoroid satellite is shown in table II-1. Total payload weight including experiments, mounting hardware, telemeters, and support structure was 127.35 pounds. Weight of spent fourth-stage motor, spent spin rockets, as well as the upper "D" section of the Scout vehicle was 62.53 pounds so that the total weight in orbit was 189.88 pounds.

SECTION II - LAUNCH OPERATIONS

General Description of Launch Vehicle.- As stated in the previous section, the micrometeoroid satellite was the payload of Scout ST-6. Only a brief description of the Scout will be presented herein.

The Scout is a small launch vehicle capable of being used as a high-altitude probe, a reentry vehicle, or as a satellite launching vehicle. A general arrangement drawing of Scout, showing staging, is presented in figure II-12. The Scout is a four-stage, solid-propellant, rocket vehicle using a preprogrammed control system for guidance. The first and second stages are steel-walled

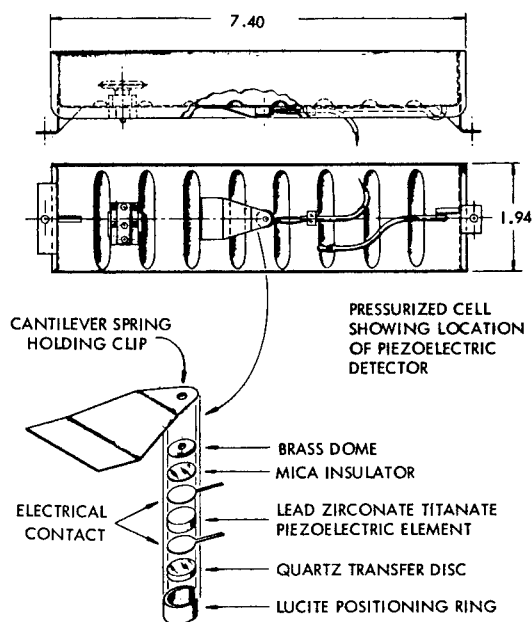


Figure II-9.- Impact detector mounted on pressurized cells. All dimensions in inches.

vessels and the third and fourth stages are of fiber-glass construction. Heat-shield-drag fairings were placed around the third-stage rocket motor, the fourth stage, and the payload in order to protect these units during flight within the dense part of the atmosphere. Aerodynamic tip controls and jet vane controls are used for attitude control of the first stage and H_2O_2 control jets are used on the second and third stages for attitude control as the flight progresses. The vehicle is attitude controlled up to fourth-stage ignition and is spin stabilized through fourth-stage burning.

Preflight Operations.- After environmental tests, calibrations, and final checkouts as described in later chapters of this paper, the micrometeoroid satellite as well as the prototype satellite was shipped to the Wallops Station for launch preparations. The prototype satellite was used for fitting checks as

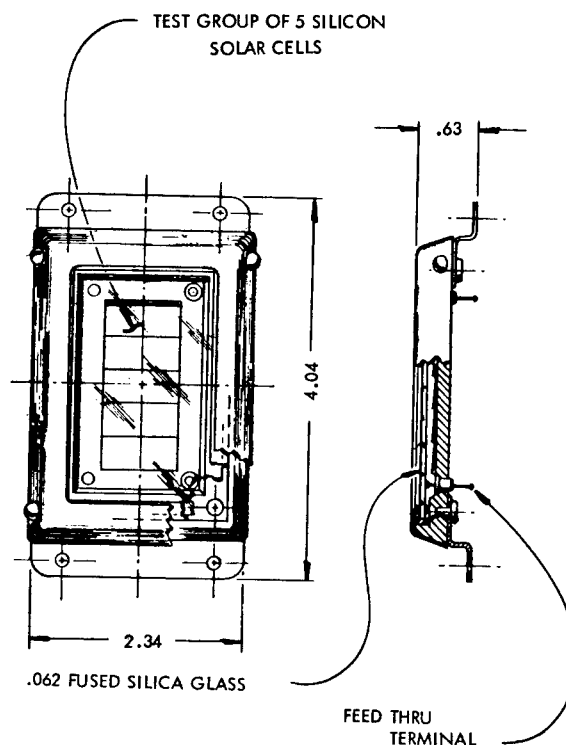


Figure II-10.- Single solar-cell test unit. All dimensions in inches.

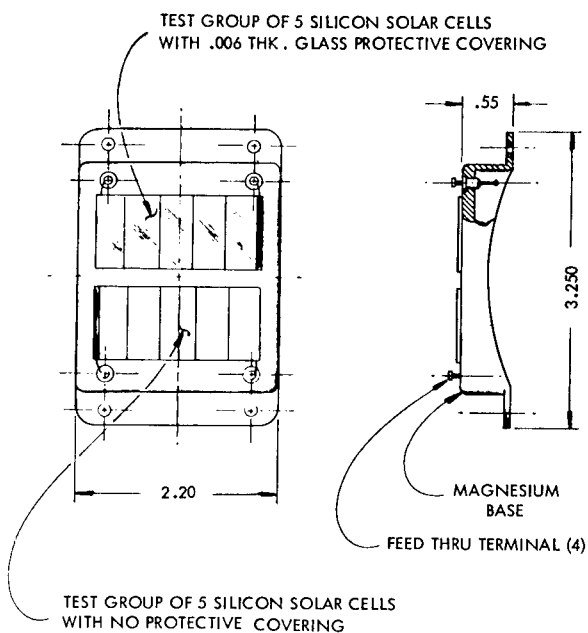


Figure II-11.- Double solar-cell test unit. All dimensions in inches.

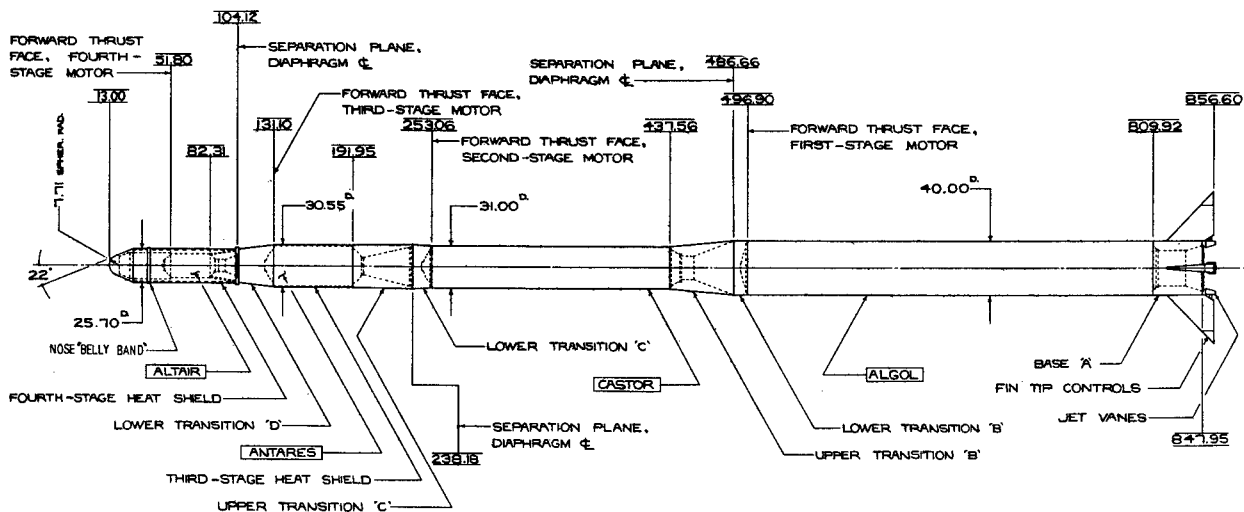
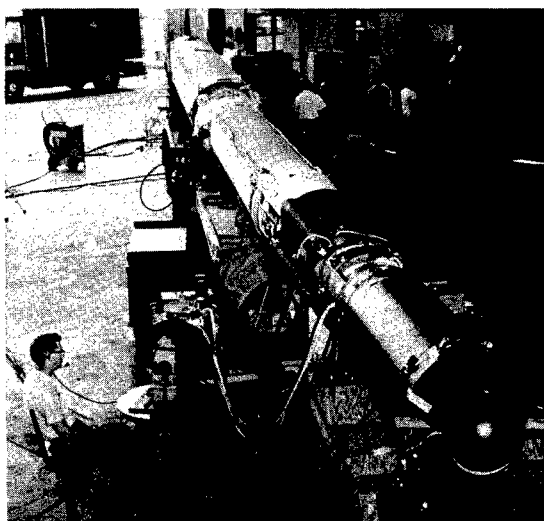


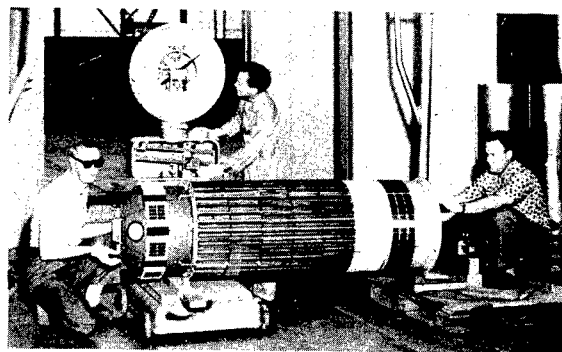
Figure II-12.- General arrangement of Scout vehicle. All dimensions in inches.

well as vehicle systems checks before the vehicle was assembled on the launch tower. A photograph of a vehicle-system check is shown in figure II-13.

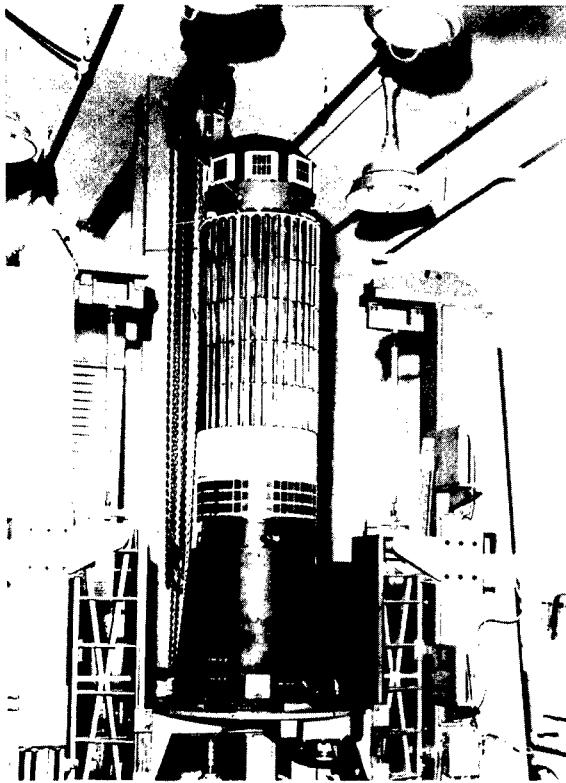
Upon arrival at the launch facility, the micrometeoroid satellite underwent a performance check to ascertain that no damage occurred in shipment. The center of gravity of the payload with a spent fourth-stage rocket motor and a fourth-stage support structure attached was then determined (fig. II-14) so that final vehicle ascent characteristics could be ascertained. Next, the satellite was disassembled, moved to an explosion-proof room, and assembled around a live fourth-stage rocket motor. Alinement checks were made and the payload and the live fourth-stage motor with fourth-stage support structure attached were dynamically balanced (fig. II-15) to insure true spinning during fourth-stage burning. After dynamic balancing and extensive instrument checks and inspections, the satellite was placed within



L-64-3077
Figure II-13.- Spacecraft-vehicle systems checks.

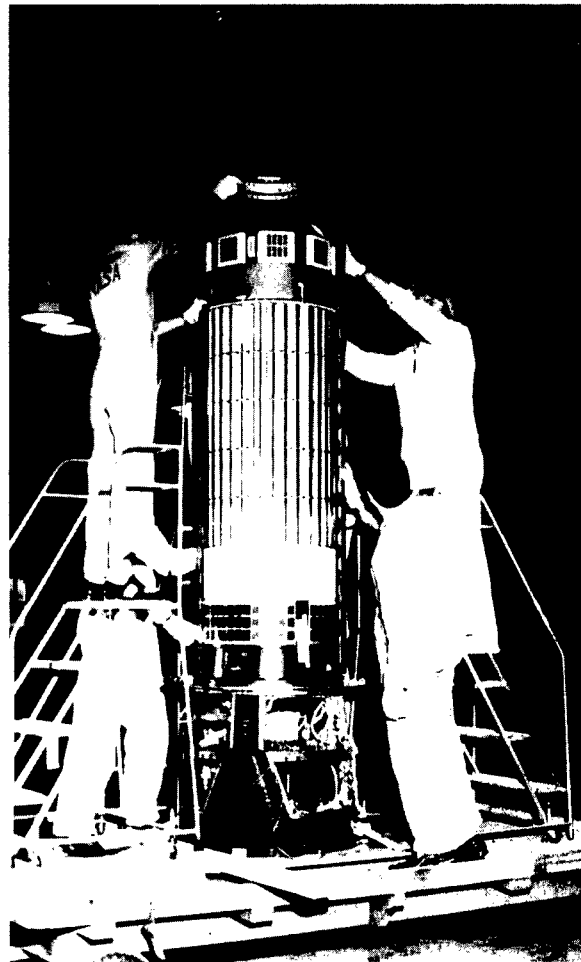


L-64-3078
Figure II-14.- Spacecraft center-of-gravity determination.



L-64-3079

Figure II-15.- Dynamic balancing of spacecraft.



L-64-3080

(a) Within one-half of heat shield.

Figure II-16.- Spacecraft within Scout fourth-stage heat shield.

the fourth-stage payload heat shield (figs. II-16(a) and II-16(b)) and transported to the launch tower. At the tower, the fourth stage with payload attached and with heat shield in place was elevated (fig. II-17) and mated to the first three stages of the Scout launch vehicle (fig. II-18). Prior to launch, the satellite underwent a series of tests and checks including electrical tests, mutual interference checks between vehicle and payload, and payload final performance checks as well as payload calibrations before the start of the launch countdown. Pre-launch reference measurements were made on all experiments during the countdown just prior to lift-off. In lieu of a backup micrometeoroid satellite payload, backup components were available at the launch site in the event of a payload failure. It was not practical to have available a complete backup payload since the fourth-stage motor is contained within the payload and only one fourth-stage motor was immediately available for the Scout ST-6 launch. In addition, the replacement of the payload with a complete backup payload would require several days, thus delaying the launch and increasing the cost of the launch operations.



L-64-3081
(b) Completely contained within heat shield.

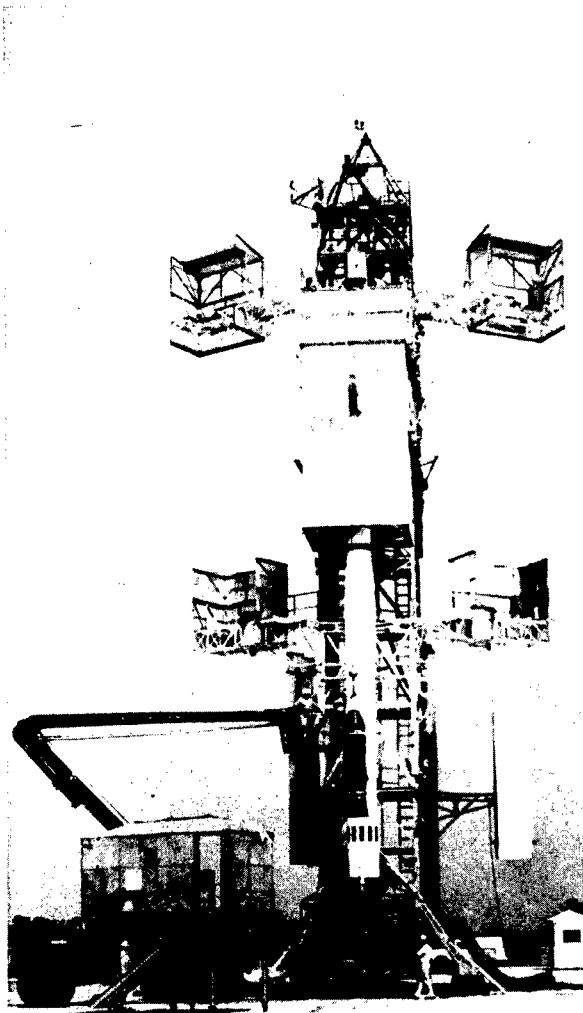
Figure II-16.- Concluded.

Launch Operations.- Near the end of the launch countdown the vehicle was positioned for launch (fig. II-19). At the end of the launch countdown the first stage was ignited at 18:29:44 hours and the Scout vehicle rose from its launch tower (fig. II-20) with the guidance and control system programed to fly the prescribed ascent trajectory. After first-stage burnout at an altitude of about 55,000 feet, the vehicle coasted to about 130,000 feet with first stage attached in order to provide aerodynamic stability and to minimize aerodynamic heating loads. At about 130,000 feet, the second stage was ignited and separated from the first stage. Second-stage burnout occurred at an altitude of about 260,000 feet and the drag-fairing heat shield around the third-stage rocket motor was jettisoned. The second stage with upper stages coasted to about 350,000 feet where third-stage ignition took place, and the second stage was separated. At third-stage ignition, the fourth-stage payload drag-fairing heat shield was jettisoned. It was not possible to jettison the fourth-stage payload heat shield below 350,000 feet since calculations indicated that aerodynamic heating might be seriously detrimental to experiments onboard the spacecraft. When the fourth-stage payload heat shield jettisoned, the spacecraft antennas erected. The fourth

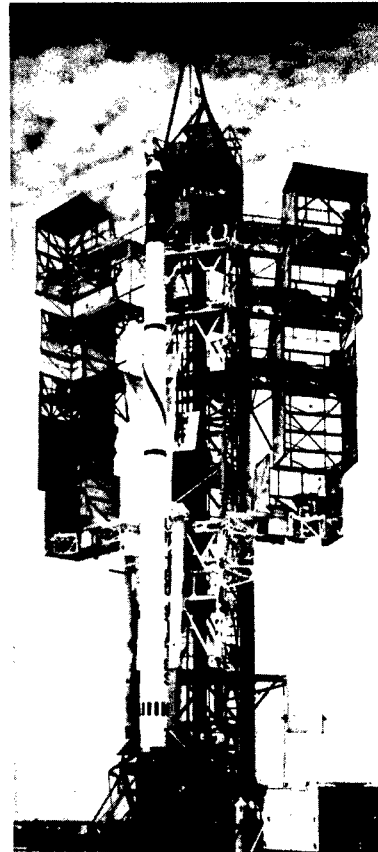
stage and the burnt-out third stage with its control and guidance system still operating coasted to the apogee of the ascent trajectory. The stages were aligned to about 0.13° with the local horizon; the fourth stage was spun up to about 190 rpm by spin rockets, ignited, and blast separated from the third stage. The velocity increment gained during fourth-stage burning was sufficient to place the spacecraft into orbit. A sequence of events from launch showing pertinent events is shown in table II-2.

SECTION III - ASCENT PERFORMANCE

Preliminary analysis of telemetry and tracking radar data immediately after launch indicated nominal performance up to fourth-stage ignition and that the ascent trajectory was very close to the predicted trajectory. However, it was not possible to determine the injection point exactly since radar data obtained beyond fourth-stage ignition were questionable and flight records were not obtained beyond fourth-stage ignition since the launch vehicle telemetry systems



L-64-3082
Figure II-17.- Spacecraft (within fourth-stage heat shield) being elevated for assembly with launch vehicle.

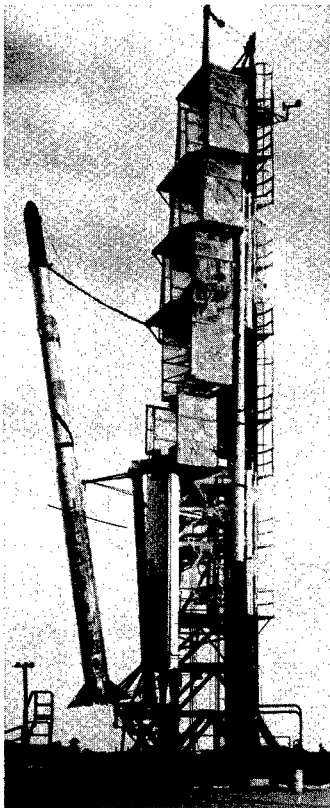


L-64-3083
Figure II-18.- Spacecraft (within fourth-stage heat shield) assembled to launch vehicle.

were located in the third stage. On this basis injection conditions were derived from subsequent Minitrack data on spacecraft position, extrapolated backward to the injection point.

In order to obtain a comparison of the actual ascent trajectory with the predicted, and with a calculation based on actual rocket performance, it was necessary to perform a postflight trajectory calculation on a digital computer by using the first- and second-stage motor performance based on accelerometer data and nominal third-stage data in place of motor performance obtained from flight records since a cursory analysis of all flight data indicated that the performance data for the third-stage motor, derived from accelerometers, was in error. Fourth-stage nominal performance was used in this calculation.

A comparison of the actual ascent trajectory as determined by radar with preflight as well as postflight calculations is presented in figure II-21. It is seen that the postflight calculation agrees well with the radar data through



L-64-3084
Figure II-19.- Vehicle in launch attitude.

fourth-stage ignition. As stated previously, Minitrack data were used to determine injection. The difference in injection altitude as shown by the preflight and postflight calculations was about 6 nautical miles.

A comparison of the actual ground track with the predicted trajectory indicates that the vehicle followed the predicted path within about 1° . This comparison is shown in figure II-22.

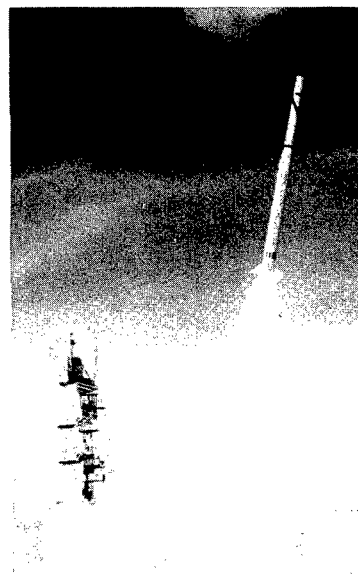
An analysis of the telemetered pitch-rate gyroscope output was undertaken to determine whether the pitch attitude of the vehicle varied as programed with time along the trajectory. This analysis indicated that the pitch rate did not go to zero at $T + 222$ seconds as programed, but continued at a negative rate of approximately 0.04 deg/sec. This amount of drift resulted in an attitude error of -11.1° at fourth-stage ignition. A trajectory computed with this pitch program resulted in an injection altitude of 246.05 nautical miles and a flight-path angle of -4.396° . These values are in close agreement with the values

derived from Minitrack data. A comparison of injection conditions as determined by preflight as well as postflight calculations and derived from Minitrack data are presented in table II-3 (see ref. II-2).

SECTION IV - ORBITAL PERFORMANCE

As indicated in the previous section, a preliminary analysis of the flight data indicates that the actual vehicle trajectory appeared to be very close to the predicted trajectory. Indications were that a satisfactory orbit had been achieved. However, postflight calculations of orbital parameters based on Minitrack data revealed that the desired orbit was not achieved. Due to the previously mentioned flight-path error, the perigee was about 61 nautical miles, and the satellite, designated Explorer XIII, remained in orbit approximately $2\frac{1}{2}$ days instead of the predicted minimum of 1 year.

A comparison of the predicted orbital parameters with those obtained from Minitrack data is shown in table II-4.



L-64-3085
Figure II-20.- Launching of spacecraft.

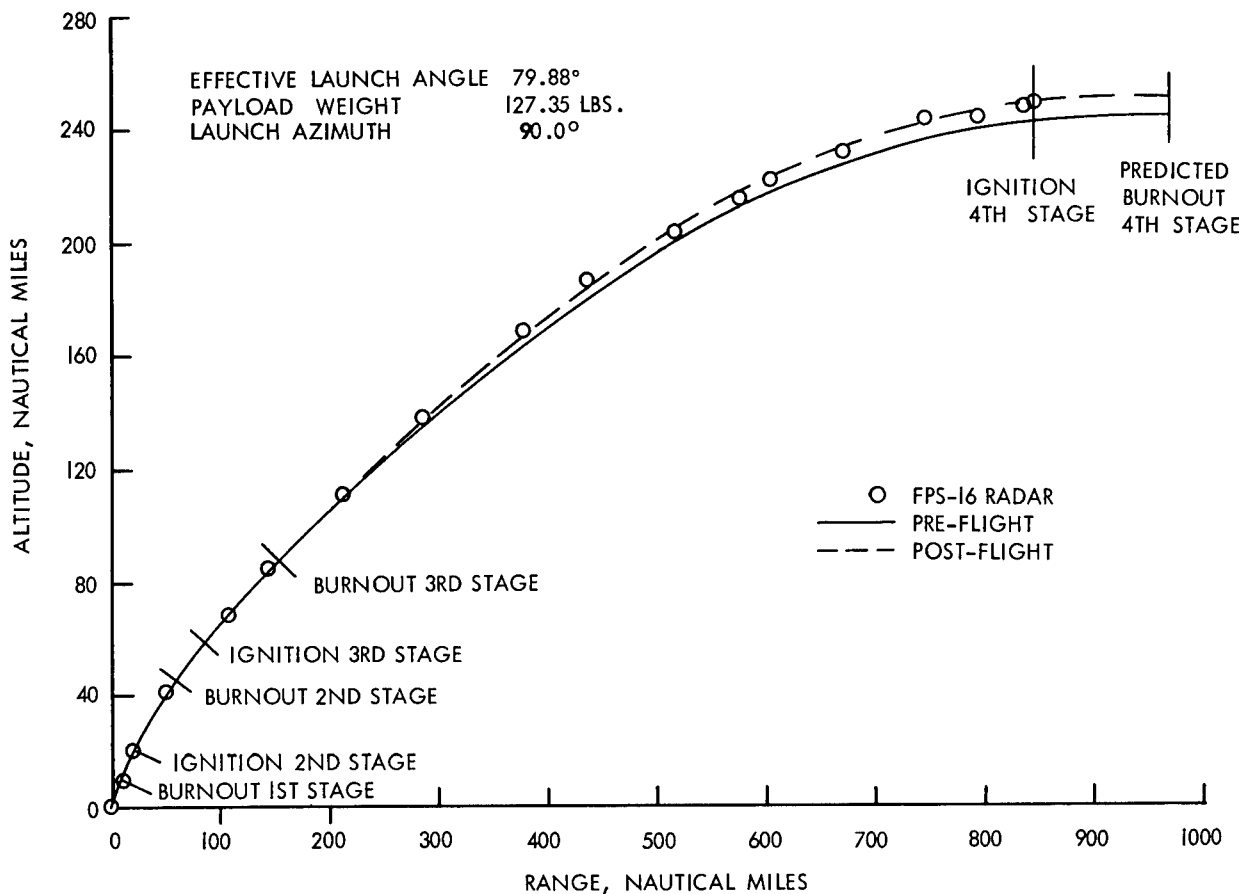


Figure II-21.- Ascent trajectory profile.

SECTION V - DATA ACQUISITION

Data acquisition from the Explorer XIII was the responsibility of the Goddard Space Flight Center, and the Minitrack Receiving Station Network had the specific responsibilities for acquiring the telemetered data. Data were received and recorded by the following stations:

Antofagasta, Chile
 Blossom Point, Maryland
 Fort Myers, Florida
 East Grand Forks, Minnesota
 Johannesburg, South Africa

Lima, Peru
 San Diego, California
 Woomera, Australia
 Quito, Ecuador
 Santiago, Chile

Acquisition of the data was accomplished in the following manner: During each period when data acquisition was required, the designated telemetry station commanded the data read-out from the Explorer XIII. Actually, since the satellite did not achieve the predicted orbit, the two telemeters were commanded whenever possible. Upon a successful interrogation, the signals from the two

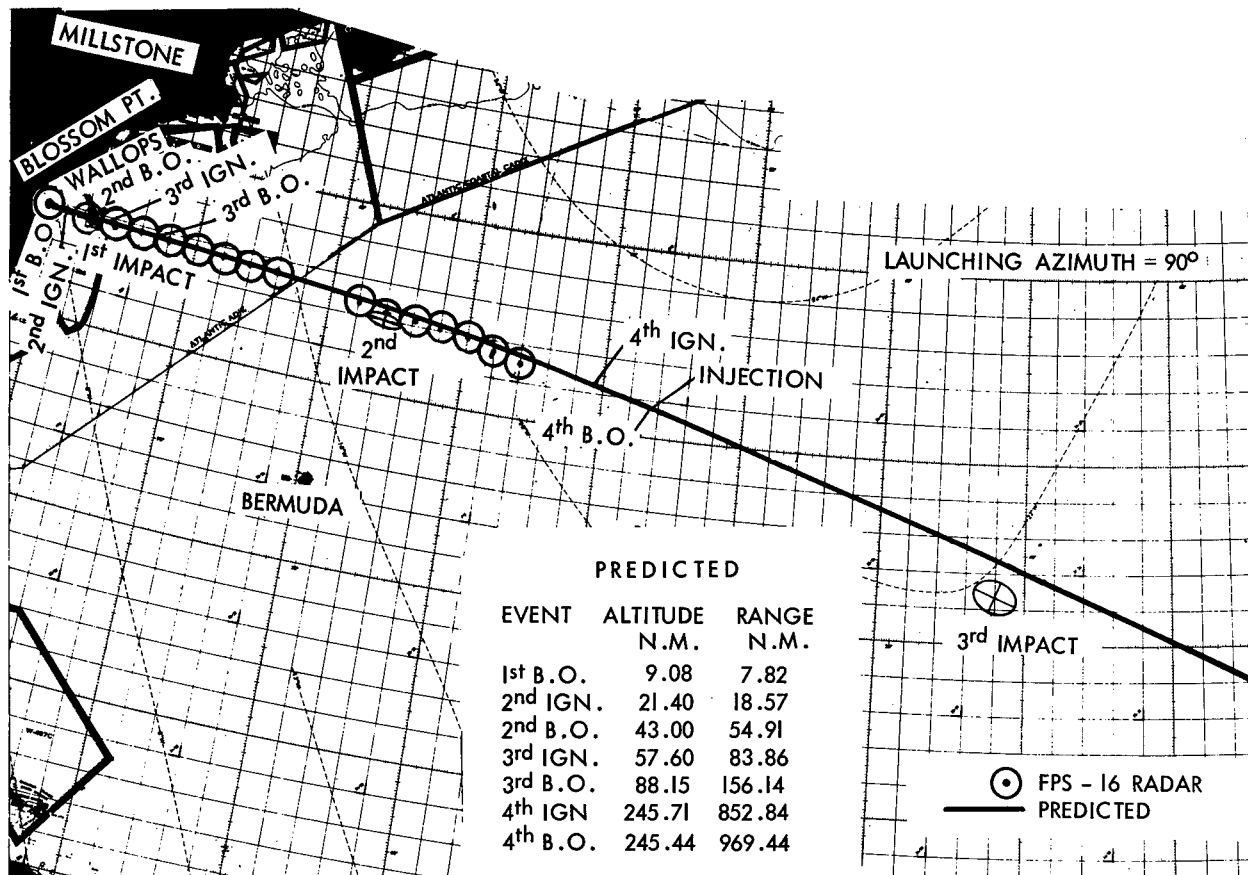


Figure II-22.- Ground track during ascent.

satellite telemeters were acquired by a circularly-polarized 136-mc antenna and fed from a pole-mounted preamplifier to a hybrid power divider. The outputs from the power divider were then separately fed to two telemetry receivers, tuned to 136.860 mc and 136.200 mc, respectively. The signals were amplitude demodulated in the receivers, with the detected outputs fed from their respective video amplifiers to a seven-channel tape recorder. At the same time that the detected signals were being recorded, the AGC (automatic gain control) level from one receiver, a 10-kc reference signal, and the Minitrack time code were also recorded.

Presented in table II-5 is a listing of the telemetry acquisitions made from the Explorer XIII from which data were obtained. Several interrogations were unsuccessful. The failure to receive data during several passes can be attributed to the rapidly decaying orbit and not knowing exactly when the satellite would be in position to be interrogated.

In addition to telemetry data acquisition, the Minitrack Network was responsible for satellite tracking. A total of 105 beacon signal acquisitions of the Explorer XIII were made.

The telemetry data received were recorded on magnetic tapes and these tapes were forwarded directly from the receiving station to the Langley Research Center for data reduction.

The telemeter receiving station set up at the launch site for final check-outs was also used to receive signals from the satellite during the first few orbits. Although the satellite was not commanded from Wallops, the radio beacon was monitored. When either Blossom Point or Fort Myers did transmit command signals, the data were received and recorded at Wallops. A photograph of the receiving station at Wallops is shown in figure II-23. In addition to an automatic tracking antenna, a manually operated antenna was used.



Figure II-23.- Wallops Island telemeter receiving station.

L-64-3086

SECTION VI - REFERENCES

- II-1. Staff of the Lewis Research Center: Micrometeoroid Satellite (Explorer XIII) Stainless-Steel Penetration Rate Experiment. NASA TN D-1986, 1963.
- II-2. Freudenberger, O. L., and Devoll, J. W.: Scout ST-6, Final Flight Report. Vought Astronautics Report No. AST/EIR-23.3, 12 Oct. 1961.

TABLE II-1.- SATELLITE WEIGHT BREAKDOWN

Component	Weight, lb
Forward shell: including sounding boards, power solar-cell trays, test solar-cell trays, heat-transfer ring, antennas, Cd-S cell experiment, mounting hardware, and wiring	27.90
Bulkhead assembly: including two 48-channel telemeters, plugs, and wiring	33.93
Pressurized-cell detector: including 160 cells at 0.137 lb each, mounting hardware, plugs, and wiring	47.98
Copper-wire-card detector: including mounting hardware	4.78
Steel-covered-grid detector: including mounting hardware	6.50
Payload support	4.37
Heat-shield bumper ring and balance weights	1.89
Total payload	127.35
Spent rocket motor	47.85
Spent spin motors	1.52
Upper "D" section	13.16
Total satellite	189.88

TABLE II-2.- SEQUENCE OF EVENTS

Time, sec	Event
0.00	First-stage ignition.
42.04	First-stage burnout.
74.16	Second-stage ignition; first-stage separation.
116.96	Second-stage burnout; third-stage rocket-motor fairing separation.
135.71	Third-stage ignition; second-stage separation; fourth-stage fairing separation; antennas erected.
172.11	Third-stage burnout.
482.19	Fourth-stage spinup.
484.04	Fourth-stage ignition; third-stage separation.
525.41	Fourth-stage burnout. Injection into orbit.

TABLE II-3.- COMPARISON OF INJECTION CONDITIONS

Injection condition	Minitrack data	Preflight calculations	Adjusted postflight
Altitude, nautical miles	246.466	244.84	246.05
Inertial velocity, ft/sec	25,381.1	25,539.5	25,260.4
Flight-path angle, deg	-3.987	-0.013	-4.396
Inertial heading, deg	102.352	103.388	103.554
Latitude, deg	35.885	35.739	35.637

TABLE II-4.- COMPARISON OF ORBITAL PARAMETERS

Parameter	Minitrack data	Predicted
Apogee altitude, nautical miles	619.4	529.2
Perigee altitude, nautical miles	60.93	244.4
Orbital period, min	97.247	99.061
Eccentricity	0.073786	0.037132
Inclination, deg	37.68	37.68
Argument of perigee, deg	180.9	108.35

TABLE II-5.- ORBITAL TELEMETRY HISTORY

Orbit	Date/Time	Minitrack station	Tape	Telemeter	Data-reduction process
Launch	25/18:29:44	Blossom Point	122A001	None	None
1	25/20:11:45	Grand Forks	122N001	B	Automatic
1	25/20:11:45	Blossom Point	122A002	B	Automatic
1	25/20:17:14	Blossom Point	122A002	A	Manual*
2	25/21:59:40	Fort Myers	122D001	None	None
7	26/06:34:00	Santiago	122J001	None	None
8	26/08:32:15	Santiago	122J001	None	None
9	26/10:02:40	Antofagasta	122H001	A	Manual
9	26/10:02:40	Antofagasta	122H001	B	Manual
10	26/11:46:00	Quito	122F001	A	Manual
10	26/11:55:00	Quito	122F001	B	Manual
13	26/15:13:30	Fort Myers	122D001	A	Automatic
13	26/15:15:02	Fort Myers	122D001	B	Automatic
13	26/15:13:30	Blossom Point	122A003	A	Automatic
13	26/15:15:02	Blossom Point	122A003	B	Automatic
14	26/16:58:06	Blossom Point	122A004	A	Automatic
14	26/16:58:06	Blossom Point	122A004	B	Automatic
14	26/16:58:06	Fort Myers	122D002	A	Automatic
14	26/16:58:06	Fort Myers	122D002	B	Automatic
15	26/18:40:57	Fort Myers	122D002	A	Automatic
15	26/18:40:57	Fort Myers	122D002	B	Automatic
20	27/03:03:00	Santiago	122J002	A	Manual
20	27/03:03:00	Santiago	122J002	B	None
21	27/04:45:56	Santiago	122J003	A	Automatic
21	27/04:45:56	Santiago	122J003	B	Automatic
22	27/06:21:30	Santiago	122J003	A	Automatic
22	27/06:21:30	Santiago	122J003	B	Automatic
23	27/08:03:14	Antofagasta	122H001	A	Automatic
23	27/08:03:14	Antofagasta	122H001	B	Automatic
25	27/11:15:40	Lima	122G01	None	None
27	27/14:03:00	Woomera	122-1	None	None
28	27/15:42:15	Woomera	122-1	A	Automatic
28	27/15:42:15	Woomera	122-1	B	Automatic
35	28/02:00:03	Antofagasta	122H001	A	Manual**
35	28/02:00:03	Antofagasta	122H001	B	Manual**
40	28/08:46:00	Antofagasta	122H001	B	Manual**

*Special process by GSFC.

**The temperatures of all systems had increased beyond design limits as a result of aerodynamic heating so that these data could not be used.

CHAPTER III

MECHANICAL DESIGN AND INTEGRATION

By Hugh C. Halliday
Langley Research Center

SECTION I - INTRODUCTION

The Explorer XIII spacecraft was designed to provide a suitable carrier for detectors selected to investigate the micrometeoroid hazard in space. The spacecraft (fig. III-1) is made up of the payload, ABL X248-A5 rocket-motor case, and the Scout fourth-stage structure. The design restraints placed on the payload by the launch vehicle were mainly upper limits as to weight and available space.

The final shape of the spacecraft was dictated, to a large extent, by the mission requirements and Scout fourth-stage configuration. During launch the vehicle subjects the payload to high static, dynamic, and centrifugal stresses which essentially determine the structural design requirements. These environmental conditions are as outlined in chapter VII, section II (see the section entitled "Environmental Test Specifications" for the vibration and shock specifications and the section entitled "Prototype Environmental Test Program" for the acceleration and spin specifications). The limited weight capability of the vehicle necessitated an extremely light-weight design. To minimize the amount of weight required for dynamic balancing, the payload was designed as symmetrically as possible about its spin axis.

SECTION II - DESIGN DETAILS

A drawing of Explorer XIII is shown in figure III-1 and an exploded view in figure II-2; a request form for an enlarged copy of this figure is included at the back of this report. The payload (fig. III-1) was mounted around the ABL X248-A5 rocket motor and fourth-stage Scout structure. The forward shell, telemeter-bulkhead, vehicle heat-shield bumper ring, and pressurized-cell-mounting-structure assemblies were attached to the payload adaptor which was bolted to the forward thrust face of the motor. The stainless-steel-grid-detector assembly and copper-wire-card-detector quadrants were mounted around the fourth-stage structure and attached to the sensor mounting ring. The aft end of the detector quadrants were restrained by the quadrant retaining ring and by leaf springs.

The forward shell (figs. III-1 and III-2) was an 0.031-inch-thick 410 stainless-steel fabrication. Mounted on it were power and test solar-cell trays, a heat-transfer band, impact detectors, cadmium-sulfide (CdS) cell detectors, and antennas (fig. III-1). The heat-transfer band was made of 1100-H14 aluminum and was 0.10 inch thick and 5 inches wide. Mylar strips,

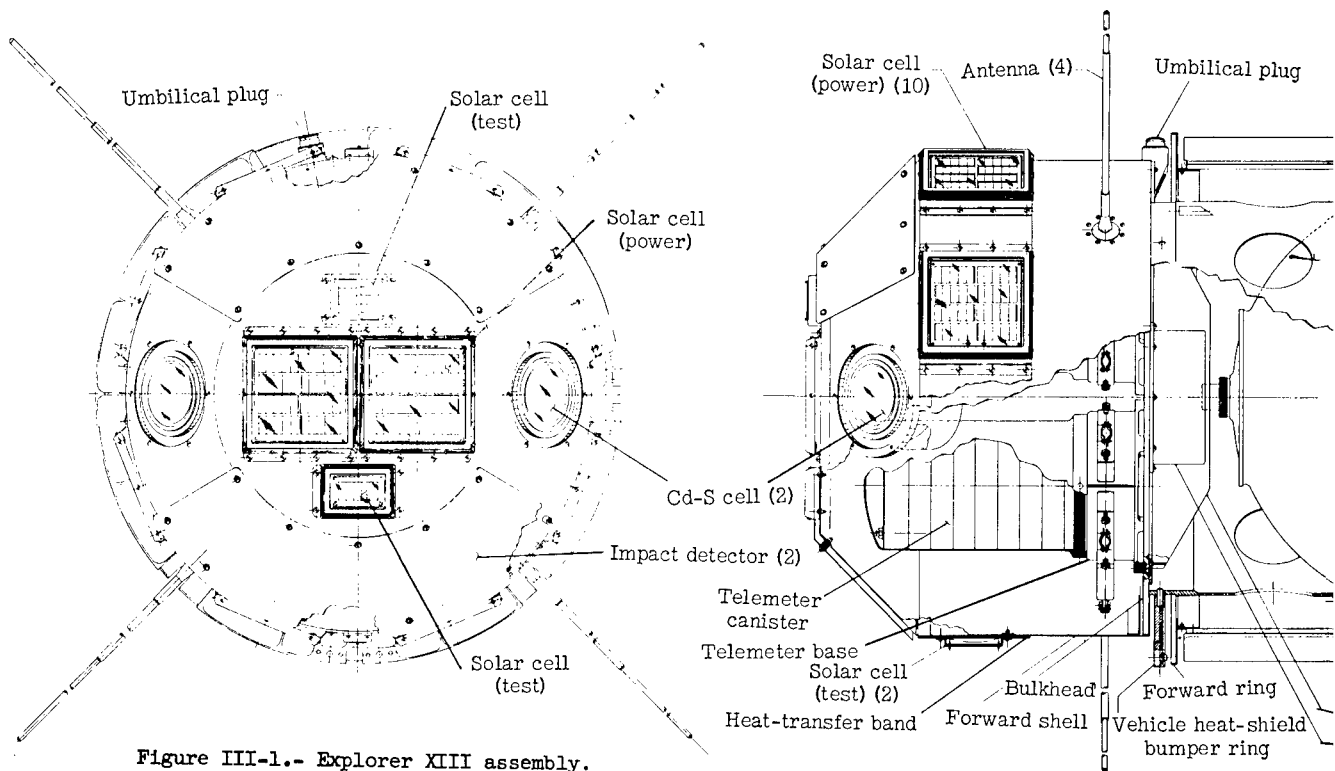


Figure III-1.- Explorer XIII assembly.

0.005 inch thick, were used to insulate this band from the forward shell. The eight power solar cells and two test solar cells were mounted on this band which was secured to the forward shell with metal-reinforced plastic screws. The antennas were made from 6061-T6 aluminum-alloy tubing, spring loaded so that they would erect after the fourth-stage heat shield was jettisoned.

The radio-beacon battery boxes, umbilical plug, power change-over relay, forward shell, telemeter stacks, and bulkhead stiffener were attached to an 0.25-inch-thick fiber-glass bulkhead (fig. III-1). The bulkhead stiffener, a magnesium fabrication, was required to provide additional support for the telemeters. The beacon battery boxes were made of glass cloth and polyester resin.

The telemeter bases (figs. III-1 and II-2) were machined from mild steel bar stock; after machining, the inside surfaces were silver plated to prevent rusting. Hermetically sealed connectors were then soldered in place and leak checked with a helium leak detector. The telemeter canisters (figs. III-1 and II-2) were machined from 2024-T4 aluminum-alloy bar stock.

The payload adaptor was an AZ31B magnesium welded structure machined to fit the rocket-motor case and receive the pressurized-cell-detector mounting structure, bumper ring, bulkhead stiffener, and bulkhead (fig. III-1). The pressurized-cell-detector mounting structure was a fabrication having forward and aft rings machined from AZ31B magnesium plate. The rings were riveted to an 0.016-inch-thick 2024-T3 aluminum-alloy cylinder. This cylinder had

This band was used to reduce circumferential temperature gradients which would affect solar-cell temperatures. The exterior surfaces of the impact detectors and forward shell were brought to a uniform finish by using a light aluminum-oxide grit blast. They were then put in an oven and heated to 600° F for 5 minutes. This gave the surface a stable finish with a known absorptivity to emissivity ratio. The back side of the impact detectors and the surfaces of the forward shell covered by the impact detectors, heat-transfer band, and solar-cell assemblies on the front surface of the forward shell were all painted black. The inside of the forward shell, exterior surfaces of the canisters, telemeter bases, and both sides of the bulkhead were coated with a film of vacuum-deposited gold. The gold plating was required to control the radiant heat exchange between the telemetry units and the inner surface of the forward shell.

The exterior penetration surface of the pressurized-cell detectors was coated with silicon monoxide. This coating not only controlled the detector temperature, but was the main factor in controlling the telemetry temperature as pointed out in reference III-2.

The outside of the pressurized-cell-detector mounting structure was painted white so that it would help to stabilize the pressurized-cell-detector temperature.

The inside and outside of the payload adaptor, the inside of the pressurized-cell-detector mounting structure, the inside of the copper-wire-card-detector quadrants, the outside of the fourth-stage structure that faced the payload, and the outside of the rocket motor that faced the payload were all covered with aluminum foil to reduce the rate of radiant-heat transfer from the hot fourth-stage motor case and nozzle to the payload immediately after burnout.

SECTION IV - FIT CHECK

In order to minimize payload-to-vehicle-integration problems that might arise during the final payload-to-vehicle assembly, a preliminary check of the assembly operation was conducted at the launch-vehicle contractor's plant. All the flight fourth-stage structure, a spent ABL X248-A5 rocket-motor case, the prototype payload, and the flight fourth-stage heat shield were used. It was found that some modifications to the heat shield were necessary. These modifications included adding additional wire hold-down clamps to prevent the pressurized-cell detectors from being damaged during launch and modifying the heat-shield bumper ring. Also, techniques had to be devised for assembling the fourth-stage heat shield in order to prevent damage to the copper-wire-card detectors.

SECTION V - BALANCING AND FINAL ASSEMBLY

In order to reduce the velocity dispersion angle of the spacecraft in flight, it is necessary that the principal axis misalignment be reduced to a

minimum, as shown in reference III-3. This was accomplished by preflight checks and balancing operations at Wallops Island.

The assembled fourth-stage structure with the third-stage structure (lower transition "D") were mounted on the balancing table and the live X248-A5 motor was installed. The misalignment of the rocket motor adjacent to the forward thrust face with respect to the spin axis was checked (fig. III-2) and found to be within acceptable limits (± 0.008). The spin drive shaft of the balancing table was coupled to the blowout diaphragm. Spinning the spacecraft in this manner allows it to spin on the spin bearing leaving the third-stage structure stationary. The assembled fourth-stage structure and motor were spun up to the specified spin rate (180 rpm) to check for unbalance. The payload was then assembled around the ABL X248-A5 motor and fourth-stage structure by using self-locking or safety-wired fasteners. Final dynamic balancing of the payload, motor, and fourth-stage structure was then accomplished by using a total balance weight of 212 grams (7.5 oz.).

The fourth-stage heat shield was then installed to provide protection for the spacecraft while it was being removed from the dynamic balancing facility (fig. III-3) and transported to the electronic checkout area where the fourth-stage heat shield was removed. After the electronic checkout and just prior to the final fourth-stage heat-shield installation (figs. II-16(a) and (b)), a final inspection was made of all detectors, hardware, and fasteners. The spacecraft with the fourth-stage heat shield installed was then transported to the launch tower where it was mated to (fig. II-17) the assembled first, second, and third stages of the launch vehicle.

SECTION VI - REFERENCES

III-1 Staff of Lewis Research Center:

Micrometeoroid Satellite
(Explorer XIII) Stainless-Steel
Penetration Rate Experiment.
NASA TN D-1986, 1963.

III-2. Hastings, Earl C., Jr., Turner, Richard E., and Speegle, Katherine C.: Thermal Design of Explorer XIII Micrometeoroid Satellite. NASA TN D-1001, 1962.

III-3. Young, George R., and Buglia, James J.: An Analysis of the Coning Motions of the Final Stages of Three NASA Scout Development Vehicles. NASA TN D-1396, 1962.



L-61-3863

Figure III-3.- Explorer XIII being removed from balancing facility.

CHAPTER IV

TELEMETRY DESIGN

By Walt C. Long
Langley Research Center

SECTION I - INTRODUCTION

The basic telemetry-system concept for Explorer XIII was selected primarily on the basis of demonstrated performance (ref. IV-1). The successful orbiting of Vanguard II (1959 Alpha) and Vanguard III (1959 Eta) had proven the basic design of the tracking and telemetry concepts which were compatible with mini-track network. It was necessary for the NASA Langley Research Center (LRC) to expand the system to provide a 48-channel telemetry system. Two of these systems were used in the Explorer XIII in order to provide the required channel capacity.

A study of the anticipated data revealed that the prime data (the micrometeoroid-penetration data) would occur at an extremely slow rate and that one data readout per day from the satellite would be adequate to satisfy the needs of the program. Some of the secondary data would have been made more meaningful by obtaining real-time data, but it was believed that the results would not justify the complexity and effort that would have been required. A study revealed that the penetration detectors gave a permanent and irreversible output upon being penetrated by a micrometeoroid and that the impact detectors gave a momentary pulse output upon micrometeoroid collision. Therefore, data storage was inherent in the penetration detectors but was required for the impact detectors. An events-counting and storing system was provided with sufficient capacity to allow up to 24 hours to elapse between readouts with little chance of recycling between readouts.

In the planned orbit, transmission ranges would be not less than 244 nautical miles (perigee) under any condition and quite often would be as great as 1,000 nautical miles. The radio-frequency links were therefore designed for the 1,000-nautical-mile range. The calculated signal-to-noise ratios are shown in figure IV-1. From this figure, it can be seen that little difficulty was anticipated in the data acquisition and data reduction. Section IV of this chapter and Section IV of Chapter VIII give some of the operational results.

SECTION II - SYSTEMS DESCRIPTION

The telemetry system for Explorer XIII consisted of two separate and independent telemeters for data transmission and a radio beacon for tracking. The two telemeters were of the data storage-command readout type wherein data were collected during the satellite's orbit(s) and read out when within range of a ground receiving station. Data storage was sufficient to allow up to 24 hours

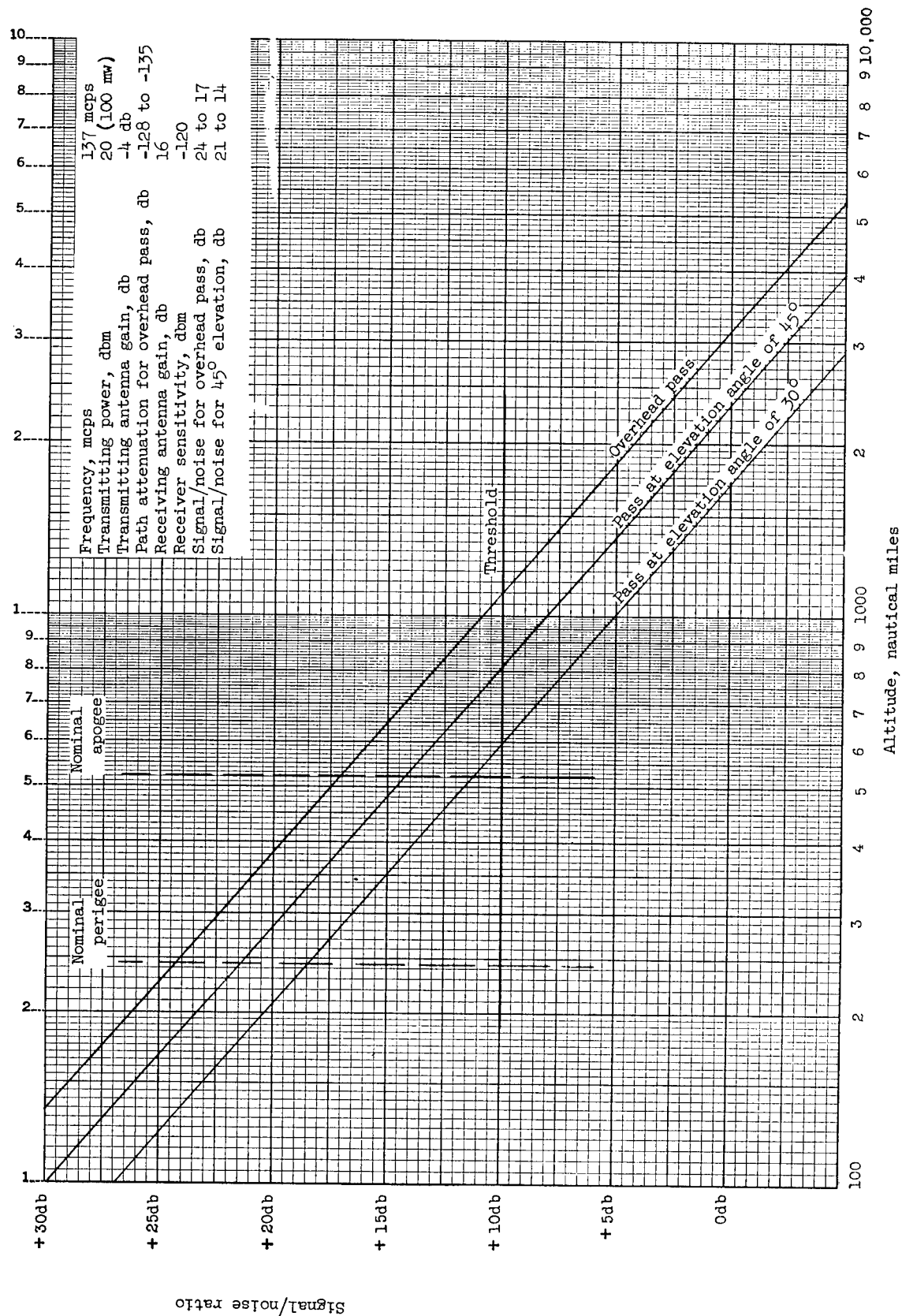


Figure IV-1.- Anticipated signal-to-noise ratios.

to elapse between readouts. Readout was nondestructive in that stored data were not erased. Two radio frequencies were used for data transmission, but only one command radio frequency was used for interrogation.

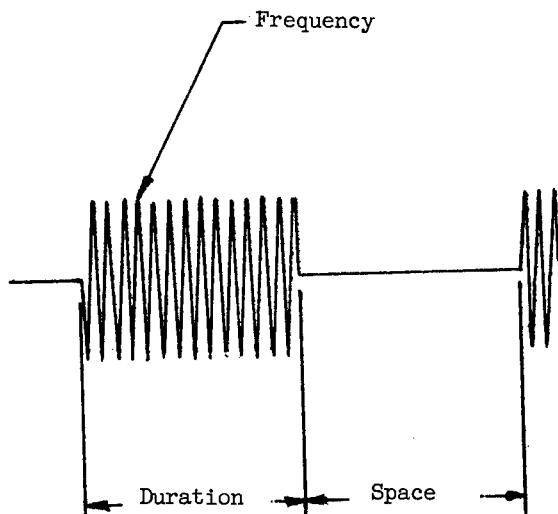


Figure IV-2.- Telemeter format.

The telemetry format was a time-division multiplex scheme wherein a series of subcarrier oscillators were sequentially pulsed on and off (fig. IV-2). Information was conveyed by the frequency of the pulsed subcarrier oscillator, by the duration of the pulse, and by the spacings between pulses. The signal consisted of 16 subcarrier oscillator pulses for a total of 48 channels of information for each telemeter.

The two telemeters were constructed as independently as was possible in order to improve overall system reliability. Separate solar cells and batteries were used to supply power as well as separate electronics for handling the data. A common antenna system was used for the two telemeters, but the two telemeters were

connected through a hybrid junction so as to be electrically isolated. The sensors were divided into two groups as nearly equal as possible and telemetered separately. Each sensor was connected to only one telemeter, but the division was made so that sensors of the same type and sensitivity were equally distributed between both telemeters. This meant that if one telemeter failed, the experiment was not lost but that the exposed area was halved. A block diagram of the telemetry system is presented in figure IV-3 and the pertinent characteristics in table IV-1. The telemetry system consisted of three major units: An "A" telemeter, a "B" telemeter, and a radio beacon.

Telemeters: The "A" and "B" telemetric assemblies were quite similar and consisted of:

1. One signal conditioning module each
2. One encoder module each
3. One 16-channel subcarrier oscillator module each
4. One events-counting and storage module in the "A" assembly and two in the "B" assembly
5. One impact-detector amplifier and wave-shaper module each
6. One transmitter and diplexer module each
7. One secondary Ni-Cd battery module each
8. One command receiver and turnoff timer module each
9. One regulated dc-dc converter each

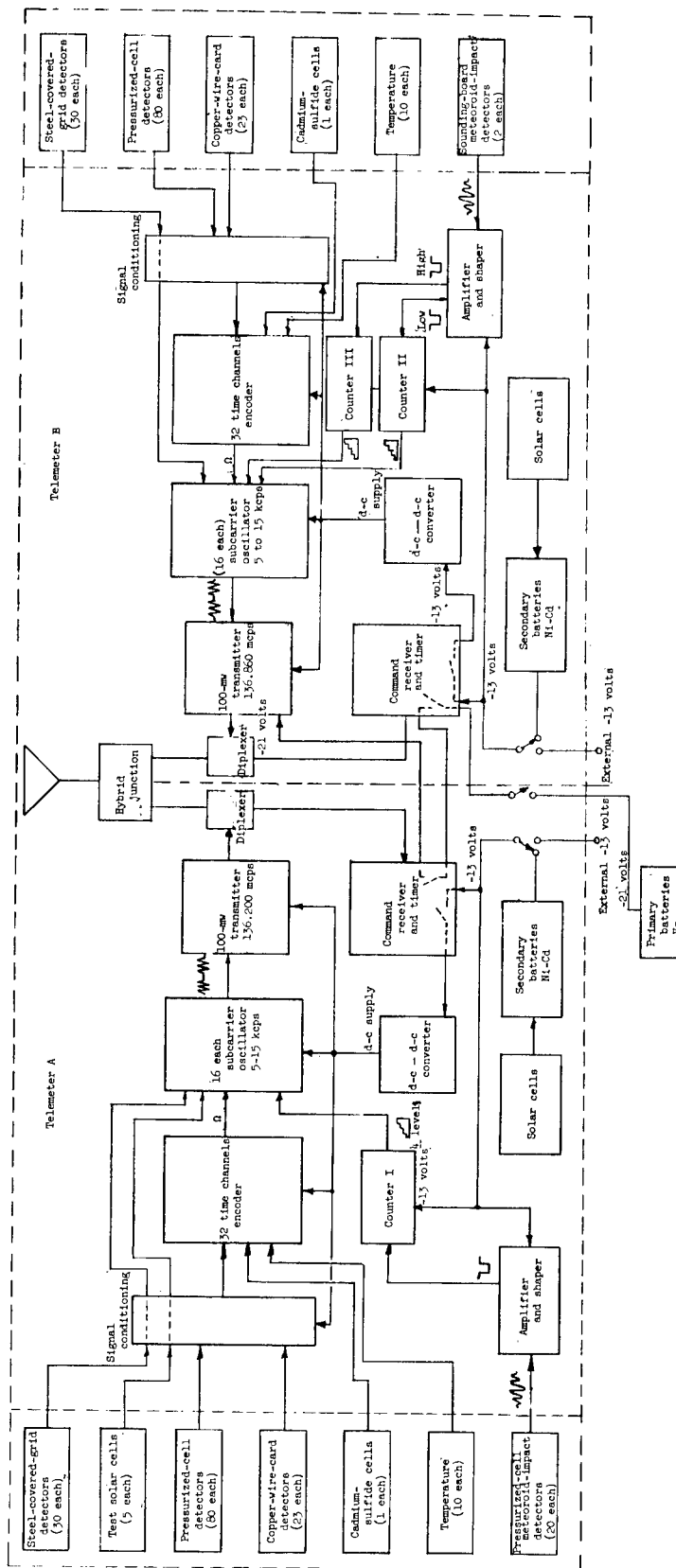


Figure IV-3.- Block diagram of telemetry system.

The command receivers, the microphone amplifiers, and the counters were continuously energized. Upon reception of an interrogation command, the dc-dc converters were energized and in turn furnished power to the encoders, the sub-carrier oscillators, and the transmitters. The encoders then sampled each sensor approximately three times per second and generated a telemetry signal which then amplitude modulated the transmitters. After a 1-minute interval, the dc-dc converters were deenergized by the internal timers. The turnoff timers were not synchronized so the turnoff times did not necessarily coincide.

Radio Beacon.- The radio beacon consisted of the "B" telemeter transmitter module (item 6) and two primary (Hg) battery packs. The radio beacon had its power turned on prior to launch and was to transmit until its primary batteries were exhausted (about 1 week). Its power was routed through interlocks in the "A" and "B" command receivers so that it was silenced during interrogation of either telemeter (fig. IV-3). This override feature allowed for interrogation of the telemeters while on the launch pad for checkout purposes and during flight for readout purposes.

Telemetry Construction.- All modules except for the transmitter, batteries, and dc-dc converter were constructed on a printed circuit board and potted with a foam-in-place polyurethane potting resin. The transmitter was constructed on an aluminum chassis and potted with the polyurethane resin. The Ni-Cd battery module was potted with epoxy for added strength. The potting material was used to obtain the final module shape 5.50 inches in diameter and 1.00 inch high.

The dc-dc converter was constructed on an aluminum chassis and had an aluminum case for added rigidity. The modules were stacked one upon another and the seven (eight for the "B" telemeter) module stack mounted upon a base containing the entrance plugs and associated wiring. Two 1/4-inch rods were run through the modules to bolt them to the base and a heavy walled canister was placed over them to give the modules the required strength and rigidity. The dc-dc converter was placed in the underside of the base and covered. Hermetically sealed connectors were used for entering the telemeters and all mechanical interfaces were sealed by using "O" rings. The telemeters were then pressurized to 20 psia. Figure IV-4 is a cutaway view of the "B" telemeter showing the construction methods and figure IV-5 is a photograph of the "A" telemeter with the canister removed. The thermal-design factors which apply to the telemeters

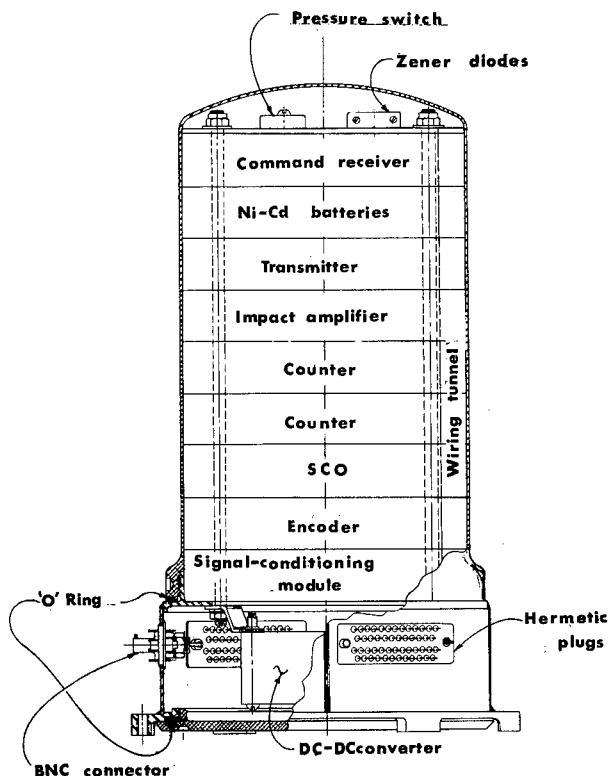
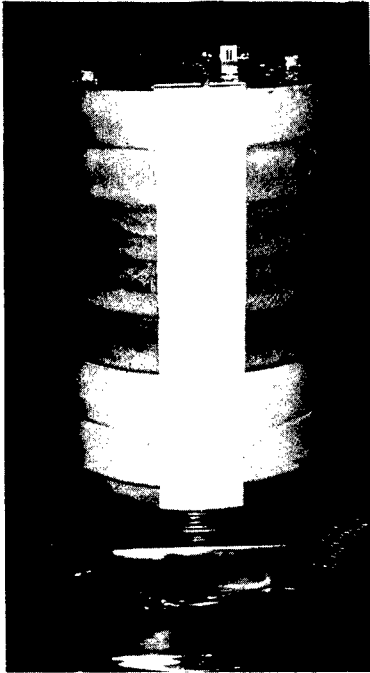
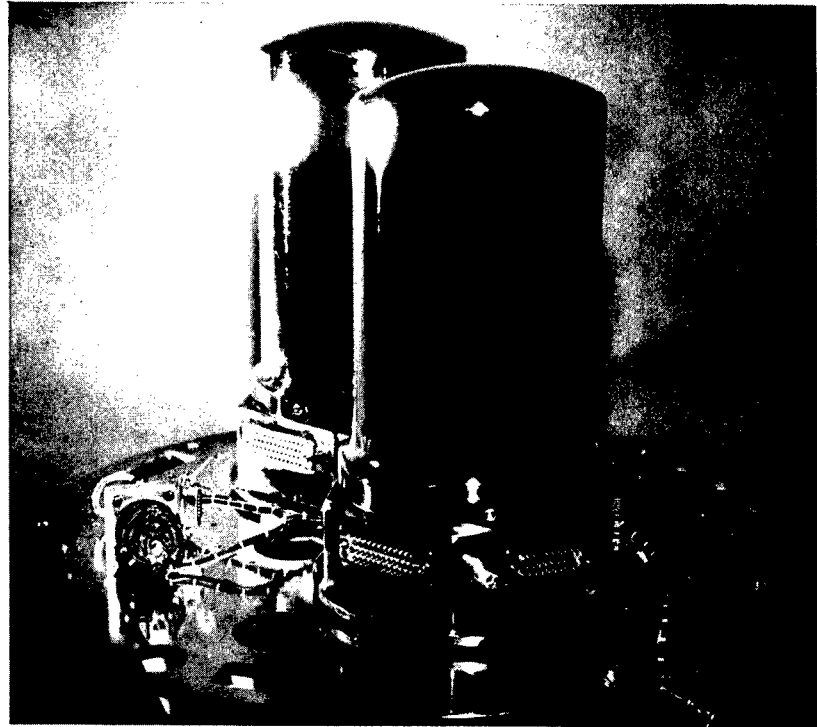


Figure IV-4.- Cut-away view of telemeter B assembly.



L-62-1572
Figure IV-5.- Telemeter A
assembly.



L-62-1568
Figure IV-6.- Telemetric assemblies on fiber-glass
bulkhead.

are covered in Chapter VI. Figure IV-6 shows the "A" and "B" telemeters mounted upon a fiber-glass bulkhead.

Encoding System.- The function of the encoding system is to sample the various sensors sequentially and to generate a signal suitable for telemetry. The encoding system is composed of three subassemblies; each subassembly consists of a signal conditioning module, an encoder module, and a subcarrier oscillator (SCO) module. The signal conditioning module accepts inputs from the various sensors and operates upon them to form inputs acceptable to the encoder module and the subcarrier oscillator module. Section IV of this chapter on "Channel Allocations" presents a discussion of these procedures. The encoder module accepts its inputs from the signal conditioning module and generates a nonsynchronous pulse-duration modulation (PDM) wave train. The SCO's accept their inputs from the signal conditioning module and generate frequencies which are determined by their inputs. The SCO's are sequentially gated on and off by the PDM and other wave trains from the encoder and their outputs are summed into a common signal line. Only one subcarrier oscillator is gated on at any time.

Encoder Module.- The encoder circuitry consists of a timing multivibrator in a Royer circuit (ref. IV-2) for generating the duration and space times, a solid-state commutator for switching in the proper sensors, and a scale of 16 matrix for control purposes. Figure IV-7 shows the encoder, and circuit diagram 1 (at the end of this chapter) is a schematic of the encoder. Transistors Q_{33} , Q_{34} , and the timing multivibrator transformer comprise the timing multivibrator; Q_1 to Q_{32} comprise the solid-state commutator; Q_{35} to Q_{39} supply

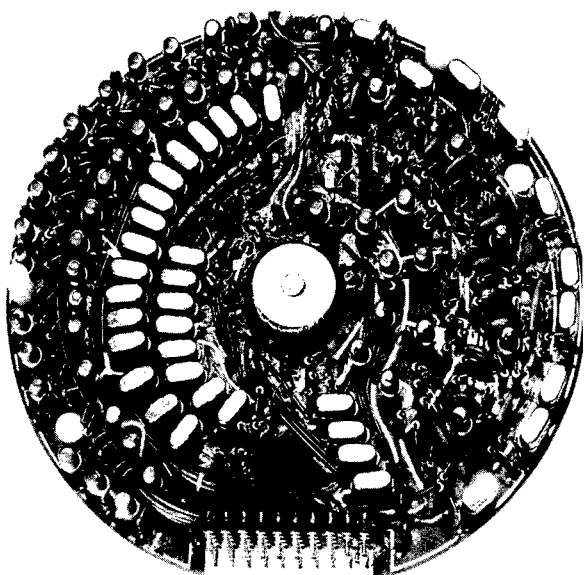


Figure IV-7.- Forty-eight channel encoder module.
L-60-3770

gating for the SCO module; Q_{40} to Q_{59} comprise the scale-of-16 counter; and Q_{60} to Q_{87} comprise the matrix which supplies gating pulses to the solid-state commutator and to the SCO module. Figure IV-8 is the timing diagram for the encoder and shows the relationship of the various waveforms. Note that the sync starts on S16 rather than on D1 and that all base gates start concurrently with a space start and step to the next base gate concurrently with spaces; that is, base gate A occurs for S16 and D1, base gate B occurs for S1 and D2, and so forth. This scheme was necessitated by the subcarrier oscillators. The scale-of-16 counter and matrix was driven from the oscillator gating and suffered a propagation delay of about 5 microseconds. If the commutation had occurred at the beginning of a duration, the wrong oscillator would be gated on during this 5-microsecond delay and would have distorted the leading edge of

the duration burst. Commutating at the beginning of a space allowed up to 4 milliseconds for switching the subcarrier oscillators.

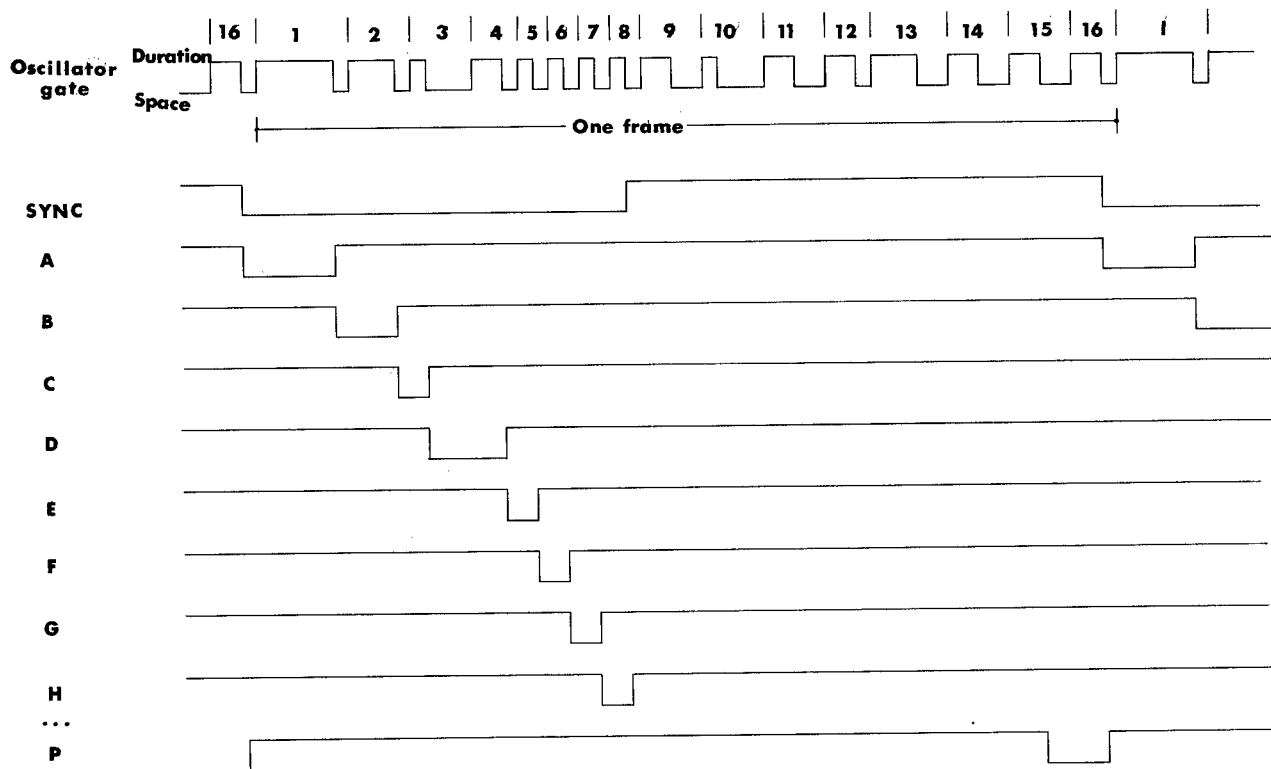
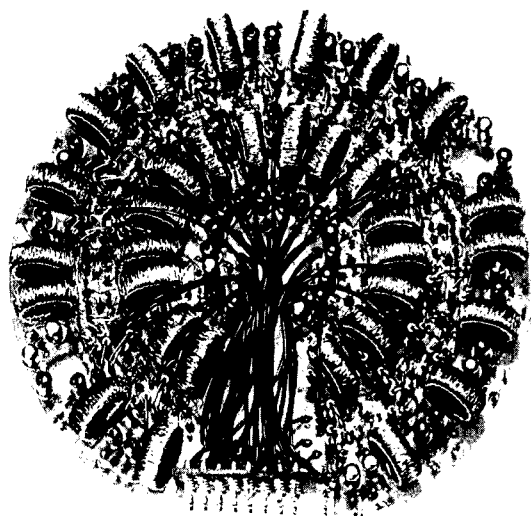


Figure IV-8.- Encoder timing diagram.



L-60-3768

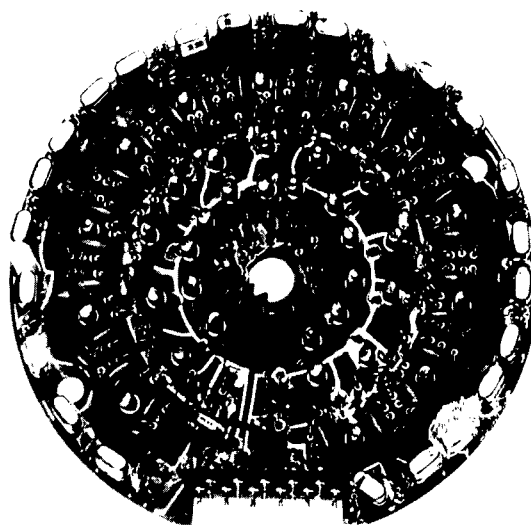
Figure IV-9.- Subcarrier oscillator module.

Subcarrier Oscillator Module.- The subcarrier oscillator module (fig. IV-9) consisted of 16 identical subcarrier oscillators. These oscillators accepted their inputs from the signal conditioning module and their gate signals from the encoder. The SCO's were sequentially gated on by the encoder and their outputs summed onto a common signal line. Since the oscillator gating was time-division multiplexed, one signal only was present at any one time.

The basic subcarrier oscillator (circuit diagram 2) consists of a magnetic multivibrator in a Royer (ref. IV-2) circuit. The theory of operation is the same as for the timing multivibrator in the encoder; Q1 and Q2 and switching transistors and are either saturated or nonconducting. Core 1 and

core 2 were tape wound with a square loop material. Transistor Q3 and core 2 form an inductive voltage absorber that varies the effective voltage across core 1, and therefore the switching frequency of core 1. The output was a square wave and was fed to the modulator. Blocking diodes were used in the output lines so that the 15 "off" subcarrier oscillators would not load down the "on" subcarrier oscillator. The absence of filtering or charging circuits permitted the SCO to be gated on and off and to become stabilized within one-half cycle of operation.

Counter Module.- The events-counting and storage system accepted pulses from the impact-detector amplifiers, counted these pulses, and generated output levels suitable for the subcarrier oscillators. The counter consisted of 12 complementary flip-flops connected in cascade which gave the unit a total-count capacity of 4,096. The counter did not have reset capability since nondestructive readout was a requirement of the system telemetry. With the application of the 4,096th pulse, the counter cycled and began counting anew. The outputs of the counters were weighted and summed so as to form octonary numbers. Four of these numbers modulated the subcarrier oscillators. The units are shown in figure IV-10 before potting; the impact-detector amplifiers are described in Chapter XII.



L-60-3767

Figure IV-10.- Events-counting and storage system.

A schematic of the complementary flip-flop (ref. IV-3) used in the events-counting and storage system is shown in circuit diagram 3. One NPN and one PNP transistor conduct in each of the two states of the flip-flop, either Q1 or Q3 or Q2 and Q4. This method of two-transistor regeneration gave a circuit gain of beta squared and thus allowed operation at a power level of less than 1 milliwatt. The steering transistor, Q5, conducted only during switching. The application of a 2-volt negative-going pulse switched the flip-flop and thus the polarity of the voltage across Q5. Transistor Q5 was chosen so as to have gain in the normal and inverted configurations.

The interconnections of the 12 flip-flops are shown in the events-counting and storage-block diagram (fig. IV-11). The 12 flip-flops were divided into two equal groups of six each and stacked to operate from the available -13-volt power supply. The outputs contained a common mode voltage which was bucked out in the subcarrier oscillator inputs.

Transmitter Module.- The transmitters were of the master-oscillator power-amplifier type wherein the oscillator was crystal stabilized at the output frequency and the final amplifier was base modulated. The transmitter provided a minimum carrier output through the diplexer of 100 milliwatts at a collector supply of -21 volts d-c. Modulated output was typically 150 milliwatts. Total transmitter input was 750 milliwatts which gave an efficiency of 20 percent.

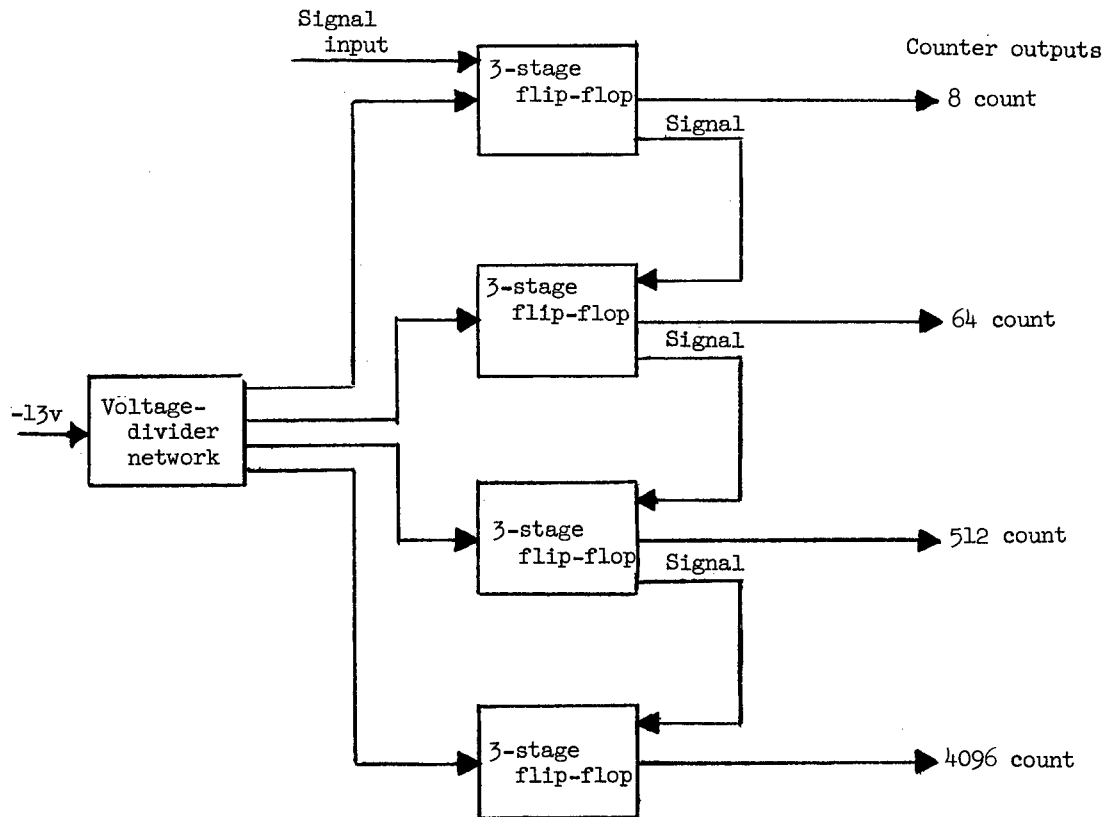


Figure IV-11.- Counter-module block diagram.

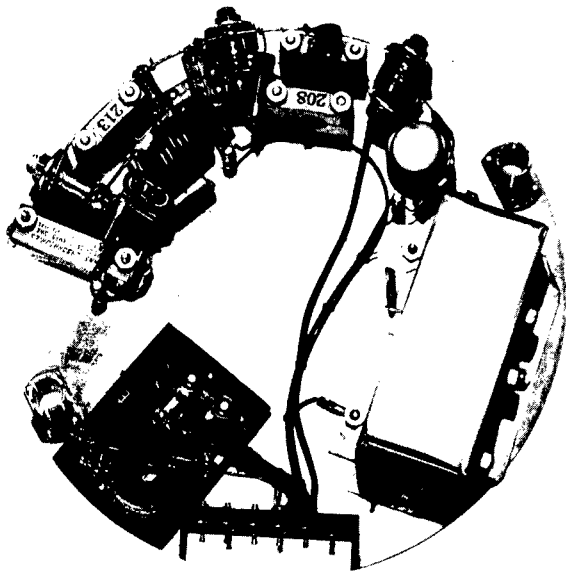


Figure IV-12.- Transmitter module. L-60-3769

The transmitter is shown in figure IV-12 and the transmitter schematic is shown in circuit diagram 4. Transistor Q1 and associated circuitry compose the crystal stabilized oscillator; Q2, Q3, and associated circuitry compose the base-modulated power amplifier; Q4, Q5, and associated circuitry compose the modulator; L6, L7, C15, and C19 compose a frequency-selective diplexer. This diplexer serves the dual purpose of routing the telemetry rf (radio frequency) signal from the transmitter to the antenna and the command receiver rf signal from the antenna into the command receiver.

The modulator was a saturating (clipping) type wherein the output amplitude was constant so long as the input remained above a threshold level.

This type of operation necessarily resulted in a square-wave output. Sine wave or linear operation could have been used with a more complex form of amplitude stabilization. An examination of the spectrum of a square wave reveals an infinite series of harmonics. Stated mathematically, the Fourier series is:

$$e(t) = E \frac{4}{\pi} \cos \omega t - E \frac{4}{3\pi} \cos 3\omega t \\ + E \frac{4}{5\pi} \cos 5\omega t - \dots$$

A typical transmitted spectrum is shown in figure IV-13 which shows both the A and the B telemeter spectra. Theoretically, there should be more than 2-percent crosstalk even with a 660-kcps spacing, but bandwidth limitations in the modulator and in the final tank circuit kept the crosstalk well below 0.1 percent. Modulating and detected waveforms are shown in figure IV-14. The detected waveforms were taken by using a receiver with a 50-kcps bandwidth.

Command Receiver Module.- The command receivers (fig. IV-15) used in Explorer XIII were similar to those used in Vanguard II and III (ref. IV-4). The major changes were to update components and to add a 1-minute turn-off timer. In

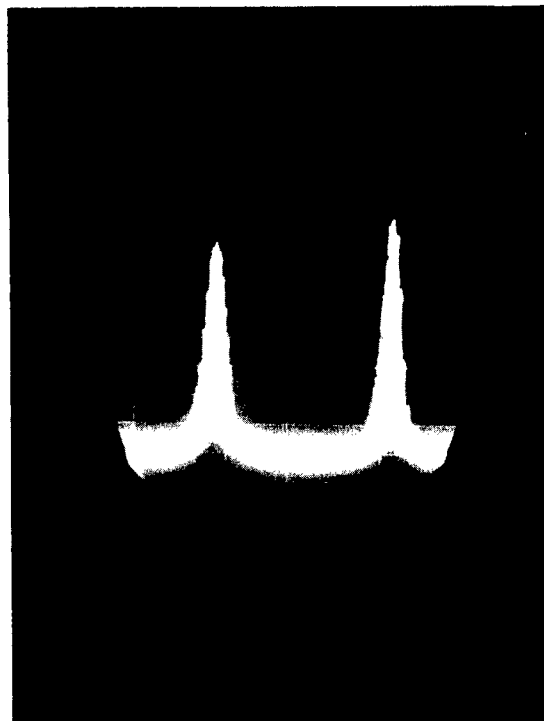
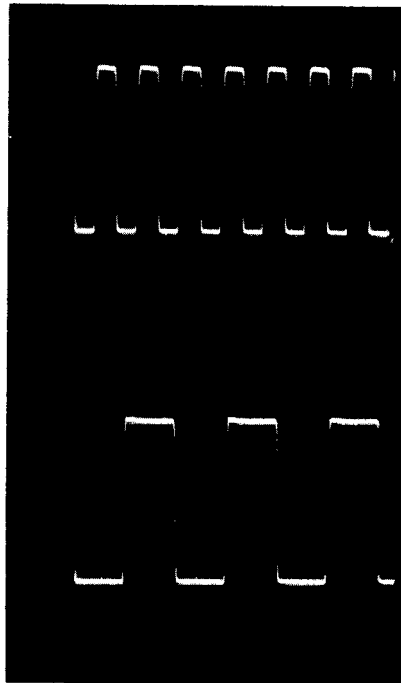
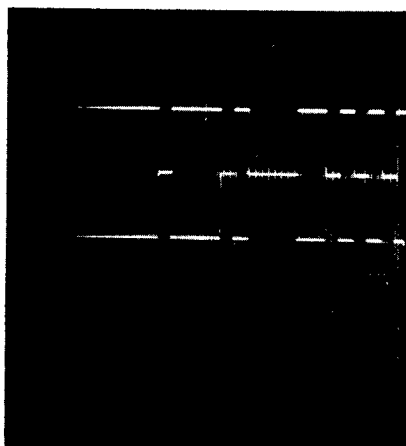
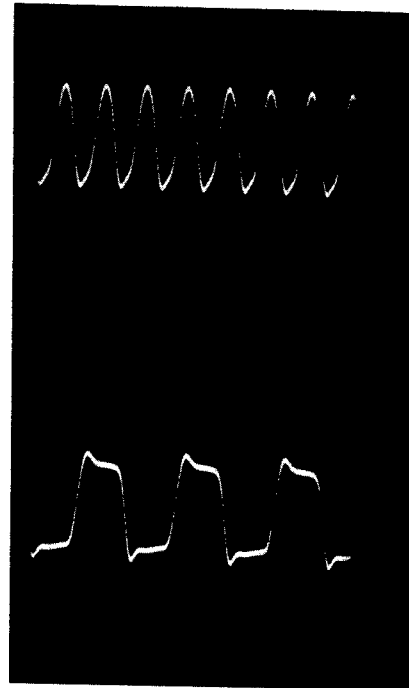


Figure IV-13.- Transmitted spectrum. L-64-3087

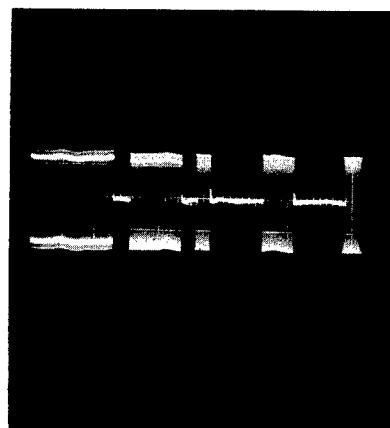


15 kcps

5 kcps



Duration - space
waveforms

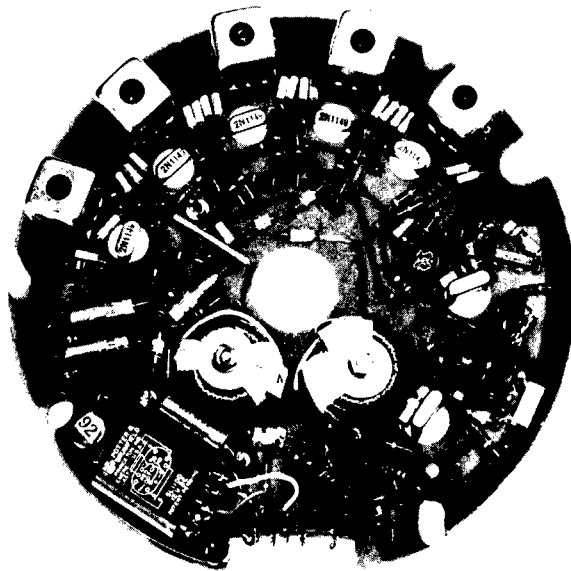


Modulator waveforms

Receiver waveforms

Figure IV-14.- Modulation waveforms.

L-64-3088



L-60-3772

Figure IV-15.- Command receiver module.

order to increase the reliability of the system, it was decided to accomplish data readout by using only one ground action; that is, the satellite telemeters were turned on by a ground command, the telemeters transmitted their data, and then automatically turned themselves off after about a 1-minute interval without requiring an additional ground action.

The command receivers were double-conversion superheterodynes and were fixed tuned to one command frequency. As shown in circuit diagram 5, the first and second converters Q1 and Q2 were crystal stabilized in order to obtain the required frequency stability. The second intermediate frequency (i.f.) amplifiers (Q3 to Q6) provided the major portion of the system gain (over 100 decibels). The i.f. stages were single-tuned transformer coupled and provided a bandwidth of 20 kcps between the 3-decibel points. Transistor Q7 and associated circuitry formed a "weak-signal" detector; L12, L13, C50, C51, and C52 composed an overcoupled double-tuned filter with a 5-percent bandwidth; Q8, D5, and associated circuitry composed a peak-to-peak detector; Q9, Q10, and associated circuitry composed the relay amplifier. RE-1 is a dual-coil magnetic-latching relay. The relay was turned on by the command receiver and turned off by the interval timer. The interval timer was comprised of Q11, Q12, and Q13, and associated circuitry.

Dc-dc Converter.- The dc-dc converter furnished power to the encoder, sub-carrier oscillators, and transmitter at the appropriate voltages. The output voltages were held to within plus or minus 1 percent over an ambient temperature range from -10°C to 60°C , with an input change of plus or minus 10 percent, and with a load decrease of 50 percent; this was accomplished with a conversion efficiency of 80 percent. The converter consisted of two units, a regulator and a dc-dc transformer in a Royer circuit (ref. IV-2). The dc-dc converter is shown in figure IV-16, and the dc-dc converter schematic is shown

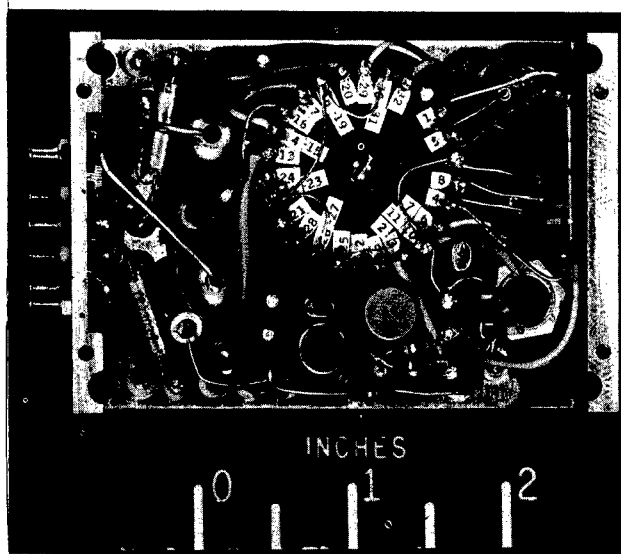


Figure IV-16.- Dc-dc converter. L-60-8607

in circuit diagram 6. Q1, Q2, Q3, D1, and D2 form a series regulator. Transistors Q4 and Q5 along with the square-loop core form the d-c-to-a-c converter and D3 and D12 supply the output voltages. Diodes D13 and D14 supplied bias for Q4 and Q5; this method of obtaining the switching-transistors bias made the dc-dc converter short-circuit proof.

SECTION III - ANTENNA SYSTEMS

Due to the initial spinning and the eventual tumbling modes of the satellite, an isotropic antenna system was a necessity. An additional requirement was that the antennas be stowable during the launch phase when the heat shields were on and that they automatically unfold when the heat shields were jettisoned. The mechanical design of this feature is covered in chapter III.

The selected antenna system consisted of four erectile monopoles spaced 90° electrically and 90° physically around the satellite body in a turnstile array. This type of antenna system provides circular polarization when viewing the satellite head on, linear polarization when viewing broadside, and circular polarization of the opposite sense when viewing tail on. Since weight considerations necessitated utilizing the same antenna system for transmission from and reception at the satellite for both telemeters, a hybrid junction (ref. IV-5) was used to tie the telemeters to the antenna system while still isolating them. A frequency-selective diplexer was used in each telemeter to separate the transmitters and receivers. The overall system is shown in the telemeter block diagram (fig. IV-3) and the hybrid-junction turnstile antenna system in figure IV-17.

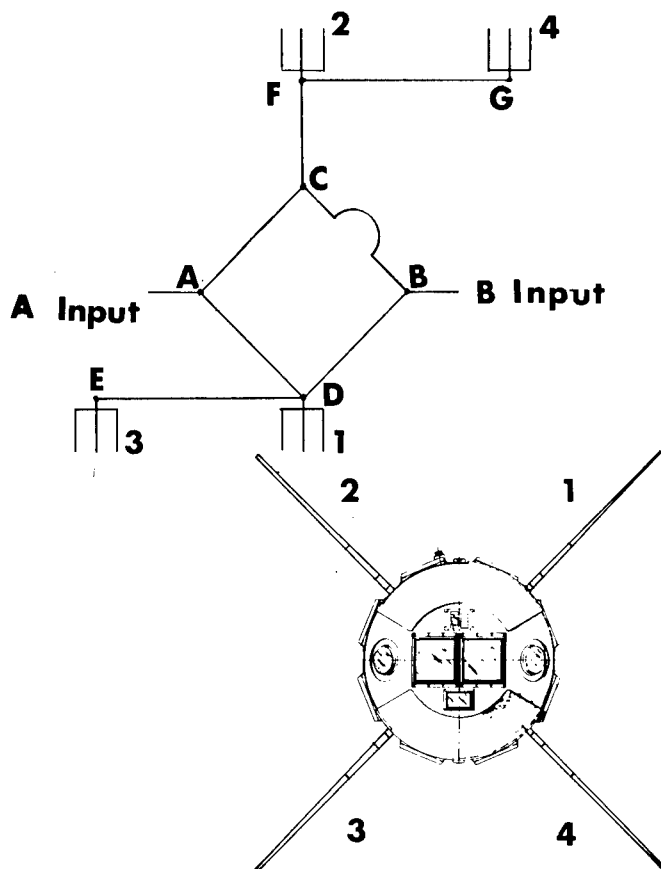


Figure IV-17.- Hybrid junction and turnstile antenna system.

The hybrid junction provides two isolated inputs and two isolated outputs with equal power division between the two outputs. The hybrid junction, when terminated in a resistive 50-ohm load, is capable of maintaining a 40-decibel isolation between inputs and a power division equal to ± 1 decibel between outputs over a 4-percent frequency range. The hybrid-junction turnstile antenna system was usable over a 20-percent frequency range.

The operation of the hybrid junction may be understood by noting that there are two paths from point A to point B (ACB and ADB) and by noting that the distances are unequal by one half wavelength or 180 electrical degrees. Assuming proper operation, the signal through path ACB will arrive 180 electrical degrees later than the signal through ADB and they will be in counterpoise. The net result is that the power at point B due to that at A is zero. The inverse process from B to A is analogous. The phasing of the turnstile array may be understood by noting the line lengths from the inputs to the individual monopoles. The lines DE and FG are one half wavelength each and are used to connect monopoles 1 and 3 (2 and 4) together as dipoles. Monopoles 1 and 3 (2 and 4) are diametrically opposed

and the two dipoles are in quadrature. The line lengths from point A to the monopoles 1, 2, 3, and 4 are $1/4$, $1/2$, $3/4$, and 1 wavelength so that the signals are electrically spaced by 90° . Therefore, the resulting voltage maxima rotate. It should be noted that the line lengths from point B to the monopoles 1, 2, 3, and 4 are $1/4$, 1, $3/4$, and $1\frac{1}{2}$ wavelengths so that the voltage maxima occur in the opposite rotating sense.

Since the system is passive in nature, the inputs and outputs may be interchanged without affecting system operation. This allows both transmission and reception through the hybrid junction and antenna system. The antenna patterns for the spinning and tumbling modes are shown in figures IV-18 and IV-19, and VSWR is shown in figure IV-20.

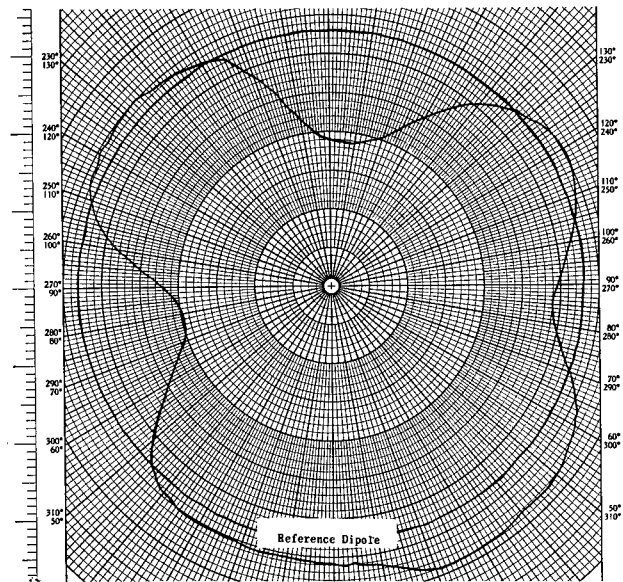


Figure IV-18.- Antenna pattern for a spinning satellite; stable mode.

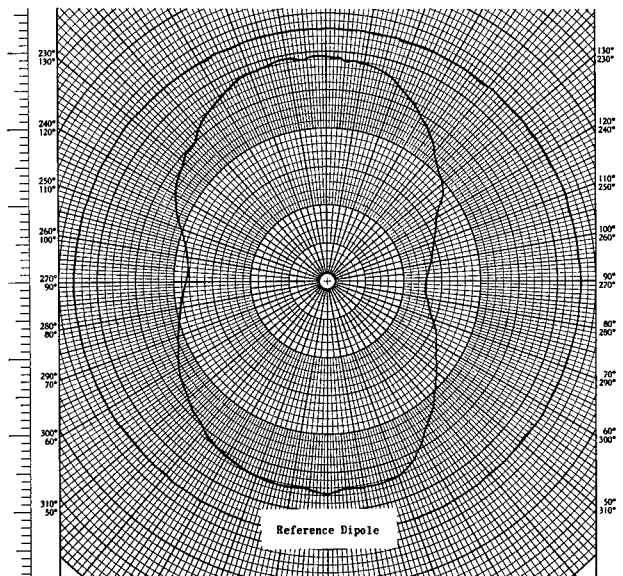


Figure IV-19.- Antenna pattern for a tumbling satellite; tumbling mode.

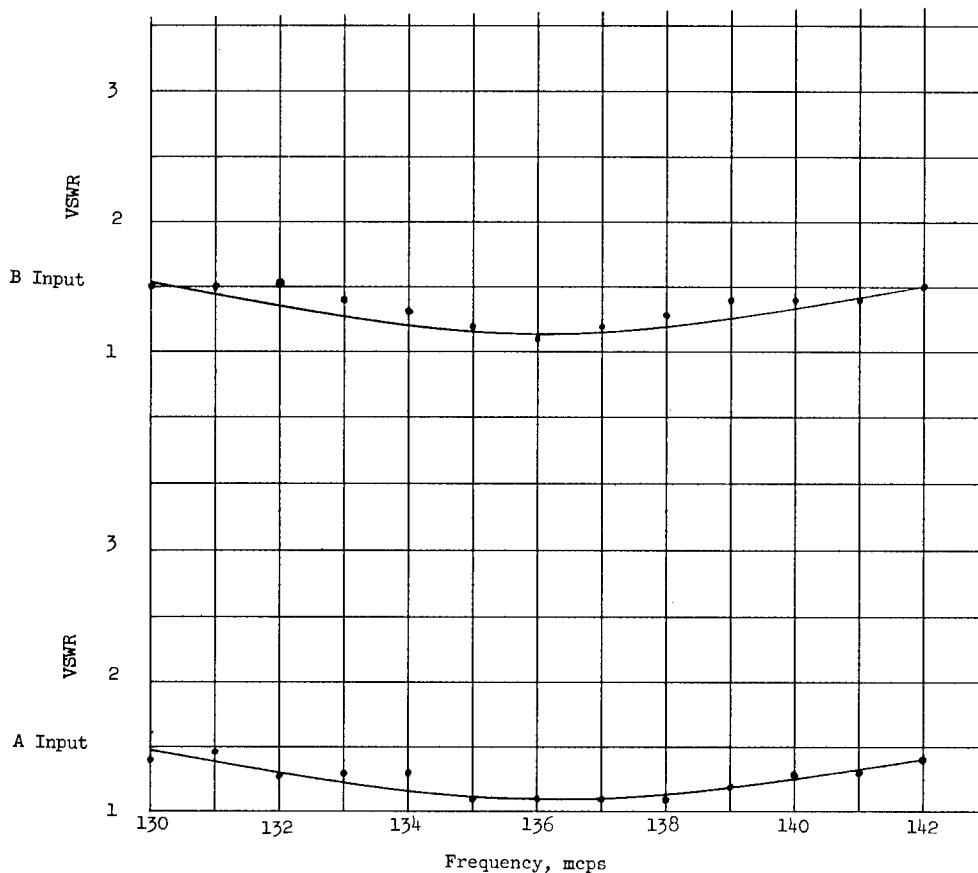


Figure IV-20.- Voltage standing wave ratio.

SECTION IV - CHANNEL ALLOCATIONS

In order to make efficient utilization of channel capacity, it was necessary to obtain a complete knowledge of the environment to be measured as well as a thorough understanding of the sensors. Only when this is done, could the telemetry system be used to its fullest advantage. As is true of all telemetry systems, the telemetry system for Explorer XIII exhibited several peculiarities which had to be designed around. The most evident of these was the crosstalk or hysteretic effect which preceding time channels had on the succeeding time channels. This effect was minimized by grouping sensors according to their measurements so that adjacent channels were functions of the same inputs, that is, the channels were grouped so that the crosstalk effects were minimized.

The inputs to the telemetry system were of two types: a voltage input to the subcarrier oscillators (frequency channels) and a resistance input to the timing multivibrator (time channels). The inputs to the frequency channels were high impedance (approximately 100 K) and the inputs to the time channels were low impedance (a maximum of 5,000 ohms). The inputs to the frequency channels were double ended and were of the type wherein common mode voltages could be bucked out. The inputs to the time channels were also double ended but were of the type that required the sensor to be isolated from ground.

The sensors to be used in any experiment may be categorized into two types: analog, where the output may take any value between two end points; and digital, where the output has only a discrete and finite number of steps. In general, when using an analog telemetry system, the analog sensors require a complete channel for telemetry while the digital sensors may be grouped several to a channel. The digital data may be grouped in two different ways: as combinations, wherein one knows when an event occurs but does not know which one of the n possible events has occurred; and as permutations, wherein one not only knows when an event occurs, but which event of the n possible events has occurred.

An examination of the digital data showed that there were only two types, penetration and impact. A scrutiny of the penetration data revealed that not only were permutations unnecessary, but that the desire to expose all sides of the satellite equally made combinations practically a requirement. Accordingly, the penetration data were telemetered as combinations and the placement of the sensors was distributed so as to give an isotropic view of space. The impacts, being scaled for storage, were weighted and therefore required treatment as permutations. In the signal conditioning process, the first assumption was that the aggregate telemetry system was capable of an accuracy not better than ± 5 percent of full scale. Accordingly, all digital data were encoded so that each step was approximately 10 percent of full scale. It should be noted that few telemetry systems are capable of much better accuracy from the sensor to the final data listings.

A puncture of the pressurized-cell detectors resulted in a switch opening. The output of this switch was an on-off action which readily lent itself to signal conditioning. Using the ± 5 -percent resolution criterion, 10 cells were encoded onto each channel as combinations which give 16 channels of information. Sixteen time channels were used for the telemetry, 8 on the "A" system and 8 on the "B" system. The cells in each channel were laid out in two rows of 5 cells each with two rows placed diametrically opposite so as to sensitize both sides of the spacecraft. Because of the nature of the detectors, a temperature correction was not required for the raw data. The final channel allocations are shown in table IV-2 and in figure IV-21; the detector layout is shown in figure IV-22. The signal conditioning is shown in figure IV-23 along with the resulting resolution.

Penetration of the steel-covered-grid detector by a micrometeoroid broke a gold grid. This breaking of continuity was the telemetered data. Reference 6 gives a detailed description of the sensor and the fabrication techniques. Again, using the ± 5 -percent resolution criterion, the foil gages were encoded onto the frequency channels to give eight bits of information per channel. This signal-conditioning scheme along with the ensuing resolution is shown in figure IV-24. (See ref. IV-6 for the actual sensor grouping and location.) It should be noted that the incompatibility of the high internal impedance of the foil gages and the low input impedance of the time encoding circuitry precluded efficient utilization of available time channels. At best, only three bits could have been placed on one time channel. Due to the swamping action of the current-limiting resistors (fig. IV-24), the temperature effects on the sensors were minimized. Six frequency channels and four time channels were used for the telemetering, three frequency channels and two time channels each on the "A" and "B" telemeters. Table IV-2 and figure IV-27 show the final channel allocations.

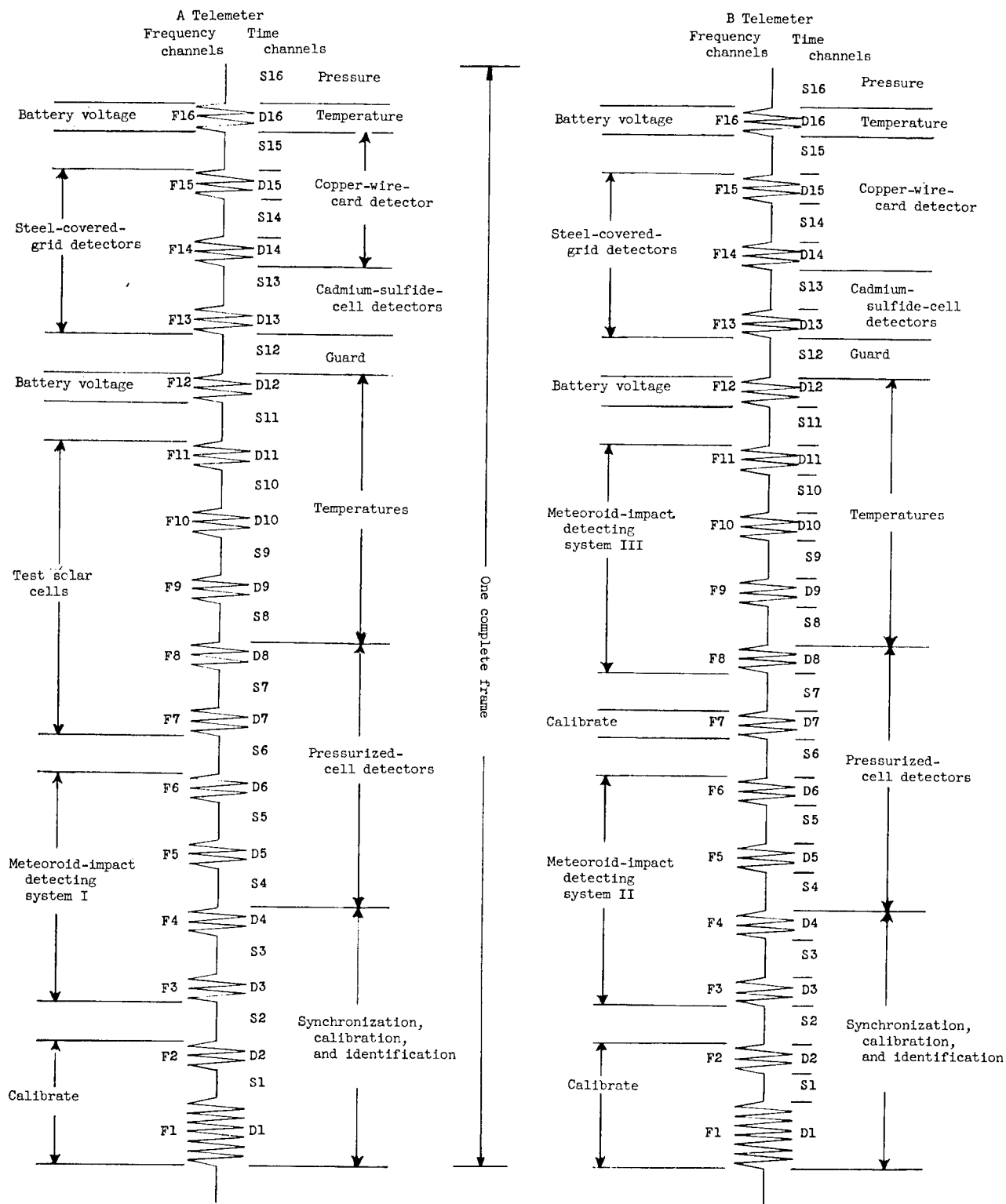


Figure IV-21.- Channel allocations.

The copper-wire-card detectors were melamine cards closely wound with copper wire. A micrometeoroid breaking the wire would cause the card to open. This interruption of continuity was the telemetered data. The signal-conditioning scheme is shown in figure IV-25 and the sensors are described in detail in chapter X. The channel allocations and the sensor layout are shown in figures IV-21 and IV-22, respectively. Ten time channels were used for telemetry, five each from the A and B telemeters.

The events-counting and storage system, which counted the pulses from the micrometeoroid-impact-detection system described in chapter XII, had as outputs octonary weighted voltage levels. These outputs had been treated as permutations and were conditioned as shown in figure IV-26. The channel allocations are shown in table IV-2 and in figure IV-21 and the microphone layout is shown in figure IV-22.

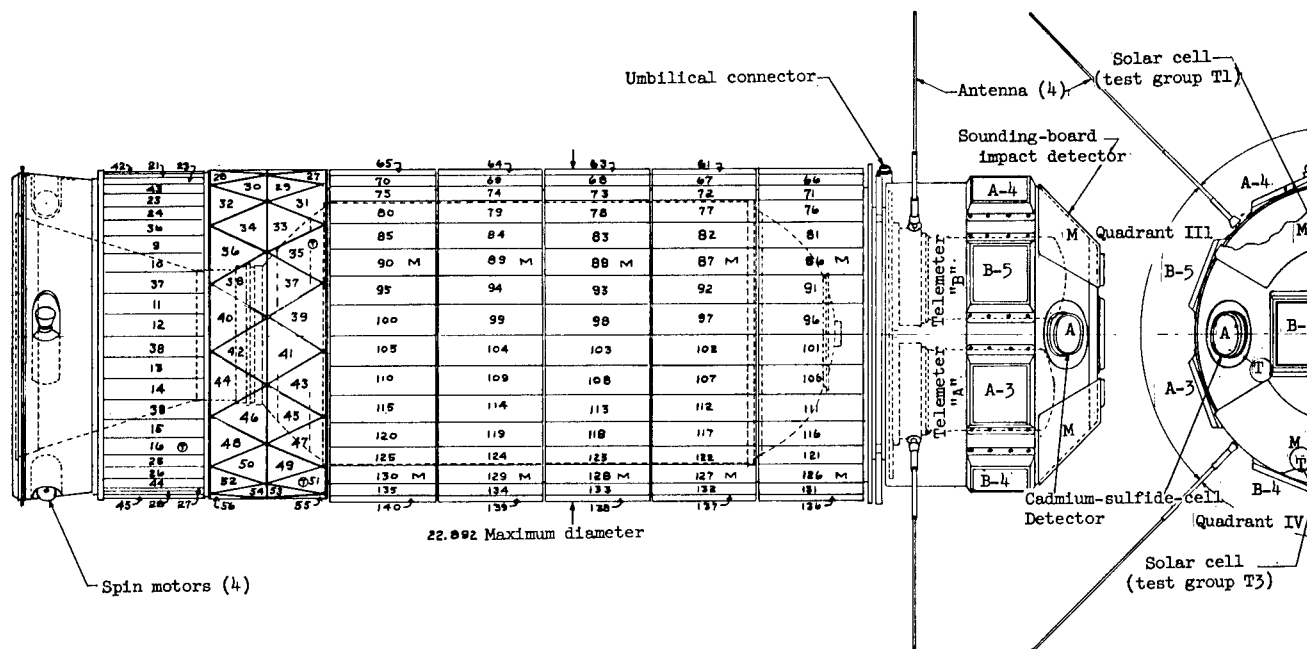
The temperature measurements located as described in chapter VI were made with thermistors, which are temperature-sensitive semiconductors having a large negative temperature coefficient of resistance. Four types of thermistors were used to cover four different temperature ranges. The types and their ranges are:

Thermistor	Temperature range, °C	Resistance at 25° C, ohms
GB25J1	-60 to 10	500
35A2	-10 to 60	5,000
38C2	0 to 70	8,000
GA42J2	10 to 100	20,000

It should be noted that the GB25J1 and the GA42J2 were used in conjunction to measure a temperature range from -60° C to 100° C. It can be shown that the thermistors have their maximum sensitivity at about 5,000 ohms and have end limits of about 500 and 50,000 ohms. Figures IV-27 to IV-29 show the temperature resolutions that were calculated for the 35A2, 38C2, and the GB25J1 - GA42J2 combination by using the criterion of ± 5 -percent telemetry resolution. Two complete sets of temperature measurements were made on the spacecraft and were diametrically opposed so as to indicate temperature gradients around the structure (one set was placed on each telemeter).

SECTION V - GROUND COMPATIBILITY TESTS

In order to insure compatibility between the orbiting satellite and the ground-receiving stations, the prototype telemeters were given an extensive series of tests at the NASA Goddard Space Flight Center (GSFC) and at Blossom Point, Maryland. The telemetry signals were demodulated by receiving equipment at GSFC and recorded on magnetic tape at various signal-to-noise ratios. This magnetic tape was then returned to the Langley Research Center where the recordings were read out and the results analyzed. The radio beacon signal



Penetra- tions	R, ohms	ΔR , ohms	Change, percent of full scale
0	0	---	---
1	470	470	9.4
2	940	470	9.4
3	1,410	470	9.4
4	1,880	470	9.4
5	2,350	470	9.4
6	2,820	470	9.4
7	3,290	470	9.4
8	3,760	470	9.4
9	4,230	470	9.4
10	4,700	470	9.4

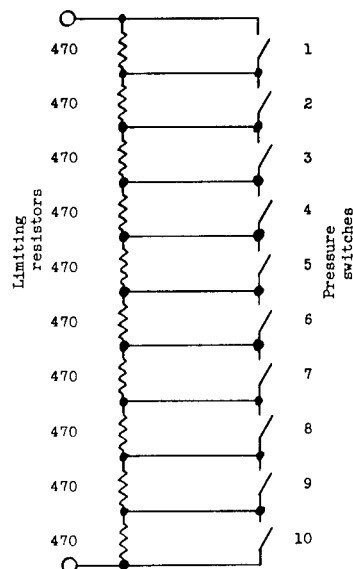
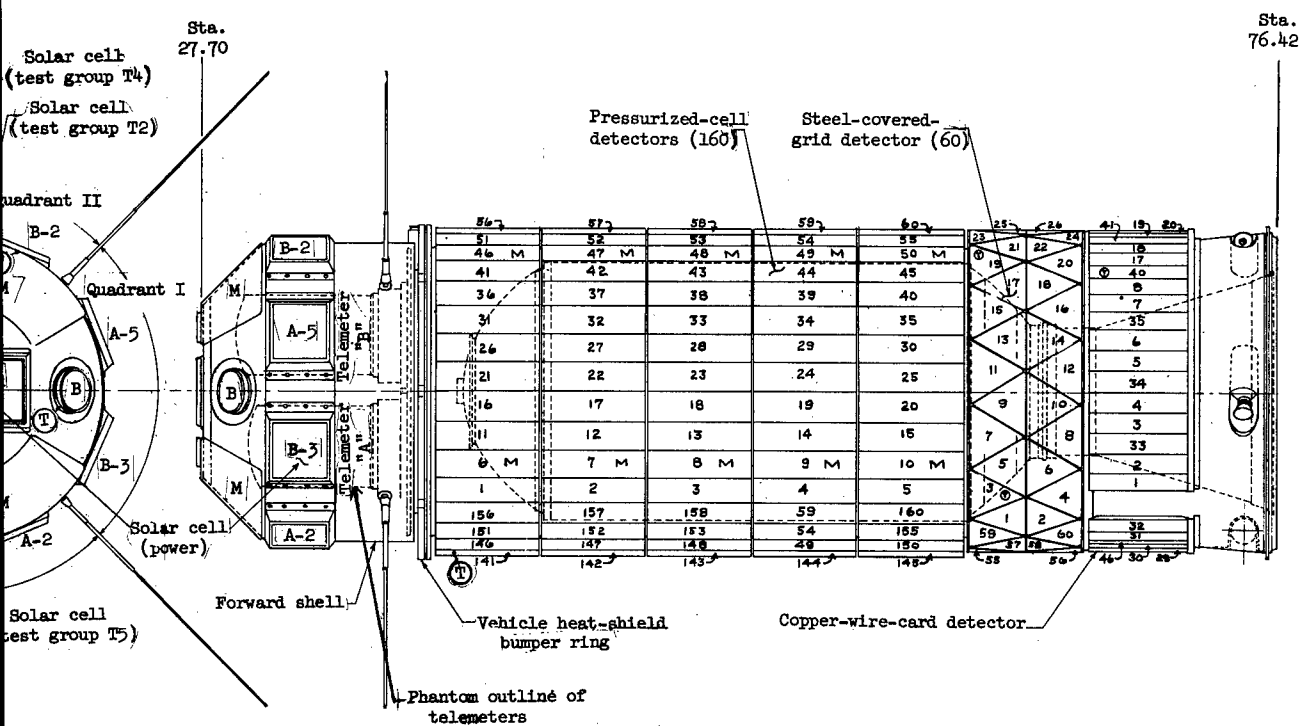


Figure IV-23.- Signal conditioning for pressurized-cell detectors.
(R is limiting resistors.)



⊙ - THERMISTOR
M - MICROPHONE

Figure IV-22.- Detector layout.

Penetra- tions	E_0 , volts	ΔE_0 , volts	Change, percent of full scale
0	2.737	-----	-----
1	2.459	0.278	10.2
2	2.167	.292	10.7
3	1.857	.310	11.3
4	1.529	.328	12.0
5	1.182	.347	12.7
6	.812	.370	13.5
7	.419	.393	14.4
8	.000	.419	15.3

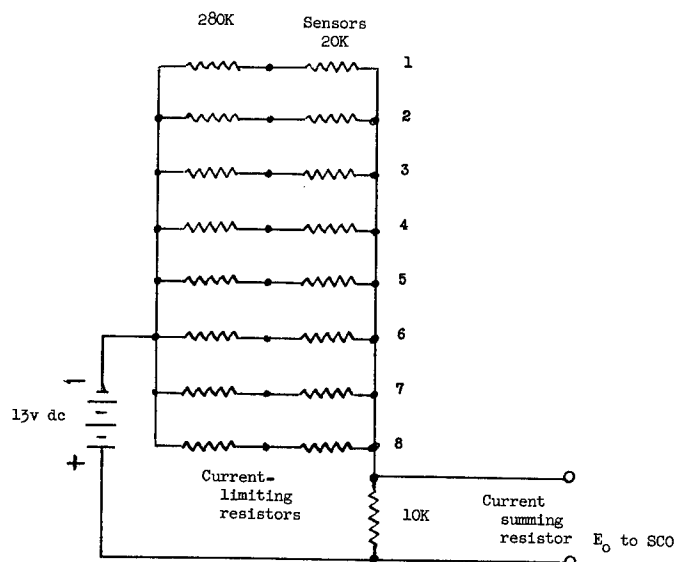


Figure IV-24.- Signal conditioning for steel-covered-grid detectors.
(E_0 is output voltage.)

Penetra- tions	R, ohms	ΔR , ohms	Change, percent of full scale
0	1,240	---	----
1	1,930	690	13.8
2	2,620	690	13.8
3	3,310	690	13.8
4	4,000	690	13.8

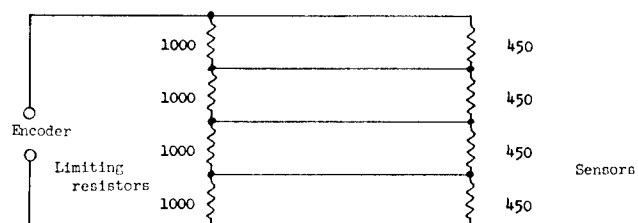


Figure IV-25.- Signal conditioning for copper-wire-card detectors.

Penetra- tions	25K	50K	100K	Percent E_o as $f(E_{in})$	Change, percent of full scale
0	0	0	0	0	0
1	0	0	1	14.3	14.3
2	0	1	0	28.6	14.3
3	0	1	1	42.9	14.3
4	1	0	0	57.1	14.3
5	1	0	1	71.4	14.3
6	1	1	0	85.7	14.3
7	1	1	1	100.0	14.3

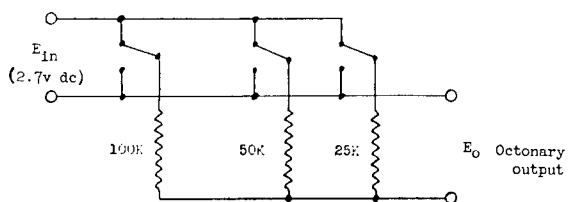


Figure IV-26.- Signal conditioning for impacts-counting and storage system.
(E_{in} is input voltage.)

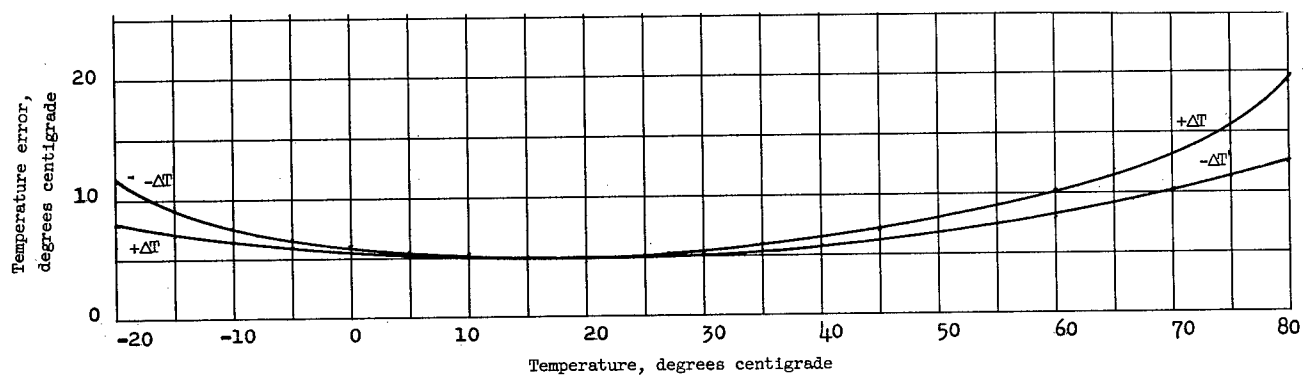


Figure IV-27.- Midrange temperature resolution for thermistor 35A2. ($+\Delta T$ is maximum up error in positive direction and $-\Delta T$ is maximum down error in negative direction.)

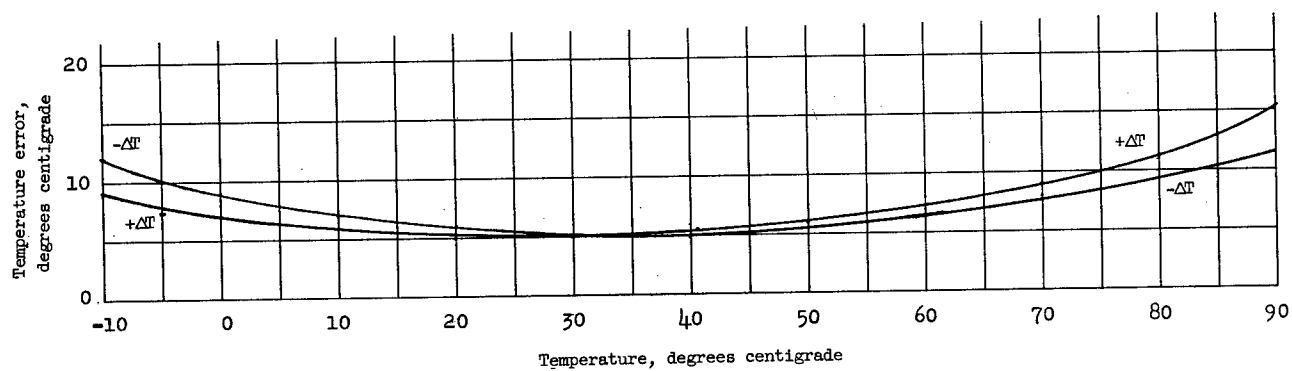


Figure IV-28.- Temperature resolution for thermistor 38C2.

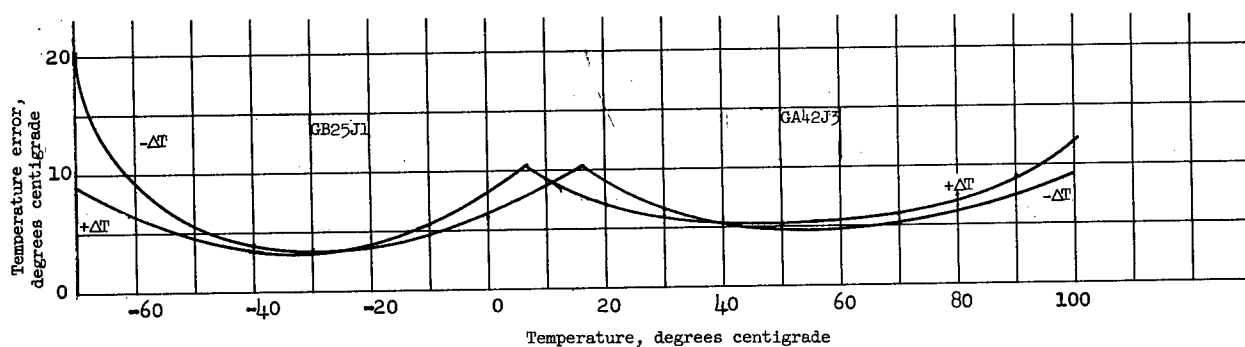


Figure IV-29.- High-low range temperature resolution.

was measured by the Minitrack Interferometer System and the results recorded on a strip-chart recorder. This record was analyzed by GSFC and LRC. The results of the tests showed that the two systems were entirely compatible.

The telemetry tests were conducted as shown in figure IV-30. The satellite electronics were placed in a shielded room to minimize rf leakage and the output at point A was adjusted by means of an attenuator to give 0 dbm carrier level. This signal was further attenuated to give inputs to the receiving system of various levels from -90 dbm down to -125 dbm. The modulation was recovered by means of an "auxiliary diode" and recorded on magnetic tape. The signals, as recovered, are shown in figure IV-31 for both the A and B telemeters. These tests did not include sky noise and therefore show signals about 4 decibels cleaner than were obtained operationally. The anticipated signal-to-noise ratios were shown in figure IV-1.

The tracking tests were conducted as shown in figure IV-32. The output at point A was again adjusted by means of an attenuator to give 0-decibel carrier level. This signal was further attenuated to give inputs to the tracking receivers of various levels from -80 dbm down to -130 dbm. The inputs to the

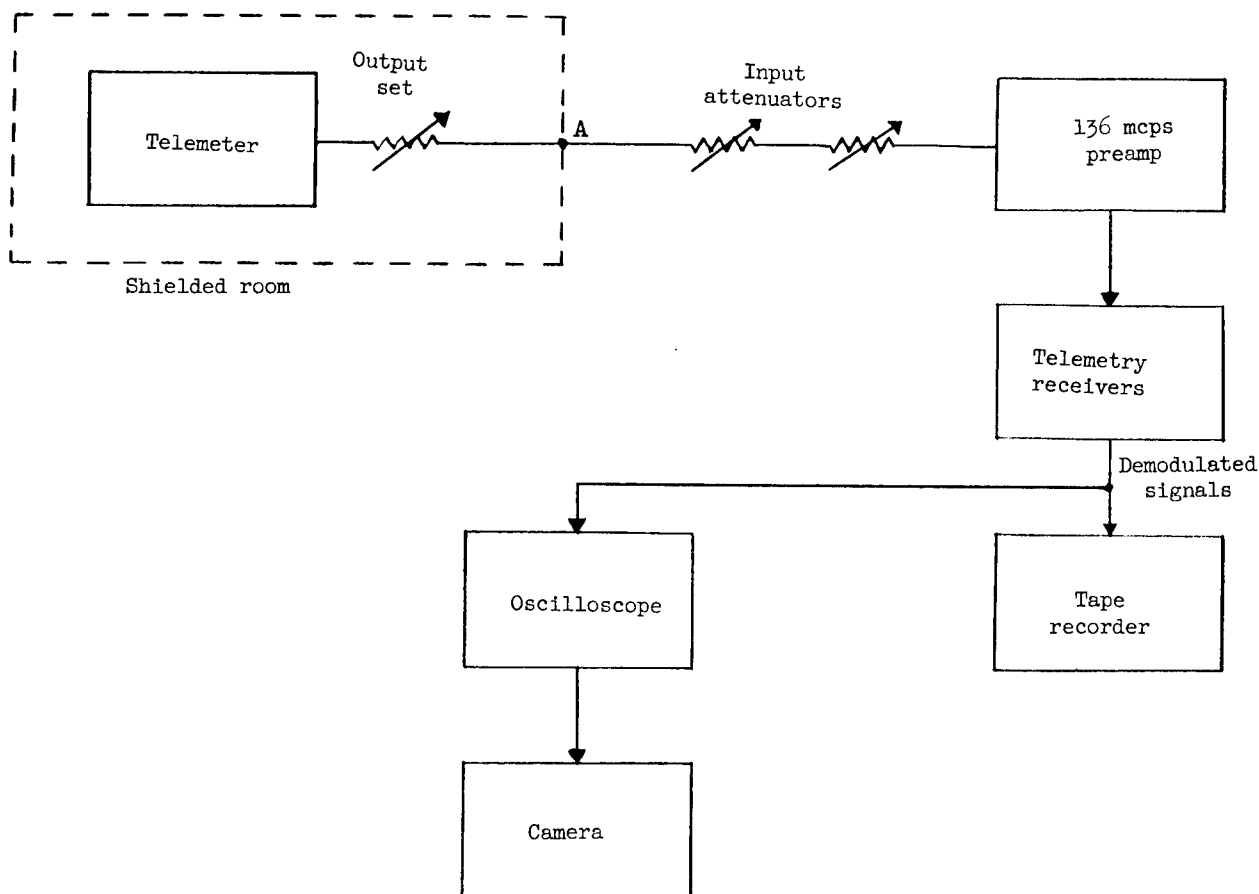
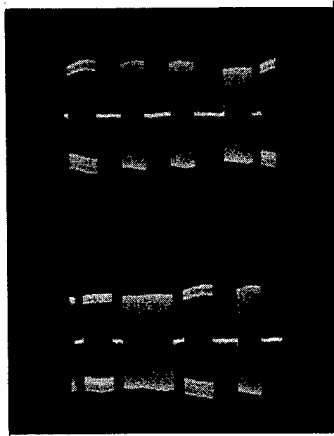
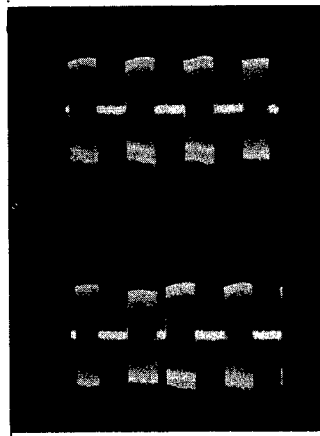


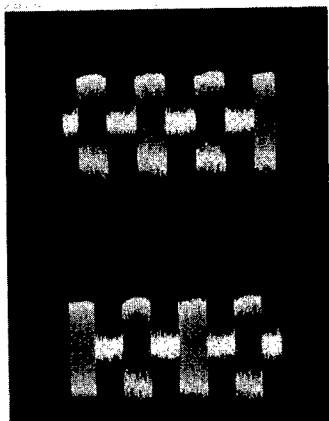
Figure IV-30.- Telemetry compatibility tests.



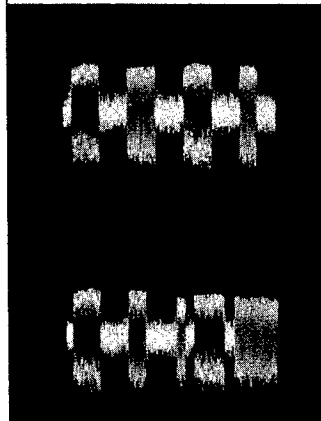
-90 dbm



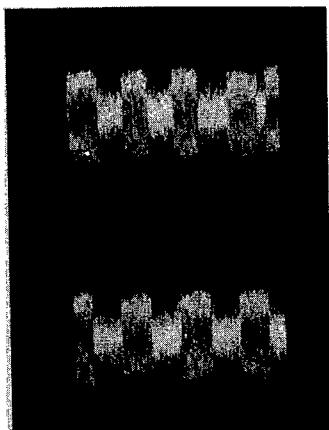
-100 dbm



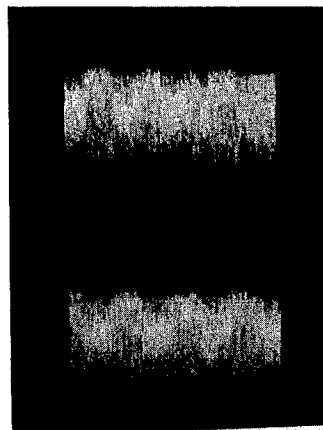
-110 dbm



-115 dbm



-120 dbm

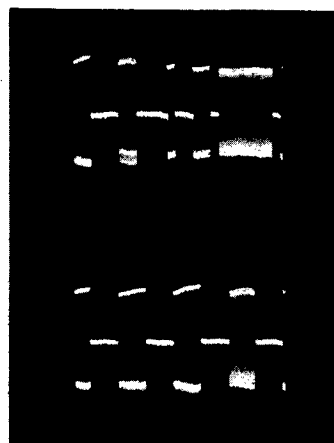


-125 dbm

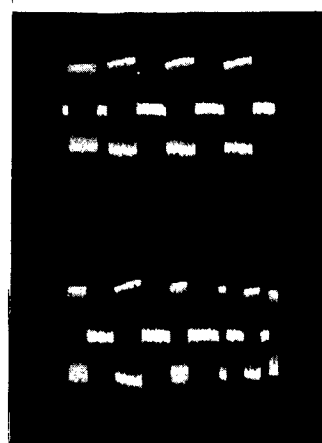
(a) Telemeter 1-B.

L-64-3089

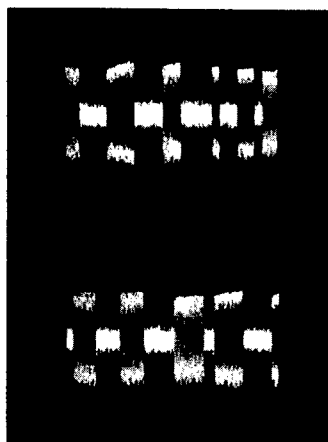
Figure IV-31.- Demodulated telemetry signals.



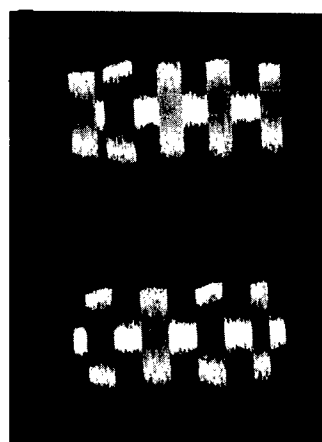
-90 dbm



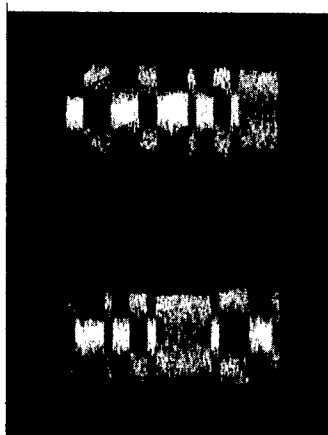
-100 dbm



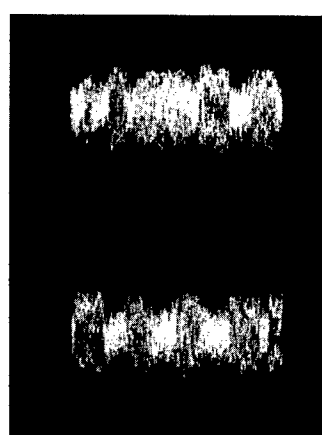
-108 dbm



-110 dbm



-115 dbm



-120 dbm

(b) Telemeter 1-A.

L-64-3090

Figure IV-31.- Concluded.

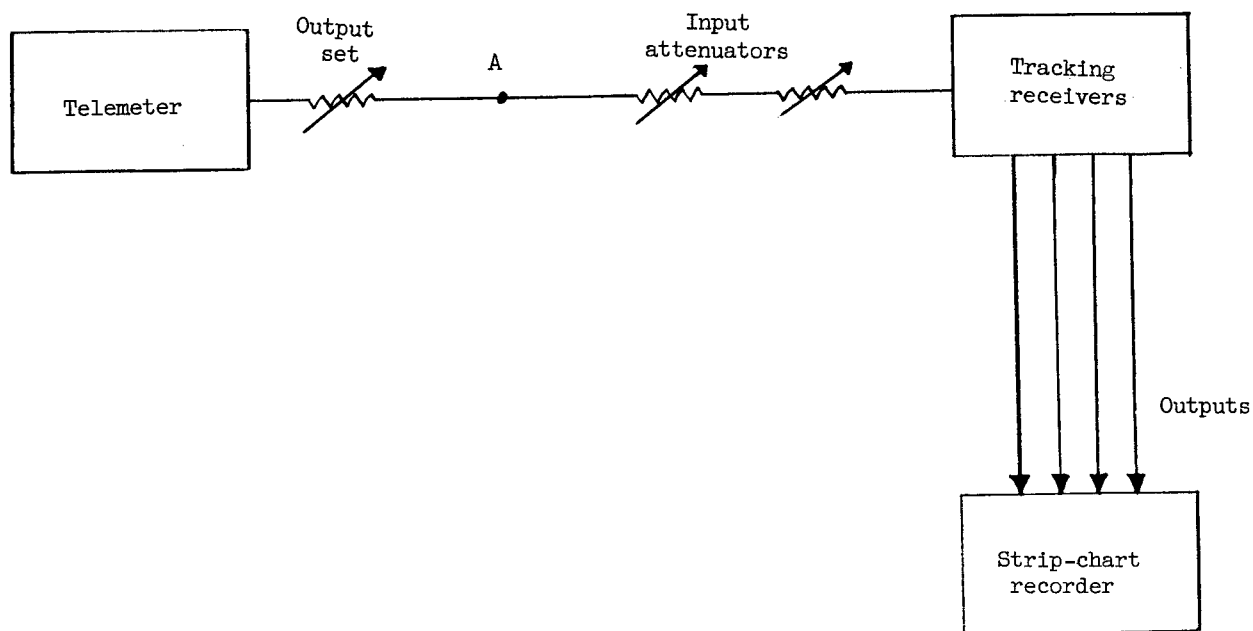


Figure IV-32.- Tracking compatibility tests.

receivers were connected together through equal line lengths so that the input signals were all of the same phase. Since the inputs differed by 0° , the outputs should be 0° . Any variance or jitter in the outputs was an error in tracking. The radio beacon showed excellent characteristics in tracking, but the telemeter signals contained modulation components which caused zero shift and jitter. Although these zero shifts and jitters were greater than desired, it was felt that satisfactory tracking could be obtained.

SECTION VI - OPERATIONAL RESULTS

After two delays caused by bad weather conditions, the final countdown for Scout ST-6 began at 12:00 midnight on August 25, 1961, and at 1:29:11 p.m. e.s.t. (18:29:11Z) of the 25th, lift-off occurred. At 18:37:56Z, Explorer XIII was injected into orbit with an unfortunate injection angle of -4.396° . This unfortunate error resulted in an abnormally low perigee of 61 nautical miles (113.5 km) which caused the orbit to decay rapidly. This departure from the nominal orbit made data acquisition extremely difficult since it was not possible to make accurate predictions of the satellite's passes. However, 21 interrogations were made during the short $2\frac{1}{2}$ -day lifetime of the satellite.

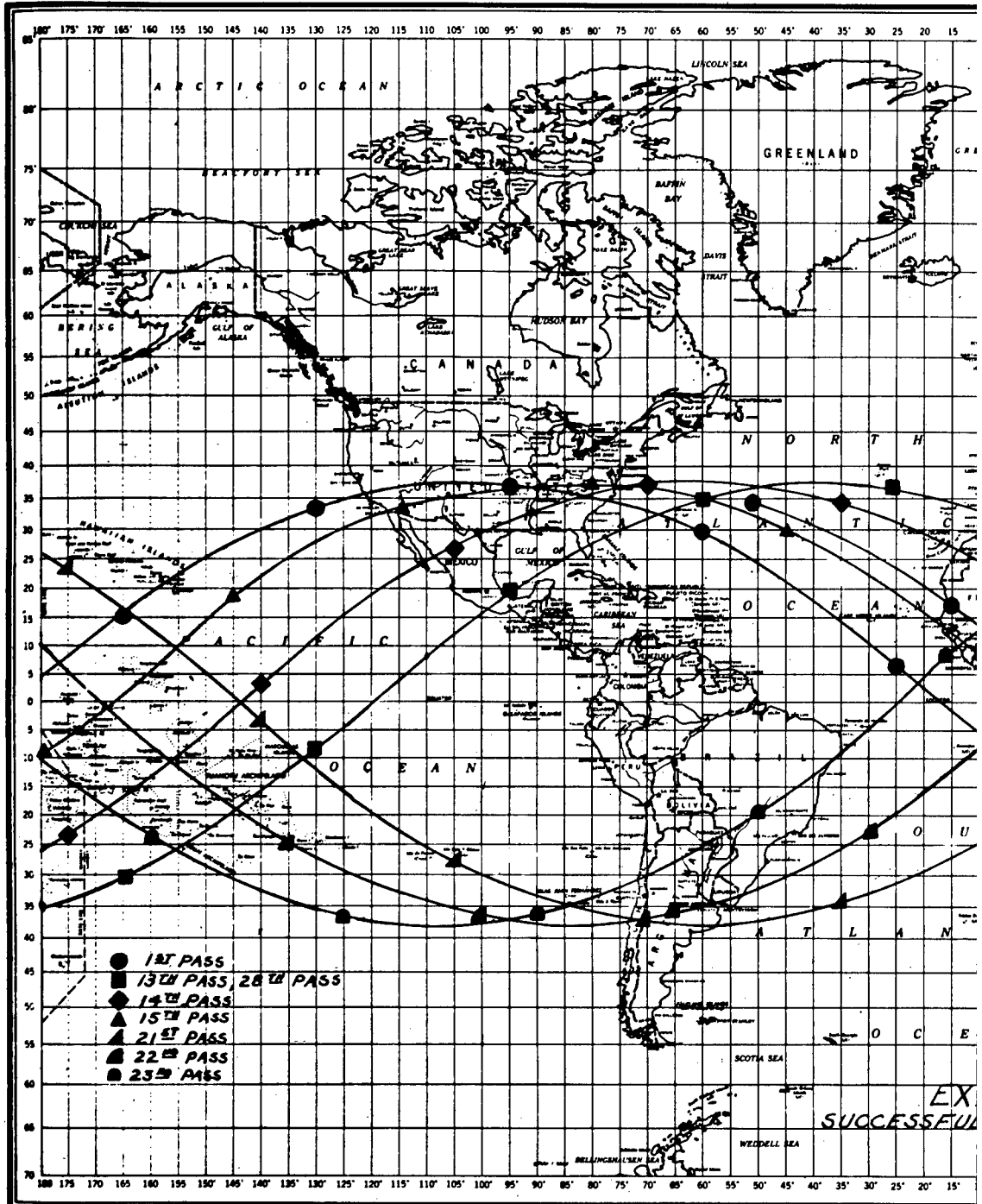
Explorer XIII was successfully tracked during ascent by Wallops Island, Virginia; Blossom Point, Maryland; Locustville, Virginia; and Bermuda by using doppler techniques and by Wallops Island and Millstone Hill, Massachusetts, by using radar techniques. The radio beacon was turned on prior to lift-off and was acquired by Wallops Island and Locustville, Virginia. The exact beacon frequency was communicated to Blossom Point which was unable to pick up the radio beacon while the spacecraft was on the launch pad.

The first station to acquire Explorer XIII in orbit was Johannesburg, South Africa (JOBURG). Time of acquisition was 19:02:00Z, 24 minutes after injection. The second station was Woomera, Australia (OOMERA); acquisition time was 19:22:00Z, 44 minutes after injection.

The first readout was accomplished by East Grand Forks, Minnesota (EGRFKS). Interrogation was at 20:11:45Z, immediately after meridian crossing. Only the B telemeter was acquired at this time. The next readout was by Blossom Point, Maryland (BPOINT) at 20:17:14Z, 60 seconds after meridian crossing at BPOINT. At this time, only the A telemeter was acquired. The next contacts with the satellite were on passes 9 and 10. Only pass 9 at 26/10:02:40Z was usable and even then could only be reduced by using laborious manual techniques. The next successful passes were 13, 14, and 15, when excellent results were obtained on both telemeters. The last successful interrogations were on passes 21, 22, 23, and 28. Figure IV-33 is a world map and shows the subsatellite track for the successful interrogation passes. Table IV-3 gives a history of the interrogations.

SECTION VII - REFERENCES

- IV-1. Matthews, Whitney: Earth Satellite Instrumentation. Elec. Eng., AIEE, vol. 76, no. 7, July 1957, pp. 562-567.
- IV-2. Royer, G. H.: A Switching Transistor D-C to A-C Converter Having an Output Frequency Proportional to the D-C Input Voltage. Trans. American Inst. Electrical Engineers, vol. 74, pt. I, 1955, pp. 322-326.
- IV-3. Baker, R. H.: Maximum Efficiency Transistor Switching Circuits. Tech. Rep. No. 110 (Contract No. AF 19(122)-458), M.I.T., Mar. 22, 1956.
- IV-4. Hepler, D. S.: The Vanguard Satellite Command Receiver. NRL Rep. 5217 (Project Vanguard Rep. No. 35, Minitrack Rep. No. 6), U.S. Naval Res. Lab., Sept. 30, 1958.
- IV-5. Reintjes, J. Francis, and Coate, Godfrey T.: Principles of Radar. Third ed., McGraw-Hill Book Co., Inc., 1952.
- IV-6. Staff of the Lewis Research Center: Micrometeoroid Satellite (Explorer XIII) Stainless-Steel Penetration Rate Experiment. NASA TN D-1986, 1963.



ORLD

REFER TO THIS MAP AS:
THE WORLD 1:36,000,000
WITH 1" PROJECTION LINE INTERVAL
SERIES 1107

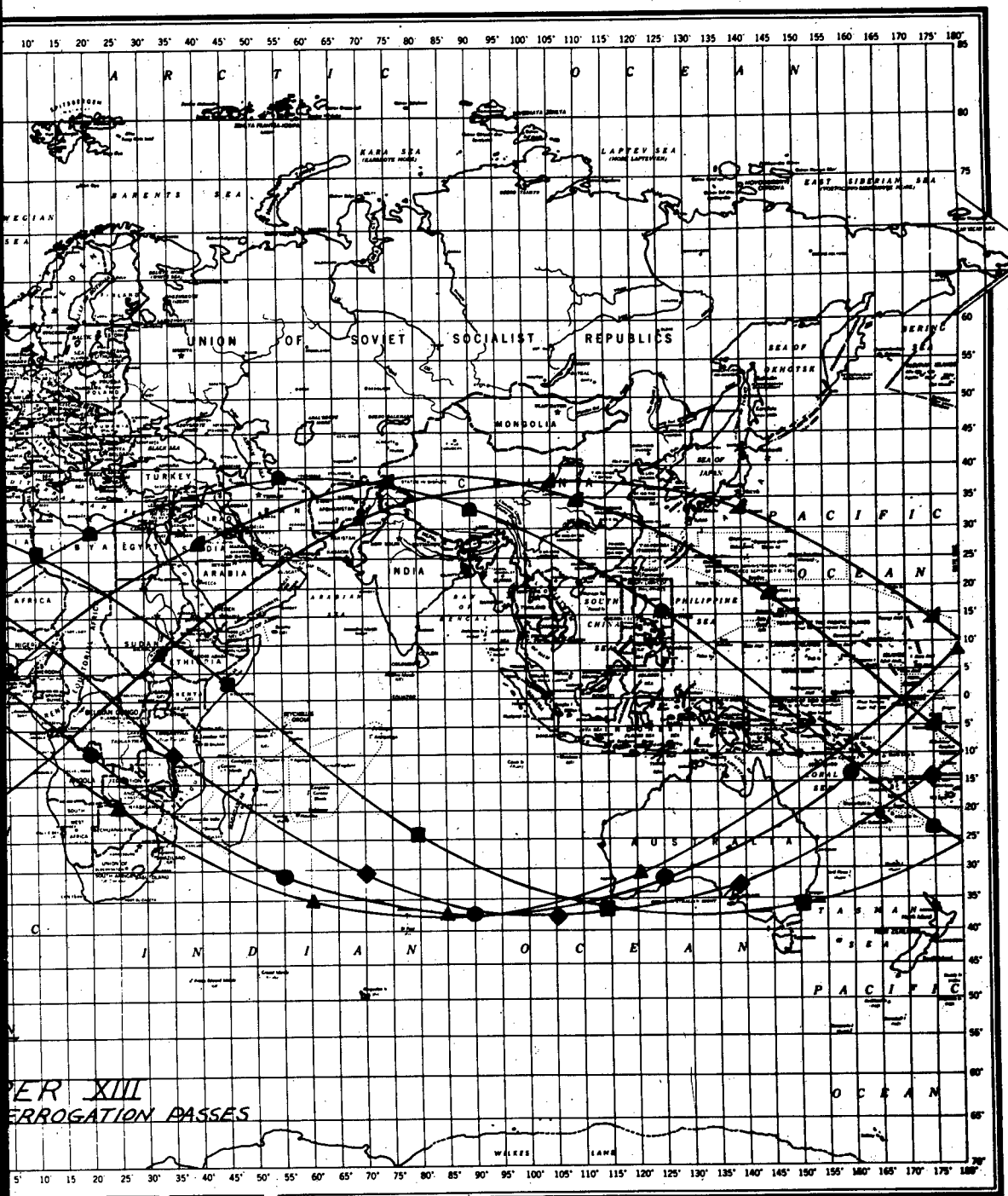


Figure IV-33.- World map of successful interrogation passes.

TABLE IV-1.- PERTINENT CHARACTERISTICS OF EXPERIMENT TELEMETERS
AND RADIO BEACON

	Telemeter A	Telemeter B	Radio beacon
Type	Minitrack PDM/FM/AM; 48 channels	Same	MOPA
Emission	30A9 for 1 minute, upon interrogation only	Same	OA0
Frequency	136.200 mcps	136.860 mcps	136.860 mcps
Power output	100 mw	Same	Same
Lifetime	Indefinite	Same	1 week
Power supply	Secondary batteries (Ni-Cd) recharged by solar cells	Same	Primary batteries (Hg)
Data period	Injection to 1 year	Same	1 week

TABLE IV-2.- CHANNEL ALLOCATIONS

Channel	Telemeter A, 136.200 mcps	Telemeter B, 136.860 mcps
F ₁	Zero calibrate	Zero calibrate
F ₂ F ₃ F ₄ F ₅ F ₆	Pressurized-cell-meteoroid-impact-detection system; sensitivity, $10^{-1} \frac{\text{gm-cm}}{\text{sec}}$ Counter I; calibrate Counter I; 8 count Counter I; 64 count Counter I; 512 count Counter I; 4096 count	Sounding-board-impact-detection system; sensitivity, $10^{-2} \frac{\text{gm-cm}}{\text{sec}}$ Counter II; calibrate Counter II; 8 count Counter II; 64 count Counter II; 512 count Counter II; 4096 count
F ₇ F ₈ F ₉ F ₁₀ F ₁₁	Test solar cells; unprotected T-1 Test solar cells; 0.006-inch glass T-2 Test solar cells; 0.062-inch quartz T-3 Test solar cells; unprotected T-4 Test solar cells; 0.006-inch glass T-5	Counter III calibrate; sounding-board-impact-detection system, $10^0 \frac{\text{gm-cm}}{\text{sec}}$ Counter III; 8 count Counter III; 64 count Counter III; 512 count Counter III; 4096 count
F ₁₂	B battery voltage	A battery voltage
F ₁₃ F ₁₄ F ₁₅	Steel-covered-grid detectors 27 to 40, 42 and 43, 0.003 inch Steel-covered-grid detectors 44 to 55 and 57 to 60, 0.003 inch Steel-covered-grid detectors 12, 26, 41, and 56, 0.006 inch	Steel-covered-grid detectors 1 to 8; 0.003 inch Steel-covered-grid detectors 9 to 11 and 13 to 17, 0.003 inch Steel-covered-grid detectors 18 to 25, 0.006 inch
F ₁₆	A battery voltage	B battery voltage
D ₁	Frame sync	Frame sync
S ₁	Identification, zero ohms	Identification, 470 ohms
D ₂ S ₂ D ₃ S ₃	Calibrate, full scale Calibrate, zero Calibrate, zero Calibrate, full scale	Calibrate, full scale Calibrate, zero Calibrate, zero Calibrate, full scale
D ₄	Temperature electronics package (35A2)	Temperature electronics package (35A2)
S ₄ D ₅ S ₅	Pressurized-cell detectors 36 to 40 and 116 to 120, 0.0025 inch Pressurized-cell detectors 1 to 5 and 81 to 85, 0.001 inch Pressurized-cell detectors 31 to 35 and 111 to 115, 0.001 inch	Pressurized-cell detectors 76 to 80 and 156 to 160, 0.0025 inch Pressurized-cell detectors 41 to 45 and 121 to 125, 0.001 inch Pressurized-cell detectors, 71 to 75 and 151 to 155, 0.001 inch

TABLE IV-2.- CHANNEL ALLOCATIONS - Concluded

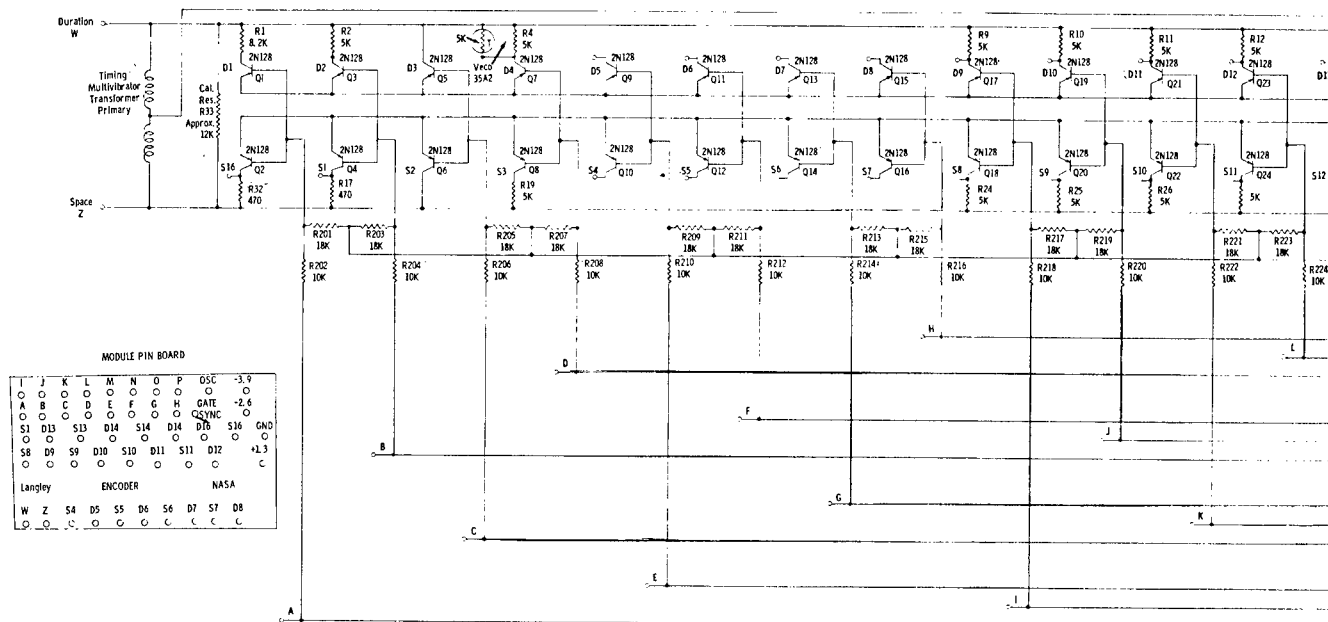
Channel	Telemeter A, 136.200 mcps	Telemeter B, 136.860 mcps
D ₆ S ₆ D ₇ S ₇ D ₈	Pressurized-cell detectors 6 to 10 and 86 to 90, 0.005 inch Pressurized-cell detectors 26 to 30 and 106 to 110, 0.0015 inch Pressurized-cell detectors 11 to 15 and 91 to 95, 0.0015 inch Pressurized-cell detectors 21 to 25 and 101 to 105, 0.002 inch Pressurized-cell detectors 16 to 20 and 96 to 100, 0.001 inch	Pressurized-cell detectors 46 to 50 and 126 to 130, 0.005 inch Pressurized-cell detectors 66 to 70 and 146 to 150, 0.0015 inch Pressurized-cell detectors 51 to 55 and 131 to 135, 0.0015 inch Pressurized-cell detectors 61 to 65 and 141 to 145, 0.002 inch Pressurized-cell detectors 56 to 60 and 136 to 140, 0.001 inch
S ₈	Forward-shell temperature (Low range, GB25J1)	Forward-shell temperature (Low range, GB25J1)
D ₉	Forward-shell temperature (High range, GA42J3)	Forward-shell temperature (High range, GA42J3)
S ₉	Test solar cells, T1 and T2 Temperature (35A2)	Test solar cell T3 Temperature (35A2)
D ₁₀ S ₁₀ D ₁₁	Pressurized-cell detectors Temperature (Low range, GB25J1) Pressurized-cell detectors Temperature (High range, GA42J3) Power-supply solar cell B4 Temperature (35A2)	Pressurized-cell detectors Temperature (Low range, GB25J1) Pressurized-cell detectors Temperature (High range, GA42J3) Power-supply solar cell B2 Temperature (35A2)
S ₁₁ D ₁₂	Steel-covered-grid detector Temperature (38C2) Steel-covered-grid detector Temperature (38C2)	Steel-covered-grid detector Temperature (38C2) Steel-covered-grid detector Temperature (38C2)
S ₁₂	Guard	Guard
D ₁₃	Cd S Cell	Cd S Cell
S ₁₃	Cd S Cell temperature (35A2)	Cd S Cell temperature (35A2)
D ₁₄ S ₁₄ D ₁₅ S ₁₅ D ₁₆	Copper-wire-card detectors 1 to 8, 0.003 inch Copper-wire-card detectors 9 to 16, 0.003 inch Copper-wire-card detectors 33 to 35, 0.002 inch Copper-wire-card detectors 36 to 39, 0.002 inch Copper-wire-card detectors Temperature (35A2)	Copper-wire-card detectors 17 to 24, 0.003 inch Copper-wire-card detectors 25 to 32, 0.003 inch Copper-wire-card detectors 40 to 43, 0.002 inch Copper-wire-card detectors 44 to 46, 0.002 inch Copper-wire-card detectors Temperature (35A2)
S ₁₆	Telemeter pressurization	Telemeter pressurization

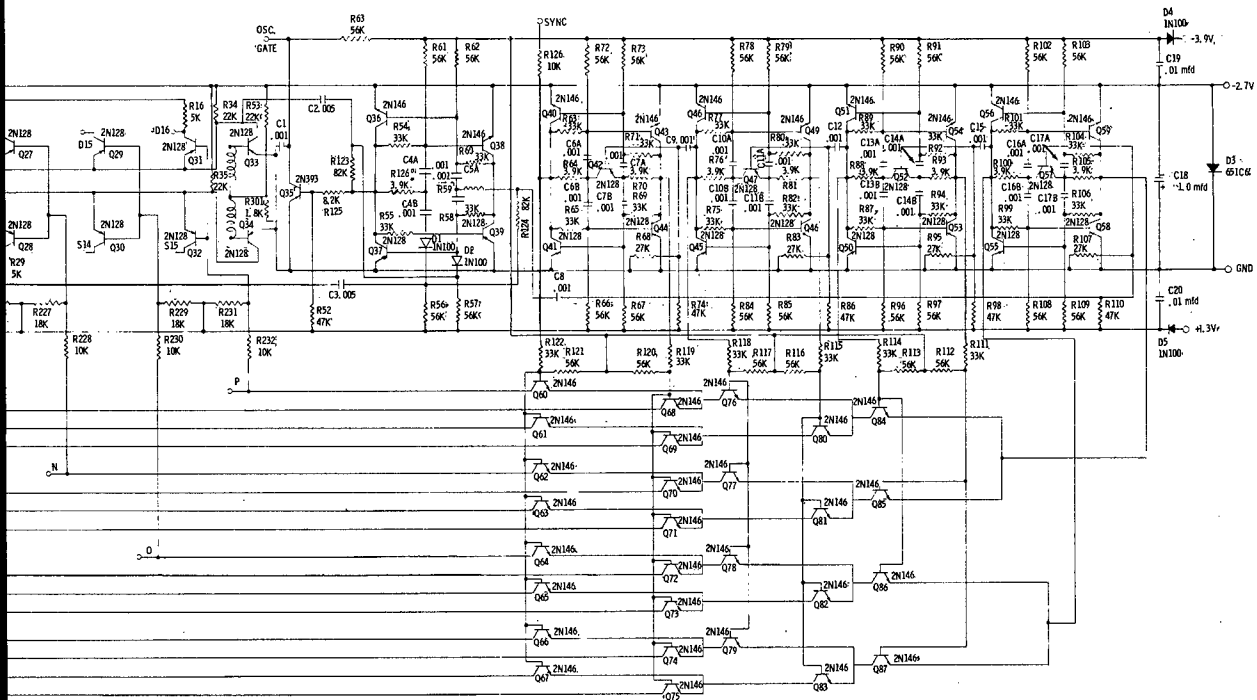
TABLE IV-3.- INTERROGATION HISTORY

Orbit	Date/time	Minitrack station	Tape	Telemeter	Data-reduction process
Launch	25/18:29:44	Blossom Point	122A001	None	None
1	25/20:11:45	Grand Forks	122N001	B	Automatic
1	25/20:11:45	Blossom Point	122A002	B	Automatic
1	25/20:17:14	Blossom Point	122A002	A	Manual*
2	25/21:59:40	Fort Myers	122D001	None	None
7	26/06:34:00	Santiago	122J001	None	None
8	26/08:32:15	Santiago	122J001	None	None
9	26/10:02:40	Antofagasta	122H001	A	Manual
9	26/10:02:40	Antofagasta	122H001	B	Manual
10	26/11:46:00	Quito	122F001	A	Manual
10	26/11:55:00	Quito	122F001	B	Manual
13	26/15:13:30	Fort Myers	122D001	A	Automatic
13	26/15:15:02	Fort Myers	122D001	B	Automatic
13	26/15:13:30	Blossom Point	122A003	A	Automatic
13	26/15:15:02	Blossom Point	122A003	B	Automatic
14	26/16:58:06	Blossom Point	122A004	A	Automatic
14	26/16:58:06	Blossom Point	122A004	B	Automatic
14	26/16:58:06	Fort Myers	122D002	A	Automatic
14	26/16:58:06	Fort Myers	122D002	B	Automatic
15	26/18:40:57	Fort Myers	122D002	A	Automatic
15	26/18:40:57	Fort Myers	122D002	B	Automatic
20	27/03:03:00	Santiago	122J002	A	Manual
20	27/03:03:00	Santiago	122J002	B	None
21	27/04:45:56	Santiago	122J003	A	Automatic
21	27/04:45:56	Santiago	122J003	B	Automatic
22	27/06:21:30	Santiago	122J003	A	Automatic
22	27/06:21:30	Santiago	122J003	B	Automatic
23	27/08:03:14	Antofagasta	122H001	A	Automatic
23	27/08:03:14	Antofagasta	122H001	B	Automatic
25	27/11:15:40	Lima	122G01	None	None
27	27/14:03:00	Woomera	122-1	None	None
28	27/15:42:15	Woomera	122-1	A	Automatic
28	27/15:42:15	Woomera	122-1	B	Automatic
35	28/02:00:03	Antofagasta	122H001	A	Manual**
35	28/02:00:03	Antofagasta	122H001	B	Manual**
40	28/08:46:00	Antofagasta	122H001	B	Manual**

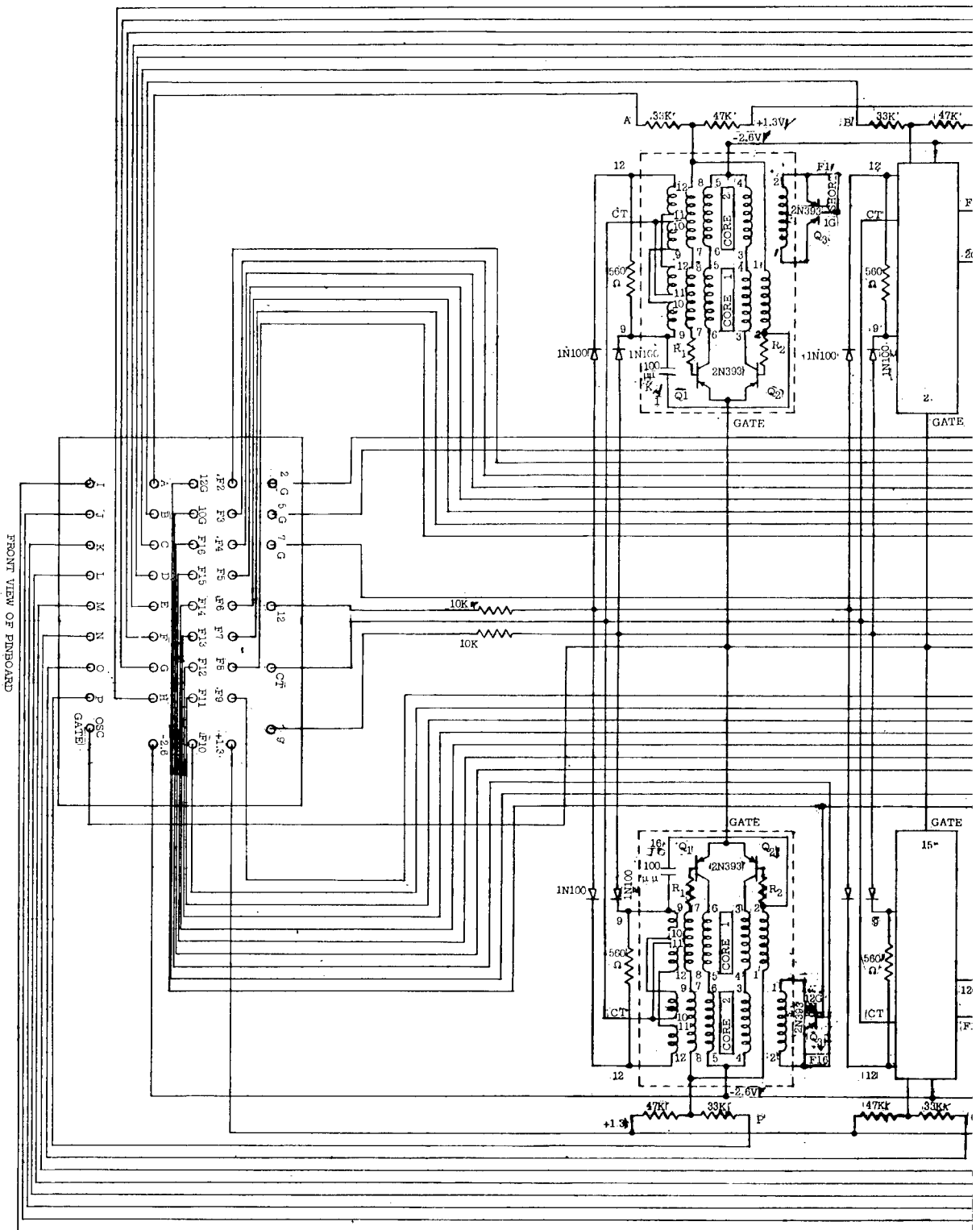
*Special process by GSFC.

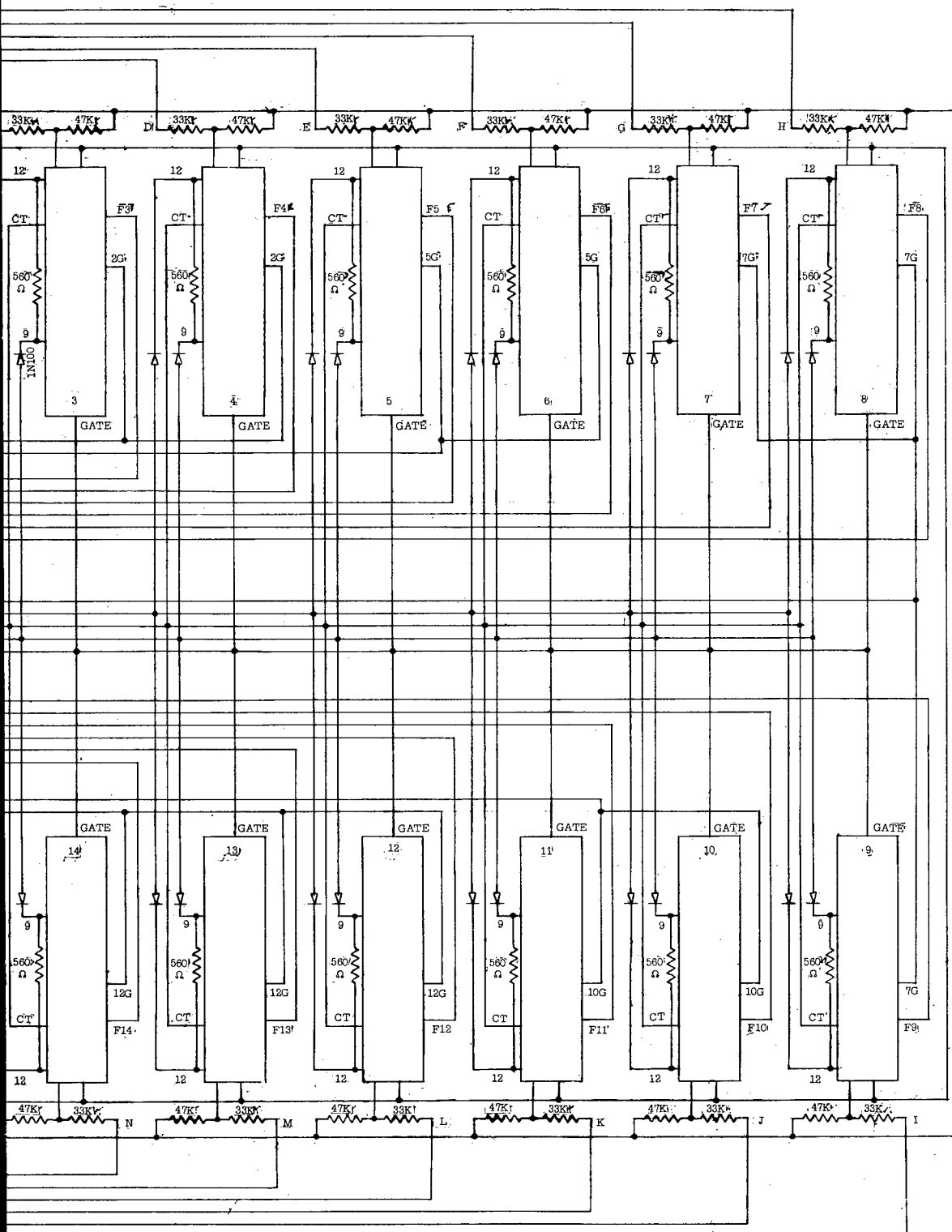
**The temperatures of all systems had increased beyond design limits as a result of aerodynamic heating so that these data could not be used.



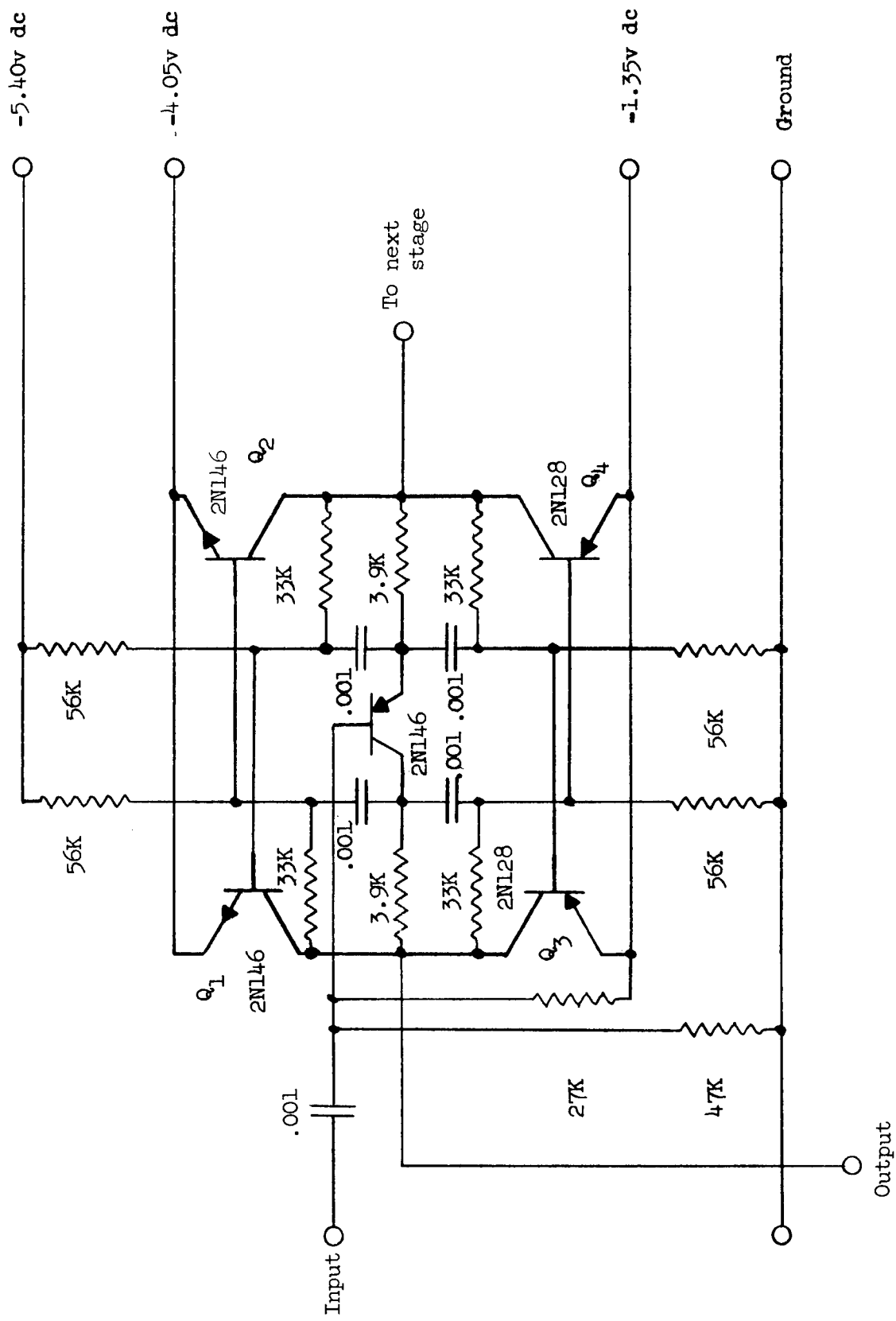


Circuit diagram 1.- Forty-eight channel encoder module schematic.

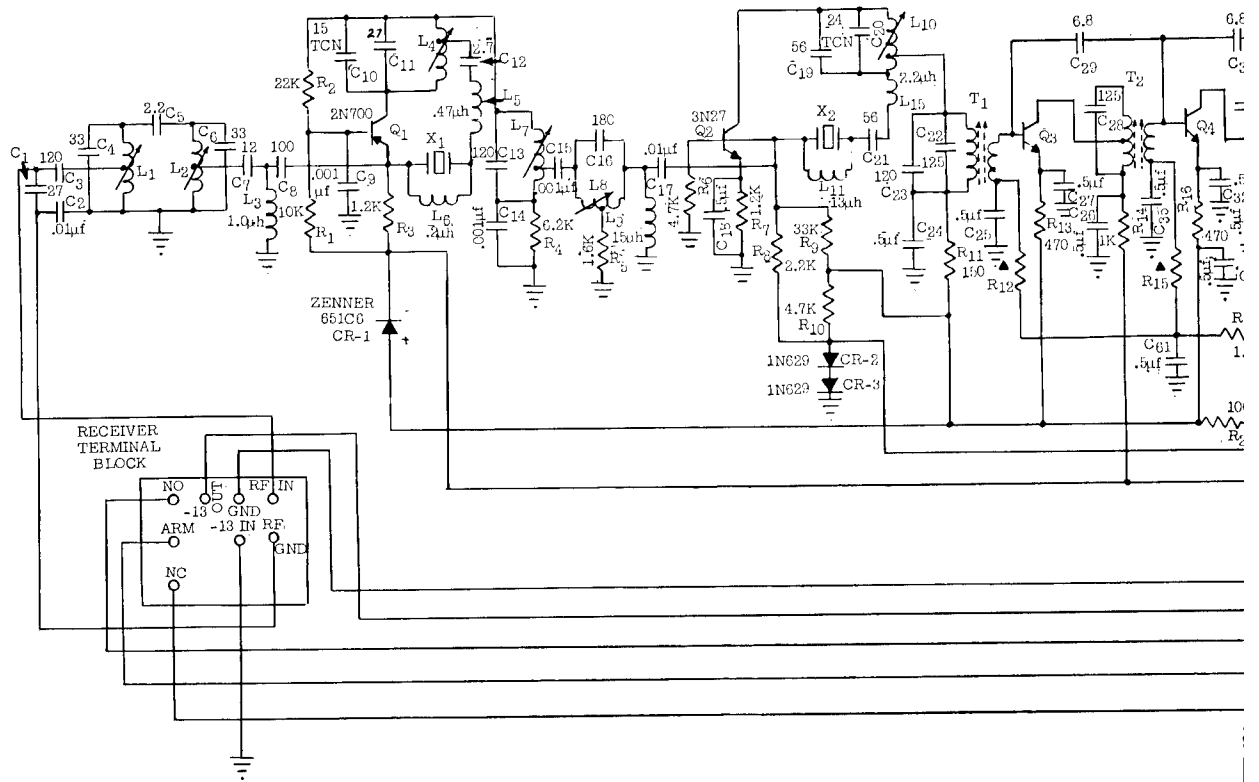




Circuit diagram 2.- Subcarrier oscillator module.



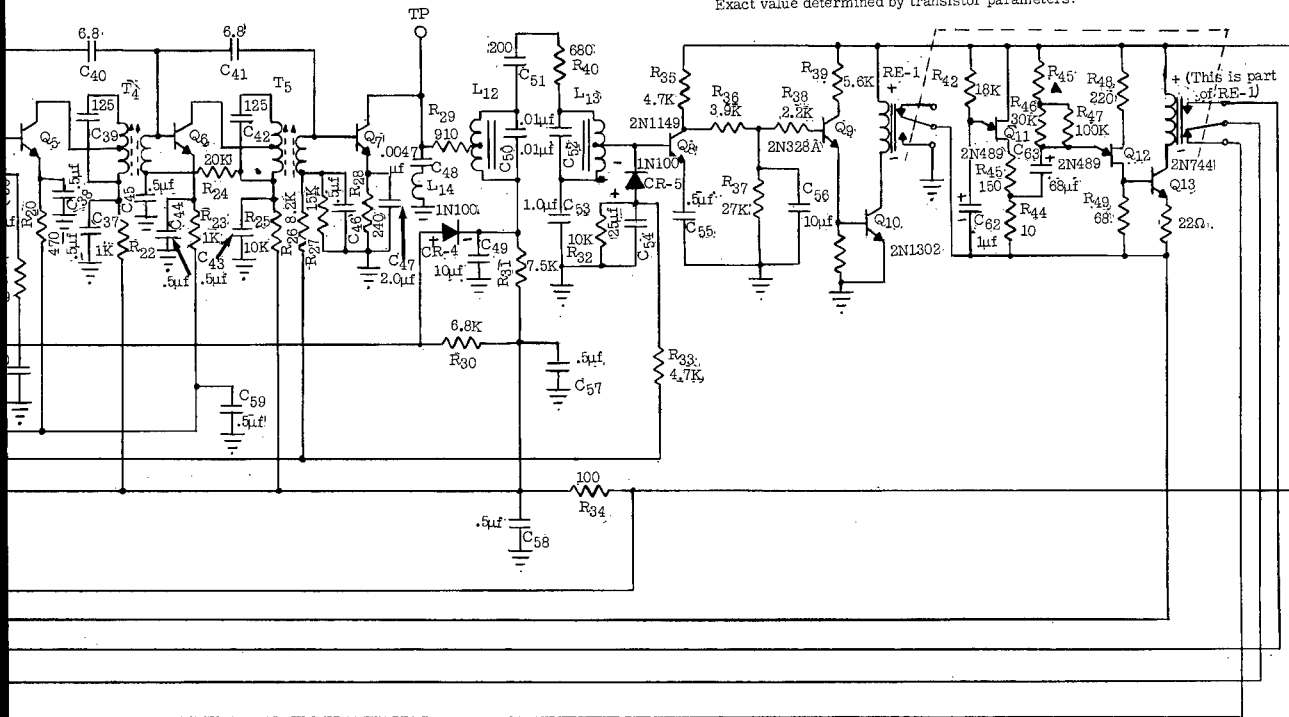
Circuit diagram 3.- Five-transistor complementary flip-flop circuit.



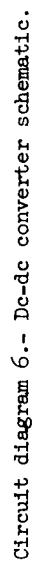
NOTE:

Relay is Potter Brumfield SL 11d
Argonne 1.F transformers rewound for 20KC bandwidth
All transistors are Texas Instr. 2N1149 unless marked otherwise
All capacitor values are in micromicrofarads unless marked otherwise

Exact value determined by transistor parameters.



Circuit diagram 5.- Schematic of command receiver.



Circuit diagram 6.- Dc-dc converter schematic.

CHAPTER V

POWER-SUPPLY SYSTEMS AND TEST SOLAR CELLS

By John L. Patterson
Langley Research Center

SECTION I - INTRODUCTION

Conversion of solar energy with photovoltaic solar cells was decided to be the most practical means of meeting the low-level power requirements throughout the desired 1-year lifetime of the satellite. Rechargeable batteries were necessary to supply all power required during the orbital dark periods, as well as to supply a large part of the power required during interrogations in sunlight.

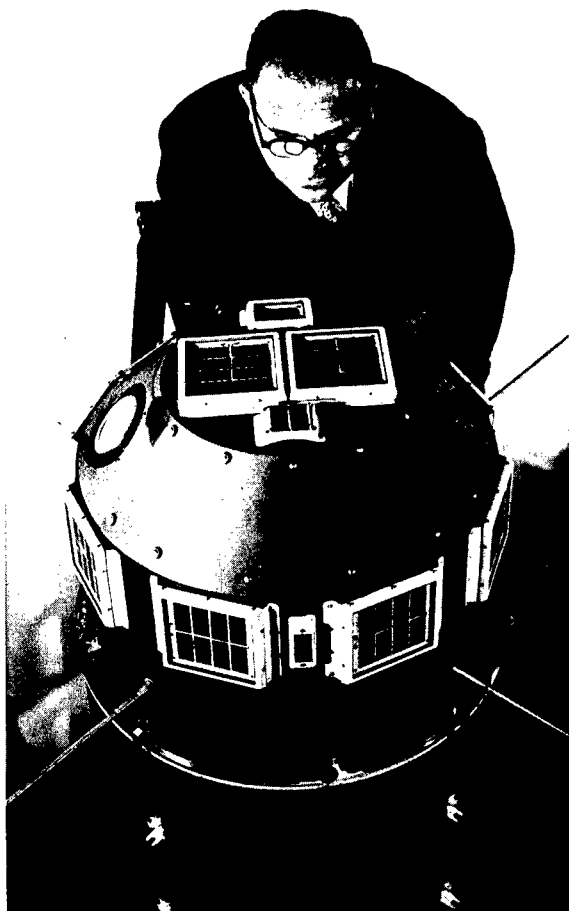
Two separate solar power supplies were installed, one for each telemeter. Each supply was required to furnish 10 milliamperes of standby current and 110 milliamperes during interrogations at 12 volts nominal. The power supplies were designed for 1-minute interrogations during each orbit; orbital periods were approximately 100 minutes and orbital dark times varied from 0 to 35 percent of each orbital period. In addition, the satellite was to be spin stabilized at 200 rpm at launch, but was expected to tumble at approximately 20 rpm after several weeks.

In addition to the solar cells used for power, five groups of solar cells were mounted on the forward shell to obtain data on the relative effectiveness of protective covers for the cells.

SECTION II - POWER-SUPPLY SOLAR CELLS

General.- The mounting arrangement of the solar cells on the forward shell is shown in figures V-1 and IV-33. Since the payload was not separated from the final rocket motor, and because of the limited diameter of the heat shield, it was not practical to have cells facing aft. For each of the two power supplies, one tray was located on the forward end of the forward shell and four were equally spaced around the cylindrical surface. This was equivalent to having cells on five sides of a cube for each power supply. The smaller trays are solar-cell test groups and are not connected to the power supplies; these are described later.

Figure V-2 is a photograph of a typical solar-cell tray, and figure V-3 is a drawing of a tray mounted on the aluminum heat-transfer band. A rather stiff tray with flexible mounting brackets was considered necessary because the forward shell (especially in its early design) could possibly experience high-amplitude vibrational deflections during the launch operations. Forty solar cells, in eight 5-cell "shingles," were cemented to the 1/8-inch-thick



L-61-2146

Figure V-1.- Nose shell of Explorer XIII showing solar-cell trays.

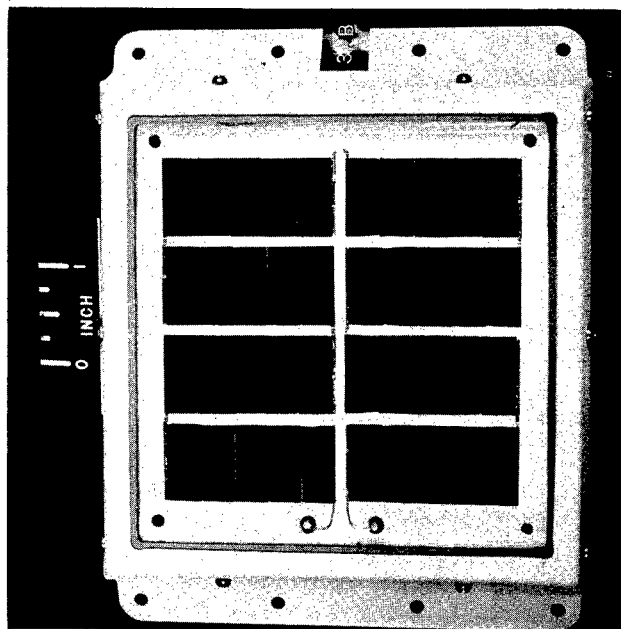
magnesium alloy base of the tray. The magnesium alloy was chemically treated to provide for the electrical insulation of the cells and to improve the cement bond.

For thermal-balance requirements, the external metal surfaces were coated with an aluminum oxide coating. For good heat transfer between the trays and the aluminum band, the surfaces in contact were left bare, and those closely spaced were coated with flat black paint. Since the transmission of the fused quartz windows is low for infrared radiation, most of the excess energy absorbed by the solar cells had to be conducted out through the base to be radiated by other external surfaces. Hence, coatings or glass covers designed to improve the emissivity of the cells were not used, and low absorptivity was specified for the other exposed surfaces under the windows.

Cements.- A number of materials were investigated to find one suitable for cementing the solar cells to the trays and for coating the exposed surfaces between and around the cells. The cement had to provide good thermal conduction, and had to be flexible enough to isolate the fragile cells from mechanically and thermally induced stresses. The latter

was critical since the thermal coefficient of expansion of silicon is 2.5×10^{-6} in./in./°C compared with 25×10^{-6} in./in./°C for the magnesium alloy, and the preliminary estimate of the expected solar-cell-temperature range was from -65° C to +135° C. The cement also had to withstand the space environment; tests were made to determine relative flexibility, immunity to a vacuum, and resistance to ultraviolet and ionized-particle radiation.

Silicone rubber cements were among those investigated. The one selected is a white, room-temperature-cured silicone rubber that remains flexible down to approximately -70° C. Its adhesive properties were excellent for this application when the surfaces were primed as recommended. It was found to have a solar absorptivity of 0.32, and its properties were unaffected when subjected to ultraviolet radiation at elevated temperatures. Its thermal conductivity of 7.44×10^{-4} gm cal-cm/cm²/sec/°C compares favorably with other cements. No trouble was experienced with entrapped gas, and its rate of weight loss in a high vacuum was found to be relatively low. This cement was subjected to



L-60-8387

Figure V-2.- Photograph of power solar-cell tray.

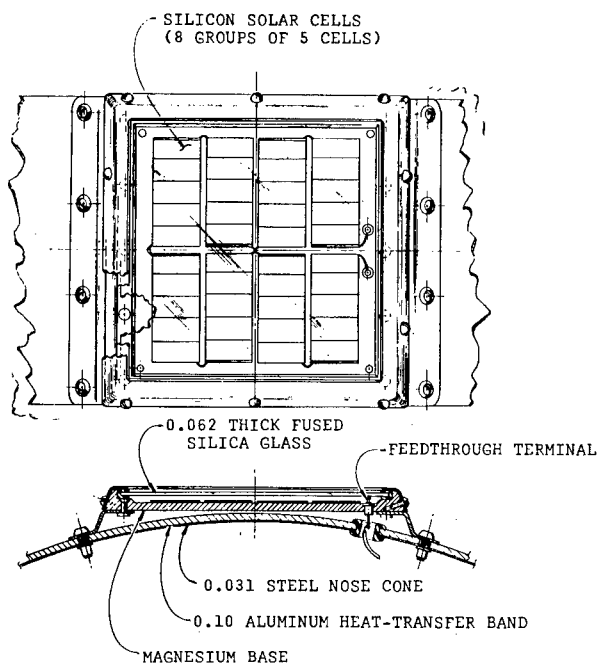


Figure V-3.- Drawing of power solar-cell tray.

proton irradiation in several cyclotrons in conjunction with solar-cell testing, and negligible damage was found.

Windows.- Fused quartz windows 1/16 inch thick (fig. V-3) were used to help protect the solar cells from possible damage by ionized particle radiation and micrometeorites. A molded silicone rubber gasket was used to cushion the windows from the stresses of launch vibrations and temperature changes. The gaskets suffered only minor surface hardening when subjected to ultraviolet irradiation at elevated temperatures.

The fused quartz was found to transmit 93 percent of normally incident light in the spectral range of the solar cells. Thoroughly sandblasting the exterior surface with fine alumina to approximate the possible effects of micrometeorite erosion was found to reduce the 93-percent transmission to 89 percent. Proton irradiation tests (ref. V-1) showed that the quartz should not be appreciably darkened by particle radiation in the expected orbit. (The artificial electron belt did not exist at this time.)

Solar-Cell Characteristics.- The nongridded silicon solar cells used for the power supplies were 1 by 2 centimeters in size, and were the P on N junction type. They were supplied in five-cell shingles without coatings or glass covers. The nominal efficiency of the cells varied from 8 to 9 percent. This efficiency rating was based on the maximum power output at 27° C when illuminated by the sun under standardized conditions on the surface of the earth (one air mass or $m = 1$). The actual efficiency in space at 27° C was estimated to be 0.83 of the nominal value because a large part of the increased solar energy available above the atmosphere (140 mw/cm²) falls outside of the spectral range of the solar cells (refs. V-2 and V-3).

Tungsten filament lamps, with their voltages adjusted to give filament temperatures of $2,900 \pm 100^\circ \text{K}$ were used with a 1-inch-thick water filter when determining the output of the solar cells. The light intensity was monitored with a "standard" solar cell which was calibrated under standardized conditions in sunlight ($m = 1$), and in light from tungsten lamps when using the same type of filter and range of filament temperatures.

The curves of current output plotted against voltage at various temperatures for a typical solar-cell tray of 40 series-connected cells is shown in figure V-4. The points of maximum power output are indicated. In these tests the light intensity was adjusted to be equivalent to one solar constant ($140 \times 0.83 = 116 \text{ mw/cm}^2$ as measured with a calibrated standard solar cell). It will be noted that the cells are essentially constant current generators up to a voltage that is dependent on temperature. The operating voltage is fixed by the load, and in this power supply, is primarily fixed by the batteries. A typical value of 14.8 volts (0.37 volt/cell) is indicated in figure V-4. The effect of temperature on output, when charging batteries at a nearly constant voltage, is further illustrated in figure V-5 where the data of figure V-4 are plotted as current and power output, at 14.8 volts, as a function of temperature. Since literature on solar cells often gives the change in maximum power with temperature, the measured values of this parameter are shown for comparison.

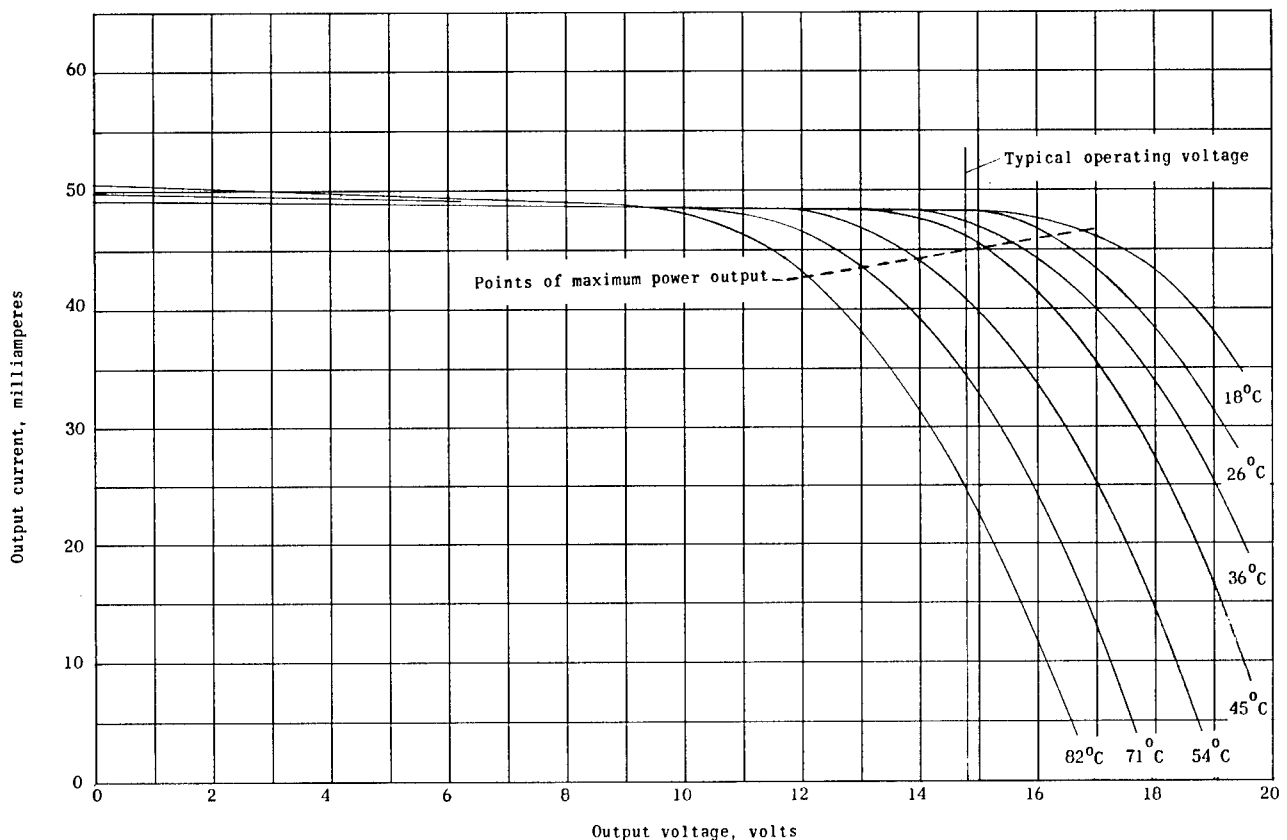


Figure V-4.- Variation of output current with voltage and temperature of a typical power solar-cell tray.

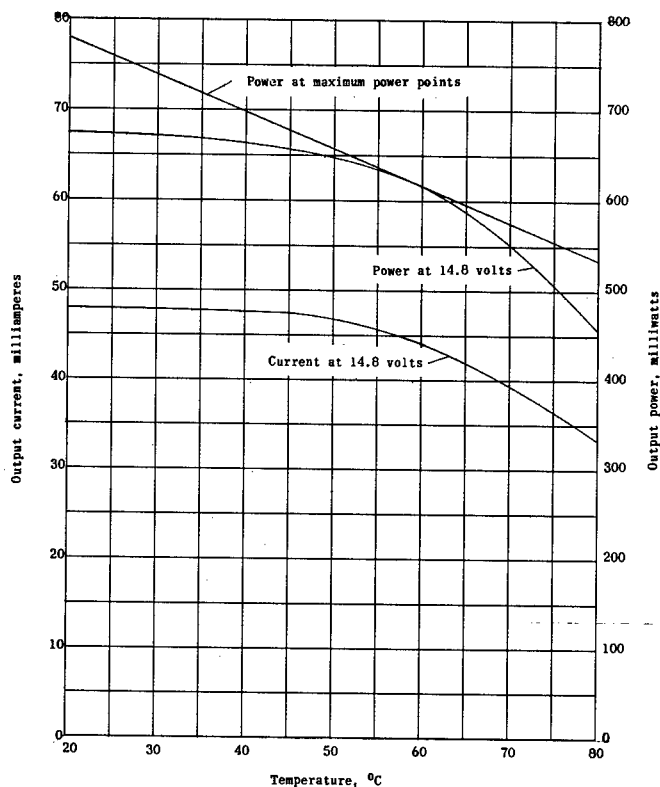


Figure V-5.- Variation of output current and power with temperature of a typical power solar-cell tray.

the effects of the tray-edge shadows were not simulated. Also shown in figure V-6 is a curve obtained in a similar manner with the sandblasted window (mentioned previously) mounted over the cells. This curve illustrates the possible effects of micrometeorite erosion, but the data were not used in the following computations.

Figure V-7 gives the predicted combined percentage of output of the solar cells of one power supply plotted against sun incidence angle computed from the experimentally determined values of figure V-6. In this case, it was assumed that the vehicle was in a pure tumbling mode (no roll), and that the rays of the sun, the vehicle roll axis, and the normal to the three trays involved were in the same plane (see sketch in fig. V-7). The ordinate is the relative output referred to one tray illuminated at normal incidence, and hence is the percentage to be applied to the output values given in figures V-4 and V-5. The computation merely required the graphical or numerical summation of the instantaneous output of each illuminated tray. The relative output is also shown as computed from the ideal cosine curve. Since the average value of a half-wave rectified sinusoidal wave is $1/\pi$, the ideal average output, over one cycle of tumbling, of the three trays is $3/\pi$ times, or 95.5 percent of that of one tray illuminated at normal incidence. This compares with a value of 87 percent found from the area under the curve of figure V-7 obtained from measured values. It can be shown that this should be very close to the minimum output averaged over any complete cycle of tumbling.

Effect of Vehicle Attitude.- The effect of the vehicle attitude on the output of the solar cells with respect to the sun was important because the vehicle had no cells facing aft, and was expected to remain spin stabilized only a short time. Also, the information was required to avoid an initial spin-stabilized attitude with insufficient solar-cell illumination. The output of a solar cell is approximately proportional to the projected illuminated area and hence to the cosine of the angle of the incident light. Measured values of the percent reduction of output current are plotted against incidence angle in figure V-6 with a cosine curve shown for comparison. Currents were measured under simulated battery charging conditions using a five-cell shingle. A quartz window was mounted over the cells during the test, but

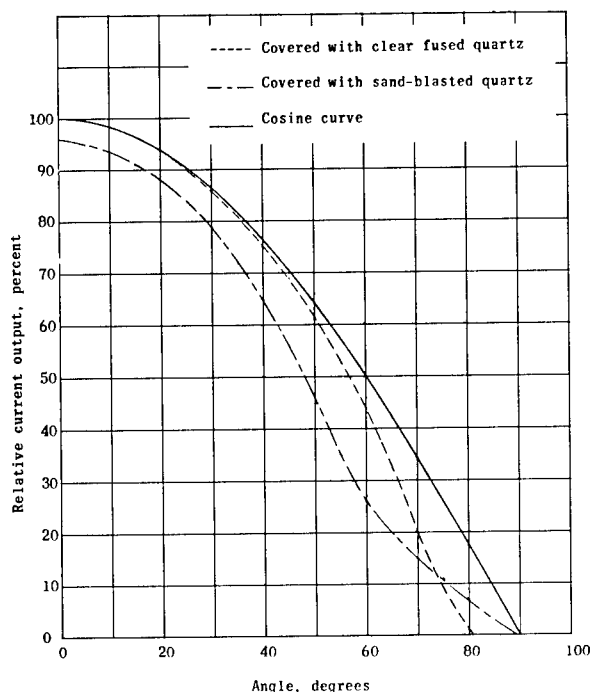


Figure V-6.- Variation of solar-cell output current with angle of incident light.

If the vehicle is assumed to be spin stabilized with the sun vector normal to the vehicle axis, four trays are illuminated in sequence, and the ideal average output is $4/\pi$ times (127 percent) that of one tray. By using measured values, the corresponding average was found to be 116 percent of one tray. In the more general case where the vehicle is spinning but the sun is not normal to the axis, the computation is more involved. When the sun is forward of the vehicle equator, a maximum of three trays can be illuminated at one time. When the vehicle is in a pure spinning mode, the tray on the forward end has a constant ideal fractional output of $\cos \phi$. From spherical trigonometry, the cosine of the angle between the sun vector and the normal to a reference tray on the cylindrical surface is $\sin \phi \cos \theta$, where ϕ is the angle between the sun vector and the vehicle axis, and θ is the angle in roll measured from the normal of the reference tray. (Refer to the sketch in fig. V-8.) The cosine of the corresponding incident

angle of the illuminated tray adjacent to the reference tray is $\sin \phi \cos(90 - \theta)$ or $\sin \phi \sin \theta$. Hence, the combined fractional ideal output of the three illuminated trays is:

$$\cos \phi + \sin \phi \cos \theta + \sin \phi \sin \theta$$

The average of this expression over a period of roll is:

$$\cos \phi + \frac{4}{\pi} \sin \phi$$

When the angle ϕ (fig. V-8) is greater than 90° , the solar-cell tray on the forward end is not illuminated, and the first term in each of these expressions becomes zero. The ideal average output while spinning, computed from the second expression for values of ϕ from 0° to 180° , is shown as the dotted curve of figure V-8. The solid curve gives the corresponding predicted values based on the experimental results of figure V-6 (with clear quartz). These were computed, at each 10° increment of ϕ , by substituting measured values for each of the terms in the first of the above expressions to get variation in the combined output over 90° of roll. The averages were then obtained with the trapezoidal rule.

When all the components of a power supply were available, a completed forward shell was rotated by a motor to various angles of ϕ while illuminated by

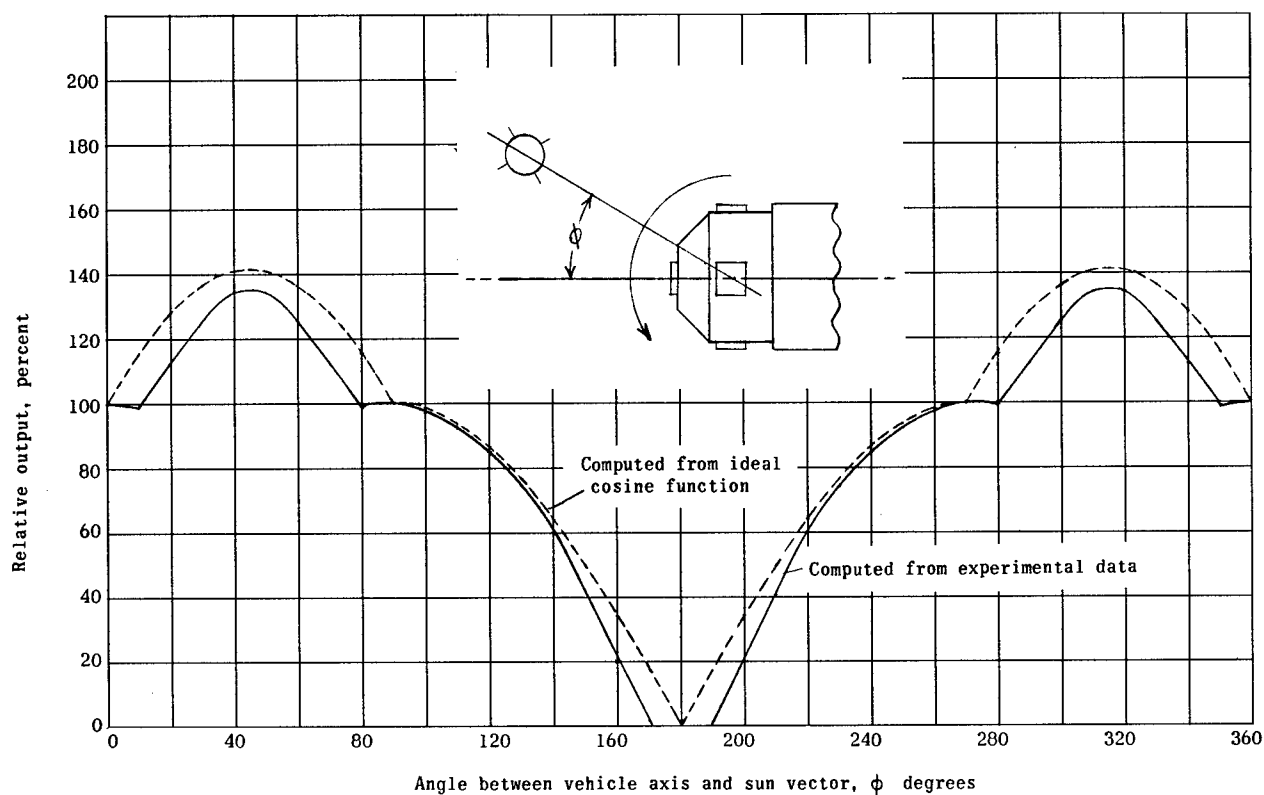


Figure V-7.- Output of solar cells in tumbling mode giving least average output.

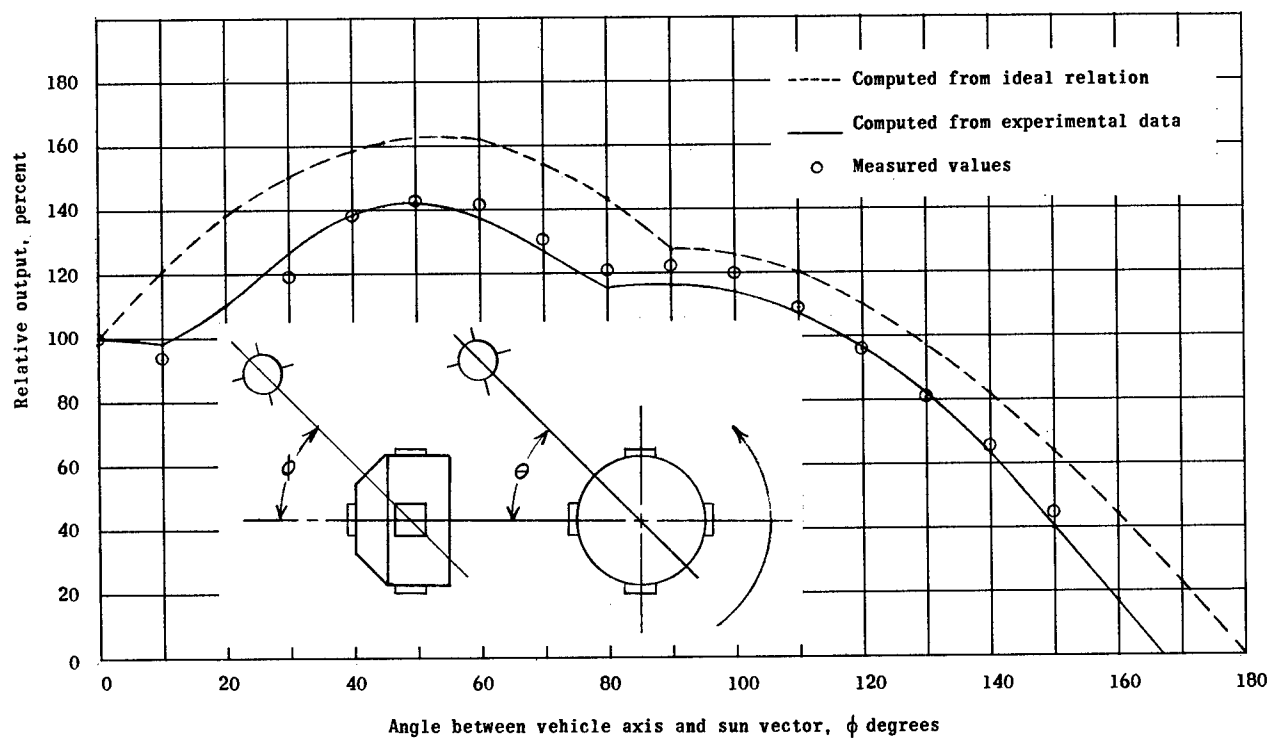


Figure V-8.- Average output of solar cells with vehicle spin stabilized at various angles between vehicle axis and sun vector.

the sun on a clear day. With the five trays properly connected in the power-supply circuit, the combined solar-cell current was plotted against angle of rotation on an X-Y plotter. Figure V-9 is an example of the curves obtained. It was plotted at $\phi = 110^\circ$, and the ragged dips occurred as the antenna shadows passed over the cells. The average values obtained from the areas under these curves are presented as the circled data points in figure V-8. Since it was not practical to eliminate all reflected sunlight, particularly when ϕ was close to 90° , some of the values are too high. All of the circled data points should be below the predicted curve because shadows from the tray edge and the antennas were not considered in the prediction. Antenna shadows appeared on the trays between ϕ of 105° and 135° , and their effect on the average output is noticeable but not excessive. This effect is due, in part, to the fact that at the time antenna shadows fall on a tray, another tray is illuminated and is therefore free of shadows. Figure V-8 indicates that while the vehicle is spin stabilized, an output almost equal to or greater than that of one tray normally illuminated is predicted for ϕ from 0° to 120° . This range approximately determines the limits on the angle between the vehicle axis and the sun vector at orbital injection.

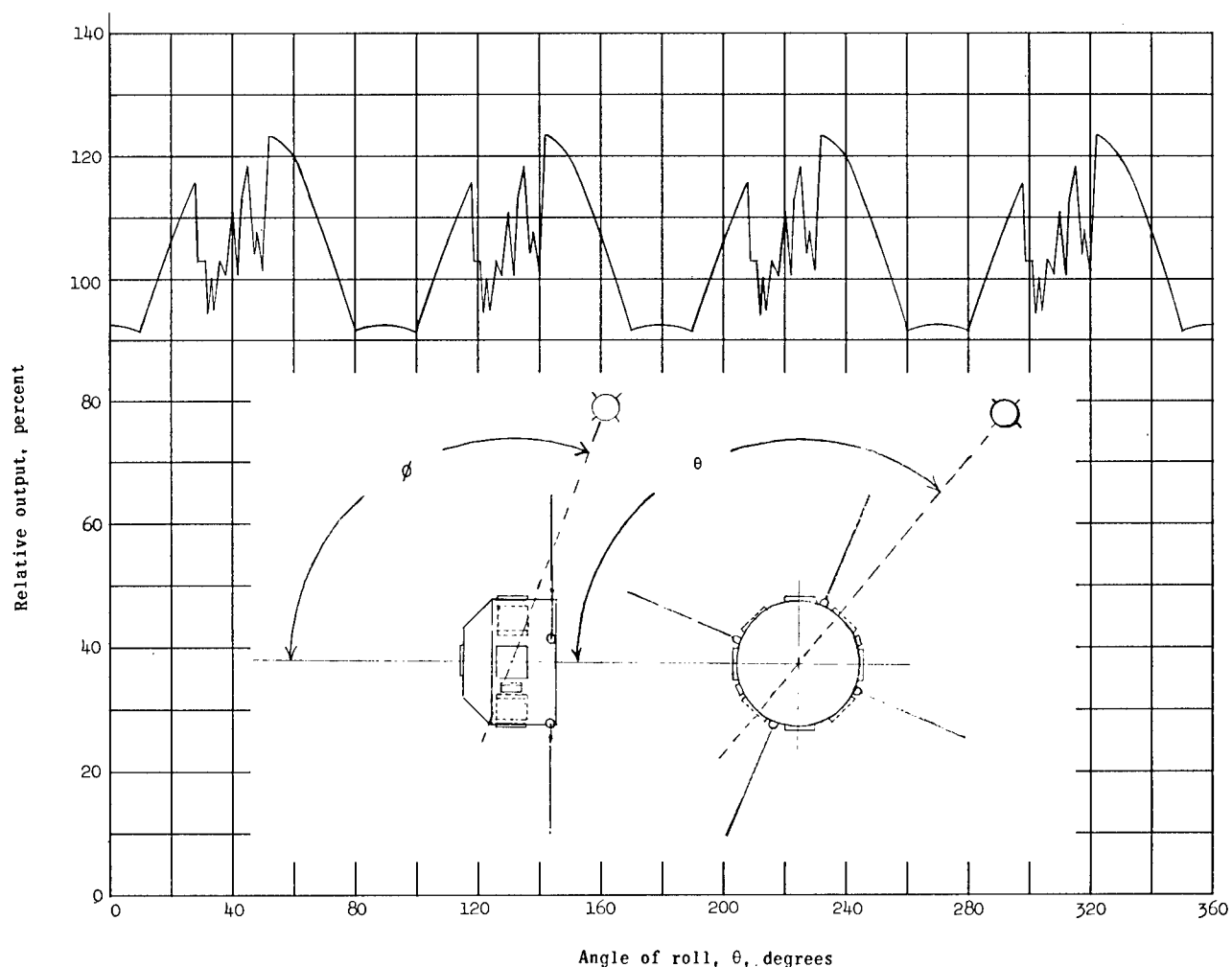


Figure V-9.- Output of solar cells with vehicle spin stabilized at $\phi = 110^\circ$.

The output of the solar cells after tumbling begins is difficult to predict. After all roll motions have ceased, the average output during tumbling could vary from the minimum of 87 percent as illustrated by figure V-7 to a maximum of about 136 percent. This maximum would occur when the sun vector is normal to the vehicle roll axis and midway between two trays. In general, the average output during tumbling (in each period of orbital sunlight) should approach the long-term average computed for random orientation to the sun, particularly when there is still some roll coupled with the tumbling motions. If a single solar cell or single tray of solar cells is randomly oriented to the sun, it can be shown (appendix A) that its long-term ideal average output will be one-fourth of its output at normal incidence. Hence, the five trays in each power supply were expected to have a combined ideal average percentage output of 125 during random tumbling. By using weighting factors proportional to the incremental solid angles involved (appendix B), the solid curve of figure V-8 was numerically integrated to obtain a value of 105 percent with respect to one tray at normal incidence for the output during random tumbling based on measured values. This was rounded off to 100 percent for estimation purposes.

The output of the power solar-cell trays due to reflected light from the earth was omitted in the preceding discussion. The additional output is difficult to predict, and in general, it will be small because when batteries are being charged, the output of a tray drops rapidly at low light intensities.

Qualifying Tests.- Before the shingles were cemented to the trays, they were all given a series of tests to eliminate defective units and to determine their electrical characteristics. To check for defective intercell bonds, the shingles were mechanically loaded in bending with a 250-gram weight while resting on supports 4.4 centimeters apart. In the routine electrical tests, values of short-circuit current, open-circuit voltage, output current at 1.85 volts (0.37 volt/cell), and output voltage at 36 ma were obtained. The acceptable cells were matched to provide the most efficient operation when connected in series on a tray. Emphasis was placed on current at 1.85 volts, and on the general shape of the current-voltage curve. The cells for the various trays of each supply were also selected to have approximately the same characteristics.

The acceptable cells with the lowest output were cemented to trays for the prototype vehicle. These were subjected to the environmental tests described in chapter VII both individually and while mounted on the forward shell. Subsequent trays were only given vacuum and temperature cycling tests before installation. Environmental testing after installation was considered more realistic - particularly vibration and impact tests because of the very large amplifications experienced. Initially, and after each test, the trays were illuminated to obtain the four parameters listed in connection with the shingle tests. Finally, data were taken to obtain the curve of room-temperature current plotted against voltage for each tray.

Proton Irradiation Tests.- The quartz windows were expected to give some shielding from the electrons and low-energy protons in space, but there was concern about the effects of high-energy protons, especially since the initial estimate of apogee was 1,275 miles. (The artificial electron belt did not exist at this time.) Hence, when a program was initiated at the NASA Langley Research Center to subject electronic components to proton irradiation, various types of

solar cells were included. A number of tests were made on cells ordered for Explorer XIII. Reference 1 gives the results from the preliminary tests made with proton energies of 22 and 240 Mev. Later unreported tests were made at 40 and 440 Mev as well as additional tests at 22 and 240 Mev. The damage rate varied with proton energy, and was not the same for supposedly identical cells, but the curve in figure V-10 is thought to be a typical plot of the degradation of the output current against integrated proton flux. If for the finally predicted orbit, 500 protons/cm²/sec be assumed for the flux of relatively high-energy protons, the curve of figure V-10 shows that the solar cells will be degraded 9 percent in 1 year.

SECTION III - BATTERIES

General.— The battery cells used were the sealed, nickel-cadmium, "button"-type cells. Their capacity rating was 500 milliampere-hours (mah) and in each power supply, 10 cells were connected in series to make a nominal 12-volt battery. A battery before potting is shown in figure V-11. The blocking diodes, described later, were also installed in the 5.5-inch-diameter, 1-inch-thick secondary battery module. To aid in sealing the cells, and to prevent working of the cases under internal pressure, the cells were potted in an unfilled epoxy resin.

A number of considerations influenced the selection of these cells for this application. A cell with a welded case closure and glass-to-metal seals around

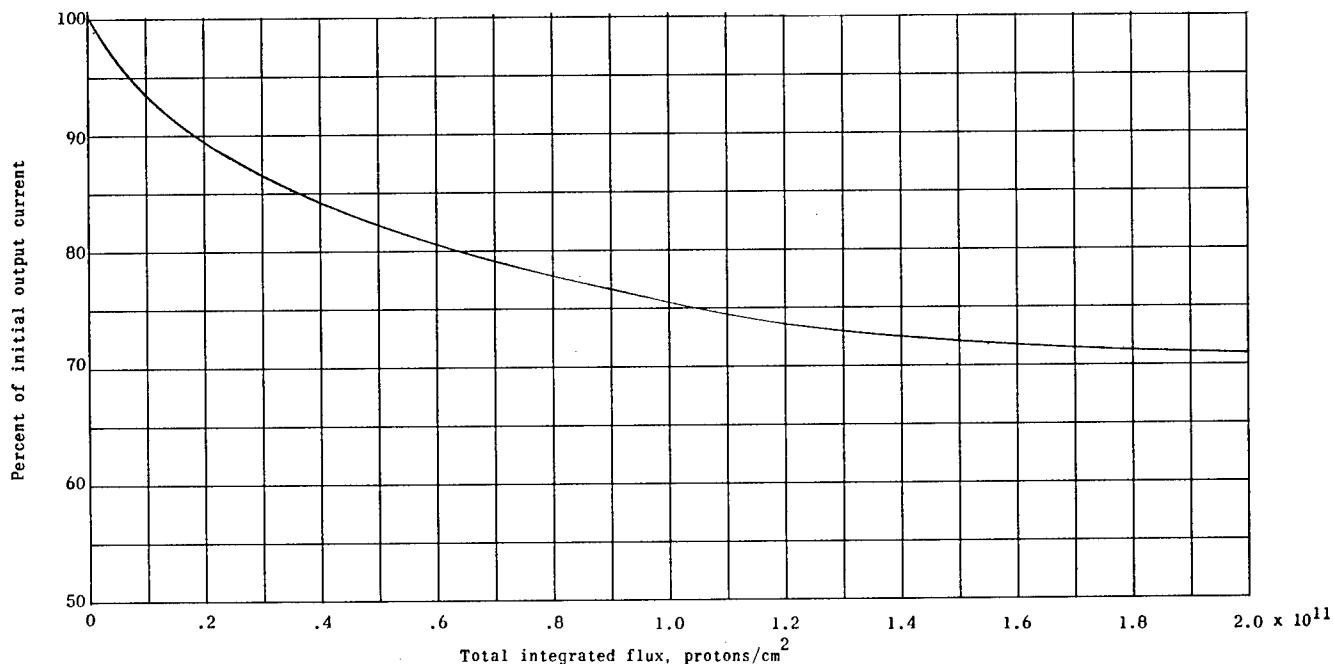
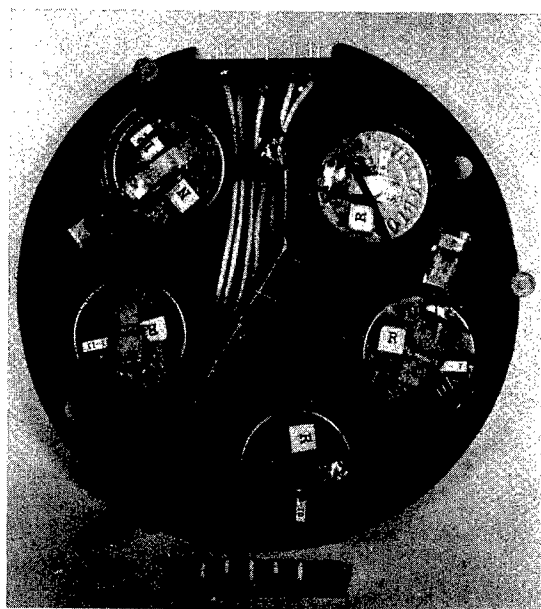


Figure V-10.— Degradation of solar-cell output-current with integrated proton flux in a 240 Mev proton beam.

the electrical leads was desired but was considered too large. Instead, it was decided to use the button cells having plastic seals, to pot them in epoxy, and to install them in the pressurized telemeter canisters. In addition, it was found that in the small cell size desired, the flat plates in the button cells were less liable to short as the separator material deteriorated than cells employing the wrapped-plate construction. For long cyclic life, it is generally recommended that the discharge per cycle be less than 10 percent of capacity. In this power supply, the maximum discharge per orbit is less than 2 percent of capacity even when interrogations are made in darkness. However, it was decided that the 115-ma load during interrogations would adversely affect the life of a cell with a capacity of much less than 500 mah. In addition, as explained later, a smaller cell would be more difficult to protect from overcharging.



L-60-7065

Figure V-11.- Secondary nickel-cadmium battery module before potting.

Battery Cell Characteristics.- Figure V-12 gives two voltage-time curves of a typical 10-cell battery used on Explorer XIII taken at room temperature while being discharged at 100 ma. This was the discharge current at which the nominal capacity of 500 mah was rated. When obtaining the solid curve, discharge was started immediately after overcharging at 30 ma. For the dotted curve, the battery was initially being overcharged but was discharged at 10 ma for 35 minutes (maximum expected orbital darkness) before start of the 100-ma discharge. These voltages vary with temperature and discharge rate and, as illustrated, are considerably influenced by prior operating conditions. The upper curve of figure V-13 gives the discharge voltage plotted against the temperature of a typical battery when interrogations in orbital sunlight were simulated. The readings were taken near the end of the 1-minute interrogation, and the battery was supplying about 75 ma (the solar cells supplied the rest of the load). The lower curve gives the voltages obtained with conditions the same except interrogations in darkness were simulated. The battery was supplying the entire 110-ma load, and before interrogation, had been supplying the 10-ma standby load. In each case, readings were taken after 10 or more cycles (simulated orbits) to allow time for the cyclic voltages to settle down.

For long life, the charging voltage of sealed nickel-cadmium cells should be limited to prevent irreversible formation of hydrogen gas. The maximum safe value is thought to be from 1.45 to 1.50 volts per cell, and to allow for cell differences, a value of 14.2 volts was used for the 10-cell batteries. The curves of figure V-14 relate charging voltage, charging current, and temperature at two typical charging conditions. The data for the solid curves were

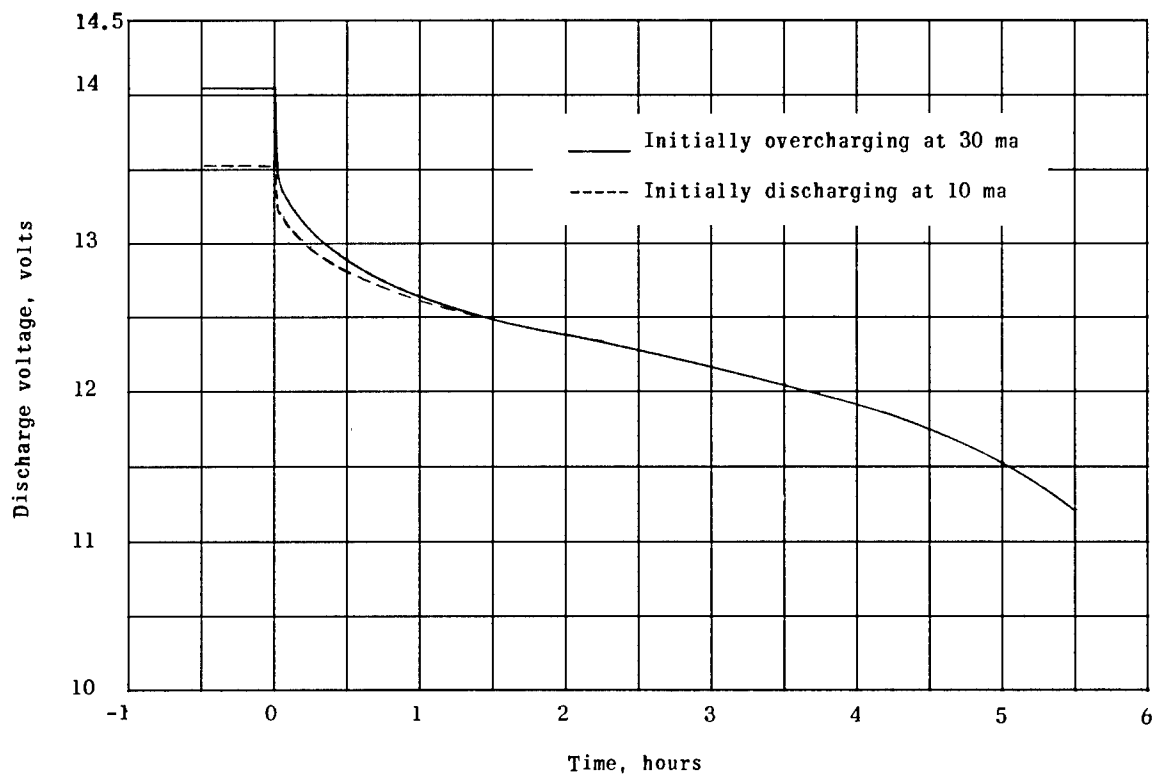


Figure V-12.- Variation of battery voltage at discharge current of 100 ma.

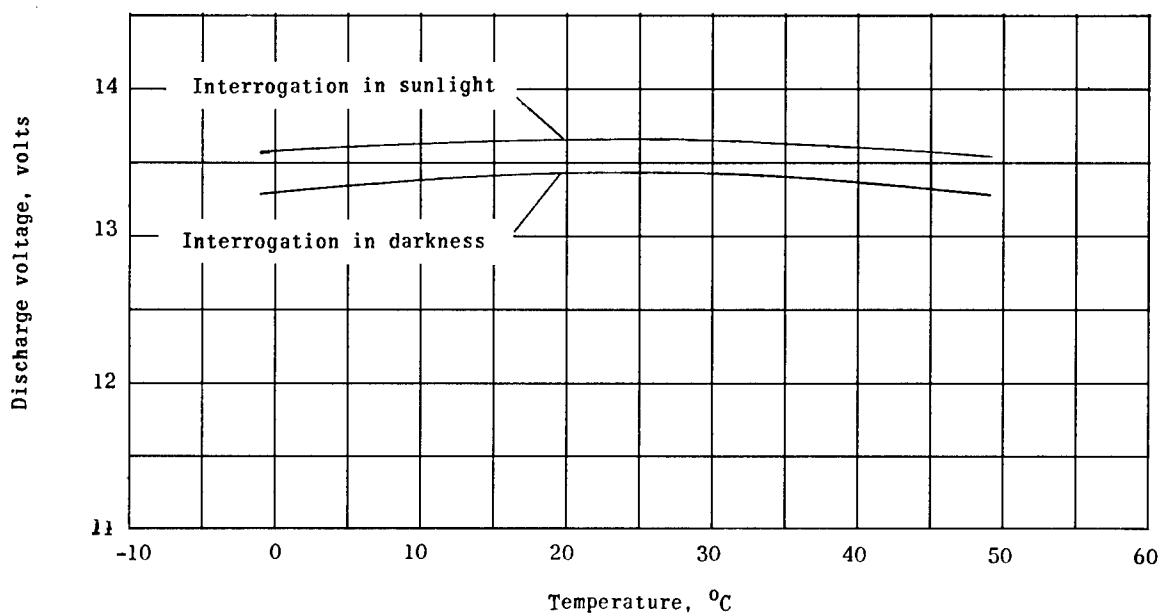


Figure V-13.- Variation of battery discharge voltage with temperature at two orbital conditions.

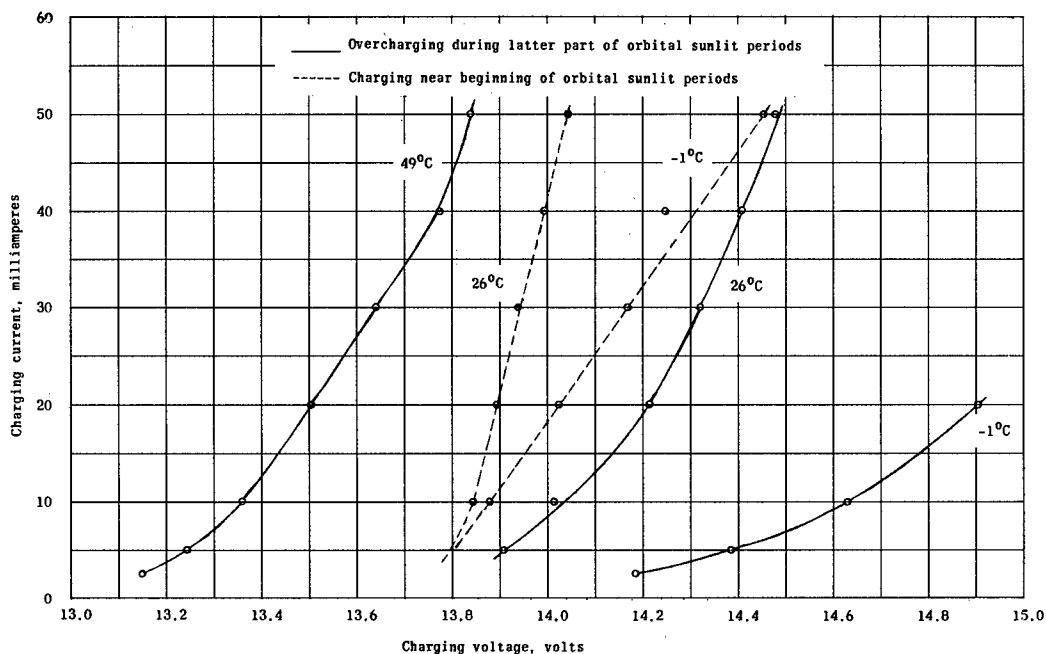


Figure V-14.- Relations between charging voltage, current, and temperature of a typical battery at two simulated orbital conditions.

taken after overcharging for 30 minutes at each current to simulate conditions during the latter part of the orbital sunlit periods. For the dotted curves, the battery was initially fully charged, then discharged at 10 ma for 35 minutes, before charging at the indicated current for 2 minutes. This simulated conditions near the beginning of the orbital sunlit periods. Since high battery temperatures are associated with 100-percent sun, only the overcharging curve is shown for 49° C. It will be noted that at low battery temperatures the charging rate, particularly when overcharging, must be sharply limited to prevent excessively high voltages. At high temperatures, the voltages are inherently low, but overcharging currents must still be limited to prevent excessive internal temperatures and pressures. It was decided that 40 ma was a safe overcharging current at voltages below the allowed maximum.

Another characteristic of these cells that should be mentioned is the possibility of reversed polarity when they are discharged below about 0.9 volt. When a number of cells in series are nearly discharged the lowest capacity cell may reverse while the total voltage is still reasonably high. The discharge current of the other cells will then attempt to charge it in the reverse direction. This results in rapid gas formation, and if a reversal occurs while battery discharge currents are high, a cell may actually explode. To prevent cell reversals, a battery should be made from matched cells thoroughly tested to eliminate defective cells, should not be fully discharged at high rates, and above all, should not be shorted. In the early phases of testing the prototype telemetry, these precautions were not strictly observed, and the damaged battery described in chapter VII was the result.

Qualifying Tests.- Since this button-type battery cell was not designed for space applications, and since the cells received had not been tested by the manufacturer, considerable attention was given to tests designed to detect sub-standard cells. This testing had to be limited so as not to affect the cell lifetime appreciably. After making a number of inquiries and thoroughly testing sample cells, it was decided to make the following tests on all cells before they were assembled as batteries:

1. Exercising cycle: Starting with the cells completely discharged as received, charge at 40 ma for 16 hours, and then at 30 ma for 4 hours; discharge at 100 ma for 4 hours.
2. Temperature cycles: After recharging the cell to 85 percent of capacity at room temperature, lower cell temperature to -10°C and charge at 10 ma for 1 hour, then discharge at 100 ma for 1 hour, return cells to room temperature and again recharge to 85 percent of capacity. At 49°C , charge at 30 ma for 1 hour, then discharge at 100 ma for 1 hour. At room temperature, discharge at 100 ma for 2 hours.
3. Electrolyte leakage: After cleaning each cell with alcohol, charge at 50 ma for 2 hours, and then at 40 ma for 5 hours. Discharge at 100 ma down to 1.1 volts per cell. Use saturated solution of phenolphthalein to look for evidence of alkalinity.
4. Internal electrical leakage: Charge to 10 percent of capacity and leave for 1 week.
5. Total capacity cycle: Charge at 40 ma for 16 hours, and then at 30 ma for 4 hours; discharge at 100 ma down to 1.1 volts per cell; individually discharge at 30 ma or less down to 1.0 volt.

During these tests, 12 cells were connected in series while in a simple test tray (fig. V-15). Voltage readings were taken periodically, and any abnormal behavior was noted.

In the first order of 120 cells only 15 percent were found to be acceptable. Some of the rejects had defective seals, but the majority of them gradually developed excessive internal resistance, and some became unstable. Internal examination revealed corrosion of the area where the combination loading spring and electrical lead contacted the case.

The supplier then furnished redesigned cells with thin stainless-steel tabs spotwelded to each outer plate and to the appropriate half of the case. About 200 of these improved cells were tested and no defects were found in approximately 75 percent of them.

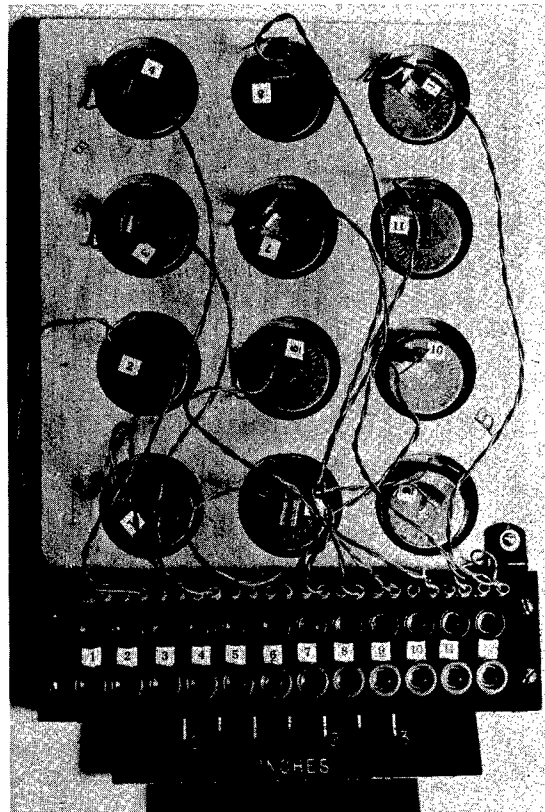
After the cells were potted in battery modules, they were given another complete charge and discharge cycle. The battery modules for the prototype spacecraft were subjected to the environmental tests described in chapter VII, both individually and while mounted in the telemetry assembly. Subsequent batteries were environmentally tested as part of the telemetry assembly. These tests included simulation of orbital cyclic conditions for several days.

During the several months between battery installation and vehicle launch, they were left unchanged whenever possible, and while charged but not in use they were trickle charged. Approximately 1 week before launching, the batteries were conditioned by a complete discharge and recharge cycle.

SECTION IV - COMPLETE

POWER-SUPPLY SYSTEM

Description.— Figure V-16 shows a simplified schematic diagram of each of the two power supplies. The points marked with a cross were available for external measurement of current and voltage during ground testing. Each of the five solar-cell trays was connected through a blocking diode to the nominally 12-volt buss. The type 1N538 blocking diodes were used to prevent the battery discharging through the solar cells when they were not illuminated. Over the current and temperature ranges of interest the forward voltage drop of these diodes varied from 0.68 to 0.78 volt, with 0.75 volt being a typical value. The reverse leakage current per diode was



L-60-3179
Figure V-15.— Nickel-cadmium cell test tray.

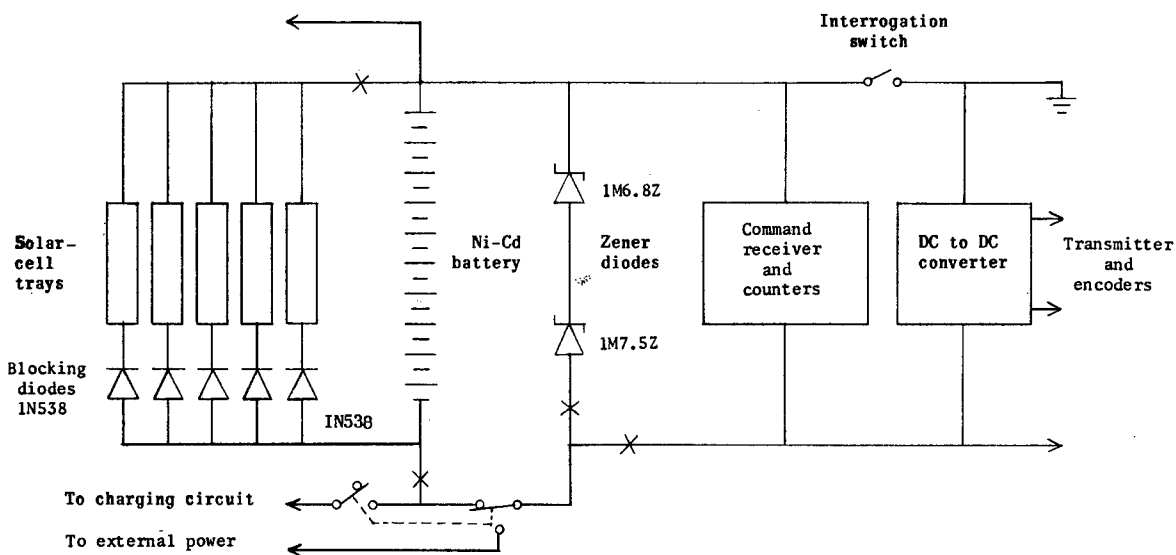


Figure V-16.— Simplified schematic of power supply.

less than $0.2 \mu\text{a}$, even at maximum expected temperature. The diode installation is shown in figure V-11.

The zener diodes were used to protect the batteries from excessive charging voltages and currents. It was necessary that zener voltages and battery voltages be well matched over the expected temperature range to insure adequate battery charging as well as protection, and to minimize battery drain by the zeners during orbital darkness. Unfortunately, the effect of temperature on the battery charging voltages (fig. V-14) was opposite to that on the voltage of high-voltage type of zeners, and the temperature coefficient of zeners increased with nominal voltage rating. It was decided to use two 1-watt, 1-percent zeners in series, one having a nominal zener voltage of 6.8 volts and the other 7.5 volts, giving a total nominal value of 14.3 volts. As indicated in figures IV-3 and IV-4, the zeners are installed on top of the telemetry assembly, where they

would be at about the same temperature as the batteries. Figure V-17 gives the relations between measured voltage, current, and temperature for a typical pair of zener diodes in series.

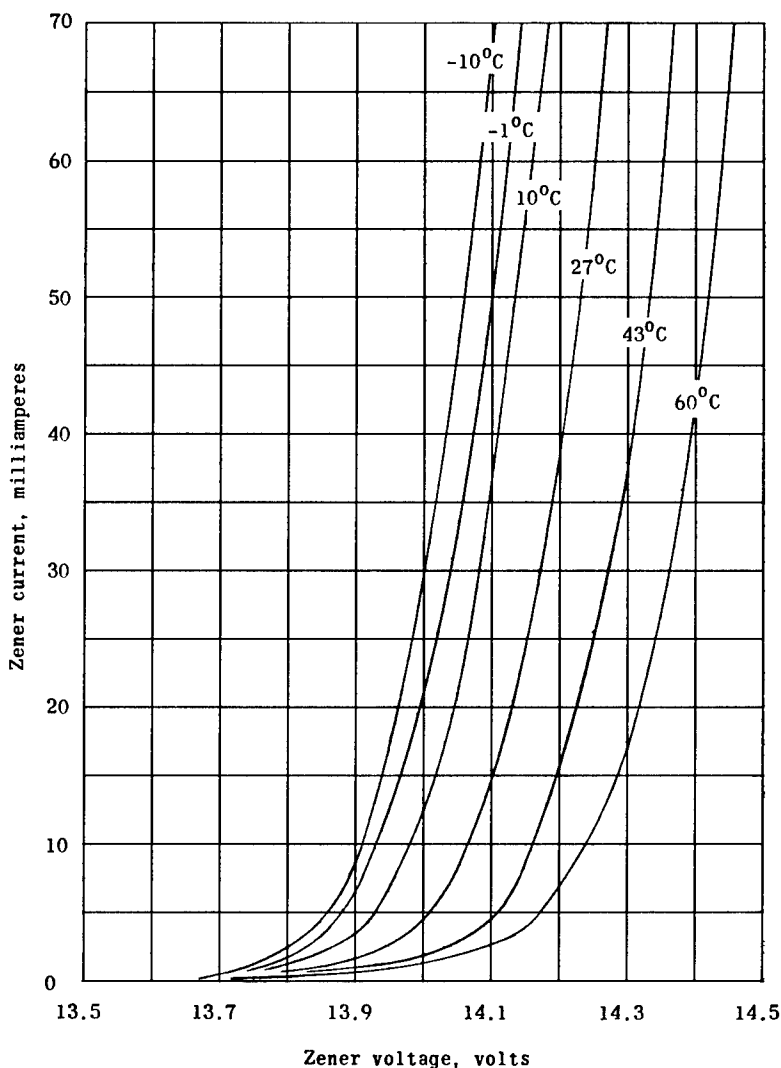


Figure V-17.- Relations between voltage, current, and temperature for a typical pair of zener diodes in series.

System Operation.- Figure V-18 illustrates the graphical method used to help to predict the power-supply buss voltages and the division of currents during various charging conditions in orbit, particularly when considering various zener diode circuits. The solar-cell output currents shown are those given by the appropriate temperature curve of figure V-4 multiplied by the applicable attitude factor from figure V-8. The other curves were obtained by adding a standby load current of 10 ma to the sum of the battery-charging currents from figure V-14 and the zener currents from figure V-17, at the same voltages and temperatures. The operating points of interest are obviously

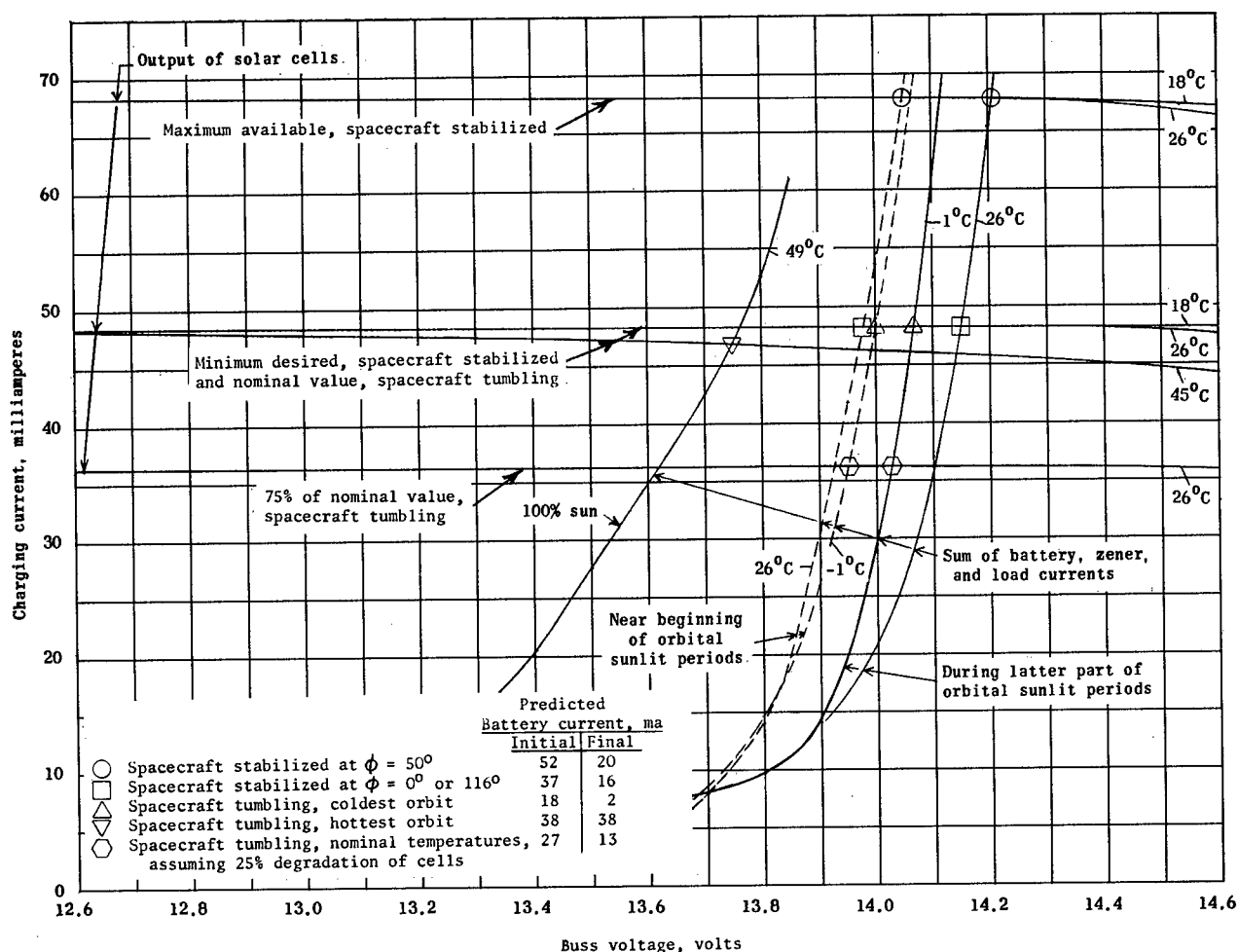


Figure V-18.- Graphical determination of power-supply voltages and currents for several extreme standby conditions in sunlight.

the intersections of the appropriate solar-cell-output curves and total load curves. These intersections determine the buss voltage, and then the battery and zener currents can be obtained from figures V-14 and V-17, respectively. Several extreme conditions are illustrated, and the predicted battery currents are listed in figure V-18. In each case, the maximum permitted charging voltages and currents were not exceeded. However, when the temperatures (and the percent time in sunlight) are near maximum, the zener diodes give very little protection against excessive overcharging currents. This lack of protection required that a launch time be selected that would give either moderate telemetry temperatures while spin stabilized or a stabilized attitude prohibiting maximum solar-cell output. In reference to the discussion of solar cells, it was unlikely that sustained overcharging above 40 ma would occur while the batteries are at elevated temperatures after the onset of tumbling.

It is during the coldest orbits, when time in darkness is maximum and telemeter temperatures are low, that recharging of the batteries is slowest. Fortunately, internal battery leakage is lowest at this time and recharging is

quite efficient. Tests were made to simulate orbital conditions for several days to see if the batteries were being adequately protected and recharged at various extreme conditions. Figure V-19 shows the recorded history, during the fourteenth cycle at coldest simulated orbital conditions, of battery voltage and current, and zener current, with the simulated solar-cell-output current kept at 40 ma. Various points on the curves agree with those previously found for a well-charged battery. The initial battery charging current was higher than inferred by figure V-18 because interrogations were made at the end of the simulated dark periods. In the cycle tests, when 25-percent degradation of solar-cell-output current (fig. V-18) was simulated, recharging of the batteries was still adequate at intermediate and elevated temperatures, but was marginal under coldest orbital conditions.

SECTION V - SOLAR-CELL TEST GROUPS

In addition to the previously described solar cells used in the power-supply system, five groups of solar cells - each consisting of a 5-cell shingle - were mounted on the forward shell to obtain data on the relative effectiveness of protective covers for the cells and to give an indication of the attitude of the vehicle. Three of these shingles can be seen mounted on the forward shell

in figure V-1 (on upper end of the spacecraft in the photograph). One of these was protected with a 1/16-inch-thick quartz window; one had 6-mil-thick glass slides cemented to the cells; the other had bare cells. The latter two shingles were cemented to the same tray. Since the three shingles had the same orientation to the sun, and since their output voltages were telemetered on consecutive frequency channels, their relative degradation in the space environment could be directly determined. Thermistors were used to monitor the temperature of each of the two mounting trays.

The other two test groups were mounted 180° apart on the cylindrical side of the forward shell. The one visible in figure V-1 had the 6-mil glass slides cemented to its cells. The other was identical except that its cells were bare. The

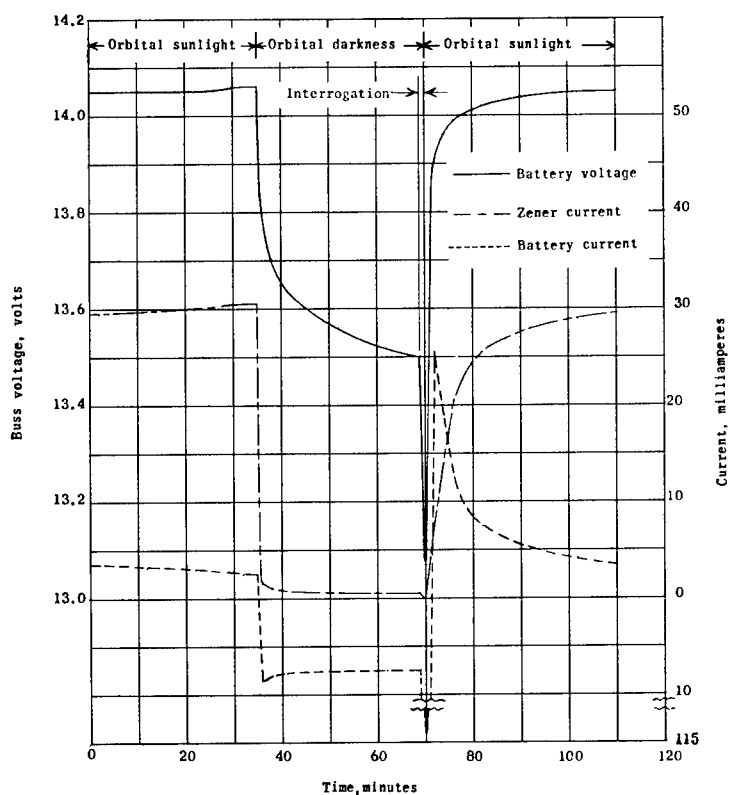


Figure V-19.- History of battery voltage, battery current, and zener current during simulation of coldest orbit.

telemetered output voltage of these two shingles, together with the data from those on the forward end, was used to estimate the orientation of the vehicle to the sun. With this information, the absolute value of the degradation of each of the five test shingles could be estimated.

Each of the five shingles of test cells consisted of five of the solar cells described previously - ungridded, P on N type, with nominal efficiencies of 8 to 9 percent. Each cell was loaded with 39.2 ohms, which gave an output voltage near the maximum power point of the cells and large enough to drive the voltage-controlled oscillators. The calibration of a typical test shingle against light intensity, at 32° C, is given in figure V-20. Corrections were made for the spectral output of the artificial lights used, and the values of light intensity shown are equivalent to those in space. Figure V-20 also gives the calibration of the same shingle against temperature, at a light intensity of 112 mw/cm² (m = 0). The calibrations against angle of incident sunlight varied slightly with the type of cell covering, if any, but in general resembled the solid curve of figure V-6. The test cells were given the same environmental tests as mentioned above for the power trays.

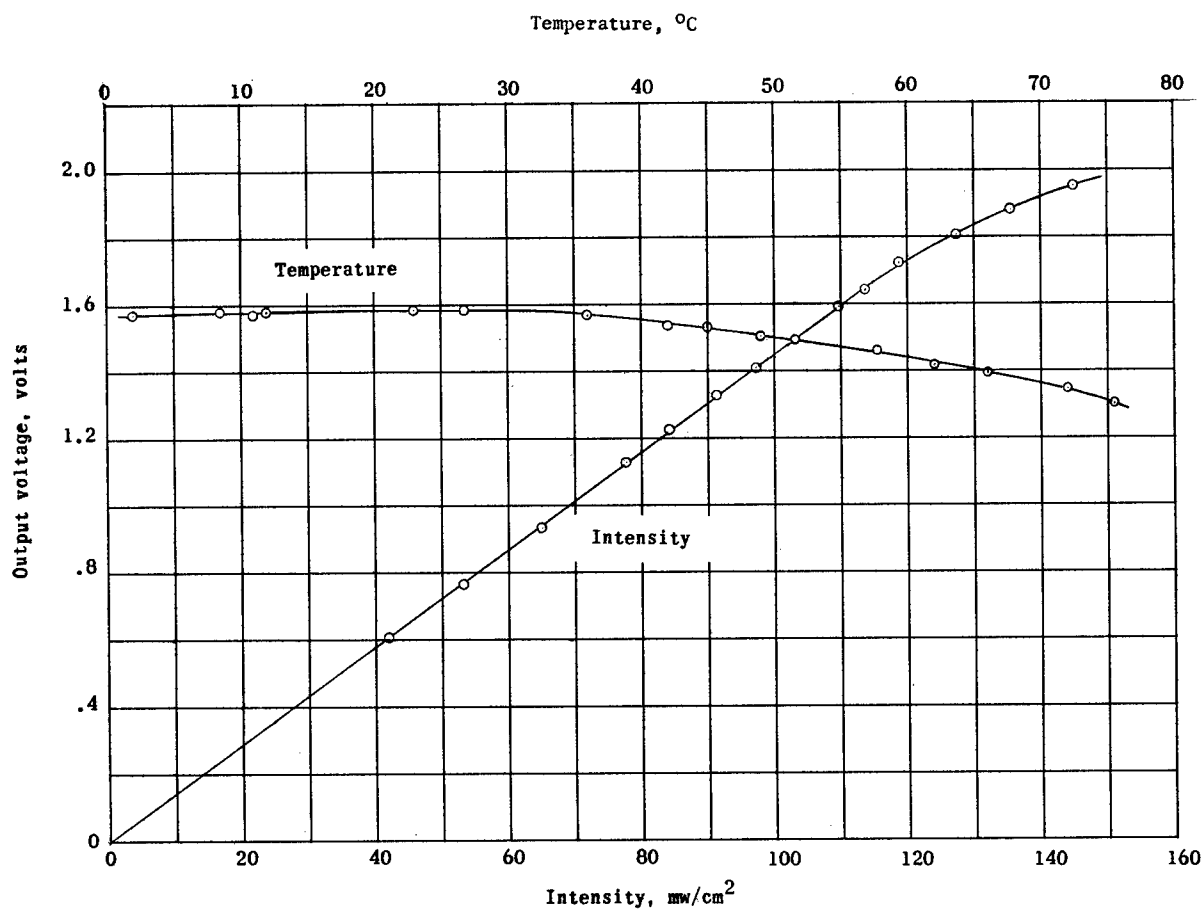


Figure V-20.- Calibration curves of output voltage against light intensity and temperature for a typical test group of solar cells.

SECTION VI - FLIGHT RESULTS

The battery voltages received by telemetry from Explorer XIII were quite close to those predicted by the preflight tests previously described. Although the outputs of the power-supply solar cells were not monitored in flight, the normal battery voltages indicated that both of the power-supply systems survived the launch operations and performed as expected during the life of the spacecraft. No deterioration of the test cells on Explorer XIII was detected. Since interrogations after the fifteenth orbit were made in darkness, the useful exposure time was only about 1 day.

The telemetered output of the test cells indicated that the spacecraft was spin stabilized with its axis approximately 90° from the sun during the interrogated sunlit orbits. Since the telemetry-framing rate was about 3.8 frames/sec compared with the roll rate of about 3.2 rps (obtained from signal strength records), a number of frames had to be examined to get even an approximate attitude. Figure V-21 gives the readings obtained from one group of test cells on the side of the vehicle during the fourteenth orbit. All the readings are plotted relative to the calibrated output obtained for the curve of solar constant against time during a single cycle of roll. Data points from the several telemeter frames during a 14-second period were superimposed to give a composite history of one roll cycle. As indicated, the calibration of output against angle of incident sunlight obtained with the axis of rotation 90° from

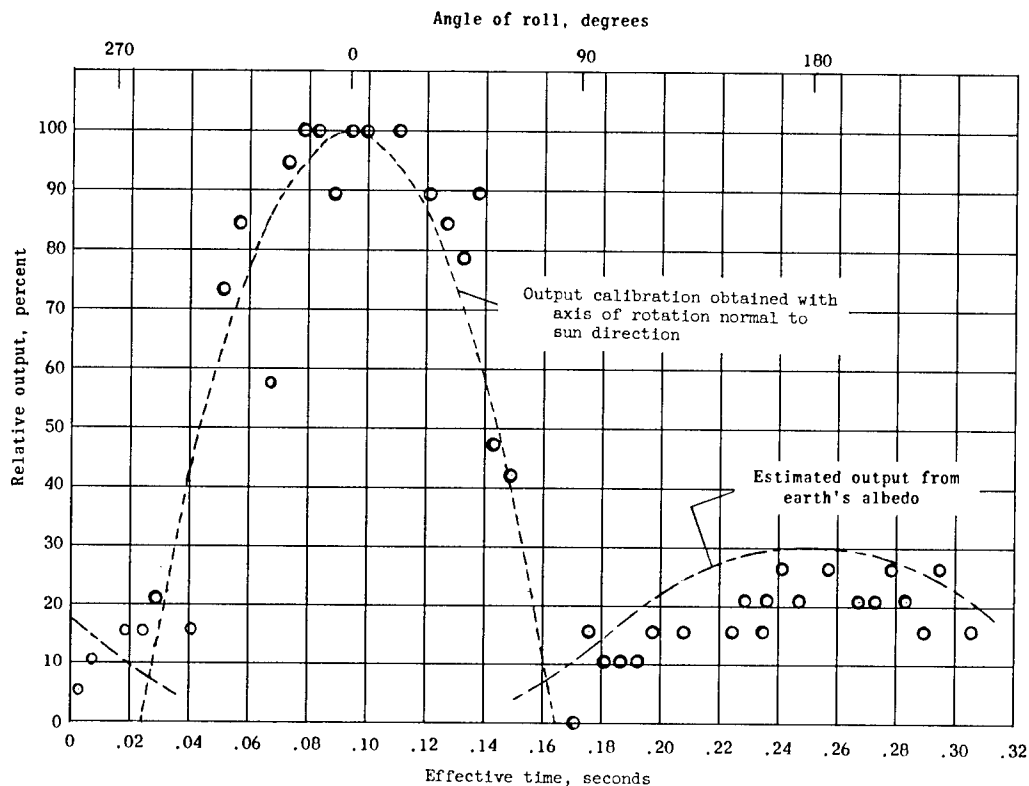


Figure V-21.- Output of test cells on side of vehicle during a portion of the fourteenth orbit.

the sun direction, roughly fitted the higher amplitude readings. The lower amplitude readings approximated the output estimated for the solar cells when rotated away from the sun and illuminated by the earth's albedo.

SECTION VII - APPENDIX A

Ideal Long-Term Average Output of a Solar Cell

Randomly Oriented to the Sun

Assume that:

I = Output of solar cell illuminated at normal incidence

$I \cos \phi$ = Output at a light incident angle of ϕ

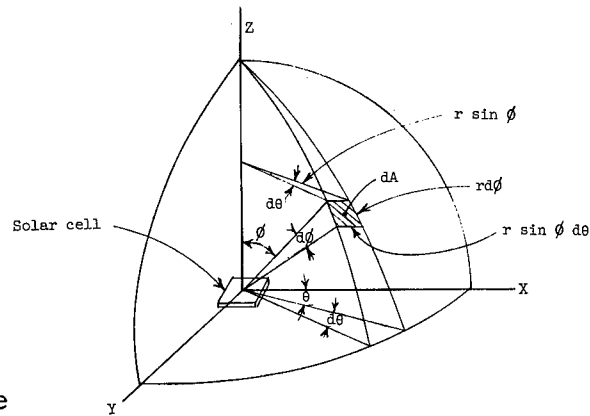
In spherical coordinates (see fig. V-22(a)),

$$\begin{aligned} d\beta &= \frac{dA}{r^2} = \frac{(r d\phi)(r \sin \phi d\theta)}{r^2} \\ &= \sin \phi d\phi d\theta \end{aligned}$$

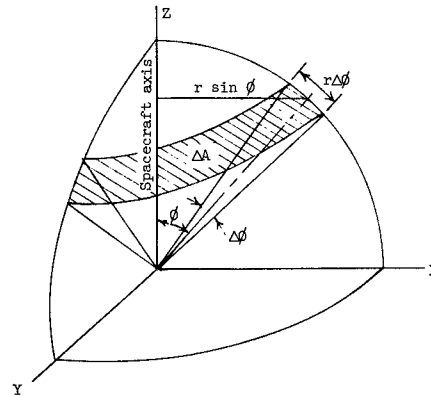
where β is the solid angle in steradians associated with an area A on the reference sphere of radius r . The output of the solar cell averaged over the 2π steradians above the X-Y plane is

$$\begin{aligned} &\frac{1}{2\pi} \int_0^{2\pi} \int_0^{\pi/2} I \cos \phi d\beta \\ &= \frac{I}{2\pi} \int_0^{2\pi} \int_0^{\pi/2} \cos \phi \sin \phi d\phi d\theta \\ &= \frac{1}{2} I \end{aligned}$$

Since the solar cell has no output when illuminated from below, its long-term average output when randomly oriented to the sun is $1/4 I$.



(a) Exact integration in ideal case.



(b) Approximate numerical integration.

Figure V-22.- Spherical axis systems employed in analysis.

SECTION VIII - APPENDIX B

Weighting Factors

To obtain the average output during random tumbling by numerically integrating the curves of figure V-8 (obtained by averaging the output over a spin cycle at various angles of ϕ), each value must be weighted by a factor proportional to the incremental solid angle involved. With reference to figure V-22(b) and the symbol definitions in appendix A, the incremental solid angle is

$$\Delta\beta = \frac{\Delta A}{r^2} = \frac{(r \Delta\phi)(2\pi r \sin \phi)}{r^2} = 2\pi \Delta\phi \sin \phi$$

If w_1, w_2, \dots, w_n is a given set of weighting factors, the weighted mean of a given set of output values I_1, I_2, \dots, I_n is

$$\frac{w_1 I_1 + w_2 I_2 + \dots + w_n I_n}{w_1 + w_2 + \dots + w_n}$$

It will be noted that the constant terms in the weighting factors will cancel, and by using equal values of $\Delta\phi$, the weighting factors of interest are given by $\sin \phi$. The curves of figure V-8 were evaluated at each 10° increment of ϕ . Letting $\Delta\phi = 20^\circ$, the expression for the long-term average output during random tumbling is

$$\frac{I_{100} \sin 10^\circ + I_{300} \sin 30^\circ + \dots + I_{1700} \sin 170^\circ}{\sin 10^\circ + \sin 30^\circ + \dots + \sin 170^\circ}$$

SECTION IX - REFERENCES

- V-1. Hulten, W. C., Honaker, W. C., and Patterson, John L.: Irradiation Effects of 22 and 240 Mev Protons on Several Transistors and Solar Cells. NASA TN D-718, 1961.
- V-2. Nash, Harry: Silicon Photovoltaic Cells for Space Vehicles. Electronic Inst., Aug. 1959, pp. 91-106.
- V-3. Zoutendyk, John A.: A Method for Predicting the Efficiency of Solar Cell Power Systems Outside the Earth's Atmosphere. Tech. Rep. No. 32-259 (Contract NAS 7-100), Jet Propulsion Lab., C.I.T., Apr. 10, 1962.

CHAPTER VI

THERMAL DESIGN

By Earl C. Hastings, Jr., Richard E. Turner,
and G. Louis Smith
Langley Research Center

SECTION I - INTRODUCTION

An essential phase of the Explorer XIII development was a thermal study and design to provide an acceptable temperature environment for the electronics components and external surfaces of the satellite during ascent and in orbit. It was necessary to establish by preflight analysis and tests that tolerable temperatures could be maintained in three regimes of flight. In the first regime (from launch until release of the heat shield) the satellite was subjected to radiative and conductive heat from the shield. In the second regime, after release of the shield at 350,000 feet, the satellite was heated by free molecular flow. In the third regime - the orbit phase - it was necessary that temperatures within limits for a 1-year lifetime be established. In addition to these three regimes, a study was made to investigate the effect of elevated rocket-motor temperatures during launch and after burnout.

This chapter will deal with some pertinent preflight estimates and correlation of these estimates with flight data.

SECTION II - SYMBOLS

a_s	absorptivity of solar radiation
a	semimajor axis of orbit, ft
A	cross-sectional area of satellite section, ft^2
B	decay constant for atmosphere, taken as $3.48 \times 10^{-5}/\text{ft}$
E	eccentric anomaly
erf	error function
g_0	acceleration due to gravity at earth's surface
$I_n()$	modified Bessel function of the first kind of order n
k	Boltzmann constant, 0.728×10^{-26} Btu/molecule- $^{\circ}\text{R}$

n	number of molecules striking surface per unit area per unit time
N	number of molecules per unit volume
P	orbit period, min
q	heat-transfer rate per unit surface area, Btu/ft ² -sec
Q	heat input per unit surface area per orbit, Btu/ft ² -orbit
\bar{Q}	total heat input to satellite section, Btu/ft ² -orbit
r	spacecraft distance from center of earth, ft
r ₀	reference altitude, ft
R _e	radius of the earth, 2.0903×10^7 ft
$s = \frac{U}{\bar{v}}$	
S	total surface area of satellite sector, ft ²
t	time, min
T	temperature, °R
T _∞	free-stream temperature, °R
U	free-stream velocity, ft/sec
\bar{v}	mean molecular velocity, ft/sec
x	argument of Bessel function
α	thermal accommodation coefficient
β	angle between flow direction and the normal to the surface, deg
γ	ratio of specific heats
ε	orbit eccentricity
ε _{TH}	total hemispherical emissivity
$\eta = s \cos \beta$	
$\mu = g_0 R_e^2, 1.42 \times 10^{16} \text{ ft}^3/\text{sec}^2$	

σ Stefan-Boltzmann constant, $2.0 \times 10^{-13} \frac{\text{Btu}}{\text{in.}^2 \cdot \text{min} \cdot \text{°R}^4}$

Subscripts:

av average
m mean
p perigee
w wall

SECTION III - ANALYTICAL METHODS

Methods were established by which analytical solutions to the heat-transfer problems could be found for all the regimes discussed. These are derived and discussed in detail in reference VI-1 and are not repeated herein. Reference VI-1 also contains detailed discussions of the test results and coatings evaluated in this thermal-design study. The estimates discussed herein have been performed for the actual launch date of Explorer XIII (August 25, 1961); however, the estimates of reference VI-1 consider a launch data of June 15, 1961.

SECTION IV - RESULTS AND DISCUSSION

Estimated temperatures.— The temperature limits specified for Explorer XIII are tabulated as follows: (These limits had been established by the designers as those which might impair reliability or proper operation of the sensors.)

Component	Maximum allowable temperature, °F	Minimum allowable temperature, °F
Telemetry	120	15
Pressurized cells	250	-50
Steel-covered-grid detectors	180	-100
Copper-wire-card detectors	300	None given
Solar cells	250	-50
Cadmium-sulfide cells	200	None given
Impact detectors	250	-50

Estimated heating calculations during ascent and in orbit to be discussed herein were based on the nominal trajectory defined as follows:

Launch characteristics:

Actual launch date	August 25, 1961
Launch azimuth	90° from north
Launch elevation, deg	79.88

Orbital characteristics:

Initial perigee altitude, n.m.	207
Initial apogee altitude, n.m.	527
Orbit period, min	98
Orbit inclination, deg	37.68
Satellite lifetime, year	>1

Prior to the launch of Explorer XIII, several nominal trajectories were considered. For this reason the values listed in this table differ slightly from the predicted orbital parameters in table II-4. Studies have established that these differences would not have a large effect on the data discussed in the present chapter.

Figure VI-1 shows a sketch of Explorer XIII in the heat shield. Temperatures were estimated during ascent for three stations on the heat shield: the stagnation point of the hemispherical tip, the conical section, and the cylindrical section (designated by 1, 2, and 3, respectively, in fig. VI-1). Both outside- and inside-wall temperatures were computed for station 3 on the cylindrical section which was located approximately over the first row of pressure cells. The temperature history of the pressure cells due to this radiant heating source was also estimated and the results are plotted in figure VI-2.

During simulated ascent, experimental values of payload temperature were obtained as part of the heat-shield qualification tests. The Explorer XIII prototype was placed inside the heat shield and the shield was subjected to the estimated outside-wall-temperature time histories of figure VI-2. Temperatures of the spacecraft during the test were monitored by a number of thermocouples on the exposed surfaces and in the telemetry canisters. Results of this test are

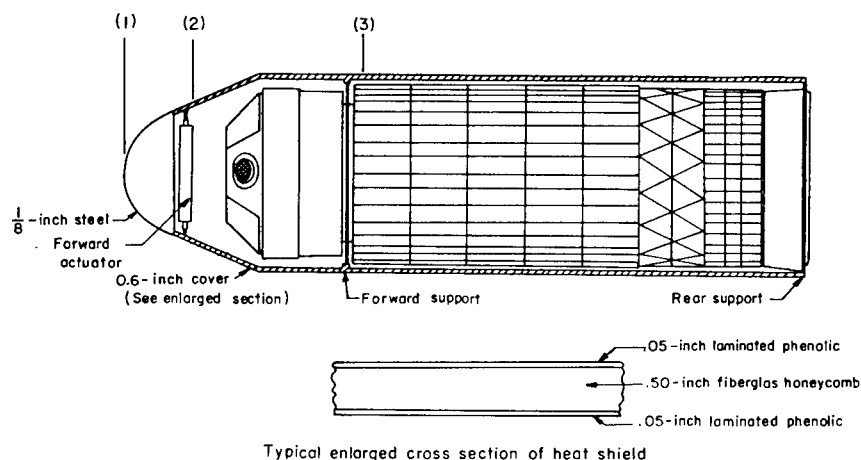
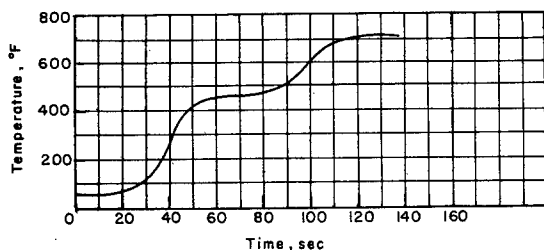
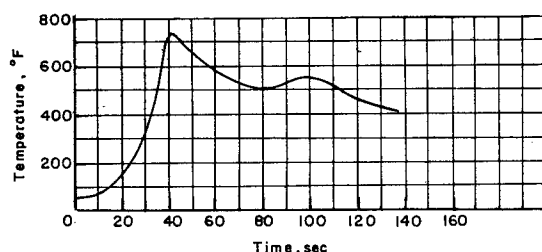


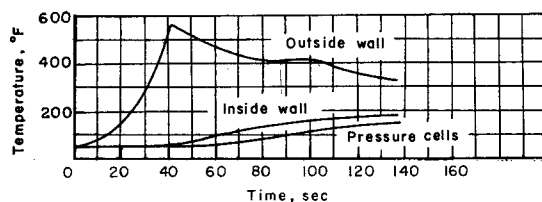
Figure VI-1.- Explorer XIII in heat shield.



(a) Temperature time history at station 1.



(b) Temperature time history at station 2.



(c) Temperature time history at station 3.

Figure VI-2.- Temperatures during ascent with heat shield in place.

presented in figure VI-3 along with pressure-cell estimates from figure VI-2 which are shown for comparison.

It can be seen from figure VI-3 that the maximum temperature of the pressure cells from the simulated ascent test was considerably lower than that predicted, and that the steel-covered-grid detectors and copper-wire-card detectors experienced temperature rises of less than 20°F during the test. Although not shown in the figure, values of telemetry-canister temperature remained constant throughout the test. It was not expected that these components would respond to external temperature sources over such a relatively short time. The analytical and experimental studies conducted in this part of the thermal-design program established that during ascent with the heat shield on, the external surfaces of the satellite would remain within tolerable temperature limits and that the telemetry temperature would not be affected by aerodynamic heating.

The method discussed in reference VI-1 was used to estimate the free-molecular flow heating for Explorer XIII after heat-shield ejection for a range of altitudes between 300,000 and 400,000 feet. These estimates were made only for the pressure cells, since they would heat most rapidly because of their surface characteristics. This study indicated that above 350,000 feet, there would be no increase in detector temperature due to this heating source for flow parallel to the flight path.

Since the last stage of the booster vehicle was an integral part of Explorer XIII, it was necessary to evaluate the effects of elevated temperatures of this booster stage on the various detectors of the satellite. Figure VI-4 shows experimentally determined temperature histories from the static firing of a rocket motor similar to the last stage of the Scout launch vehicle at reduced external pressures (ref. VI-2). These data indicate that following burning of the last stage the temperatures of the rocket-motor case generally reached maximum values at or before 500 seconds after ignition and then decreased with increasing time.

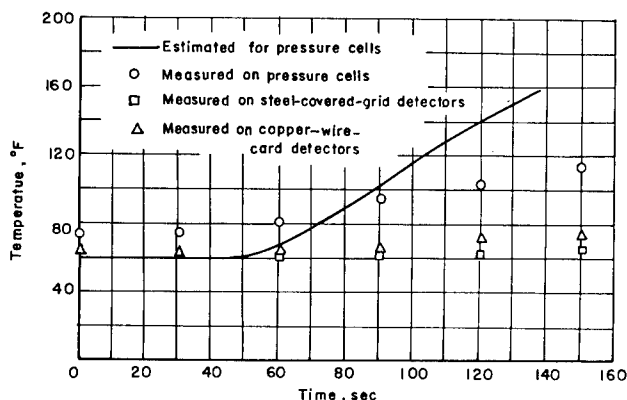


Figure VI-3.- Estimated and measured spacecraft temperatures during simulated ascent heating test.

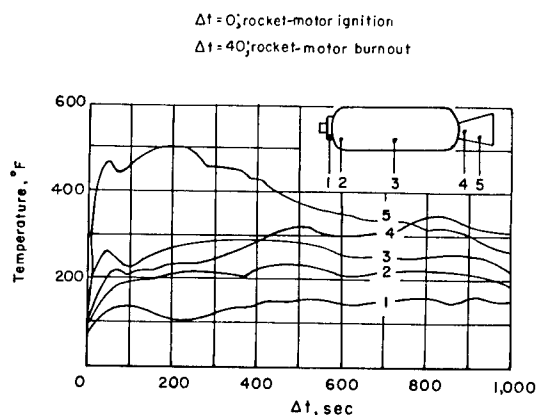


Figure VI-4.- Measured temperatures from static firing of the X248-A9 rocket motor.

An analytical program was used to consider the influence of the nozzle temperature (point 5) and the motor-case temperature (point 3) on the rear row of pressure cells and the steel-covered-grid detectors and copper-wire-card detectors. To be conservative, a constant temperature of 600°F at point 5 and a constant temperature of 400°F at point 3 were assumed to exist from $\Delta t = 0$ minute to $\Delta t = 20$ minutes. Direct and reflected solar radiation and earth thermal radiation were also considered in these calculations. The results are shown in figure VI-5.

These data show a constant increase in the temperature of the steel-covered-grid detectors after $\Delta t = 4$ minutes reaching a value of 144°F when the satellite enters the earth's shadow at $\Delta t = 20$ minutes. After $\Delta t = 20$ minutes the temperatures will decrease since the solar-heating input is removed. The temperatures of the copper-wire-card detectors and last row of pressure cells are 118°F and 125°F , respectively, at this time. The temperature values computed for the last row of pressure cells should be representative of all the pressure cells because of the excellent thermal conductivity of the pressurized-cell mounting structure and the existence of a heating source from the support at the rocket-motor headcap. Estimates were also made to determine the increase in telemetry temperature associated with a constant headcap temperature of 200°F for 20 minutes. These estimates established that a rise of less than 5°F would result from this heating source.

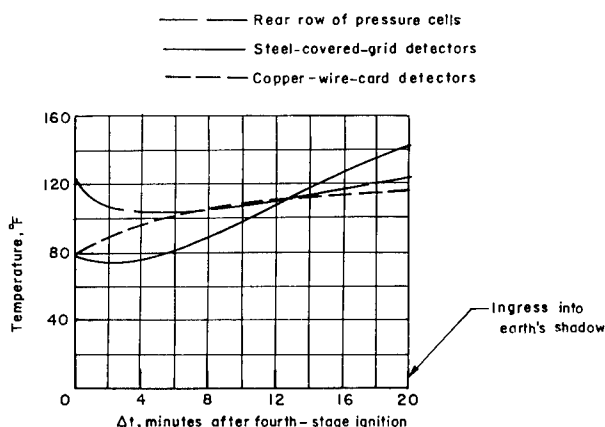
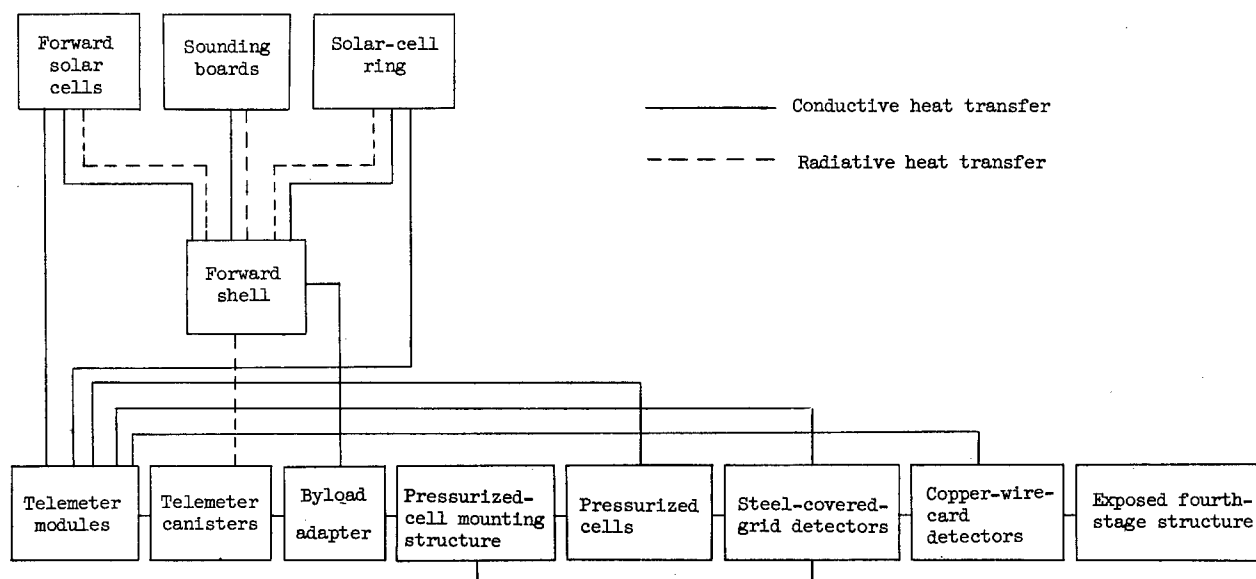


Figure VI-5.- Estimated satellite surface temperature due to last stage rocket-motor heating.

This phase of the study established that of all the heating sources

investigated during ascent, the effects of the rocket-motor temperatures had most pronounced effects on the detectors. All the detector temperatures were found to remain within tolerable limits; however, the increase in telemetry temperature was expected to be less than 5° F from the ascent heating sources.

Orbital heating calculations were performed on an electronic data processing machine which computed 12 time-dependent temperatures simultaneously. The satellite was considered to be composed of a number of sectors with the heat-flow paths shown in the schematic diagram below:



Passive thermal design was used, and heat-flux equations were written for each of the sectors by considering conductive and radiative heat transfer between the sectors, and where necessary direct and reflected solar radiation and earth thermal radiation were considered. (See ref. VI-1.)

The following are the absorptivity and emissivity values of the exposed sectors of the satellite:

Component	Absorptivity, α_s	Emissivity, ϵ_{TH}	Surface finish*
Forward shell	0.71	0.42	410 stainless steel; sand blasted with 100 mesh grit; heated in air at 600° F for 5 minutes
Sounding boards	.71	.42	Same as above
Composite solar cell ring	.57	.79	Black and white mosaic
Composite solar cells on forward face	.41	.89	Black and white mosaic
Pressurized cells	.19	.16	Vapor-deposited aluminum and silicon monoxide films
Steel-covered-grid detectors	.32	.82	Lusterless white enamel
Copper-wire-card detectors	.66	.69	Enameled copper wire
Exposed fourth-stage structure	.93	.74	Black lacquer

*For details of surface finishes, see ref. VI-1.

Interior surfaces were prepared with low-emissivity coatings to reduce heat transfer from the motor case. The last stage rocket motor and the satellite surfaces which were exposed to radiation from the motor case were covered with aluminum foil. The mounting bulkhead, the inside of the forward shell, and the outside of telemeter canisters, and the bases were gold plated.

Since there was no system on Explorer XIII to orient the spacecraft it was necessary to consider temperatures both for the mode of spin about the principal axis (the condition at injection into orbit), which will be referred to herein as the "stable" mode, and for the mode of spin about the axis of maximum moment of inertia, referred to herein as the "tumbling" mode. Studies indicated that the initial spin motion should convert to a tumbling motion in less than 2 weeks as shown in figure VI-6. The first computations of orbital temperatures were made for the tumbling mode since the hottest and coldest cases could be made to occur in this mode with proper selection of launch time. Estimates discussed in reference VI-1 establish that for the coatings used, telemetry-temperature values for Explorer XIII in the tumbling mode should be between 30°F and 111°F for a 1-year lifetime.

A study of the parameters governing the launch time (stable mode of spin) established that for an August 25 launch date, the hours between 0900 and 1330 e.s.t. were satisfactory. Figure VI-7 is an estimated temperature time history of the sensors for a 1330 e.s.t. launch. The telemetry temperature of 51.6°F during orbital heating is also noted. Figure VI-8 shows calculated percent-time-in-sunlight histories for three launch times on August 25.

Flight-test results.- Explorer XIII was instrumented with 18 thermistors to measure temperatures in flight (fig. VI-9). Solar-cell temperatures were measured under the mounting frames of two units 180° apart on the heat-transfer band. Forward-shell temperatures were measured on the inside wall of the cylindrical section, also at stations 180° apart. Two of the 0.002-inch-thick pressure cells in the first row had thermistors mounted on the bottom of their base plates. The steel-covered-grid detectors had four thermistors (spaced 90° apart) located directly under the steel grids. Two wire-card-detector temperatures were measured in the fiber-glass backing under individual cards. Thermistors located in each of the telemeter stacks (in the second module forward of the base) were used to measure telemetry temperature. The cadmium-sulfide cells had thermistors located inside the flask below the light-sensing element.

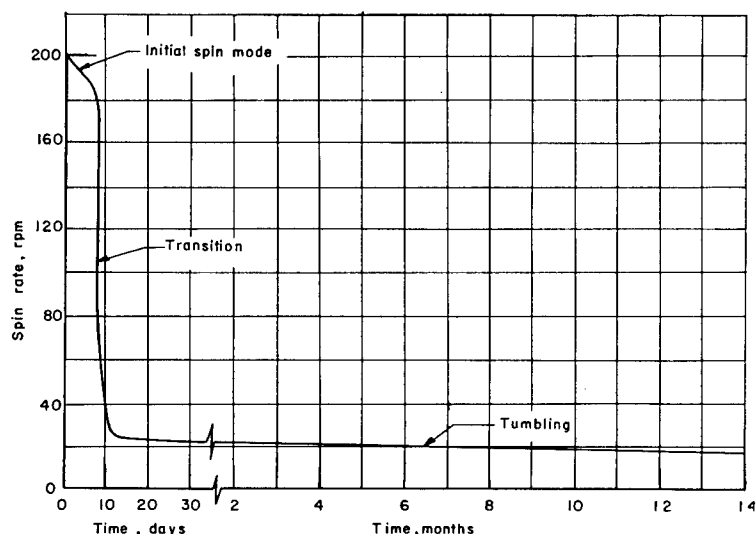


Figure VI-6.- History of spin rate due to magnetic torques.

Telemeter temp. = 51.6 °F

- Pressure cells
- △ Solar cells
- ▽ Forward solar-cells
- Copper-wire-card detectors
- ◇ Steel-covered-grid detectors

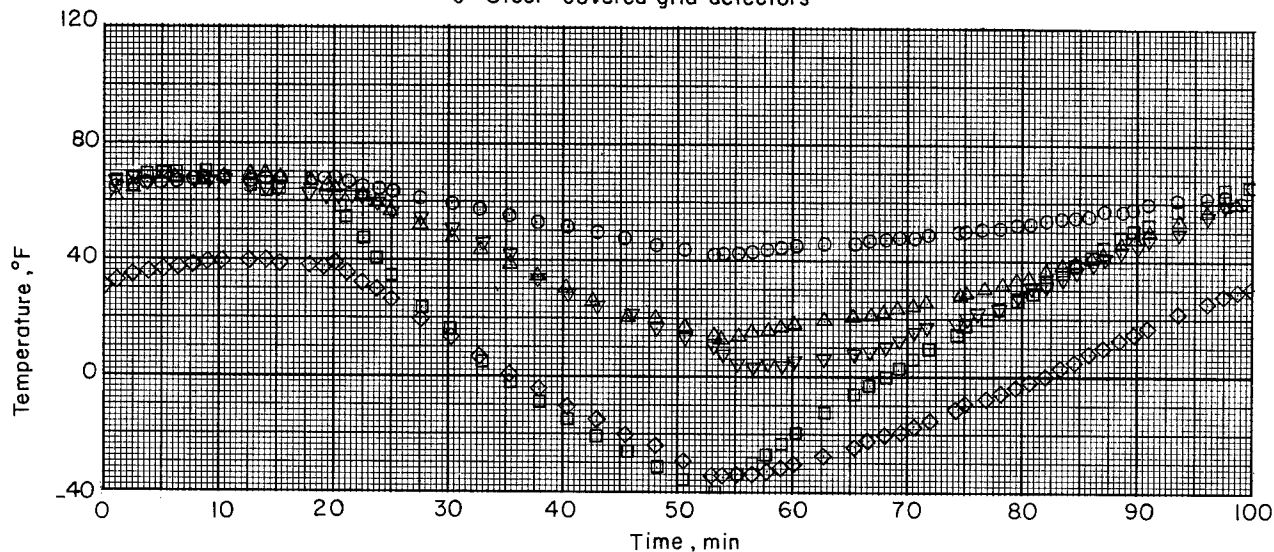


Figure VI-7.- Calculated temperature history for the stable satellite launched 1330 on August 25, 1961.

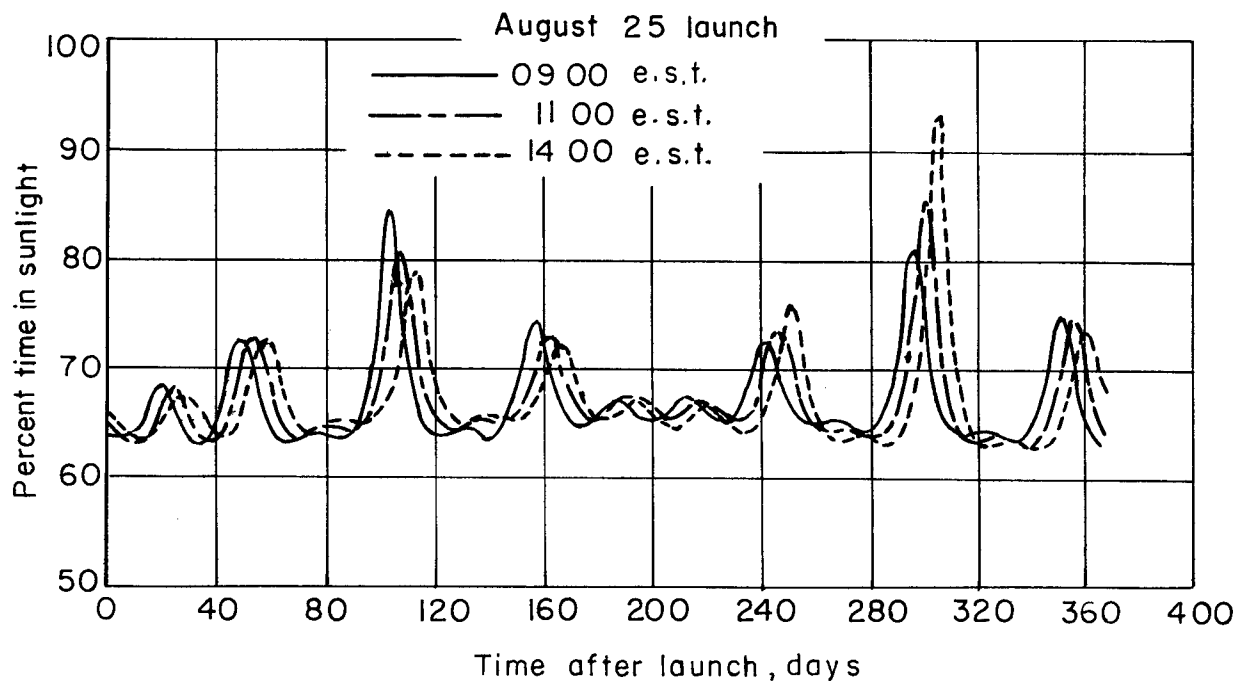


Figure VI-8.- Percent time in sunlight as a function of days after launch.

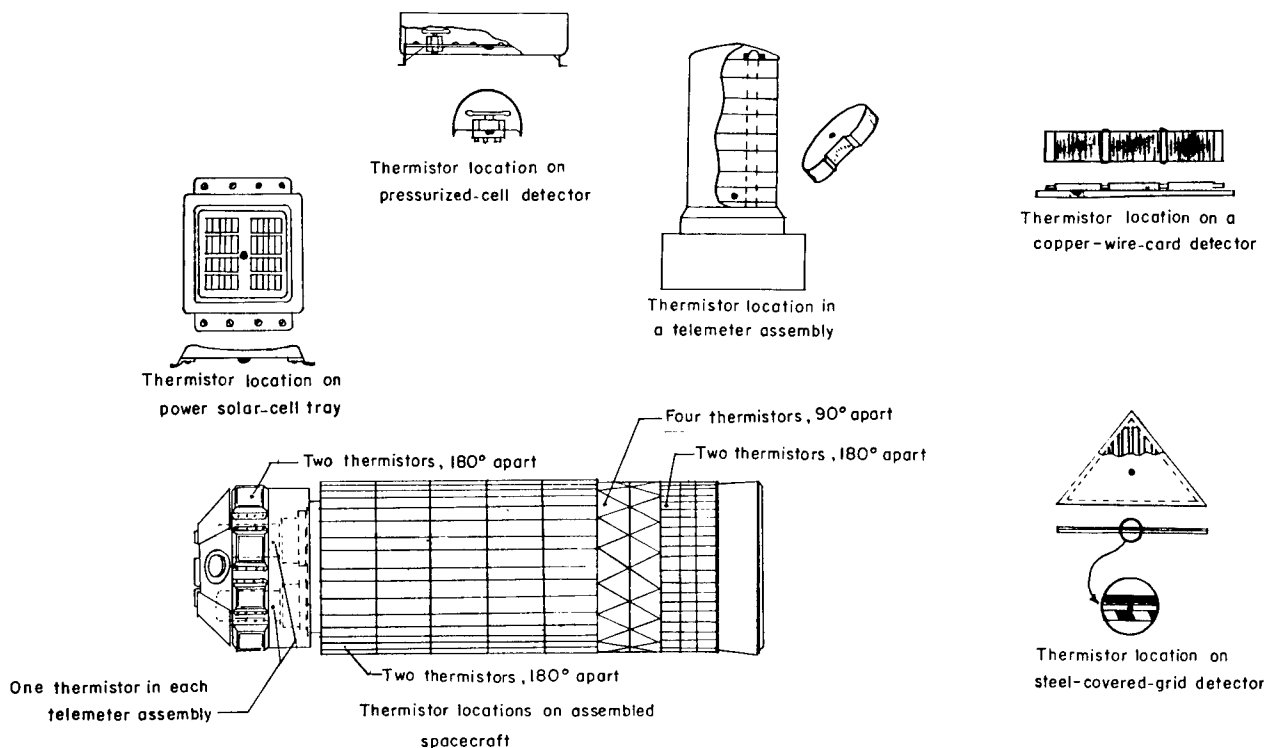
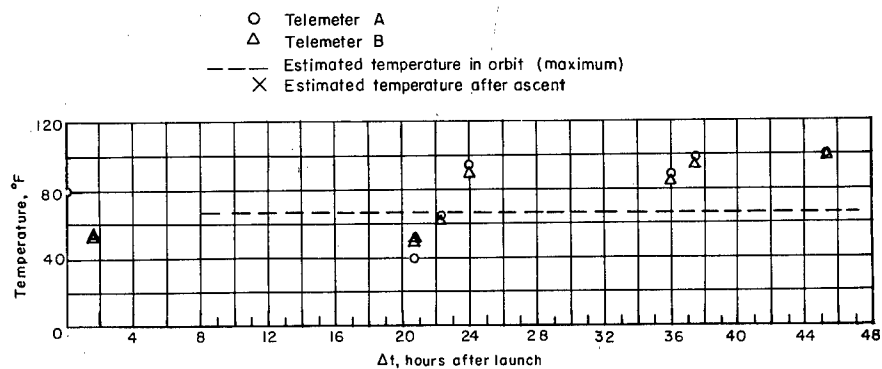


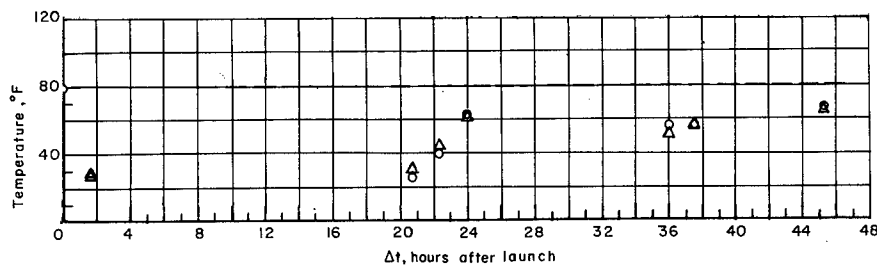
Figure VI-9.- Thermistor locations.

Temperature data during orbit were obtained by interrogating the satellite as it passed the stations of the Minitrack network. Since temperature data were not stored by the satellite, values recorded during an interrogation represented temperatures only at the time of the interrogation so that the orbital-temperature cycle could not be read out directly. No temperature data were transmitted during ascent.

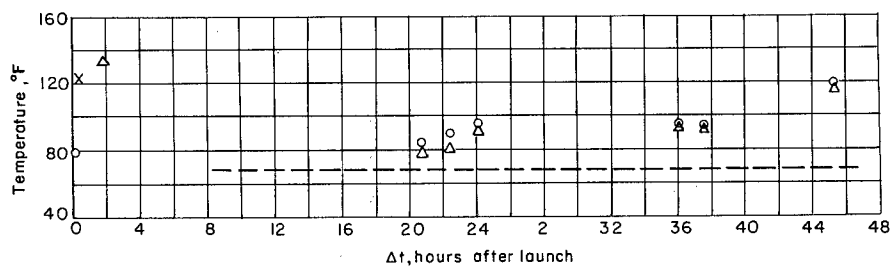
Recorded flight-temperature data for about 46 hours after launch are shown in figure VI-10. Also shown in figure VI-10 are maximum orbit heating values of temperatures from figure VI-7. In figures VI-10(c) and (d) maximum estimated ascent heating values of temperature (from fig. VI-5) are shown for the pressurized cells and telemeter packs. These latter values were taken as constant from 8 to 46 hours. The flight-data value at $\Delta t = 0$ was a prefiring value taken with the satellite inside the heat shield prior to launch. Flight-test-temperature data for the copper-wire-card detectors and cadmium-sulfide cells are discussed in chapters X and XI and are therefore omitted from figure VI-10. Steel-covered-grid-detector temperatures are also omitted, since these data are presented in reference VI-3. Figure VI-10 indicates that at the first interrogation at about 1.5 hours, temperatures were generally close to the estimated value for the ascent heating effects, which indicates reasonable estimates for the ascent heating effects. Measured telemeter temperatures were 6°F higher than prelaunch at the first interrogation. Later interrogations show that all the flight data are near to, or greater than the maximum expected orbital heating values from figure VI-7.



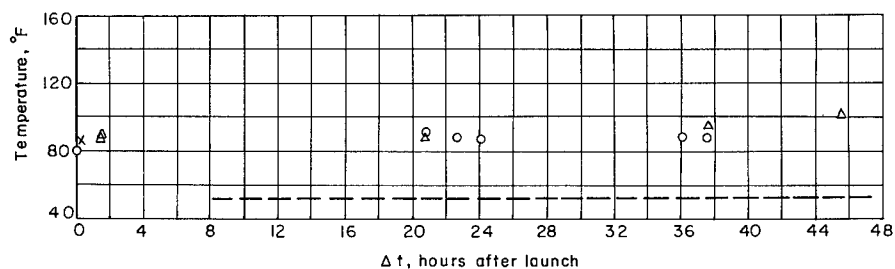
(a) Forward-shell temperatures.



(b) Solar-cell temperatures.



(c) Pressurized-cell temperatures.



(d) Telemeter temperatures.

Figure VI-10.- Comparison of estimated and measured temperatures from Explorer XIII.

Since the orbit of Explorer XIII was known to be different from the nominal orbit used for the estimates, an investigation was made to study the orbital heating effects of free molecular flow resulting from the low perigee. The method employed was to determine the total free-molecular-flow heat input for various orientations of the satellite at perigee passage and to reduce this to a surface-temperature increase.

The aerodynamic heat-transfer rate to a body in free molecular flow is given by the corrected form of an equation in reference VI-4 as

$$\frac{q}{\alpha N k T_{\infty} U} = - \frac{\gamma + 1}{2(\gamma - 1)} \frac{n}{N \bar{v} s} \frac{T_w}{T_{\infty}} + \left(s^2 + \frac{\gamma}{\gamma - 1} \right) \frac{n}{N \bar{v} s} - \frac{e^{-\eta^2}}{4s \sqrt{\pi}} \quad (1)$$

where n is given by

$$n = \frac{N \bar{v}}{2\sqrt{\pi}} \left[e^{-\eta^2} + \sqrt{\pi} \eta (1 + \operatorname{erf} \eta) \right] \quad (2)$$

For satellite velocities, $s \gg 1$ so that $e^{-\eta^2} \rightarrow 0$ and $\operatorname{erf} \eta \rightarrow 1$ for $\cos \beta \rightarrow 0$. For $\cos \beta < 0$, $\operatorname{erf} \eta \rightarrow -1$ so that equation (2) becomes

$$n = NU \cos^* \beta \quad (3)$$

where

$$\cos^* \beta = \cos \beta \quad \text{for } \cos \beta > 0$$

$$\cos^* \beta = 0 \quad \text{for } \cos \beta < 0$$

The second term on the right-hand side of equation (1) predominates, so that equation (1) reduces to

$$q = \alpha \left(\frac{N k T_{\infty}}{\bar{v}^2} \right) U^3 \cos^* \beta \quad (4)$$

The atmospheric term is fitted to an exponential variation of geocentric radius

$$\frac{N k T_{\infty}}{\bar{v}^2} = \left(\frac{N k T_{\infty}}{\bar{v}^2} \right)_{r_0} e^{-B(r-r_0)} \quad (5)$$

where r_0 is the reference altitude. Thus the heating rate on a flat-plate element is

$$q = \alpha \left(\frac{N k T_{\infty}}{\bar{v}^2} \right)_{r_0} U^3 \cos^* \beta e^{-B(r-r_0)} \quad (6)$$

Orbit mechanics give the equations (ref. VI-5):

$$r = a(1 - \epsilon \cos E) \quad (7)$$

$$U^2 = \frac{\mu}{a} \left(\frac{1 + \epsilon \cos E}{1 - \epsilon \cos E} \right) \quad (8)$$

$$\frac{dE}{dt} = \frac{\mu^{1/2}}{a^{3/2}(1 - \epsilon \cos E)} \quad (9)$$

The total aerodynamic-heating input to a flat-plate element of unit area during one orbital pass is then

$$\begin{aligned} Q &= \int_0^P q \, dt = \oint \frac{q \, dE}{dE/dt} \\ &= \alpha \mu \left(\frac{NkT_\infty}{\bar{v}^2} \right)_{r_0} e^{-B(a-r_0)} \oint \cos^* \beta(E) e^{Ba\epsilon \cos E} \times [1 + 2\epsilon \cos E + O(\epsilon^2)] dE \quad (10) \end{aligned}$$

Now, assume $\cos^* \beta$ is constant, and with the relations from reference VI-6 that

$$\oint e^x \cos E \, dE = 2\pi I_0(x)$$

and

$$\oint \cos E e^x \cos E \, dE = 2\pi I_1(x)$$

equation (10) becomes

$$Q = 2\pi \alpha \mu \left(\frac{NkT_\infty}{\bar{v}^2} \right)_{r_0} e^{-B(a-r_0)} \cos^* \beta \left[I_0(Ba\epsilon) + 2\epsilon I_1(Ba\epsilon) + O(\epsilon^2) \right] \quad (11)$$

For large values of x

$$I_n(x) \approx \frac{e^x}{\sqrt{2\pi x}}$$

so that, choosing $r_0 = r_p$, equation (11) can be written as

$$Q = \alpha \mu \left(\frac{NkT_\infty}{\bar{v}^2} \right)_{r_p} \cos^* \beta \sqrt{\frac{2\pi}{Ba\epsilon}} \left[1 + 2\epsilon + O(\epsilon^2) \right] \quad (12)$$

Consider the case where the satellite is assumed to enter perigee broadside ($\beta = 0^\circ$). Integrating Q over the surface and denoting the cross-sectional area as A , the total aerodynamic-heating input in one orbit is

$$\bar{Q} = \alpha A \mu \left(\frac{NkT_\infty}{\bar{v}^2} \right)_{r_p} \sqrt{\frac{2\pi}{Ba\epsilon}} \left[1 + 2\epsilon + O(\epsilon^2) \right] \quad (13)$$

The resulting mean temperature is determined by the following considerations: Neglecting the aerodynamic heating, the satellite will be at a mean temperature T_m , and will thus be radiating heat at a rate $PS\epsilon_{TH}\sigma T_m^4$, so that the total heat radiated during the orbit is $PS\epsilon_{TH}\sigma T_m^4$. This is also the radiative heat input. With aerodynamic heating, the temperature will increase to a value T_1 such that

$$PS\epsilon_{TH}\sigma T_1^4 = PS\epsilon_{TH}\sigma T_m^4 + \bar{Q} \quad (14)$$

Hence the temperature is found to be

$$T_1 = \left(T_m^4 + \frac{\bar{Q}}{PS\epsilon_{TH}\sigma} \right)^{1/4} \quad (15)$$

The approximation is intrinsically made that $(T_{av})^4 = (T^4)_{av}$, which is valid for reasonable temperature fluctuations.

This method of analysis was applied to a cylinder having the properties of the pressure-cell sector and the estimated-temperature time histories for four different orientation angles are shown in figure VI-11. Atmospheric properties from reference VI-7 were used in these calculations.

Also plotted in figure VI-11 is a line representing the measured pressure-cell temperatures shown in figure VI-10. It can be seen that the flight temperatures lie within the calculated temperatures for values of β between about 60° and 80° . Although the calculated time histories shown in figure VI-11 are somewhat questionable because of uncertainties in atmospheric data at the higher altitudes, they do serve to illustrate that the addition of the free-molecular-flow heating effects were sufficient to cause the elevated flight temperatures encountered.

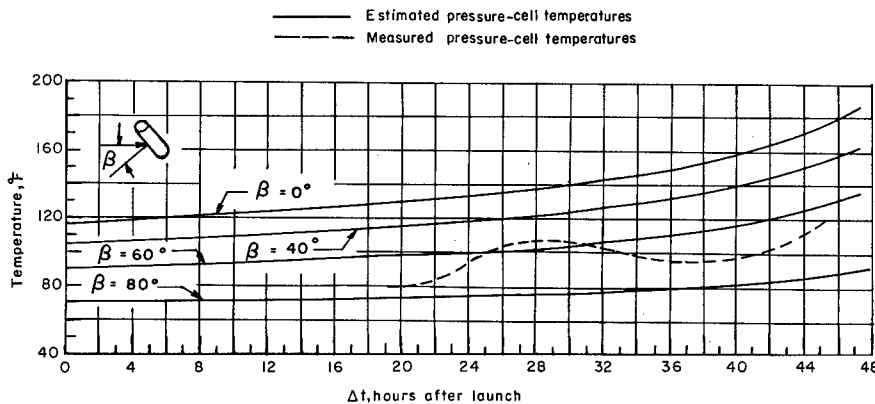


Figure VI-11.- Estimated and measured pressure-cell temperatures for Explorer XIII.

This analysis was applied to the pressure cells since it had been previously established by ground tests that the telemetry temperature in orbit would be controlled by the mean temperature of the pressure cells. It is felt, therefore, that the high flight temperatures on the pressure cells were caused by free-molecular-flow heating due to the low-perigee passage at an inclined angle to the flight path and as a result that the telemetry temperatures were higher than estimated. Equation (15) shows that the temperature increase of the surface is influenced by the emissivity of the surface. Since the values of ϵ_{TH} for the forward shell and steel-covered-grid detectors were much higher than that of the pressure cells, the temperature of these components would be expected to be generally lower. This fact is shown to be the case from the flight data of figure VI-10 and also by the steel-covered-grid-detector data shown in reference VI-3.

In figure VI-10, there is a noticeable fluctuation in the temperature of a number of components with time. This fluctuation can be explained as follows: The orbit is approximately fixed in space, while the Minitrack stations move relative to the orbit path because of the earth's rotation. Thus, the true anomaly of the satellite, as it passes over a given longitude increases by about 24° per orbit. This effect is shown in figure VI-12. Since most of the temperature data gathered from Explorer XIII and shown in figure VI-10 were read out by Minitrack stations at approximately the same longitude, between $\Delta t = 20$ and $\Delta t = 46$ hours, the given temperature history over a 24-hour period corresponds to actual temperature cycling of the components as the satellite completes one orbital revolution.

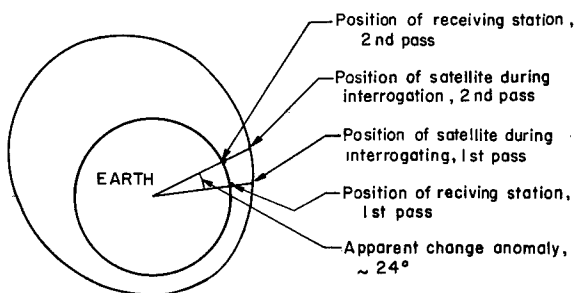


Figure VI-12.- Change in anomaly of successive passes of satellite over a station.

Factors demonstrating that this effect is the predominant cause of these fluctuations are:

1. The period of the fluctuation is 24 hours.
2. The amplitude of the fluctuation is roughly equal that calculated for each component. (For the pressure cells this is approximately 20° F as shown in fig. VI-7.)
3. Temperature changes in figure VI-11 are rapid when the satellite is interrogated near perigee.
4. Since the satellite revolves about the earth in the same direction as the earth rotates, an increase in time in figure VI-10 corresponds to an increase in true anomaly.

From these considerations, it is apparent that data of the type shown in figure VI-11 could provide a typical one-orbit-pass temperature history if allowances were made for the change in orbital elements over a 24-hour period. A close study of predicted temperature histories for Explorer XIII made by using the previous considerations, verifies that the fluctuations in the temperature histories shown in figure VI-11 are due to the normal temperature fluctuations encountered in one orbital pass, with the effects of rapidly changing orbital elements superimposed on it.

The orbital characteristics of Explorer XIII were also used to determine (by the method of ref. VI-1) the percent time in sunlight for correlation with predictions. These results are shown in figure VI-13. Excellent agreement with predictions is indicated for the initial orbits with increasing rate of decay of percent time in sunlight with increasing orbit passes. This decrease was found to be associated with the decrease in apogee altitude. Since the apogee was occurring in sunlight, the decrease in apogee altitude manifested itself as a decrease in percent time in sunlight.

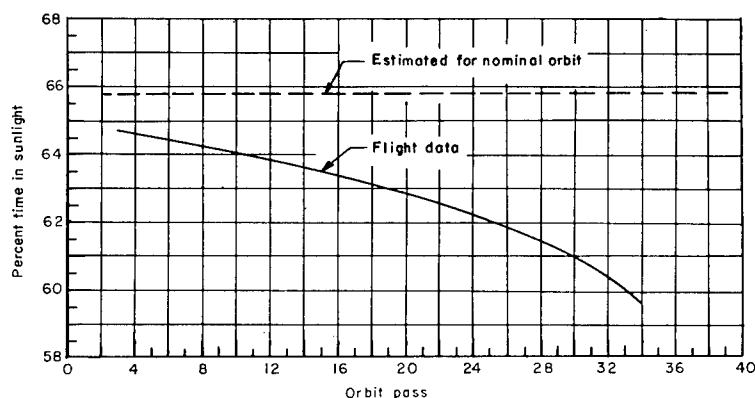


Figure VI-13.- Comparison of estimated and actual percent time in sunlight.

Flight data for Explorer XIII showed a spin rate of 178 rpm during burning and for a short period after burnout of the last stage. This value was 22 rpm less than the expected value (fig. VI-6). It was not possible with the instrumentation used to determine the decay of the spin rate accurately over such a short lifetime, although it would have been possible to determine the time of transition from stable to tumbling spin had the lifetime of the satellite been longer.

SECTION V - CONCLUDING REMARKS

Examination of the temperature data recorded during the lifetime of Explorer XIII indicates surface temperatures and telemetry temperatures which were higher than expected based on calculations for the nominal orbit but were still within the prescribed limits. An analytical study indicated that the high flight temperatures could reasonably be attributed to the existence of free-molecular-flow heating at the low perigee. This heating source would not have been present had the Explorer XIII orbit been as expected.

SECTION VI - REFERENCES

- VI-1. Hastings, Earl C., Jr., Turner, Richard E., and Speegle, Katherine C.: Thermal Design of Explorer XIII Micrometeoroid Satellite. NASA TN D-1001, 1962.
- VI-2. Morris, J. A., and Byrd, R. J.: Ballistic Performance and Outgassing Studies of X248-A9 Rockets at Simulated Altitude Conditions. AEDC-TN-60-229 (Contract No. AF 40(600)-800 S/A 11(60-110)), Arnold Eng. Dev. Center, Dec. 1960.
- VI-3. Staff of the Lewis Research Center: Micrometeoroid Satellite (Explorer XIII) Stainless-Steel Penetration Rate Experiment. NASA TN D-1986, 1963.
- VI-4. Eckert, E. R. G., and Drake, Robert M., Jr.: Heat and Mass Transfer. Second ed., McGraw-Hill Book Co., Inc., 1959.
- VI-5. Moulton, Forest Ray: An Introduction to Celestial Mechanics. Second rev. ed., The Macmillan Co., c.1914.
- VI-6. McLachlan, N. W.: Bessel Functions for Engineers. Clarendon Press (Oxford), 1934.
- VI-7. Minzner, R. A., Champion, K. S. W., and Pond, H. L.: The ARDC Model Atmosphere, 1959. Air Force Surveys in Geophysics No. 115 (AFCRC-TR-59-267), Air Force Cambridge Res. Center, Aug. 1959.

CHAPTER VII

TEST PROGRAM

By W. S. Haywood and Hugh C. Halliday
Langley Research Center

SECTION I - INTRODUCTION

A test program was set up early in the Explorer XIII program to simulate as nearly as possible all expected environmental conditions to which the spacecraft would be subjected during the ascending phase of the trajectory and while in orbit. These tests included spin, acceleration, thermal-vacuum, vibration, and shock. Functional tests were performed on individual modules of the telemeter system.

The test procedure started with breadboard construction of telemeter components. Circuits were evaluated in this phase, and components chosen for prototype construction. Prior to the prototype environmental tests, it was found desirable to construct a mock-up structure for preliminary evaluation of the spacecraft hardware.

SECTION II - ENVIRONMENTAL TEST SPECIFICATIONS

A. Flight Qualification (Prototype Payload).-

1. Spin: The prototype payload shall be subjected to a spin rate of 225 rpm, which is $1\frac{1}{4}$ times the expected flight value. This spin rate shall be achieved in 1 second and held for 15 minutes. The data telemeters shall be operated and checked before and after this test. They shall also be operated for 10 repeated duty cycles after the payload has achieved the specified spin rate.

2. Acceleration:

(a) Thrust axis - The payload shall be subjected to a static acceleration of 24g at its center of gravity, which is equal to $1\frac{1}{2}$ times the expected value. The variation along the thrust axis shall not exceed -15 percent at the forward end and 10 percent at the aft end of the payload. This force shall be held for 3 minutes. The payload telemeter shall be in an operational status and shall be checked before and after this test.

(b) Lateral (normal to thrust axis) - The payload shall be subjected to a static acceleration of 10.5g, which is equal to $1\frac{1}{2}$ times the expected

value, in the direction most likely to produce damage. A second test shall be conducted with the force at 90° to this direction. This force shall be held for 3 minutes in each direction. The payload telemeter shall be in an operational status and shall be checked before and after this test.

3. Temperature: With the payload mounted in a suitable test chamber, it shall be subjected to a temperature environment at atmospheric pressure in accordance with the following schedule:

(a) Lower the test-chamber temperature to -22° F and hold for 6 hours. Operate the data telemeters for a normal duty cycle during the holding period.

(b) Raise the test-chamber temperature to 140° F (18° F above the maximum expected flight temperature) and hold for 6 hours. Operate the data telemeters for a normal duty cycle during holding period.

(c) Lower the test-chamber temperature to 10° F (18° F below the minimum expected flight temperature) and operate the data telemeters.

(d) Raise the test-chamber temperature to 140° F and operate the data telemeters for several duty cycles.

(e) Lower the test-chamber temperature to room temperature and operate the data telemeters.

4. Thermal vacuum: The prototype shall be subjected to a thermal-vacuum test as outlined below. The maximum and minimum temperatures of the components as tabulated below shall not be exceeded.

Component	Temperature, °F	
	Maximum	Minimum
Solar cells	250	-50
Pressurized cells	200	-25
Grid detectors	150	-50
Telemeters	140	-30

(a) Vacuum - The test chamber shall be evacuated to 1×10^{-4} mm Hg or less with the payload remaining at ambient temperature. The telemeters shall be operated while the chamber is being evacuated.

(b) Hot Soak - While maintaining the aforementioned vacuum, raise the chamber temperature until the temperatures of the telemeters reach 140° F. Hold the vacuum and temperature for at least 7 days. Operate the data telemeters for a normal duty cycle.

(c) Cold Soak - While still maintaining the vacuum, lower the test-chamber temperature until the temperature of the telemeters reaches 10° F.

Hold the vacuum and temperature for at least 3 days. Operate the data telemeters for a normal duty cycle.

(d) Cycle - While maintaining the vacuum, the temperature of the forward shell shall be varied to duplicate the temperature time profile of a typical orbit. The test shall be conducted for 14 typical orbits (approximately 24 hours). Operate the data telemeters for a normal duty cycle.

(e) Ambient Conditions - Bring the test chamber back to atmospheric pressure and the payload to ambient temperature and operate the data telemeters a few cycles.

5. Vibration: The payload shall be in an operational status during the vibration test and checked electrically and mechanically after completion. A detailed examination for evidence of cracks, wear, loose parts, and the like shall be made.

The payload shall be subjected to a low-level vibration of $\pm 2g$ for 90 seconds by using a sine-wave logarithmic sweep from 15 to 2000 cps. In addition, it shall be subjected to vibrations in three orthogonal directions in accordance with the following schedule. The prototype test levels and durations are 50 percent more than those expected in flight.

(a) Sinusoidal

Frequency range, cps	Amplitude, g-rms along -	
	Thrust axis	Transverse axis
5 to 50	2	1
50 to 500	5	2
500 to 2000	12	3

The sweep rate shall be approximately 2 octaves per minute with a duration of approximately $1\frac{1}{2}$ minutes per frequency range.

(b) Random

Direction	Frequency range, cps	Amplitude, g-rms
Thrust axis	20 to 2000	13
Transverse axis	20 to 2000	3

The duration shall be 5 minutes in each direction.

(c) Resonance

Direction	Frequency range, cps	Amplitude, g-rms
Thrust axis	550 to 650	45
Transverse axis	550 to 650	10

The duration shall be 12 seconds in each direction.

6. Shock: The payload shall be subjected to a 45g shock load parallel to and in the direction of the thrust of the rocket motor. The duration of the shock pulse shall be not less than 5 milliseconds. This shock load is $1\frac{1}{2}$ times greater than that expected in flight. The telemeters shall be operational during this test. The payload shall be checked electrically and mechanically after this test.

B. Flight Acceptance.-

1. Thermal vacuum: The payload shall be subjected to a thermal-vacuum test as outlined below. The temperature of the components as tabulated below shall not be exceeded.

Component	Temperature, °F	
	Maximum	Minimum
Solar cells	250	-50
Pressurized cells	*160	-25
Grid detectors	*125	-50
Telemeters	140	-30

*The temperature limits were reduced due to experience gained in the flight qualification tests.

(a) Vacuum - The test chamber shall be evacuated to 1×10^{-4} mm Hg or less with the payload remaining at ambient temperature. The telemeters shall be operated while the chamber is being evacuated.

(b) Hot Soak - While maintaining the aforementioned vacuum, raise the chamber temperature until the temperatures of the telemeters reach 110° F. (The temperatures presented represent the expected minimum and maximum flight temperatures.) Hold the vacuum and temperature for at least 3 days. Operate the data telemeters for a normal duty cycle.

(c) Cold Soak - While still maintaining the vacuum, lower the test-chamber temperature until the temperature of the telemeters reaches 25° F. Hold the vacuum and temperature for at least 2 days. Operate the data telemeters for a normal duty cycle.

(d) Cycle - While maintaining the vacuum, the temperature of the forward shell shall be varied to duplicate the temperature time profile of a typical orbit. The test shall be conducted for 14 typical orbits (approximately 24 hours). Operate the data telemeters for a normal duty cycle.

(e) Ambient Conditions - Bring the test chamber back to atmospheric pressure and the payload to ambient temperature and operate the data telemeters a few cycles.

2. Vibration: The payload shall be in an operational status during this test and checked electrically and mechanically after completion. A detailed examination for evidence of cracks, wear, loose parts, and the like shall be made.

The payload shall be subjected to a low-level vibration of 1g for 60 seconds by using a sine-wave logarithmic sweep from 15 to 2000 cps. In addition, it shall be subjected to vibrations in three orthogonal directions in accordance with the schedule listed below. The payload test levels and durations are the same as those expected in flight.

(a) Sinusoidal

Frequency range, cps	Amplitude, g-rms along -	
	Thrust axis	Transverse axis
5 to 50	1	5
50 to 500	3	1
500 to 2000	10	2

The sweep rate shall be approximately 4 octaves per minute, with a duration of approximately 1 minute per frequency range. The amplitudes on the vibration table shall be limited to 0.5 inch peak to peak.

(b) Random

Direction	Frequency range, cps	Amplitude, g-rms
Thrust axis	20 to 2000	8
Transverse axis	20 to 2000	2

Duration shall be 4 minutes in each direction.

(c) Resonance

Direction	Frequency range, cps	Amplitude, g-rms
Thrust axis	550 to 650	40
Transverse axis	550 to 650	6

Duration shall be 10 seconds in each direction.

3. Shock: The payload shall be subjected to a 30g shock load parallel to and in the direction of the thrust of the rocket motor. The duration of the shock pulse shall be not less than 5 milliseconds. This shock load is equal to that expected in flight. The telemeters shall be operational during this test. The payload shall be checked electrically and mechanically after this test.

SECTION III - FUNCTIONAL AND DESIGN TESTS

Subsystem.- Early in the project, a program of evaluations of the electrical system of each subassembly was devised for the telemeter prototype. Before any telemeter module was incorporated into the telemeter stack, it had to be operated in a temperature chamber from 32° F to 140° F without deterioration of its operation. At the same time, electrical performance was evaluated under varying voltage conditions. Each telemeter was enclosed by a pressurized container which was mounted on the telemeter bulkhead. Early results led to several changes in the d-c voltage converter. Complete calibrations to determine temperature effects were made on the subcarrier oscillator module before it was incorporated into the telemeter. After each module had been qualified under these tests, it became a part of the telemeter.

Systems.- The bulkhead, with its two telemeters, underwent extensive electrical tests before flight qualification.

Command rf signals were transmitted to the telemeters. Proper operation of the command receivers would allow the satellite transmitters to operate for approximately 1 minute and then return to the off condition. During these tests, trouble developed in the time-delay turn-on circuit which required that the circuit be redesigned. Also, because modulation trouble was experienced during the electrical tests, the push-pull modulator output circuitry was redesigned.

An operational test was performed on the telemeter assembly in which an rf signal was sent to the telemeter once every 3 minutes. After 500 of these cycle tests, a calibration check was made; the past calibration agreed with the present calibration and indicated that no change occurred during the test.

The telemeters were then submitted to a 10-hour hot and cold test with stabilized temperatures ranging from 20° F to 120° F. Power was supplied to the telemetry system from an external source, and operation of the system was

commanded through an rf link. Over this 10-hour period, the telemeter was operated on a 1-minute "on" and 1-minute "off" basis. This hot and cold test was accomplished without a telemeter failure.

Next, the telemeter was connected to its sensors. Each sensor input was individually shorted while each telemeter channel was interrogated. Interference experienced between the impact-detector and the pressurized-cell-detector inputs was located in the pressurized-cell mounting-structure wiring tunnels. The trouble was apparently caused by proximity of lead wires in the wiring tunnels. It was discovered that the pressurized-cell-detector leads had an induced voltage pulse ranging from 3 to 5 volts (this pulse came from the encoder) and had caused crosstalk. Additional shielding of the impact-detector leads and a complete wire rerouting reduced the interference voltage to an acceptable level.

At this stage of the test program, the battery supply modules were installed in the telemeter system. Electrical checks were performed to ensure the proper operation between the power supply and the solar-cell charging system. All prototype tests were conducted by using this internal power system.

Mock-up Vibration Test.- Vibration tests were also made early in the program on a complete satellite payload with mock-up instrumentation. The telemeter canisters were filled with a potting compound to simulate the actual weight. The telemeter bulkhead was completely assembled, including the external-internal power relay, battery supply, and the support spider. The mock-up was first vibrated in two sections and finally as a complete unit. This test was conducted to qualify the structural worthiness of the payload hardware. A vigorous vibration test program was initiated using an electronic shaker located at Langley. Readout equipment necessary for this test consisted of the following:

1. 12 accelerometers
2. Data-write equipment for oscillograph
3. Tape recorder and assorted playback equipment

Mock-up Payload Adaptor, Telemeter Bulkhead, and Forward Shell.- The first tests were made on the forward shell, telemeter bulkhead, and payload adaptor that mounts on the Scout fourth-stage X-248 rocket motor. Vibrometers were located at the center top of the forward shell to check the vibration expected at the base of the solar cells. Vibration pickups were located at the base and top of the telemeter canisters, and at the input to the payload adaptor. A pickup was located on the support bracket located under the bulkhead.

Input g-levels were applied to the base longitudinally from 2 to 20g in three separate steps and over the frequency range from 20 to 2000 cps; each test lasted about 3 minutes. From past experience gained from X-248 rocket motor firing, a random vibration test over the range from 550 to 650 cps at 11 g-rms for 5 minutes was conducted.

Amplification factors approached 100 on the telemeter bulkhead, while the X-, Y-, and Z-axis vibrometers mounted on top of the telemeter canisters

exceeded this amplification. Three of the four antennas broke off during the test at a frequency of 125 cps on the 12g run.

The bulkhead support was redesigned, stiffened, and also made lighter. X-ray pictures were taken of the old antennas and revealed their structural flaws; new antennas were designed and made. The vibration tests were repeated and the structure withstood each test without damage.

Pressurized-Cell Support Structure.- The pressurized-cell support structure with pressurized cells installed was mounted on the vibration table and vibrated in the same manner as the forward shell. Only 40 pressurized cells were mounted on the structure for this test. Small vibrometers were mounted on several of the cells along with monitors on the structure itself and on the shaker table. During preliminary tests, the lower support foot showed fatigue on 20 percent of the pressurized cells.

The tests were halted at this point and a method of supporting the pressure cell by the addition of a rubber shock mount was tried. In this new configuration 10 percent of the cells were lost. This method of support was abandoned. Modifications were made to the support foot through the addition of a gusset, and the tests were rerun and completed without structural damage.

Complete Mock-Up Payload Assembly.- After the modifications had been made to the payload hardware and detectors, the vibration tests were rerun successfully.

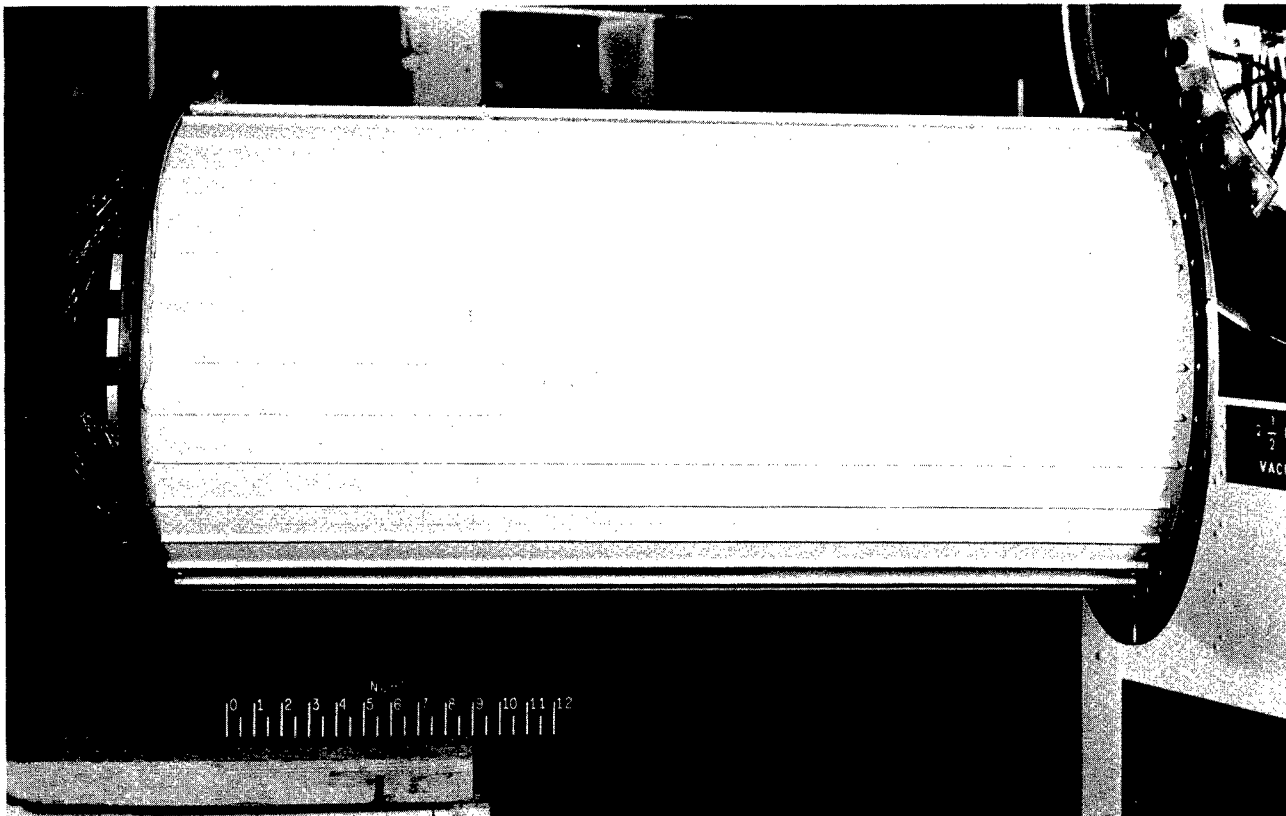
Fourth-Stage Rocket-Motor Heat-Transfer Test.- As pointed out in chapter VI, it was necessary to keep the temperature of the satellite detectors below 180° F. The fourth-stage rocket-motor case is a major source of heat immediately after burnout. In order to determine the heat transfer from the motor case to the payload, a series of tests were conducted in a vacuum chamber at low pressures which simulated the altitude at which the motor burnout occurs.

Temperatures measured during actual rocket-motor test firings were fed into a programmer which used a point on the outside surface of the motor case midway between the rocket-motor mounting flanges as the control point. The case was heated by six 2,500-watt quartz lamps inserted through the nozzle end of the rocket



L-60-2958

Figure VII-1.- Rocket-motor heat-transfer test; vacuum chamber and test hardware.



L-60-2962

Figure VII-2.- Rocket-motor heat-transfer test; painted pressurized-cell mounting structure and monitor thermocouple.

motor. Figure VII-1 shows the assembly in the vacuum chamber. The tests were conducted until the outside of the pressurized-cell mounting structure (fig. VII-2) reached peak temperature and started to decline. Generally, peak temperature was not reached in less than 30 minutes.

It was found that by covering the outside of the X-248 rocket motor, inside and outside of the payload adapter and inside of the pressurized-cell mounting structure with aluminum foil and painting the outside of the pressurized-cell mounting structure with acrylic white lacquer that the temperature of the outside of the pressurized-cell mounting structure did not exceed 145° F 45 minutes after simulated motor burnout. Figure VII-3 shows the spent X-248 motor case covered with aluminum foil and the array of six 2,500-watt quartz lamps, mounting hardware, and test equipment. Figure VII-4 shows the payload adapter and pressurized-cell mounting structure with foil applied. Figure VII-2 shows the pressurized-cell mounting structure painted.

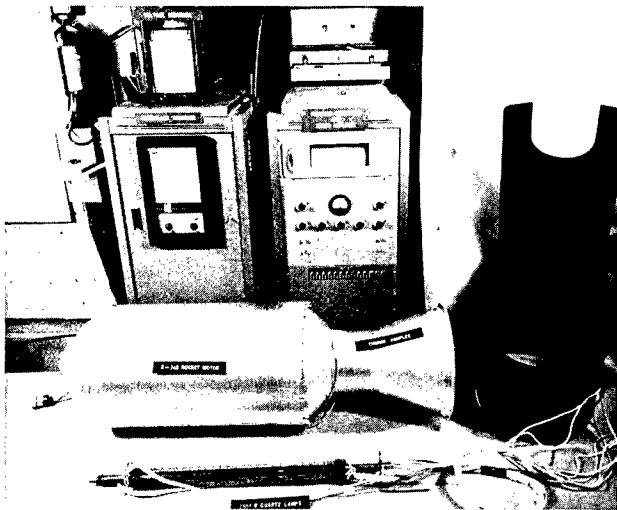
SECTION IV - FLIGHT QUALIFICATION TESTS

After the component and mock-up test outlined in section III, the assembled prototype payload was subjected to a series of mechanical, electrical, temperature, and thermal-vacuum tests. These tests were conducted to ascertain the soundness of design both mechanically and electrically. The test specifications are outlined in section II.

Spin Test.- The prototype was first subjected to a spin test to approximate the spin imparted to the satellite (180 rpm) by the spinning fourth-stage motor of the Scout launch vehicle. The prototype payload was mounted in a lathe (fig. VII-5) and minor adjustments made to minimize eccentricities. The telemeters were operated and sensors examined; all were found to be in satisfactory condition. A slow-speed run was made to check for unbalance; balance weights were not required. The payload was then spun up to 154 rpm, the maximum rpm of the lathe. This spin rate was held for 15 minutes while the telemeters were operated satisfactorily for 10 duty cycles. After despinning, the telemeters were operated again; the sensors inspected; and antennas checked. All were found in satisfactory condition.

Acceleration Test.- The prototype was completely enclosed in a windshield and only mounted in the plane of the vehicle spin bearing. The antennas had to be in the folded condition thereby rendering the telemeters inoperative.

The sensors were examined and telemeters checked and found to be in satisfactory condition before the payload was installed in the windshield. The windshield was then mounted on a centrifuge and the payload subjected to 24g acceleration in the longitudinal thrust direction (fig. VII-6) and $10\frac{1}{2}g$ in the normal and transverse directions (fig. VII-7). These g-levels were held for 3 minutes in each condition. When the test was completed, the telemeters were checked and found in satisfactory condition. One pressurized-cell detector and the front pressurized-cell mounting-structure ring were damaged during this test; all other sensors were in satisfactory condition. It is believed that this damage was incurred during handling, when the wind shield bent under one of the lifting rig supports.



L-60-2959
Figure VII-3.- Rocket-motor heat-transfer test;
test hardware and instrumentation.



L-60-2960

Figure VII-4.- Rocket-motor heat-transfer test; pressurized-cell mounting structure with aluminum foil on inside surface on the right and dome (forward end) of the X-248 rocket motor covered with aluminum foil.

Thermal-Vacuum Test.- A complete telemeter receiving station was set up for this test (fig. VII-8). This station consisted of a tape recorder and quick-look readout equipment. Thirty-six additional thermocouples were located on the prototype and recorded through auxiliary equipment.

Performance checks prior to the thermal-vacuum test indicated a loss in command-receiver sensitivity, on internal power only, for telemeter B. The sensitivity loss was not present when the telemeter was operated from an external power source. Telemeter B contained a radio-tracking beacon that was to operate continuously for the first 3 weeks of the orbital flight. This beacon signal was blocking the command transmission to telemeter B. (A method of rf shielding within the canister reduced the problem to an extent such as to allow the test to be continued.) Normal receiver sensitivity for both telemeters was between -96 to -98 dbm, and power output of the transmitters was 92 mw.

Before the thermal-vacuum test was begun, a short 12-hour temperature test was conducted. This test covered excursions of telemeter temperatures from -22° F to 140° F. The purpose of the test was to study heat balance and the only instrumentation mandatory were recorders and the 36 thermocouples mounted on the structure of the prototype. Prior knowledge of the telemeter indicated it would not operate at temperatures below 0° F. Although the telemeter could

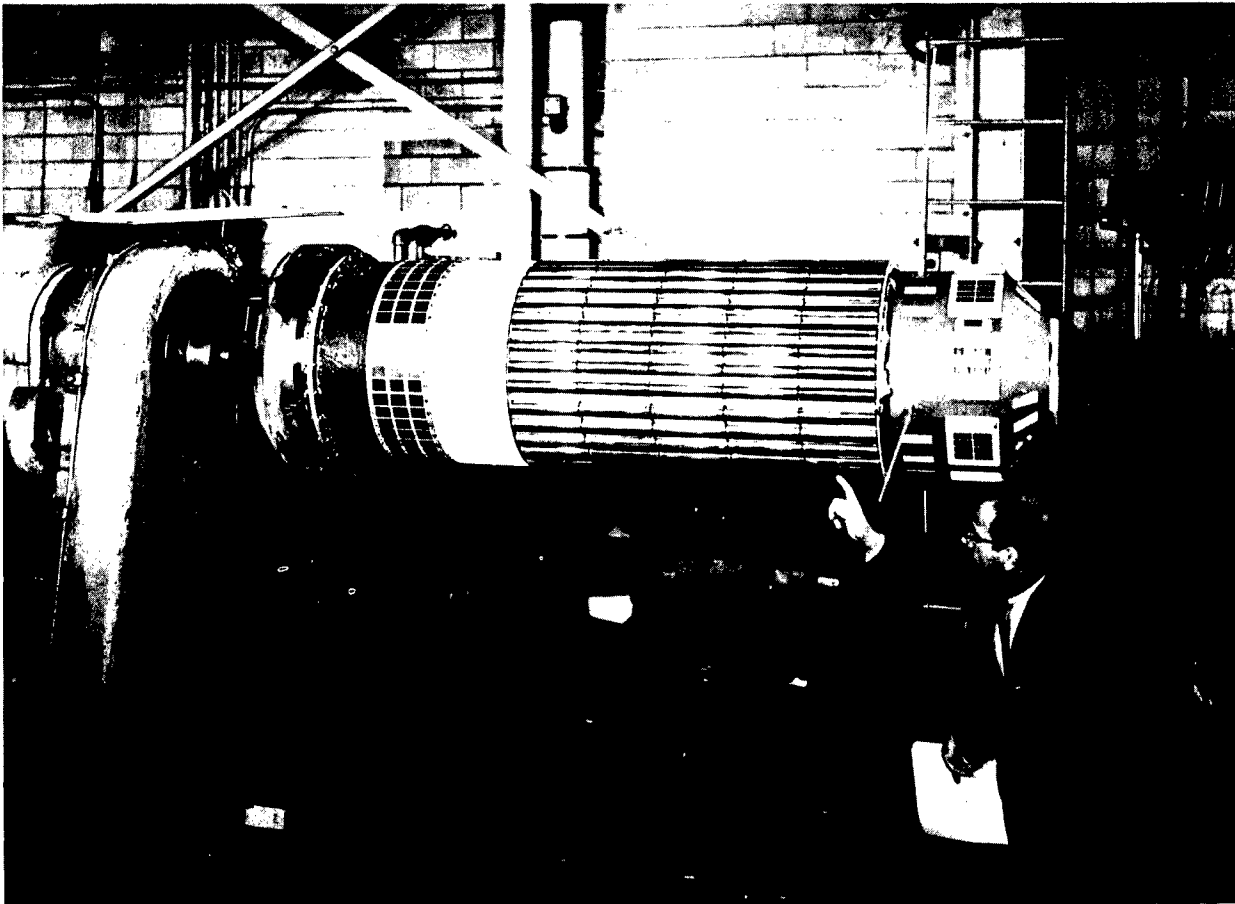


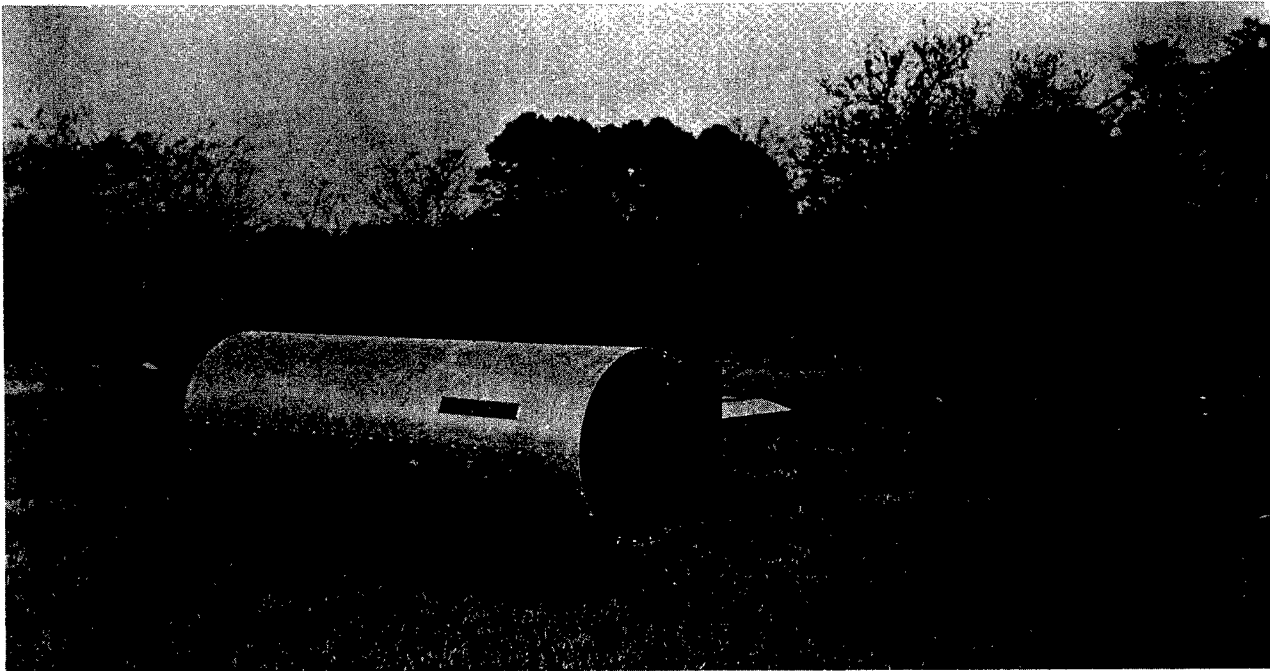
Figure VII-5.- Spin test; prototype payload mounted on a lathe.

L-60-7270



Figure VII-6.- Acceleration test (thrust axis); prototype payload (in windshield) mounted on centrifuge.

L-60-7269



L-60-7267

Figure VII-7.- Acceleration test (transverse axis); prototype payload (in windshield) mounted on centrifuge.

not be expected to operate under these conditions, this test afforded an opportunity to check the lower limit of the telemeter operation.

A complete set of telemeter zero references was made for each of the 96 channels at room temperature with the prototype mounted in the chamber. Test procedures required that the telemeter be commanded on every 30 minutes and complete tape records made. The temperature was dropped to -22° F for the 6-hour cold test. At the end of the first $1\frac{1}{2}$ hours of the test, the modulating tone necessary to operate the telemeter B receiver had drifted 50 cycles. After 3 hours of testing, the internal telemeter temperature had reached 5° F and telemeter B could not be commanded on. Four hours after the test began, the base of the telemeter canisters was reading -30° F and neither telemeter could be commanded. The cold test was continued for 2 more hours. It was still impossible to operate either telemeter.

Heat was applied and the prototype underwent a 6-hour hot soak. The prototype was not removed from the chamber and was still in an inoperative condition. Four hours after the hot soak began, when the base of the telemeter had reached 55° F, it was possible to operate telemeter B. Five hours after the test began, both telemeters were operating normally, but the frequency shift that occurred during the cold soak in telemeter B had not rectified itself.

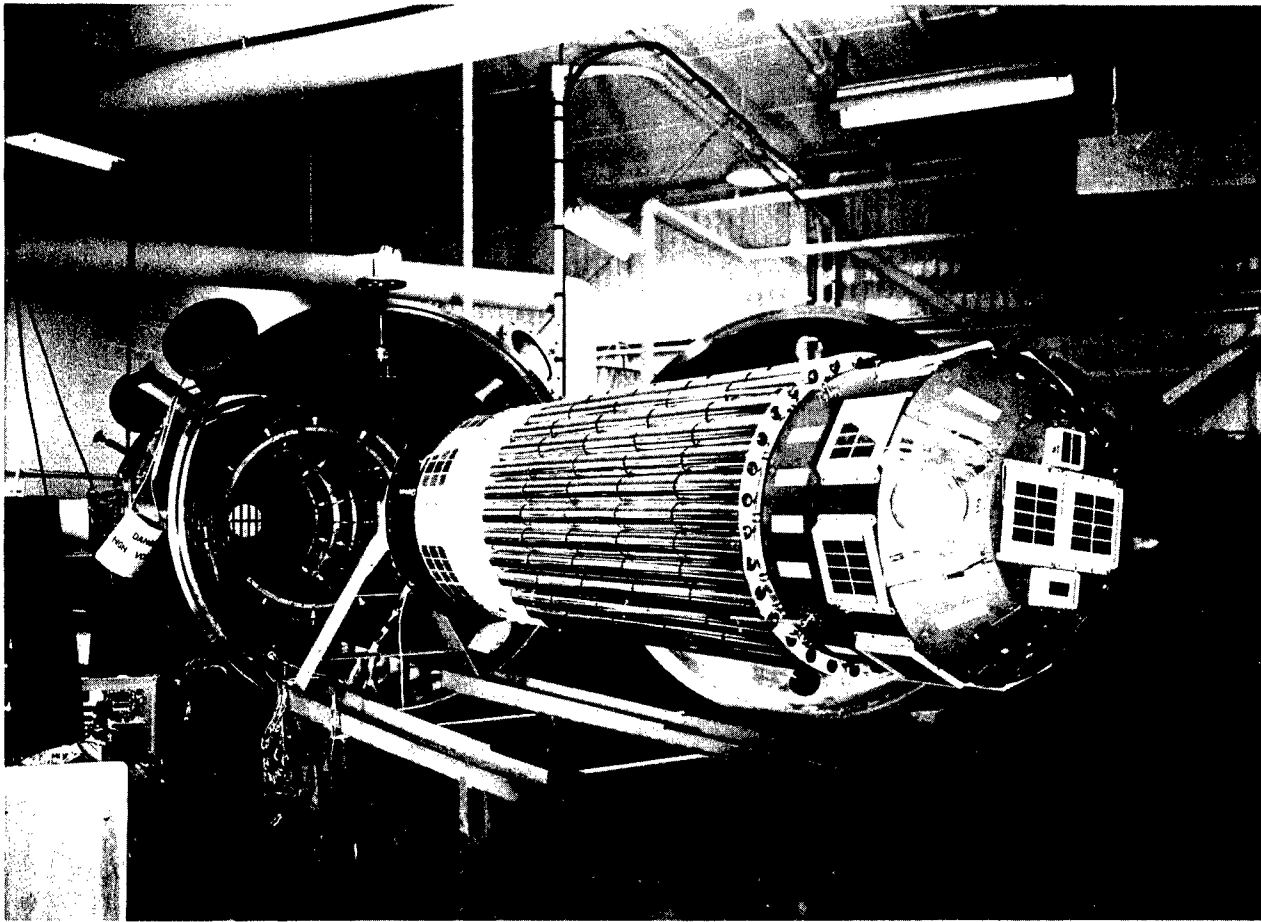


Figure VII-8.- Temperature and thermal-vacuum test; prototype payload readied for test. L-60-8225

Immediately following the temperature tests, the prototype was subjected to thermal-vacuum tests which simulated conditions in the space environment. The following tests were performed while under a vacuum of 10^{-5} mm of mercury, as outlined in section II.

- (1) The temperature was raised to 140° F and held at this point for 7 days.
- (2) Still holding the vacuum, the temperature was lowered to 10° F and held for 3 days.
- (3) The final test consisted of a cycle every 98 minutes, between 10° F and 140° F for 14 cycles.

The telemeters were operating continuously during these tests.

A complete set of zero calibrations was made at room temperature, and preparations were made to make a 7-day hot test at 140° F. After determining

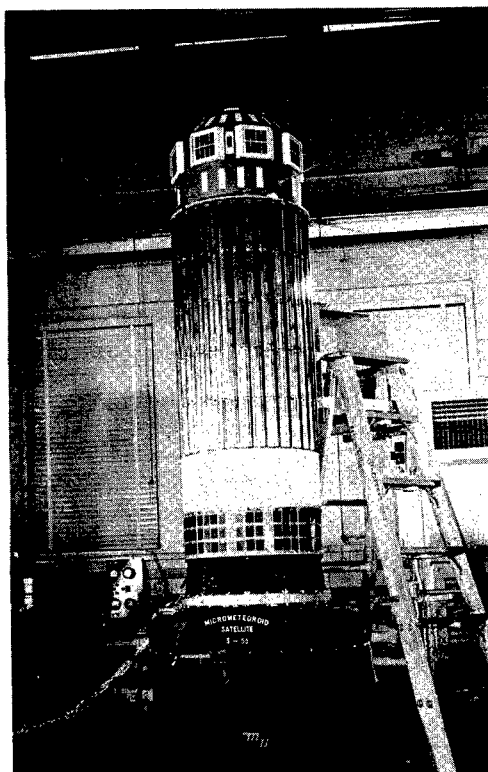
that the telemeters were working properly, heat was applied. Interrogations were made every 30 minutes, by using a signal generator and an audio generator for the modulating tone. Complete magnetic tape records were made in addition to the quick-look setup which used a counter and paper tape. Internal package temperature, channel D-4, was telemetered and monitored through the rf link along with internal battery voltage, channel F-12. The third day of the test, the 1-minute transmitting time of telemeter B after interrogation had changed from 58 seconds to 15 seconds. Before the final day of the test, telemeter B began operating properly upon interrogation and worked for the full 58 seconds. The complete 7-day hot and 3-day cold tests were completed.

Upon completion of these tests, the telemeter deck was removed from the prototype, and an extensive program of modification was begun on the telemeters. The oscillator circuit in the receiver modules was reworked and the bandwidth of the interrogation tone increased by 50 cycles. The internal batteries were examined and their charge circuitry modified.

Vibration Test.— The vibration-test program conducted on the prototype ranged from 1g to 45g in amplitude with a frequency excursion from 20 to 2000 cps as outlined in section II (fig. VII-9). Operation of the telemeter was required throughout this test. A complete telemeter station was used to monitor the prototype during vibration.

Operation of the telemeter rf transmitter into the antenna system interfered with the vibration-table level-indication system to such an extent as to eliminate the rf type of test. Therefore, the transmitter output was directly coupled through coaxial cable to the receiving station. Satisfactory operation of the vibration table was then accomplished. Tape recordings were made of the telemeter operation during the vibration test. An analysis was made of the tape and showed that operation was normal during vibration. Vibration records were obtained from the numerous vibrometers located on the structure. These vibration records are shown in figures VII-10 and VII-11. The prototype was vibrated without mechanical or electrical failure to approximately $1\frac{1}{2}$ times the expected flight

environmental conditions. Experience gained from the vibration test of the mock-up payload contributed to the success of this test.



L-60-7113
Figure VII-9.— Vibration test; prototype payload mounted for test.

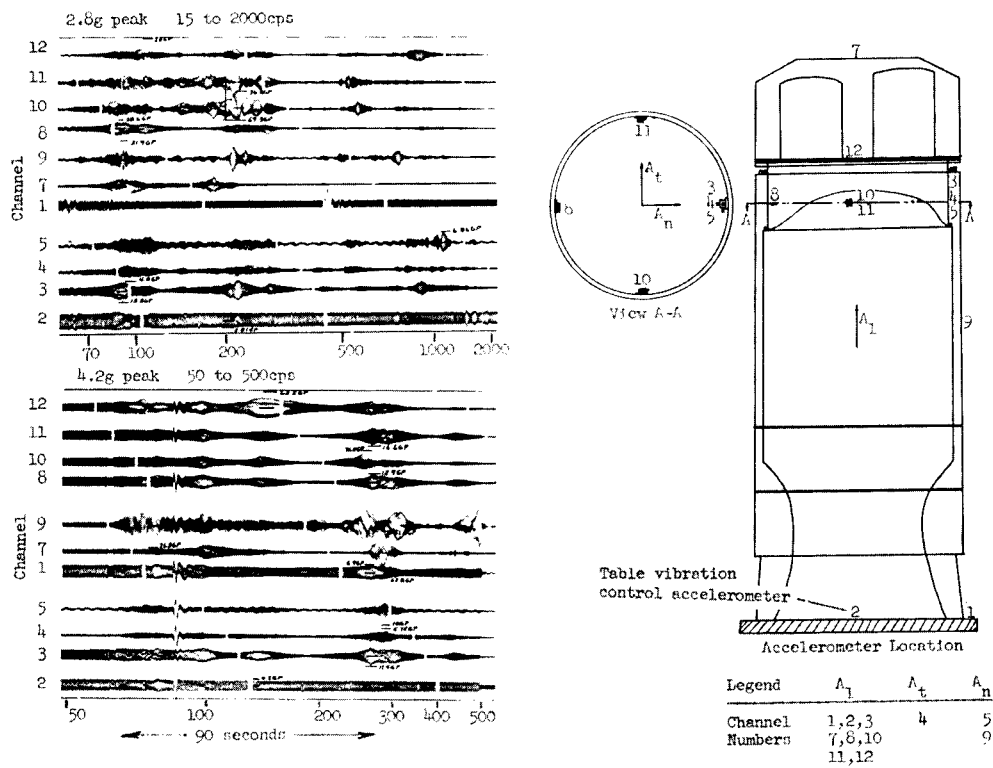


Figure VII-10.- Vibration test; prototype payload accelerometer locations and test records.

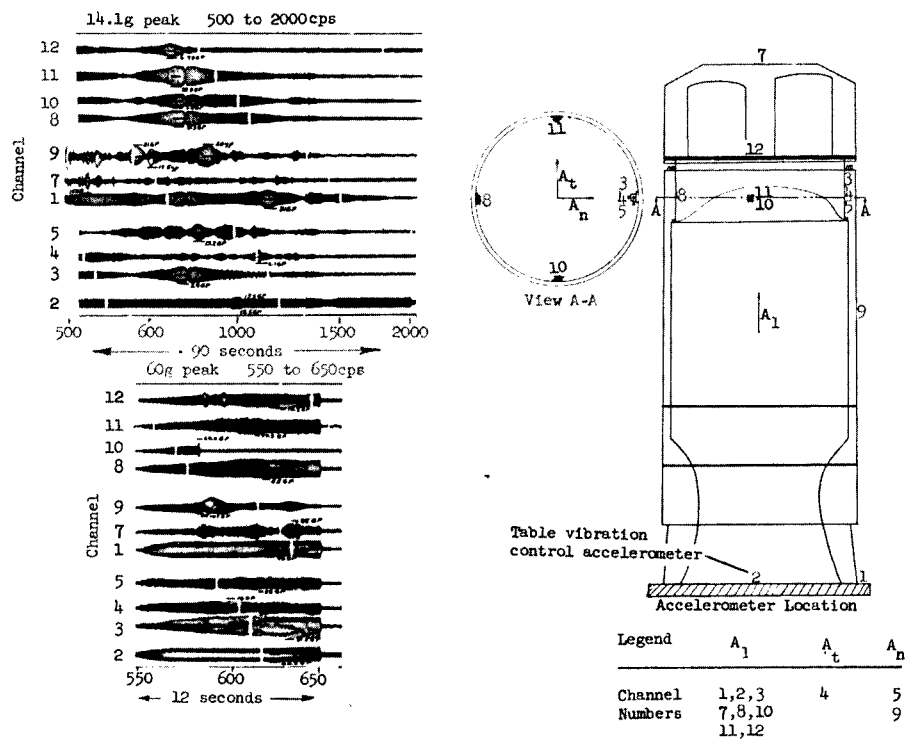


Figure VII-11.- Vibration test; prototype payload accelerometer locations and test records.

Shock Test.- The prototype was assembled on a test fixture (fig. VII-12) which had an aluminum honeycomb pad 31 inches square by 8 inches thick attached to its base. The prototype and test fixture assembly were raised 10 inches off the floor and dropped. Figure VII-13 is a record of this test showing an excursion of 45g and a duration of 10 milliseconds. The telemeters were operating on their internal power during this shock test. The signals transmitted by the telemeters were picked up and recorded on magnetic tape at a receiving station near where the test was conducted.

Telemeter zero calibrations were made before and after the shock test and indicated that the telemeter and detectors were not affected by this test. Because of the short duration of the shock pulse, it was impossible to detect any telemeter changes during that period. A visual inspection showed no damage to the hardware or detectors.

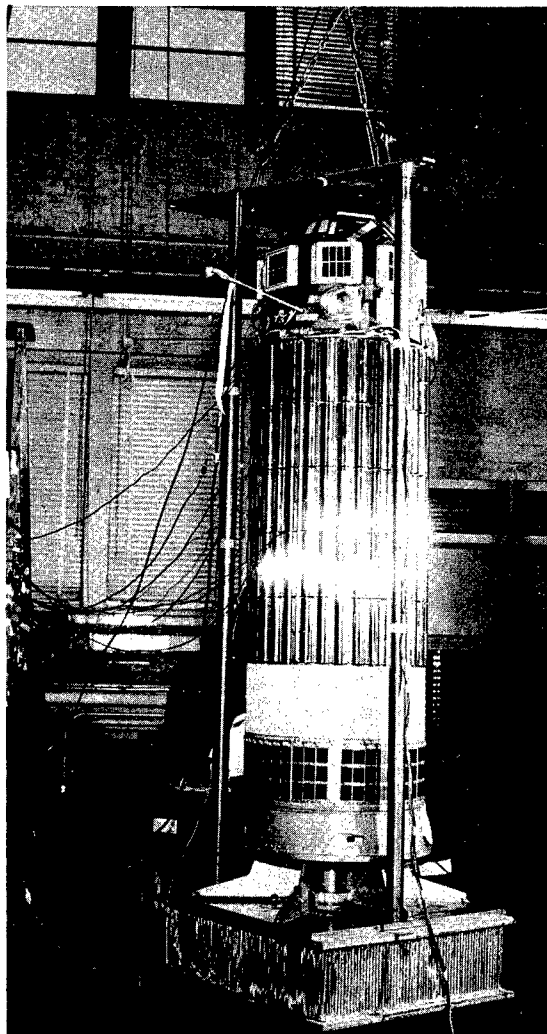
SECTION V - FLIGHT ACCEPTANCE TESTS

The flight payload was subjected to thermal-vacuum, vibration, and shock tests simulating the environment expected during launch and orbital flight. The tests were conducted in accordance with the specifications outlined in section II.

Thermal-Vacuum Test.- This test consisted of the 3-day hot soak at 110° F, 2-day soak at 25° F, and 14 simulated orbital cycles with temperature variations from 110° F to 25° F. All conditions were carried out at a pressure of 10^{-4} mm Hg.

A complete telemeter station was used to readout the data. The quick-look counter and printer used in the prototype test were again employed. The rf coupling to the telemeters was direct through the coaxial cable, and additional battery monitoring equipment was used in this test.

The flight model was subjected to 180 hours of continuous testing as described previously. The malfunctions associated with prototype thermal-vacuum



L-60-8297
Figure VII-12.- Shock test; prototype payload mounted in shock fixture.



Figure VII-13.- Shock-test record; prototype payload.

tests were not present during the flight-acceptance tests. Figures VII-14 to VII-16 show telemetered data recorded through the rf link and compared with data from thermocouples located in the same area and recorded by a strip-chart recorder. Figures VII-17 to VII-22 indicate internal battery voltage, package temperature, full-scale and zero calibrations as telemetered through the rf link. Figure VII-23 shows the variation in the vacuum throughout the tests as recorded by gages located in the chamber (ion gage 1), and at the inlet to the diffusion pump of the vacuum chamber (ion gage 2).

Mechanical and Electrical Tests.- The complete flight satellite was assembled and each sensor input tested and recorded through an rf link. Operation of the system was performed for each module as previously done in the prototype telemeter construction. Complete calibration of each of the 96 telemeter channels was accomplished before and after every major test. The flight satellite was shock tested in the same manner as described for the prototype. The telemeter was operating on its flight batteries for this test and complete tape records were made of the operation during this test. Calibration of each channel was made before and after the test. Figure VII-24 is a record of the shock test indicating 35g peak for 10 milliseconds. No structural or telemeter damage was experienced during this test.

Test results of the flight-acceptance tests are shown in figures VII-25 and VII-26. Locations of monitoring vibrometers are also indicated in these figures. Some desirable vibrometer locations were deleted because of the possibility of contaminating the gold-plated surface of the telemeters and the flight bulkhead. Location of vibrometers on the forward-shell surface was impossible because of the heat-transfer coating. The vibration tests were performed with the telemeter operating on its internal battery supply. Monitoring of the telemeters was accomplished through the rf link, and recorded on magnetic tape. The complete test was carried out without mechanical or electrical failure.

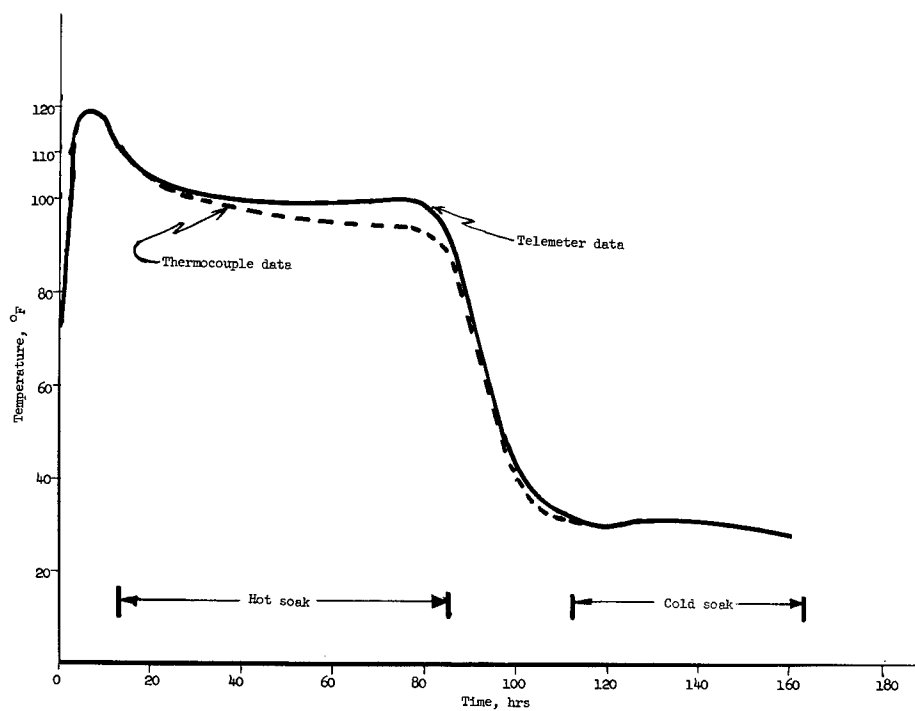


Figure VII-14.- Thermal-vacuum test record; flight-payload grid detector; channel S-11; telemeter "A".

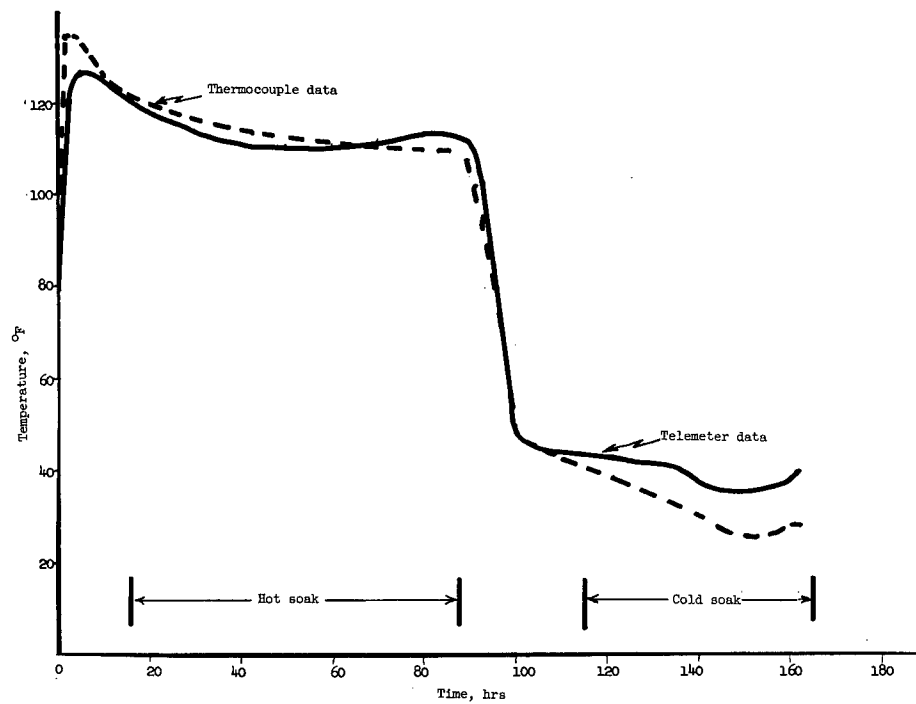


Figure VII-15.- Thermal-vacuum test record; flight-payload pressurized-cell detector; channel S-10; telemeter "A".

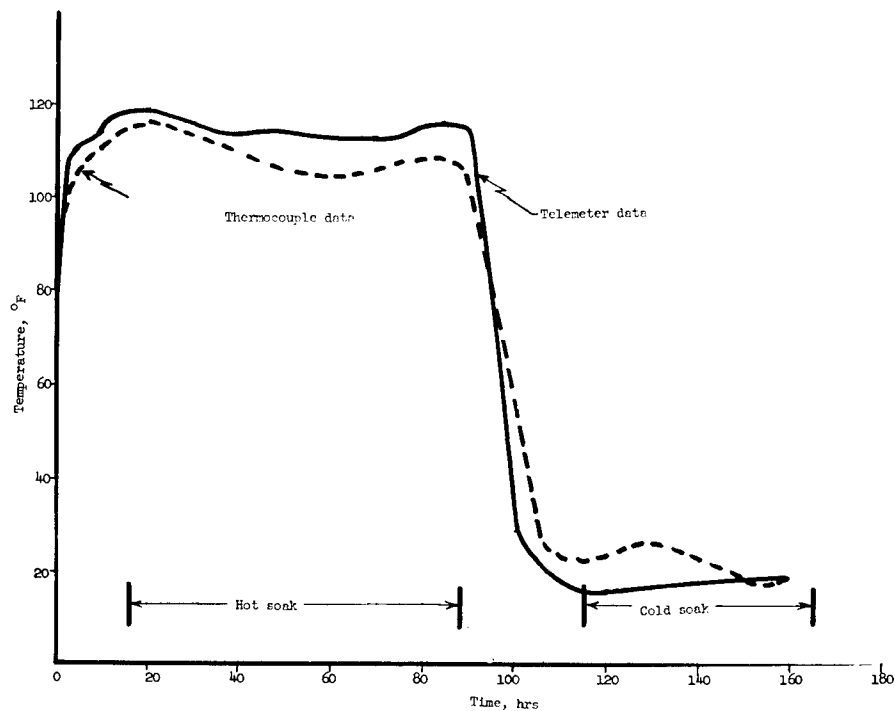


Figure VII-16.- Thermal-vacuum test record; flight-payload solar cell; channel D-11; telemeter "A".

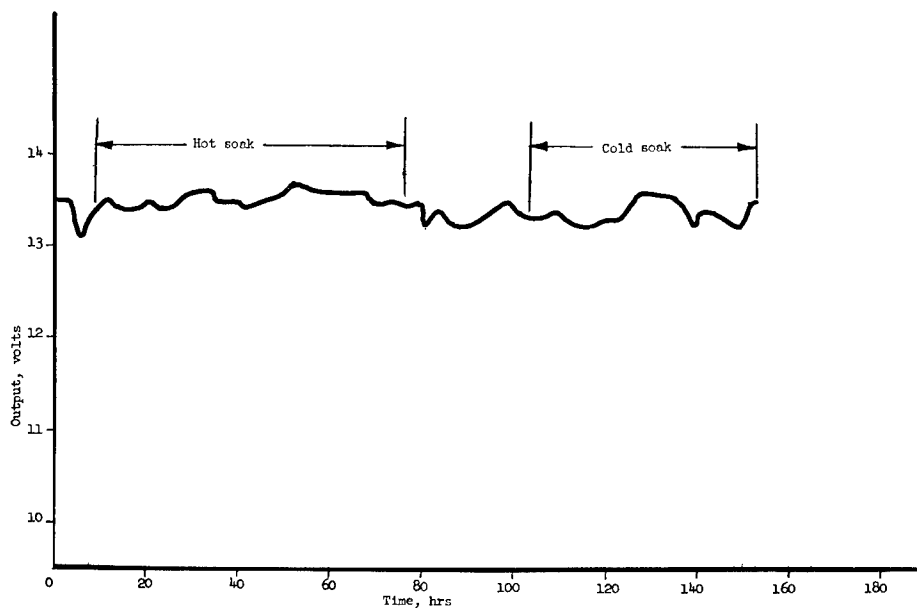


Figure VII-17.- Thermal-vacuum test record; flight payload; "B" battery voltage; channel F-12; telemeter "A".

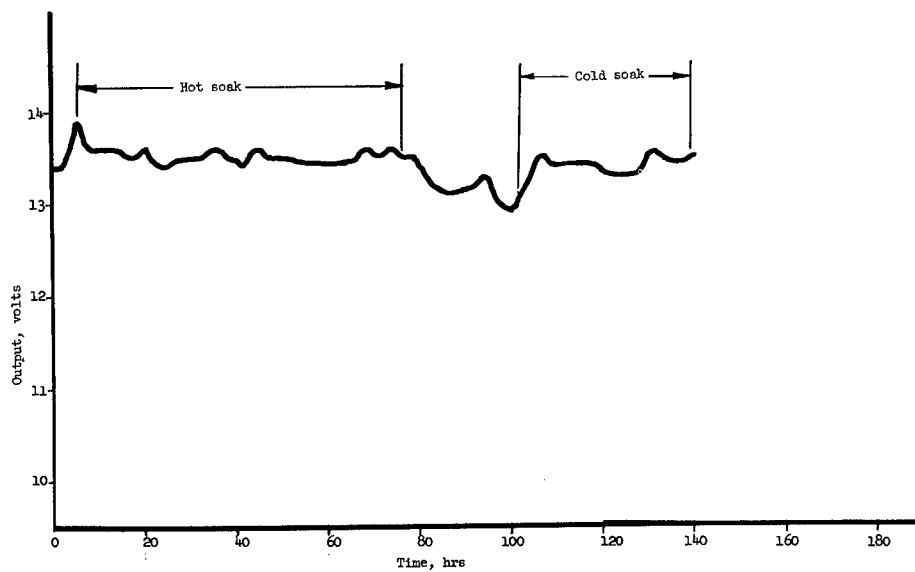


Figure VII-18.- Thermal-vacuum test record; flight payload; "B" battery voltage; channel F-12; telemeter B.

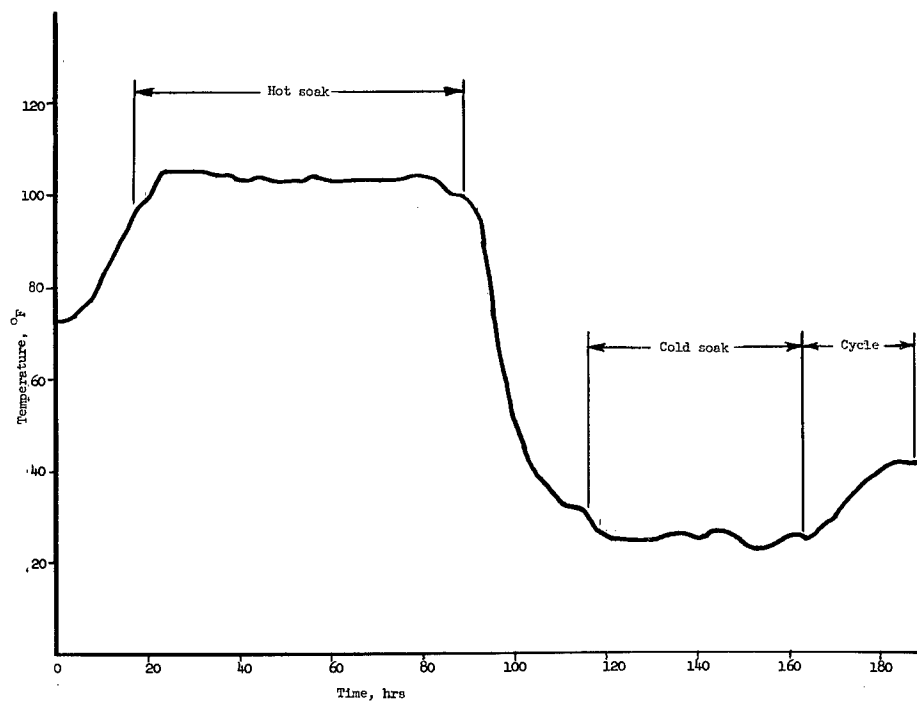


Figure VII-19.- Thermal-vacuum test record; flight-payload telemeter temperature; channel D-4; telemeter "A".

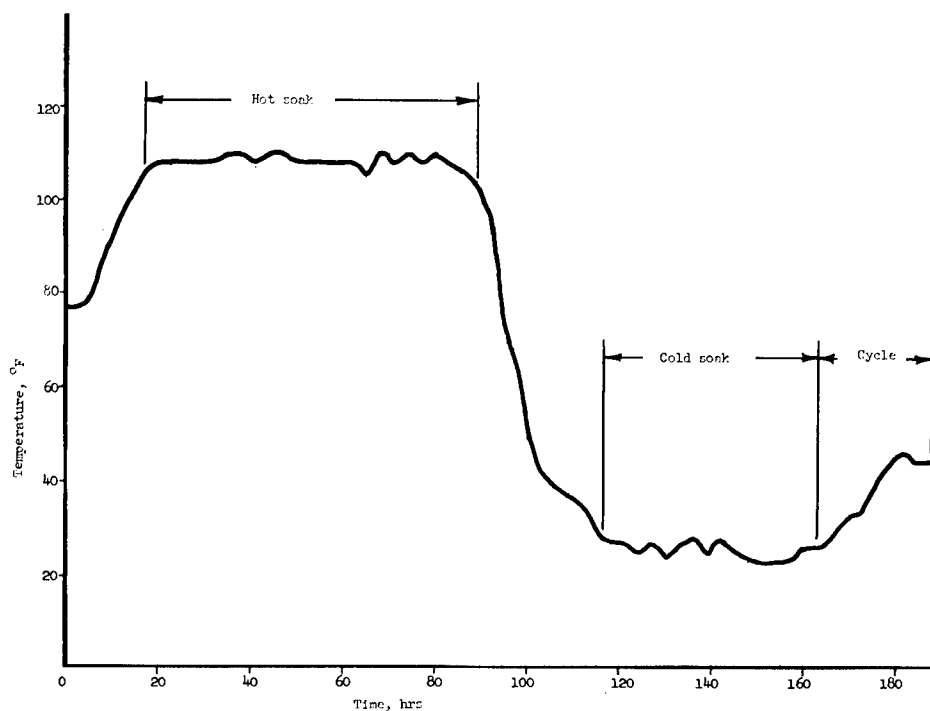


Figure VII-20.- Thermal-vacuum test record; flight-payload telemeter temperature; channel D-4; telemeter "B".

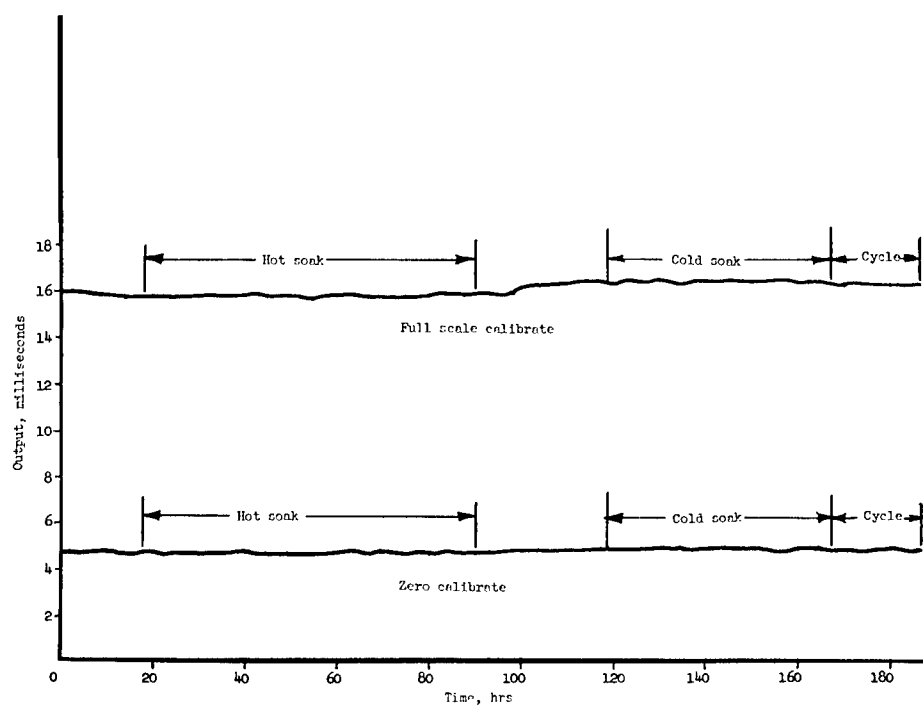


Figure VII-21.- Thermal-vacuum test record; flight payload; full scale and zero calibrate; channels 18 and 19; telemeter "A".

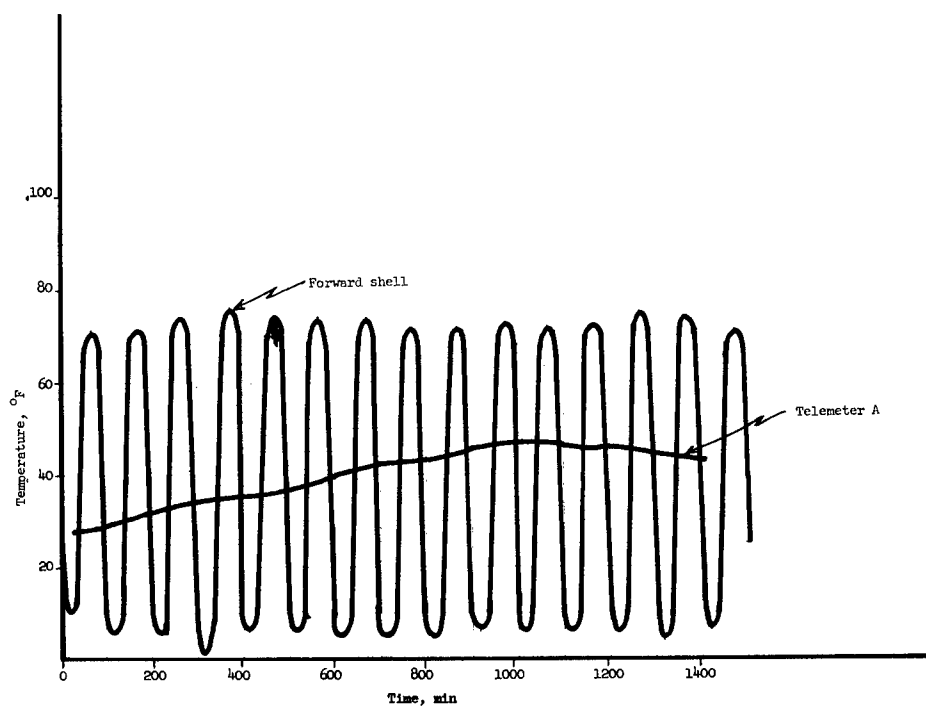


Figure VII-22.- Thermal-vacuum cyclic test record; flight-payload telemeter temperature; channel D-4; telemeter "A".

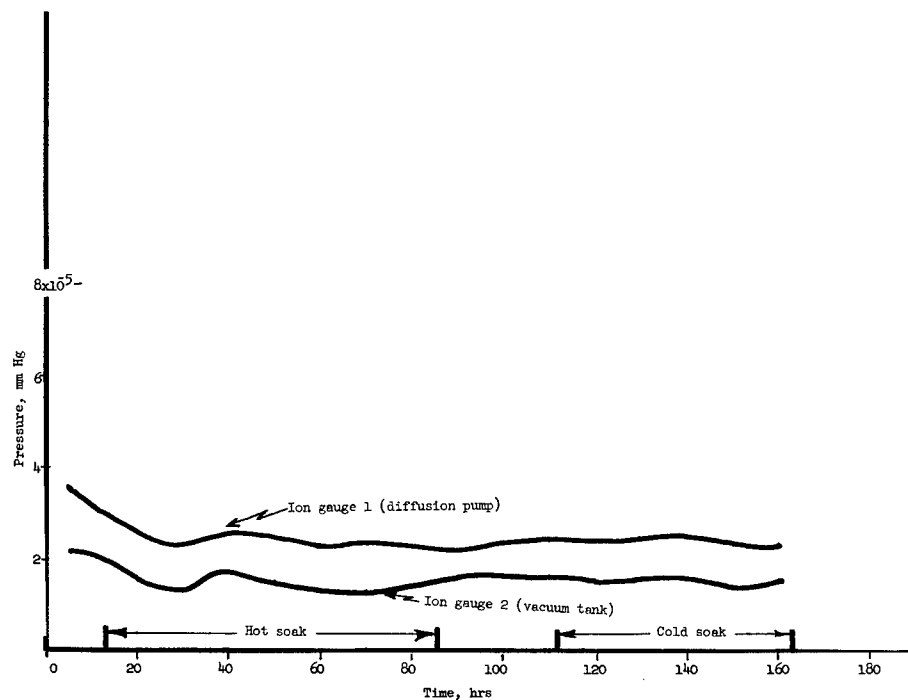


Figure VII-23.- Thermal-vacuum test record; flight payload; test-chamber pressure.

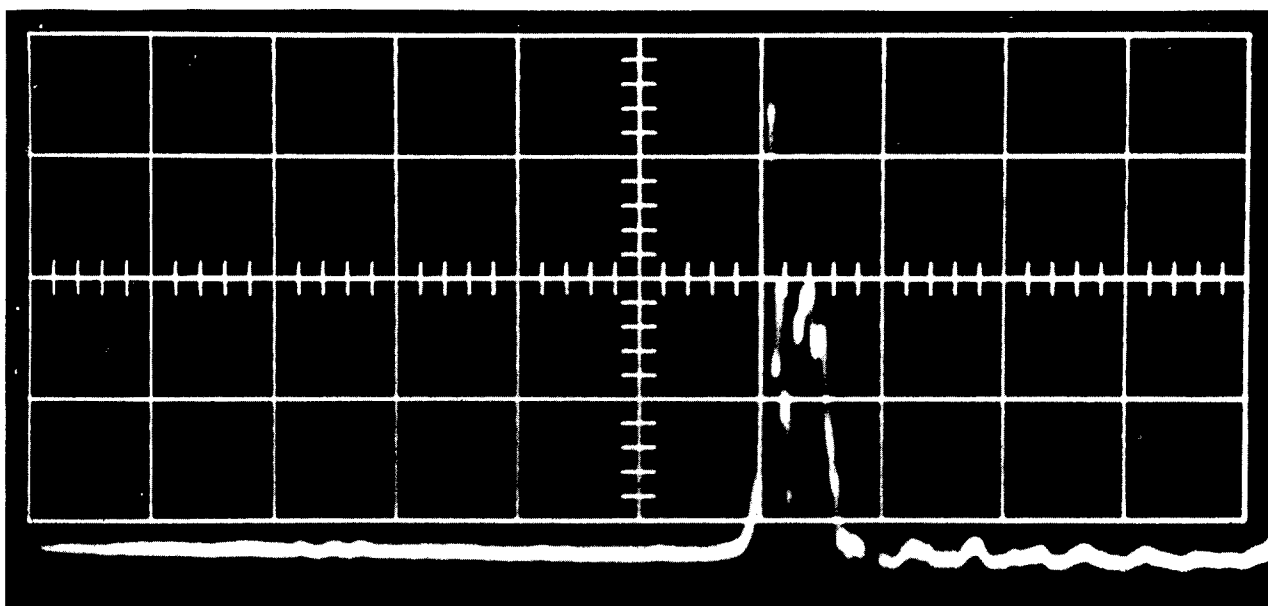


Figure VII-24.- Shock-test record; flight payload.

L-61-2107

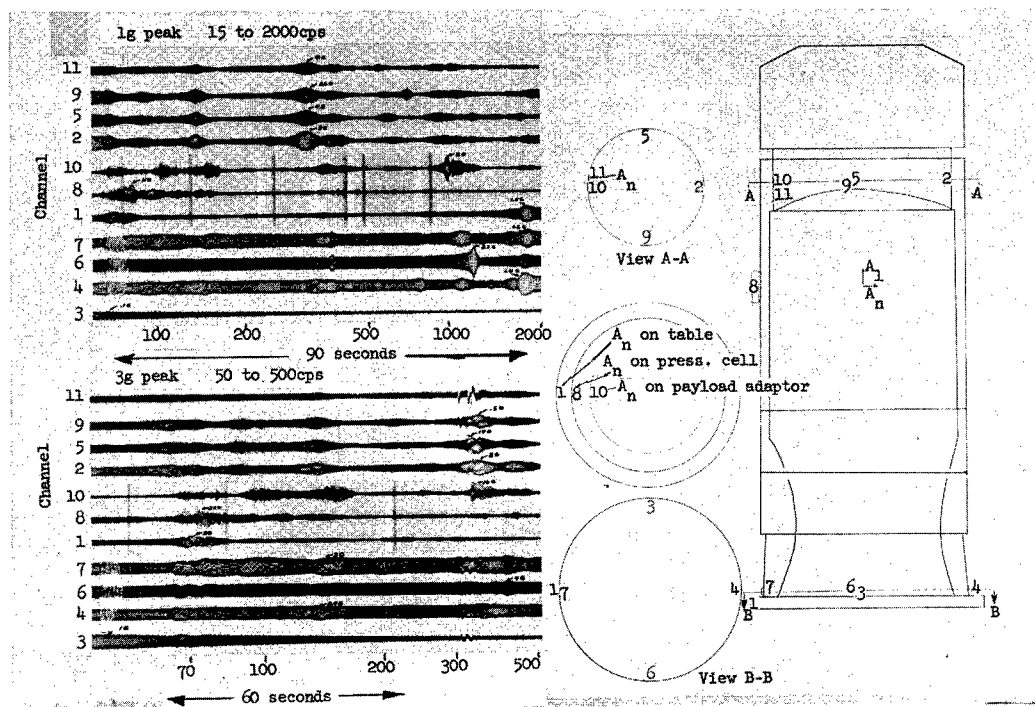


Figure VII-25.- Vibration test; flight payload; accelerometer locations and test records.

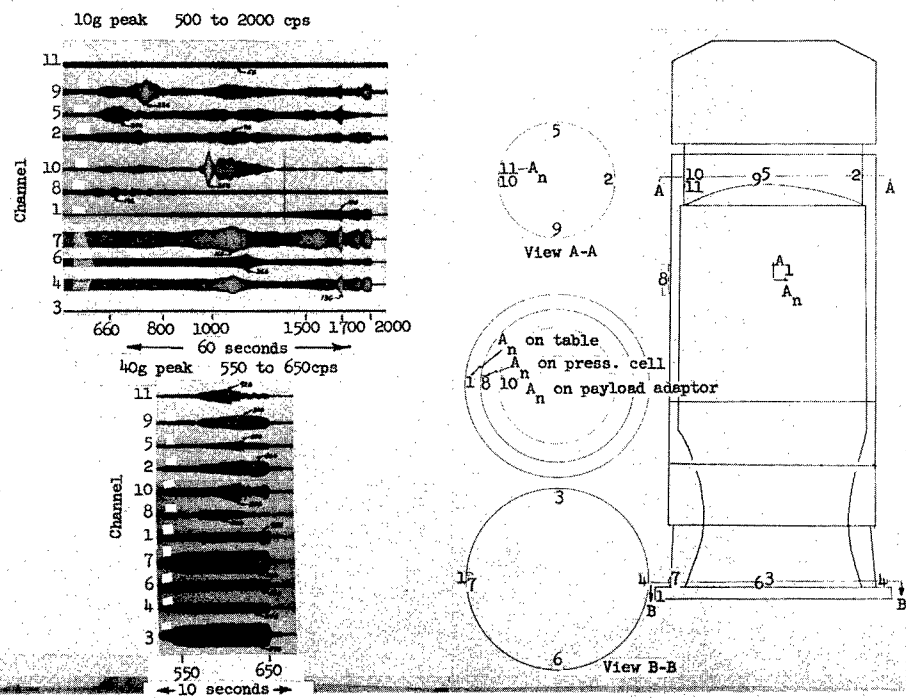


Figure VII-26.- Vibration test; flight payload; accelerometer locations and test records.

CHAPTER VIII

DATA REDUCTION

By Sheldon Kopelson
Langley Research Center

SECTION I - INTRODUCTION

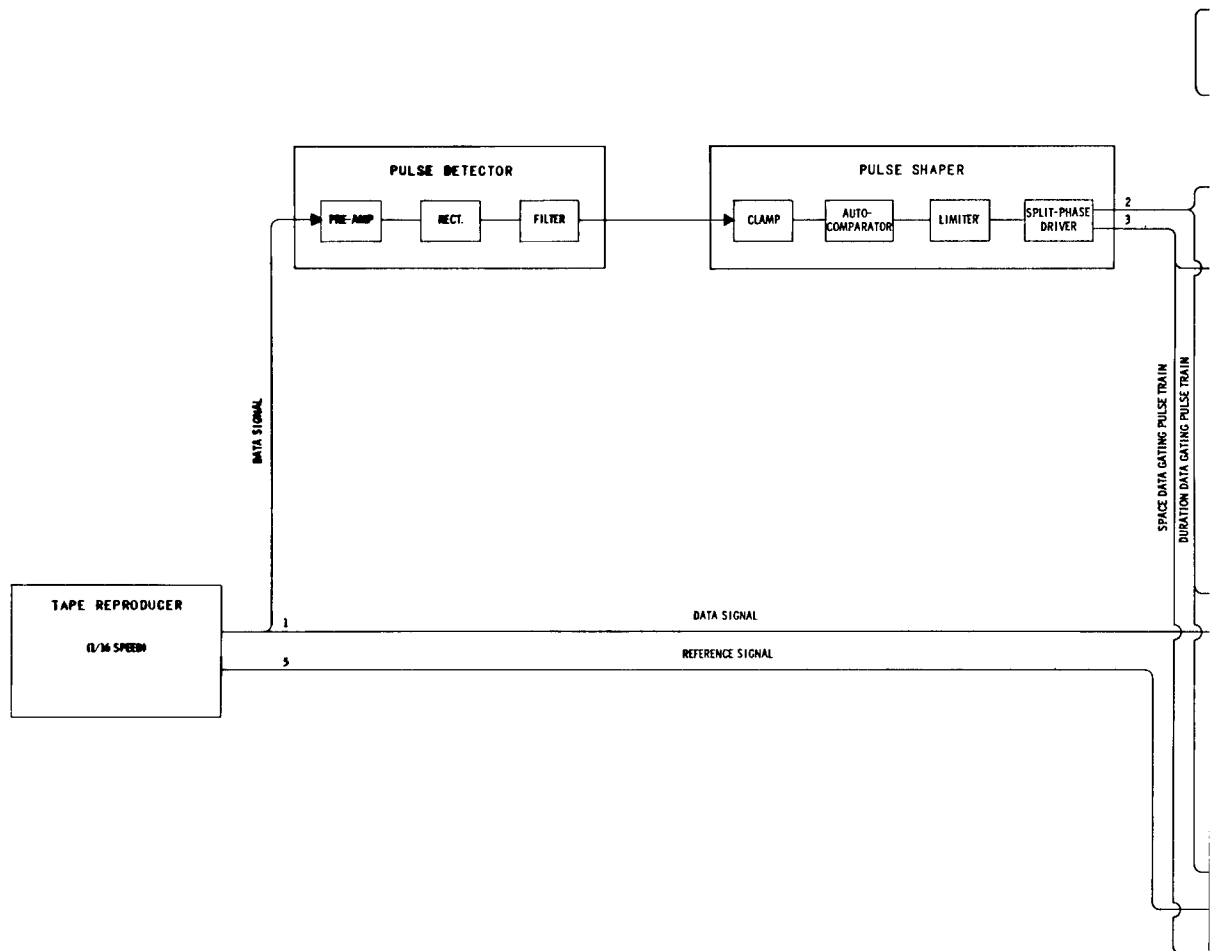
A large volume of data were generated both during the development program and the flight lifetime of the Explorer XIII Micrometeoroid Satellite. These data, in the form of payload telemeter signals, were recorded on magnetic tape. To facilitate the reduction of these data, the development of an automatic data readout system, suited both to the special characteristics of the data signals and to the requirements of high-speed digital computing equipment, was initiated at the start of the satellite development program.

As indicated earlier in this report, the telemeter signal is a nonsynchronous time-division multiplex containing information coded in three independent forms: Duration of subcarrier oscillation bursts, frequency of the oscillations, and the time (spacing) between the bursts. The data readout system decommutates and digitizes this information and records the digitized data on magnetic tape in computer format. The readout of data coded in all three forms is simultaneous and is done at a rate of up to 25 channels per second. A major design criterion of the data readout system was that the performance should be satisfactory when there was a significant amount of noise in the telemeter signal.

The design concept of the data readout system included the shared use of digital formatting and tape recording equipment that was a part of other data readout systems in existence at the NASA Langley Research Center.

SECTION II - DATA READOUT SYSTEM

General description.- The block diagram of the data readout system for the Explorer XIII Micrometeoroid Satellite is shown in figure VIII-1. The wave shapes of typical data and control signals, at indicated points, are shown in figure VIII-2. The telemeter data tape is reproduced at 1/16 recorded speed so that the readout rate is within the capability of the formatting equipment. The pulse detection and shaping circuits generate a duration data gating pulse train and a spacing data gating pulse train, both of which lag the input signal by 8 milliseconds. Because of the nonsynchronous nature of the telemeter signal, all of the automatic system control signals are derived from these pulse trains, in addition to representing the basic time-coded data.



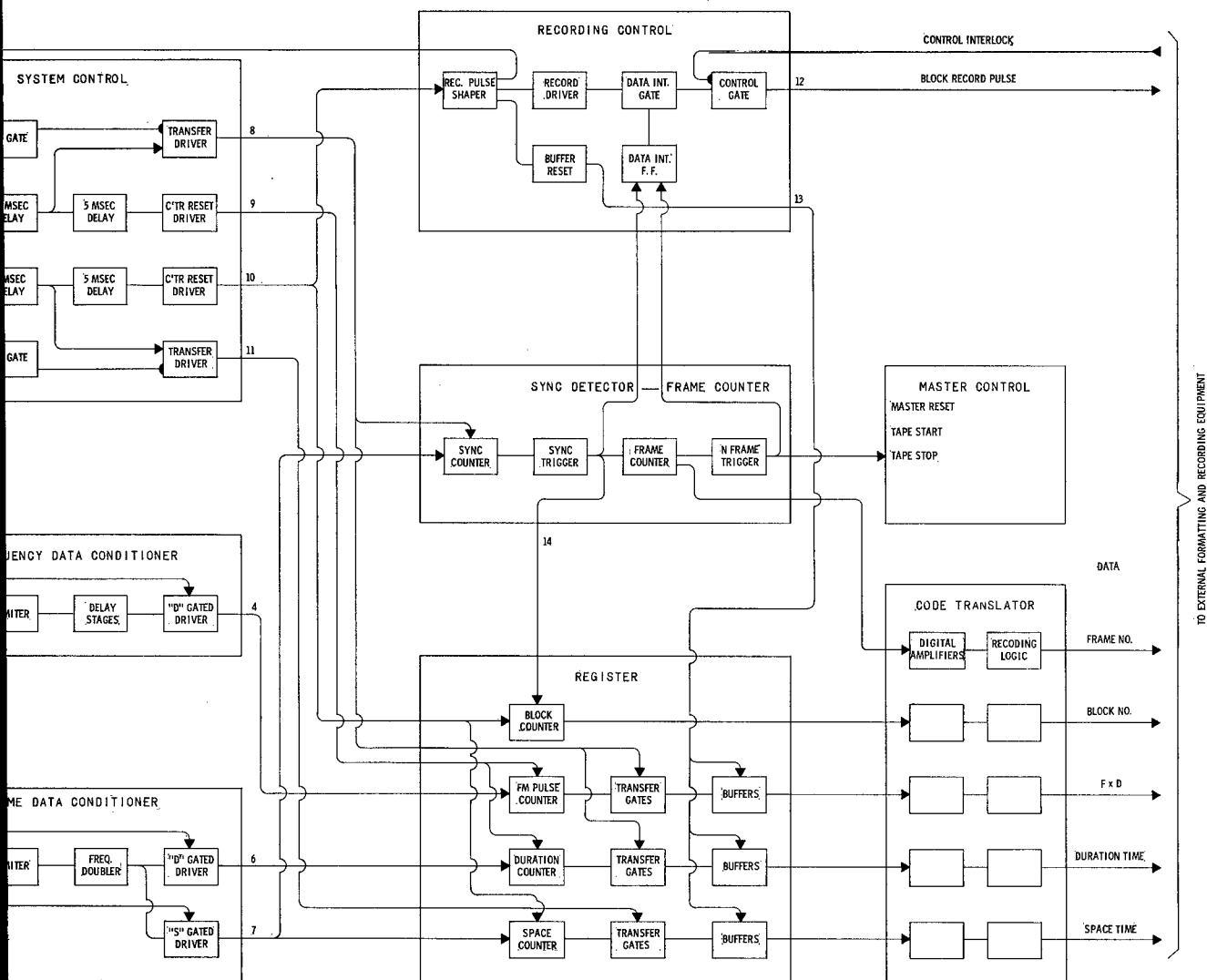


Figure VIII-1.- Block diagram of data readout system.

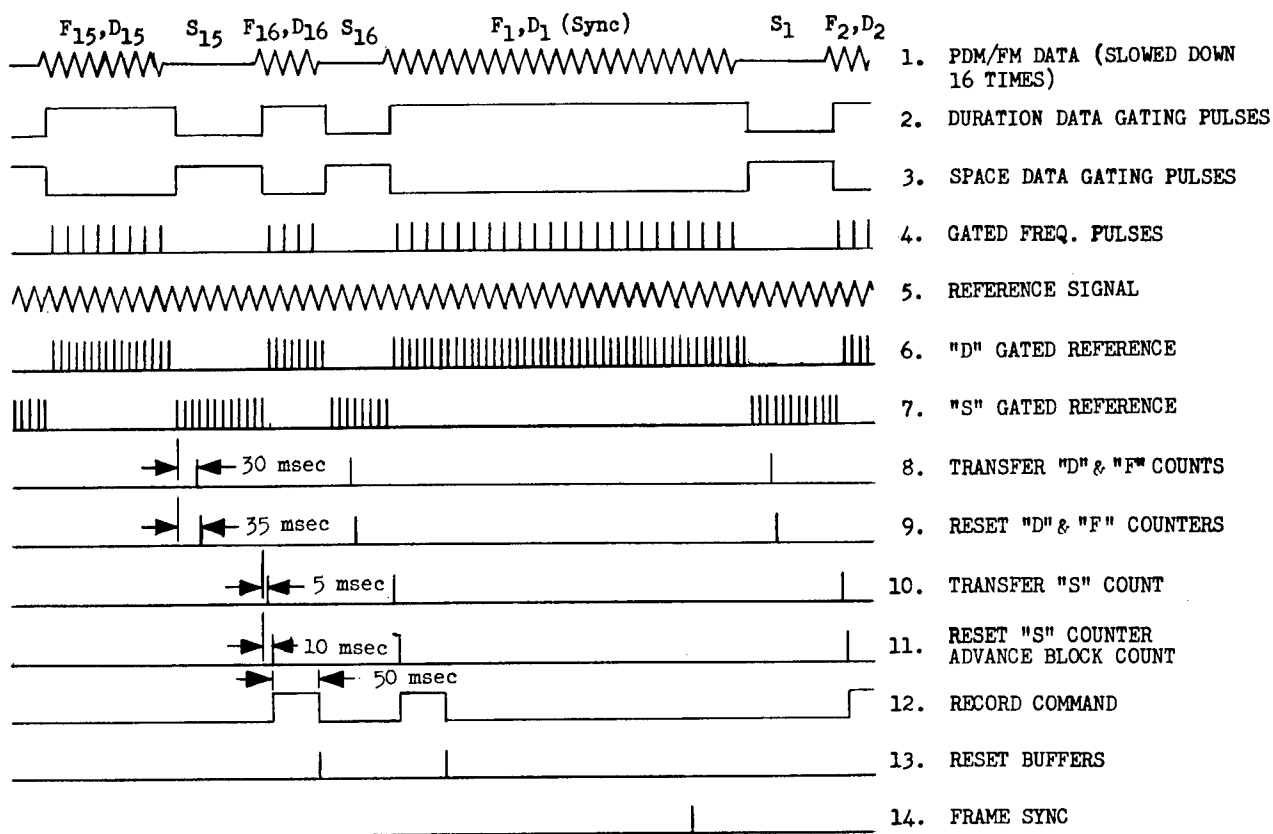


Figure VIII-2.- Data readout system signals.

The durations of the data gating pulses are measured by gating clock pulses into each of two counters. A clock pulse is generated at each zero crossing of a 10-kilocycle (real time) reference signal which had been recorded on one track of the input data tape, thus providing an effective 20-kilocycle clock pulse train. The number of subcarrier cycles in a burst are counted simultaneously with the measurement of the burst duration. Frequency is subsequently computed from these two measurements. The subcarrier cycles are also gated by the duration data gating pulse in order to prevent counting noise cycles. Before gating, the subcarrier pulses are therefore delayed by 8 milliseconds to match the delay of the data gating pulse. The block of data accumulated in the counters during a subcarrier burst and the following space is transferred to a set of three flip-flop buffers at appropriate times (see fig. VIII-2). The data are then recorded on digital magnetic tape as a single block of three channels. A block-identifying counter is advanced just before the initiation of each digital readout. Each time frame sync is detected, this counter is reset and a frame-identifying counter is advanced one count. When the block of data being recorded on the digital tape is followed by a block having a minimum burst duration, the second "space" occurs before the recording has been completed. Buffering is therefore required for the "space" data as well as the other data. Since the block and frame counters are not advanced during the recording of a block of data, they do not require buffering.

The timing of control signals 8 to 12, shown in figure VIII-2, is based upon the characteristics of the external digital formatting equipment and an allowance for actual durations and spacings to be as short as 60 percent of the minimum expected from the telemetry encoder. However, as is shown later, false data pulses of very short duration can be generated when the readout system input signal is very noisy. A transfer pulse could then occur either while data were being read out from a buffer or while a counter was active. The result of this transfer would be the recording, on the digital magnetic tape, of an invalid code. To prevent the recording of an invalid code, the transfer of data from a counter to its buffer is inhibited whenever that counter is active or the readout of a block of data is in progress.

The outputs of the buffers and the identification counters are in the 1-2-2-4 code usually required for digital printers rather than the binary coded decimal (BCD) code required by the external digital formatting equipment. Before entering the formatting equipment, the digital data are fed to the code translator (see fig. VIII-1) which changes the bit level voltages and converts the code to BCD. A digital printer, driven directly from the buffers and identification counters, was initially included in the readout system as a quick-look device but it was discarded when the required maintenance outweighed its usefulness.

As was mentioned previously, the readout system utilized digital formatting and tape recording equipment that was a part of existing systems. The signals from the Explorer XIII data readout system were connected via a patchboard network to any one of three Beckmann Inc. Model 210 data recording systems which are operated as a central data recording facility. The outputs of the latter systems are recorded on magnetic tape in IBM 7070 computer format.

Data resolution.— As stated previously, the durations of the data gating pulses are measured by gating 20-kc (real time) clock pulses into counters. The measurement resolution R_t , for the time-coded data are, therefore, the time represented by ± 1 count, or ± 0.05 millisecond.

The resolution of the measurement of the number of subcarrier cycles N during a burst is also ± 1 count. However, the subcarrier frequency is computed by dividing this measurement by the measurement of the independent burst duration D . The computed frequency F_c is:

$$F_c = \frac{\frac{N \pm 1}{20D \pm 1}}{20} \quad (1)$$

but

$$N = F \times D \quad (2)$$

where F is the actual frequency. Therefore:

$$F_c = \frac{20(FD \pm 1)}{20D \pm 1} \quad (3)$$

where F_c and F are in kilocycles and D is in milliseconds. The resolution R_f , of the frequency measurement is:

$$R_f = F - F_c = \frac{\pm F \mp 20}{20D \pm 1} \approx \frac{\pm F \mp 20}{20D} \quad (4)$$

R_f is not, therefore, constant as is R_t .

The rms resolution scatter is determined from the expected distribution of R_f which includes cases of zero resolution error in the measurement of N and/or D , and is given by

$$R_{f,rms} \approx \frac{1}{20D} \sqrt{\frac{2}{3}(F^2 + 400)} \quad (5)$$

The ranges of the telemetric frequency and duration channels were 6 kilocycles to 15 kilocycles and 4 milliseconds to 15 milliseconds, respectively. The expected range of the resolution scatter for the frequency-coded flight data was 0.057 kilocycle, rms to 0.256 kilocycle, rms. Calibrations of the telemetry frequency channels were made with the time channels set at full scale, thereby holding the resolution scatter to a maximum of 0.068 kilocycle, rms.

Noise suppression.— It was expected that, in general, the telemeter signals received from the Explorer XIII Micrometeoroid Satellite would be fairly noisy. The recorded intelligence signal thus appeared as a series of bursts containing subcarrier oscillations and noise. However, the spaces between the bursts contained pure noise, with some noise peaks exceeding the signal peaks even when the rms signal-to-noise ratio was of the order of 7 to 10 decibels. In order to differentiate between the subcarrier bursts and the noise filled spaces under these conditions, the pulse detector was designed as an approximation to a root-mean-square voltage detector. The pulse detector consisted of a preamplifier, rectifier, and filter. The output of this circuit was a pulse train which exhibited the following characteristics. The peaks of the pulses were equal to 90 percent of the rms amplitudes of only the subcarrier oscillations, provided the input-signal-to-noise ratio was greater than +6 decibels. The base level of the pulse train was equal to 70 percent of the rms amplitude of the noise in the "space," provided the noise had a Gaussian distribution. Since the frequency spectrum of a rectified random noise is continuous to zero cps, it was necessary that the filtering after the rectifier be as heavy as possible without imposing an excessive pulse rise time. The filter was chosen so that the pulse rise time (10- to 90-percent amplitude) was 20 milliseconds. Since the input data tapes are played back at 1/16 of the recorded speed, this time corresponds to 1.25 milliseconds, referred to real time. With this filter, some residual noise ripple was present in the detector output signal.

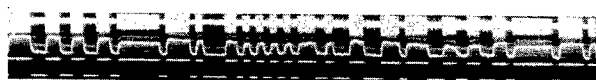
The time between the points at which the detector output signal is halfway between pulse base and pulse peak is equal to the duration of the subcarrier bursts. In order to generate sharp-edged data gating pulses which corresponded to these intervals, the pulse shaper employed a self-referenced amplitude

comparator. The base of the detector output signal was clamped to ground and the clamp circuit output was connected to one input of the comparator. In addition, the detector output signal, attenuated by 50 percent, was connected to a second clamp circuit which was followed by a long time constant diode detector. This circuit held the reference input of the comparator at one-half the difference between the base and peak levels of the detector output signal. The comparator was designed so that its output was constant until the reference level was exceeded. The remainder of the pulse shaper consisted of a three-stage limiter to provide further pulse shaping and an inverter to provide two data gating pulse trains of opposite phase. These pulses lagged the detector input signal by 8 milliseconds.

In figure VIII-3, the detector input and output signal and one of the shaper output signals are shown for several signal conditions. The rise of the base level of the detector output signal, as the input noise increased, is not evident as it was necessary to adjust the oscilloscope trace of this signal to keep it from overlapping with the trace of the input signal. For noise-free input signals, the shaper output pulses have the same durations as the subcarrier bursts. As the noise in the input signal increases, the residual detector ripple causes some scatter in the durations of the data gating pulses at the output of the pulse shaper. When a residual noise peak is great enough to cross the comparator threshold or when there are rapid variations in the rms noise level which prevent clamping, false data gating pulses are generated. The blocks of data become misnumbered and the resultant loss of synchronization is carried on to the digital magnetic tape. However, the data computing program includes a check of both the block count and the sync channel duration. This check detects the loss of synchronization and causes the entire frame to be rejected.



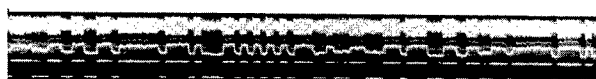
(a) Mean signal-to-noise ratio,
19.7 decibels.



(b) Mean signal-to-noise ratio,
10.8 decibels.



(c) Mean signal-to-noise ratio,
8.6 decibels.



(d) Mean signal-to-noise ratio,
7.4 decibels.

Figure VIII-3.- Pulse detector and shaper signals.

SECTION III - DATA PROCESSING OPERATIONS

The data readout system previously described and high-speed digital data handling equipment (IBM 7070, 1401, 407-tabulator) were used to process the payload telemeter calibration data and flight qualification test data as well as data received from the orbiting spacecraft.

The computing process for the calibration and qualification data included computation of the subcarrier frequencies. The basic data measurements (frequency, "duration" time, and "space" time) were sorted by channel and frame, and simultaneously listed and plotted on the tabulator. Approximately 711,000 points were processed in this manner during the qualification and calibration of the flight payload telemeters.

Processing of the data telemetered from the spacecraft required two computing and listing operations for each set of data. The result of the first operation was a listing of the mean values of the basic time and frequency measurements of each channel. From these listings, the telemeter identification was verified and the mean values of the calibration channels and the telemeter temperature, which were used in the second operation, were determined.

The computing program for the second operation included the correction of the time multiplexed data for zero and sensitivity changes and selection of the subcarrier oscillator calibrations applicable for the measured telemeter temperature. The physical quantities measured in the various satellite experiments were then computed and were listed as a function of time.

The computing programs for both of the experimental data operations included the detection and rejection of frames in which channel synchronization had been lost. Since tabulator plotting was not required for the experimental data, only the IBM 7070 and 1401 were used in the data processing operations. Approximately 43,000 points of experimental data were processed.

SECTION IV - PERFORMANCE EVALUATION

The performance of the data readout system was evaluated as a function of the quality of the recorded telemeter signal. The mean signal-to-noise ratio and the noise level variation, caused by spacecraft spinning, were measured by recording the output of the signal burst detector (fig. VIII-1). The characteristics which were evaluated were the ability to maintain channel synchronization (i.e., identification) and the reading scatter.

Table VIII-1 lists the interrogation history of the spacecraft telemeters. The recorded data which, after preliminary oscilloscope monitoring were judged to be automatically readable to any extent, are indicated. The range of the measured signal-to-noise ratios of these data recordings was from 7.4 to 19.7 decibels.

The data readout system was programed to read out 50 frames of data from each telemeter record. In cases where frame sync was not detected in each frame, the number of telemeter frames that were processed was greater than 50. For these cases, the exact number of frames was determined from the reading of a block counter in the digital formatting equipment. In figure VIII-4, the percentage of frames for which complete channel synchronization was maintained is plotted as a function of the mean signal-to-noise ratio, in decibels, of the telemeter signal. The data readout system has a pronounced "performance threshold" at a signal-to-noise ratio of approximately 10 decibels. For input signal-to-noise ratios between 10 and 20 decibels, channel synchronization is maintained for an average of 90 percent of the telemeter frames. Automatic readability performance of 100 percent could be expected for input signal-to-noise ratios on the order of 40 decibels.

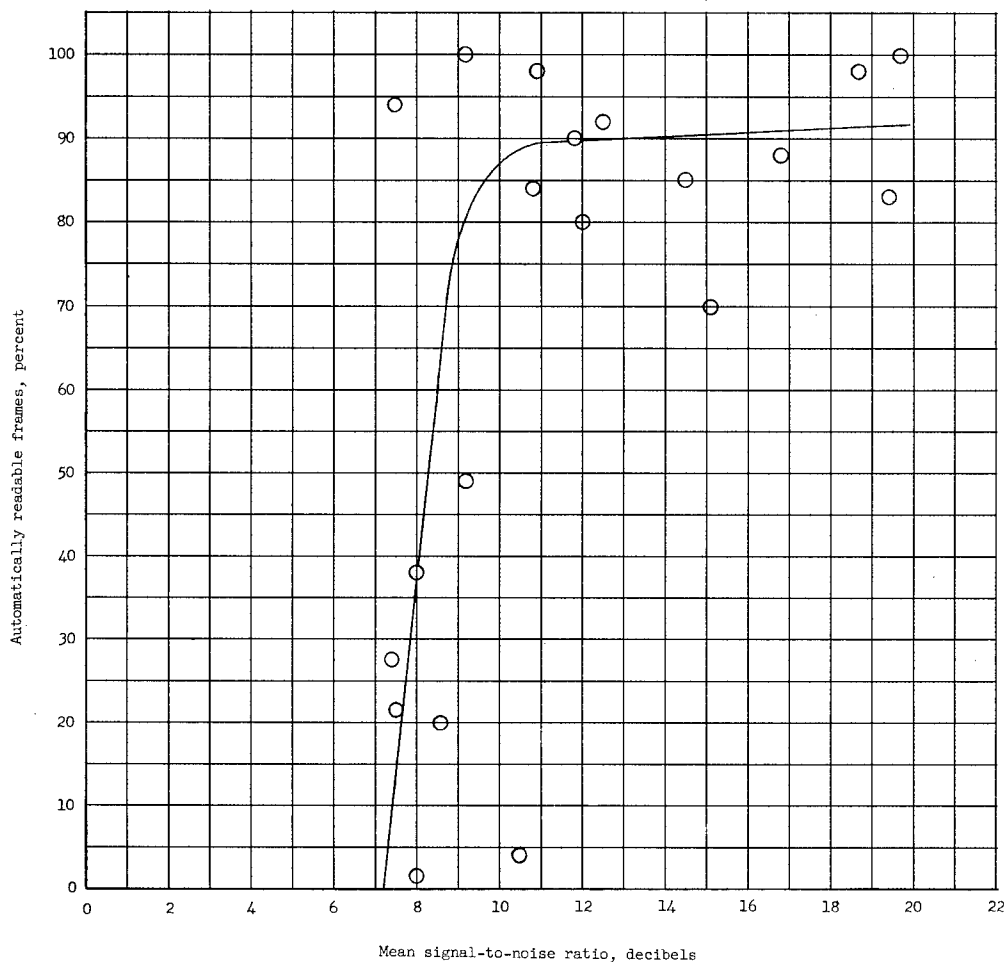


Figure VIII-4.- Detection performance of data readout system.

Figure VIII-5 is a plot of the root-mean-square reading scatter of the time-coded data as a function of the mean signal-to-noise ratio of the data signal. The results are shown for signal-to-noise ratio greater than the performance threshold which is evident in figure VIII-4. Below this level the

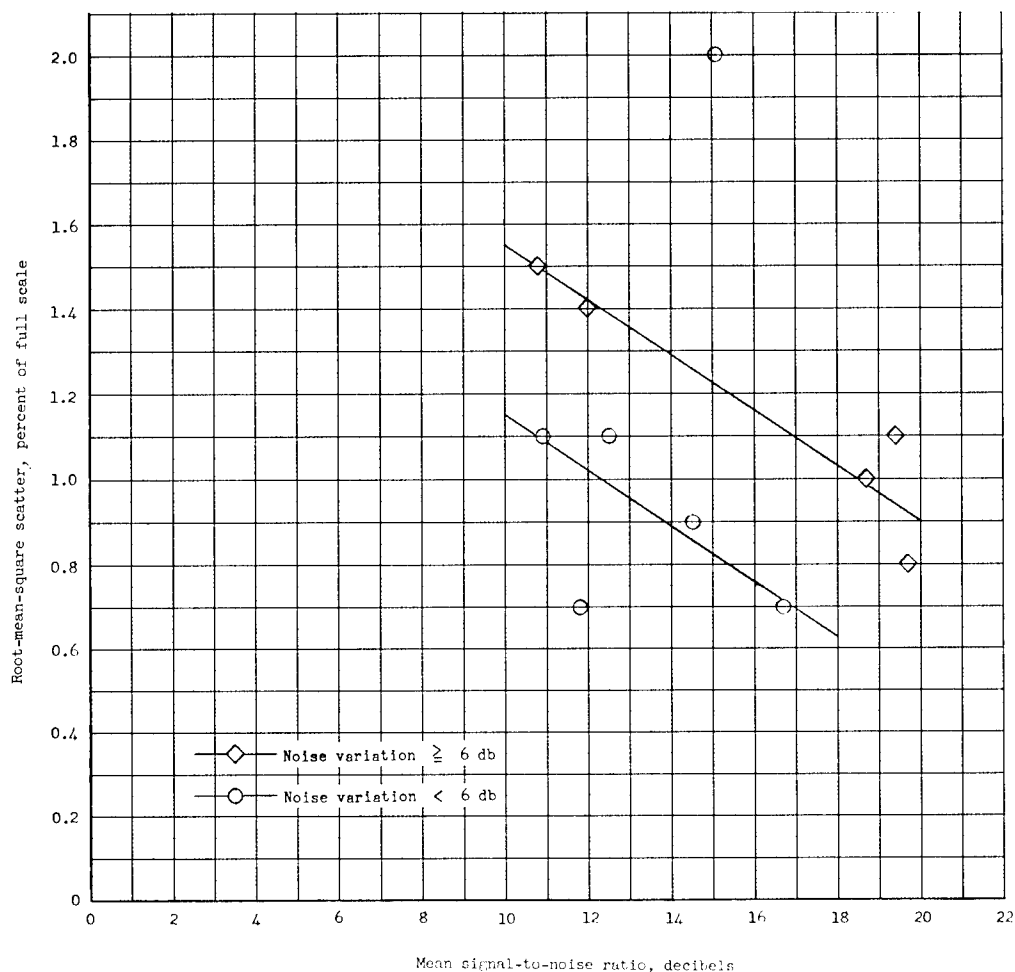


Figure VIII-5.- Reading scatter; time-coded data.

number of readings available were, in general, not sufficient for a statistically significant calculation of the rms scatter. The effect of the fluctuations in noise level is indicated by classifying the results as to whether the noise level variation was less than 6 decibels or greater than 6 decibels. At the threshold, the rms scatter levels are 1.1 and 1.5 percent of full scale, respectively. For the range of signal quality encountered, the scatter decreases linearly with increasing signal-to-noise ratio. If the linearity should continue beyond this range, the reading scatter would be expected to reach the basic resolution limit (rms scatter, 0.37 percent of full scale) at 22 decibels and 30 decibels.

As previously shown, the resolution scatter of the data readout system, for frequency measurement, is a variable which reaches a significant level under conditions of high subcarrier frequency and coincident low burst duration. The performance of the system for frequency coded data was therefore evaluated by determining the ratio of the measured scatter to the expected resolution scatter. The results are shown in figure VIII-6 and represent the group correlation for

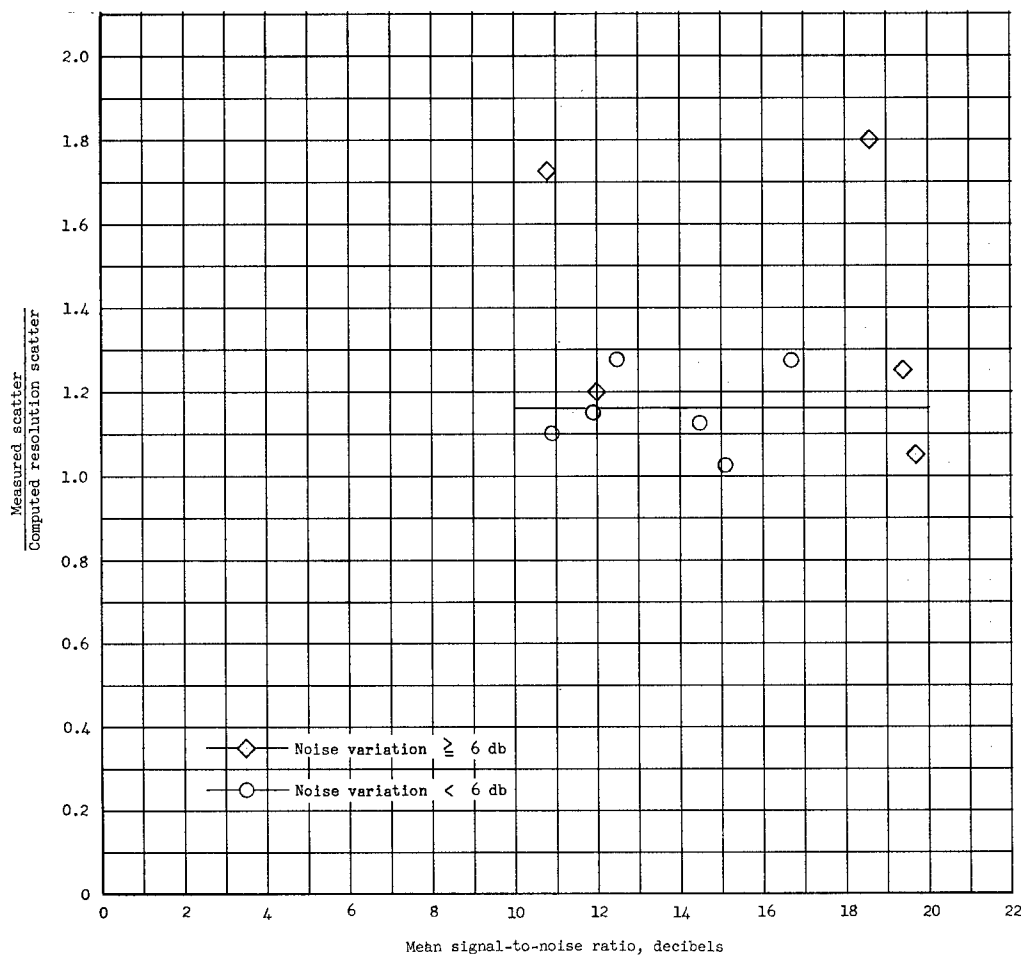


Figure VIII-6.- Scatter correlation; frequency-coded data.

all of those channels for which nonvariance of the subcarrier oscillators could be assumed. The expected group resolution scatter σ_N was calculated from the equation

$$\sigma_N = \sqrt{\frac{\sigma_1^2 + \sigma_2^2 + \dots + \sigma_n^2}{n}} \quad (6)$$

where $\sigma_1, \sigma_2, \dots, \sigma_n$ are expected scatter values for each channel. For the range of signal-to-noise ratios encountered, the average correlation was 1.16, indicating only minor degradation of performance due to noise. The two points for which the correlation is 1.8 and 1.7 correspond to interrogations of the "B" telemeter near the end (orbits 23 and 28) of the orbiting lifetime of the satellite.

TABLE VIII-1.- ORBITAL TELEMETRY HISTORY

Orbit	Date/Time	Minitrack station	Tape	Telemeter	Data-reduction process
Launch	25/18:29:44	Blossom Point	122A001	None	None
1	25/20:11:45	Grand Forks	122N001	B	Automatic
1	25/20:11:45	Blossom Point	122A002	B	Automatic
1	25/20:17:14	Blossom Point	122A002	A	Manual*
2	25/21:59:40	Fort Myers	122D001	None	None
7	26/06:34:00	Santiago	122J001	None	None
8	26/08:32:15	Santiago	122J001	None	None
9	26/10:02:40	Antofagasta	122H001	A	Manual
9	26/10:02:40	Antofagasta	122H001	B	Manual
10	26/11:46:00	Quito	122F001	A	Manual
10	26/11:55:00	Quito	122F001	B	Manual
13	26/15:13:30	Fort Myers	122D001	A	Automatic
13	26/15:15:02	Fort Myers	122D001	B	Automatic
13	26/15:13:30	Blossom Point	122A003	A	Automatic
13	26/15:15:02	Blossom Point	122A003	B	Automatic
14	26/16:58:06	Blossom Point	122A004	A	Automatic
14	26/16:58:06	Blossom Point	122A004	B	Automatic
14	26/16:58:06	Fort Myers	122D002	A	Automatic
14	26/16:58:06	Fort Myers	122D002	B	Automatic
15	26/18:40:57	Fort Myers	122D002	A	Automatic
15	26/18:40:57	Fort Myers	122D002	B	Automatic
20	27/03:03:00	Santiago	122J002	A	Manual
20	27/03:03:00	Santiago	122J002	B	None
21	27/04:45:56	Santiago	122J003	A	Automatic
21	27/04:45:56	Santiago	122J003	B	Automatic
22	27/06:21:30	Santiago	122J003	A	Automatic
22	27/06:21:30	Santiago	122J003	B	Automatic
23	27/08:03:14	Antofagasta	122H001	A	Automatic
23	27/08:03:14	Antofagasta	122H001	B	Automatic
25	27/11:15:40	Lima	122G01	None	None
27	27/14:03:00	Woomera	122-1	None	None
28	27/15:42:15	Woomera	122-1	A	Automatic
28	27/15:42:15	Woomera	122-1	B	Automatic
35	28/02:00:03	Antofagasta	122H001	A	Manual**
35	28/02:00:03	Antofagasta	122H001	B	Manual**
40	28/08:46:00	Antofagasta	122H001	B	Manual**

*Special Process by GSFC.

**The temperatures of all systems had increased beyond design limits as a result of aerodynamic heating so that these data could not be used.

CHAPTER IX

PRESSURIZED-CELL EXPERIMENT

By Charles A. Gurtler
Langley Research Center

SECTION I - INTRODUCTION

Pressurized-cell detectors were developed and constructed at the Langley Research Center to obtain a direct measurement of the micrometeoroid puncture hazard to thin structural material. A total of 160 detectors were mounted around the periphery of the rocket motor used on the Explorer XIII satellite. (See fig. IX-1.) Material thicknesses of 0.001, 0.0015, 0.002, 0.0025, and 0.005 inch were used on the detectors. The exposed surface of the test material of each detector was 21.8 square inches and the total exposed surface of the 160 detectors was 24.2 square feet. The average weight of the detectors was 68 grams.

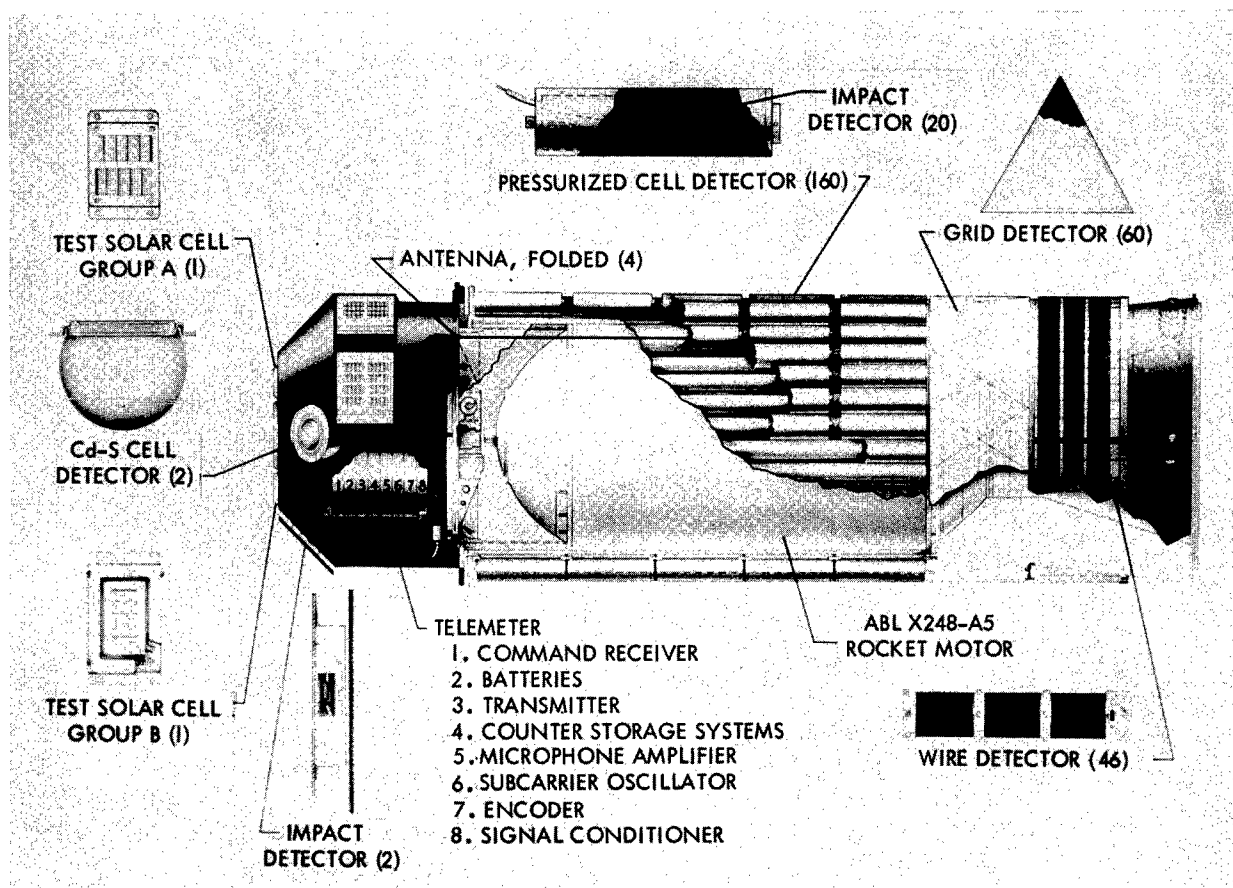


Figure IX-1.- Cut-away view of micrometeoroid satellite.

SECTION II - DESCRIPTION

The pressurized-cell detector was designed so that a puncture of the thin test material by a micrometeoroid would allow the pressurized helium to leak out. This pressure loss would create a pressure change across a pressure-sensitive metal-corrugated diaphragm. The deflection of the diaphragm was transmitted to a snap-action switch which was used to signal the telemeter of the puncture. Details of the detector are shown in figure IX-2.

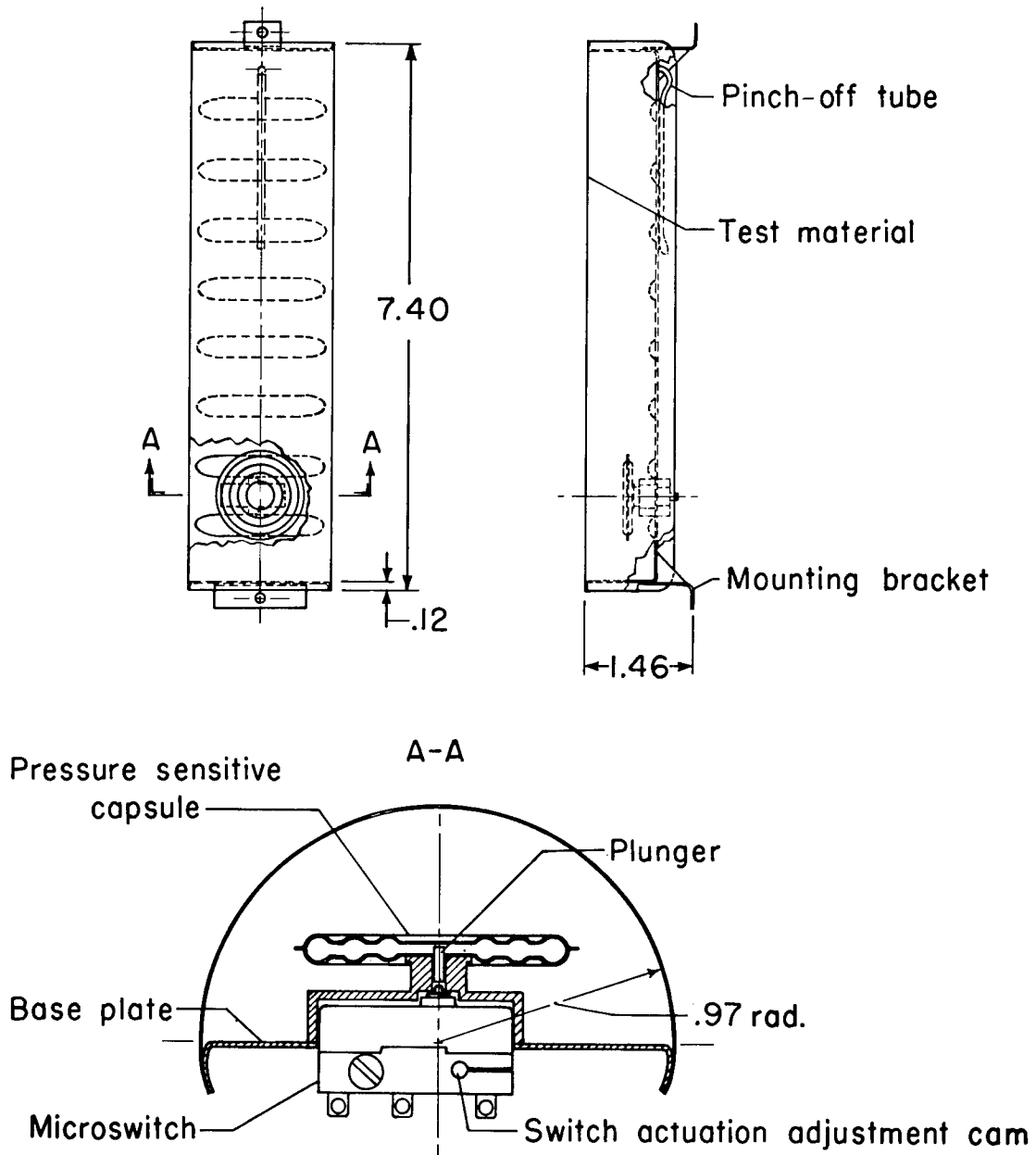
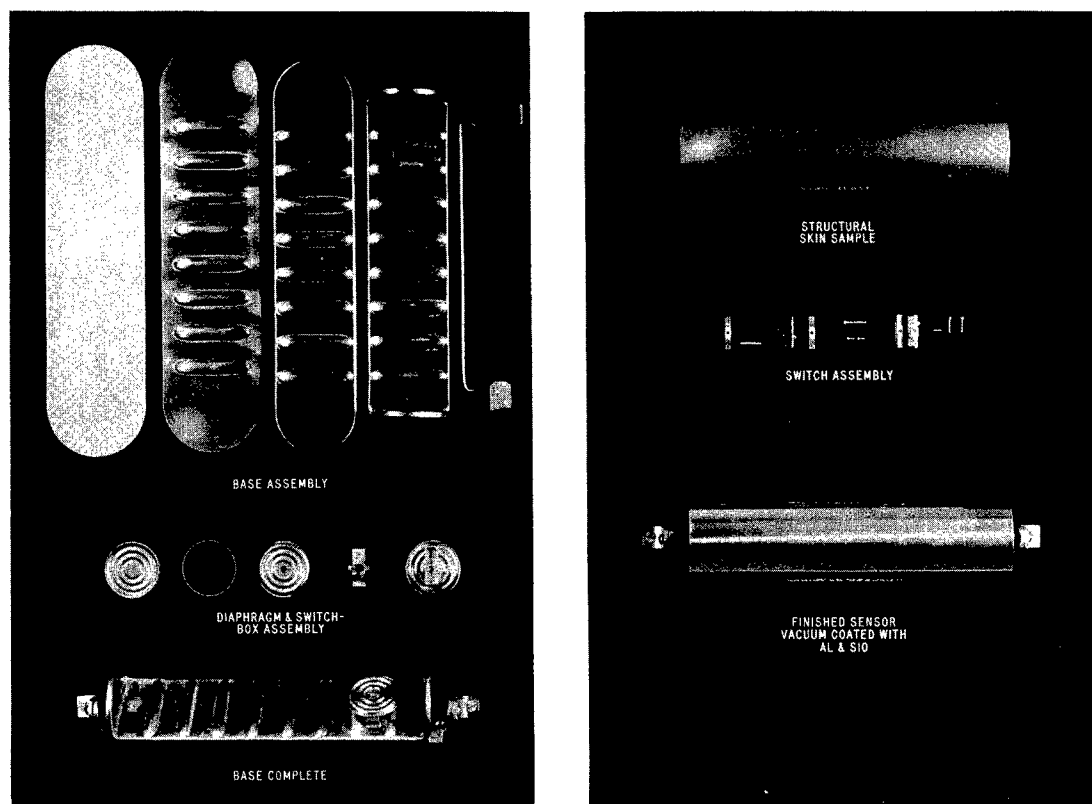


Figure IX-2.- Pressurized-cell detector. Dimensions are in inches.

The material used in the thin test section of the detector was beryllium copper. Carefully selected fine-grain pressure-diaphragm stock was used because it could be rolled to very thin sheets and still be impervious to the internal gas. Figure IX-3 shows all the component parts of the detector and the sequence



L-62-332

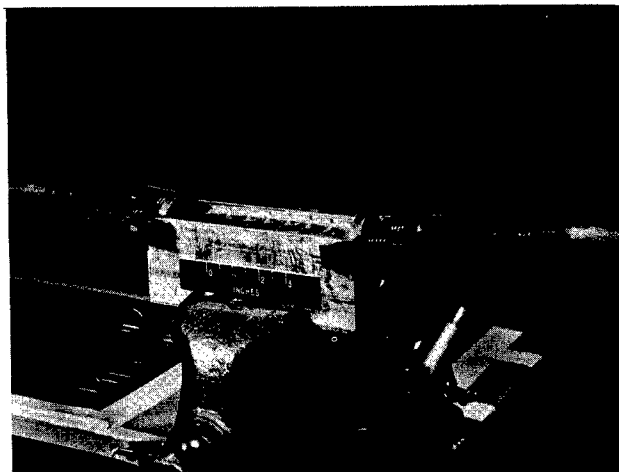
Figure IX-3.- Component parts of pressurized-cell detector.

of fabrication. The base assembly was fabricated from beryllium-copper sheet material with a thickness of 0.014 inch. The material was placed in a forming die (see fig. IX-4 and fig. IX-5) where 8 corrugations were formed with hydraulic pressure to rigidize the base plate. The strip was then placed in a die which formed a rim around the outer edge of the base plate. (See fig. IX-6.) A bending fixture was used to complete the fabrication of the base plate by turning up the semicircular ends and punching the holes for the switch body and the fill tube. (See fig. IX-7.)

The pressure capsule was fabricated from two pressure-sensitive diaphragms which were hydraulically formed from 0.008-inch-thick beryllium-copper sheet material. Figure IX-8 shows the die used to fabricate the diaphragm. The diaphragms were silver-brazed together to form a pressure-tight capsule and were then silver-brazed to the switchbox by induction heating. (See fig. IX-9.) Figure IX-3 shows the parts of the diaphragm switchbox assembly and the assembled unit. A fixture was constructed to position the diaphragm-switchbox assembly,

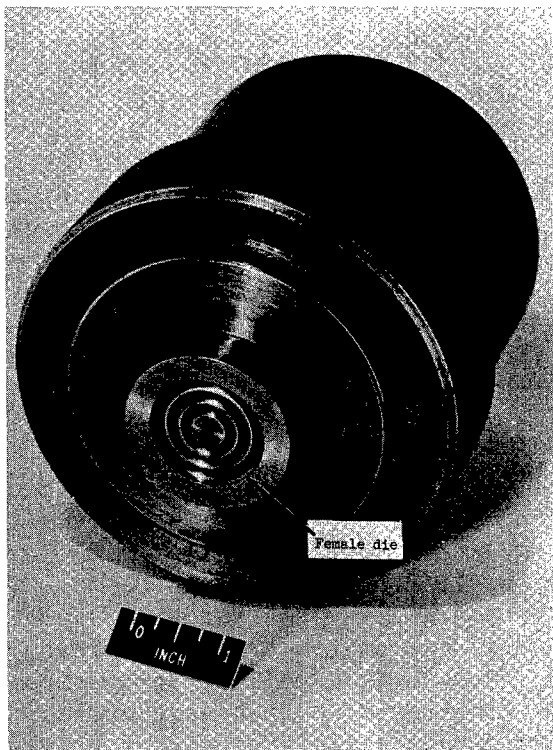


(a) Before bending. L-64-3092

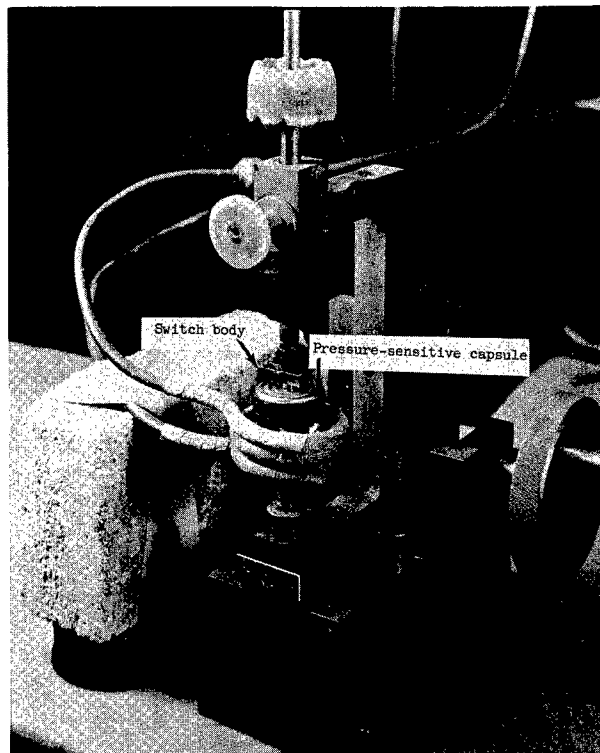


(b) After bending. L-64-3093

Figure IX-7.- Detector-base-end forming die.



L-62-334.1
Figure IX-8.- Detector pressure-sensitive diaphragm die.



L-62-340.1
Figure IX-9.- Induction-heating fixture for silver-brazing pressure capsule and switch body assembly.

fill-tube, and mounting feet while they were silver-brazed in place. A heat-treating fixture was designed and constructed to hold 10 complete base assemblies during the precipitation hardening cycle. The fixture held the critical surfaces in position during the stress-relieving and hardening cycle. (See fig. IX-10.) The age hardening of the beryllium copper was accomplished by controlling the temperature at 600° F for 3 hours.

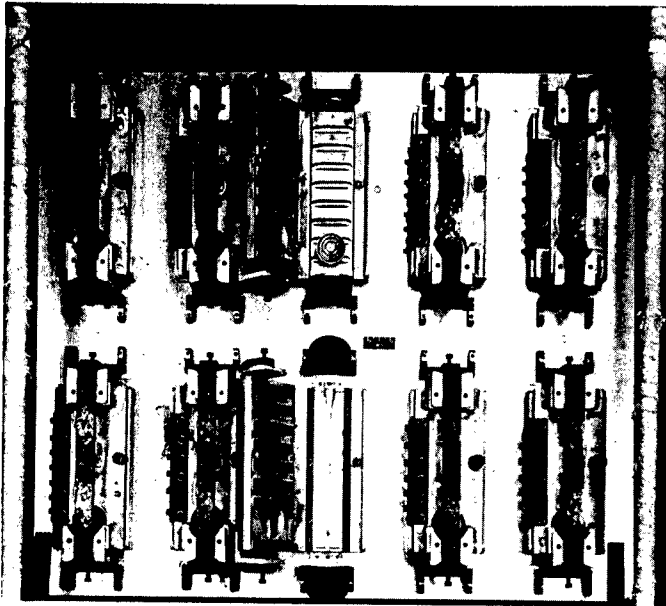


Figure IX-10.- Detector-base-assembly heat-treating fixture. L-62-342

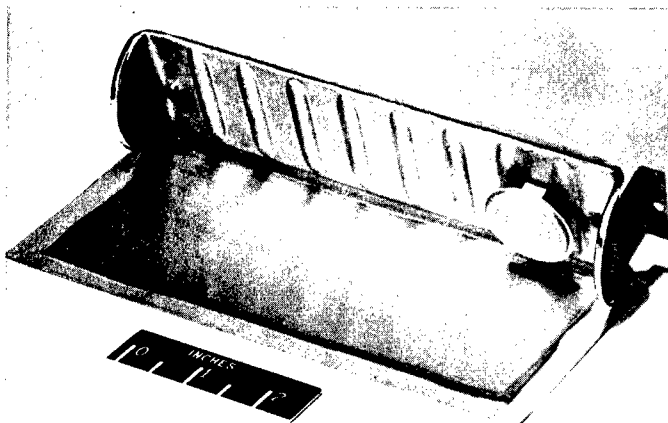


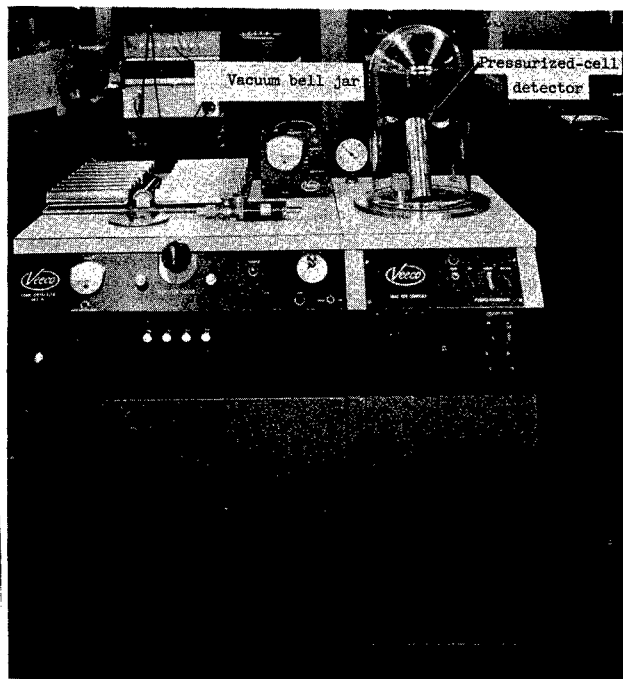
Figure IX-11.- Assembly of detector base and test material. L-62-335

After the heat-treating cycle was completed, the oxides were removed from the base assembly with a solution of phosphoric acid and then the edges were tinned with 100-percent-tin solder. The test material was tinned around the outer edge and then thoroughly cleaned of flux and foreign matter. The test material was wrapped on the base plate (see fig. IX-11), the joints were crimped and then sweat soldered in place. One-hundred-percent tin, which had a melting point of 450° F, was used to solder the joints.

The detector was charged with helium to a pressure of 25 psia after the fabrication and assembly were completed. The fill tube was used to admit the gas to the detector and was then sealed by mechanical crimping and soldering. Each detector was checked for leaks in the vacuum chamber of a helium leak detector (see fig. IX-12) and discarded if there was any indication of a leak. The sensitivity of the leak detector was sufficient to indicate a leak of 2×10^{-5} micron cubic feet per hour which would have given the pressurized-cell detector a lifetime of 3.5×10^4 years before leaking to the switch-actuation pressure. Pressurized-cell detectors that indicated no leak were marked with a serial number and complete records were maintained on each unit so marked throughout the test program. The last step in the construction program consisted of vapor depositing thin

films of aluminum and silicon monoxide on the detectors for temperature control in the space environment.

The pressure-sensitive-capsule switch assembly was designed so that the force-transmitting member and the pressure switch were installed on the outside of the pressure chamber. This eliminated the need for electrical and mechanical feed throughs in the pressure-chamber wall. Switch-actuation pressure could also be adjusted without disturbing any pressure seals in the chamber. The switch contacts were in a closed position until the sensor was punctured and the helium allowed to escape. This switching arrangement eliminated the possibility of foreign matter collecting on the contacts while the vehicle was being assembled, and allowed the switch-contact resistance to be monitored during the prelaunch checks.



L-62-337.1
Figure IX-12.- Pressurized-cell-detector leak-checking system.

SECTION III - ENVIRONMENTAL TESTING

Pressurized-cell detectors were exposed to numerous pressure and temperature cycles and vibration tests to yield information concerning the expected life of the detector. The thermal-design study of the vehicle indicated the maximum orbital temperature of the pressurized cells should be approximately 117° F and the coldest orbital temperature approximately 10° F. Since the pressurized-cell detector was sealed at 25 psia at 70° F, the pressure over the expected orbital-temperature extremes could have ranged from 22.2 psia to 27.2 psia. Pressure-cycling apparatus was set up to apply a linear pressure pulse between the pressures of 14 and 34 psi. A group of 12 detectors was exposed to 6,600 cycles to determine if there were any areas that showed metal fatigue. The helium leak detector indicated no leak in any of the tested detectors.

The ultimate strength of the detectors covered with 0.001-inch-thick material was tested by applying pressure until a rupture occurred. Ten detectors were tested and all failed within the pressure range of 65 to 75 psi.

Temperature-cycling apparatus consisting of a 260° F glycerin bath, a 70° F water bath, and a -10° alcohol bath was used to expose the detectors to a cyclic accelerated temperature test. The water bath was used between the hot glycerin and the cold alcohol bath. This served as a rinse since both alcohol

and glycerin were soluble in water and minimized the contamination of the baths. The water bath also brought the detector to an intermediate temperature and reduced the amount of thermal capacity required to maintain uniform temperatures in the baths.

A group of 10 detectors sustained 2,000 cycles through the baths without any failures. The temperature of the detectors was measured with thermocouples. The detectors were allowed to soak in the hot and cold baths until they were within 5° F of the bath temperature.

This type of testing subjected the detectors to thermal shock which was much more severe than would exist in the space environment. Although severe, this procedure was a means of obtaining a large number of temperature cycles in a relatively short period of time.

The pressure switch was set to actuate when the internal pressure reached 5 psig. The stability of the setting was checked through various stages of the environmental testing by placing the detector in a glass tubular pressure chamber. (See fig. IX-13.) Electrical connections from the detector were fed through the pressure chamber to an ohmmeter which monitored the switch actuation; the internal pressure of the detector was determined by noting the pressure applied to the chamber when the thin test material of the detector began to deflect. When the external pressure exceeded the internal pressure by only a



Figure IX-13.- Pressurized-cell detector switch-setting chamber.

L-62-336

few hundredths of a pound, large inward deflections of the thin test material would occur. All the pressurized-cell detectors used in the Explorer XIII payload were checked in this manner as well as in the helium leak detector after the payload environmental test program. Switch settings were within 2 percent of their initial setting in all cases, and there was no indication of any leak or loss of pressure in any of the detectors. Details of the payload environmental test program are covered in chapter VII.

SECTION IV - CALIBRATION

The pressurized-cell detectors used 16 time channels in the telemetering system to transmit the 160 bits of information. The information from 10 detectors was transmitted by each channel. The full-scale range of the telemetering channel was divided into 10 steps. Each time a detector switch opened, a permanent change of one step (approximately 10 percent of full scale) occurred in the telemetry channel. The telemeter zero- and full-scale values were transmitted each time a channel was read to indicate any changes that may have occurred from environmental temperature effects. Since the pressurized-cell-detector signal consisted of a switch opening, the temperature of the detector did not affect the accuracy of the telemeter. Continuous monitoring of the detectors by the telemeter (or use of a storage device) was not required because once the detector is punctured, the switch will remain in the open position, and the data are thus maintained in a nondestructive state. The telemeters could be turned on by a command signal from the ground station and would transmit data for approximately 1 minute before they were automatically cut off. A calibration of one of the telemetry channels containing 10 pressurized-cell detectors is shown in figure IX-14.

SECTION V - FLIGHT RESULTS

The payload was launched into orbit and information was telemetered and recorded through the twenty-ninth pass. There were no switch openings of the pressurized-cell detectors during this time. Data were processed

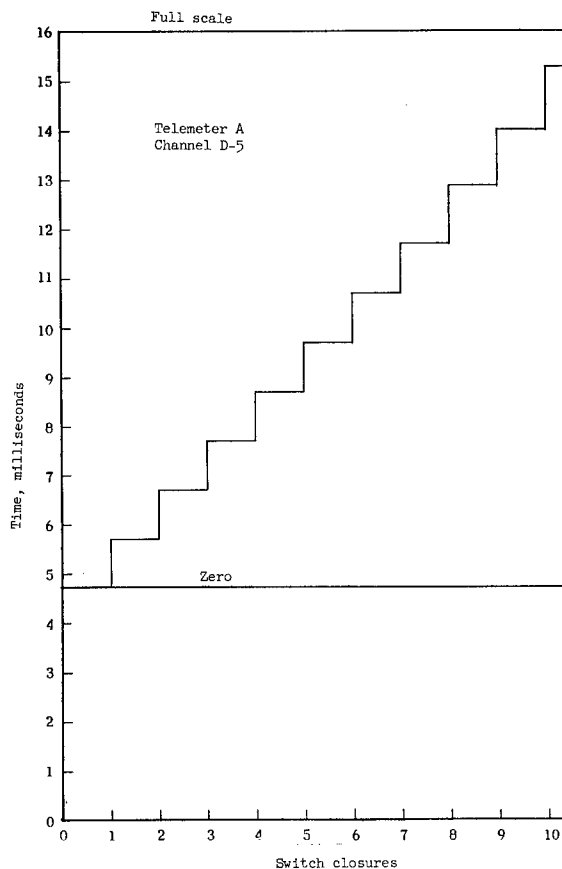


Figure 14.- Calibration of telemeter channel D-5 containing 10 pressurized-cell detectors. (These data are time coded on telemetry system.)

from tape recordings taken on orbits 1, 9, 13, 14, 15, 21, 22, 23, and 28. The last recording was taken 45 hours after launch. Pressure-cell temperatures recorded during the flight are shown in figure VI-10. The maximum temperature recorded was 133° F which occurred on the first orbit and the minimum temperature was 80° F which occurred in the fourteenth orbit. The temperature readings are taken during the time the telemeter is transmitting to the ground station which represents a small portion of the orbital time. With the limited number of temperature recordings, it is difficult to determine the maximum and minimum temperatures that were obtained during the flight. There was no indication of any malfunctioning of the 160 pressurized-cell detectors during the launch and orbital life of the vehicle.

CHAPTER X

COPPER-WIRE-CARD DETECTORS

By Luc Secretan
Goddard Space Flight Center

SECTION I - DESCRIPTION

Card Design.- Each copper-wire-card detector consisted of a winding of fine wire mounted to a 1.45- by 7.00-inch rectangular card. Two wire sizes were used - 2-mil and 3-mil (fourteen 2-mil cards and thirty-two 3-mil cards). The total exposed effective area was about 1.2 square feet (0.11 square meters). A sketch of a detector is shown in figure X-1. These detectors are similar to the detectors flown on previous satellites.

Quadrant Design.- The 36 cards are arranged in four groups of 12 cards each with four pairs of 3-mil cards in parallel and four single 2-mil cards in parallel. Each group is mounted on a fiber-glass support that can readily be removed from the payload for repairs or replacements with appropriate spares. Individual cards can be replaced readily if necessary. The assembly of the quadrants is shown in figure II-2.

Temperature-Balance Experiment.- The grids for the temperature-balance experiment were wound with insulated wire. The thermal balance of such a

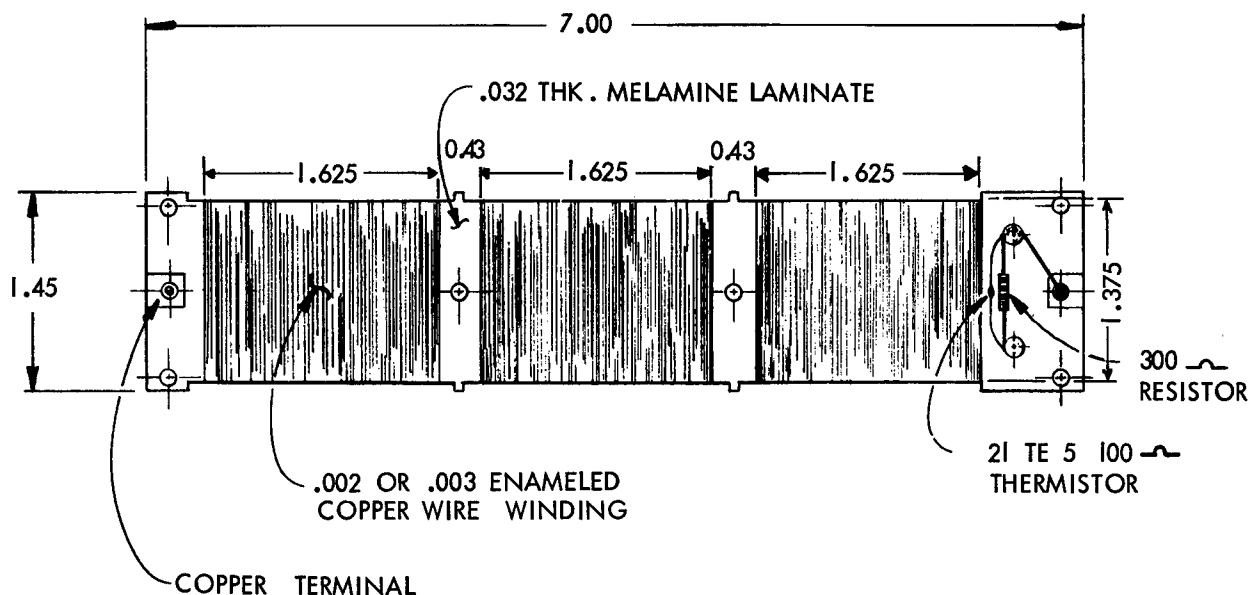


Figure X-1.- Copper-wire card detector. All linear dimensions are in inches.

winding has been examined under conditions approximating flight environment. One card of 3-mil wire with a thermistor attached was enclosed in a bell jar and exposed to the sun after evacuation. External radiation was reduced by shading the bell jar except for a window which allowed the sun's rays to strike the winding. The temperature of the thermistor was recorded at intervals. Figure X-2 shows that the temperature does not rise beyond 65° C in 20 minutes of continuous exposure to the sun. Complementary tests made by Dr. Roger E. Gaumer of Lockheed Aircraft Corp. give a ratio of absorptivity to emissivity of 1 for this type of enamel insulated wire.

Compensation for Resistance Changes.— Temperatures at the wire-card surfaces were expected to extend from -10° C to a maximum of 60° C. Since copper has a thermal coefficient of resistance of 0.33 percent per °C, the resistance of the wire would change 22 percent and a compensator had to be provided. A

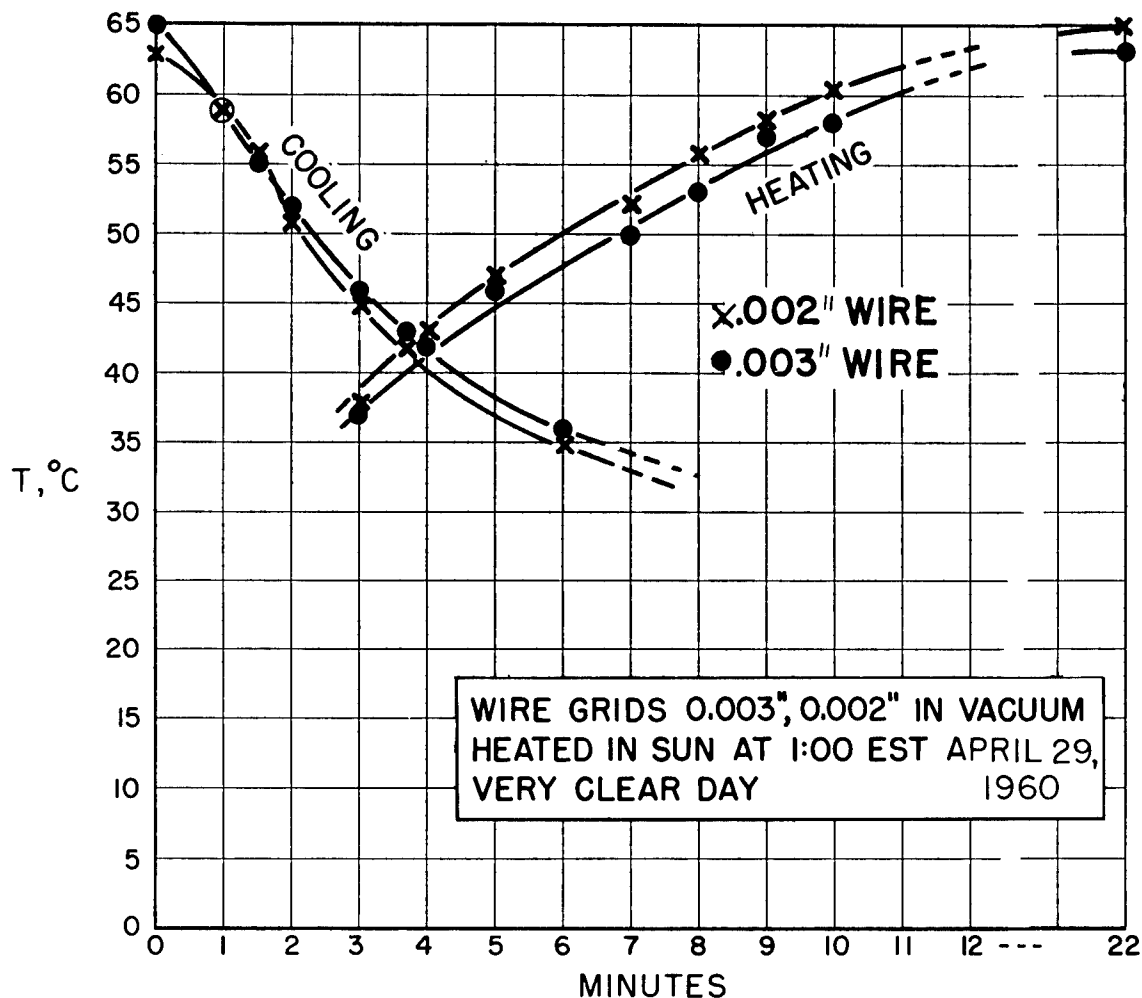


Figure X-2.- Thermal cycles of wire grids in sun.

100-ohm thermistor with a negative coefficient of -3.9 percent per $^{\circ}\text{C}$ was selected, wired in parallel with a 300-ohm fixed resistor and installed in series with each 2-mil card and with each pair of 3-mil cards. The effective resistance of 2-mil and 3-mil compensated cards is shown in figure X-3 for various temperatures and compared with the resistance of uncompensated copper. The increase in resistance from 20°C to 60°C is 12 ohms or 2.7 percent. Below 20°C the effective resistance also increases and the curve is similar to that obtained for high temperatures.

Since the telemetry was conceived so that the failure of one detector in a group of four would change the signal length (time coded data) by 10 percent of full-scale value, a resistance change of 3 percent resulting from temperature extremes would not cause a spurious signal. The resistance of individual cards varied somewhat from card to card, and the resistance of one of the 2-mil cards was only approximately equal to that of two 3-mil cards in series. Uniformity was obtained by adjusting all the cards of one quadrant to a common resistance value of ± 1 percent by adding small fixed resistors.

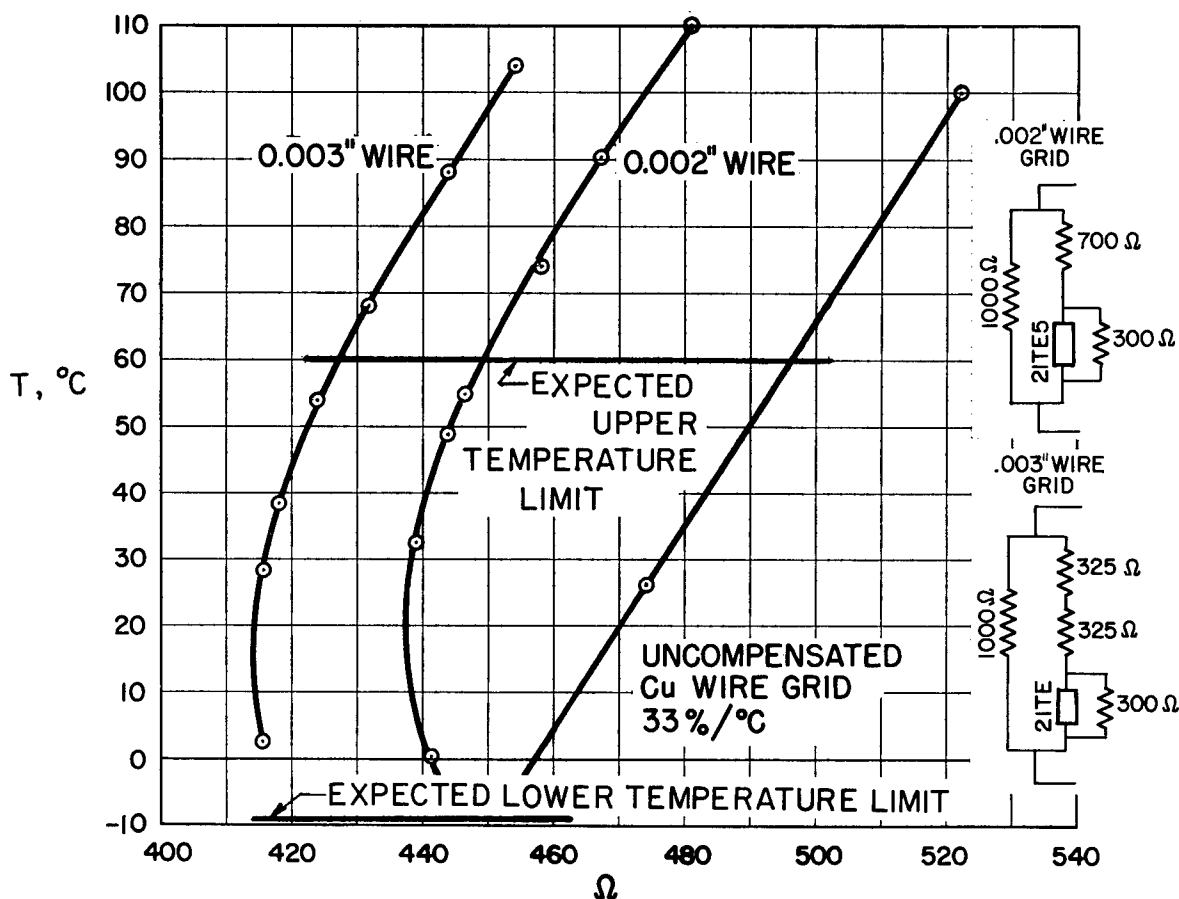


Figure X-3.- Resistance-temperature charts for wire grids.

SECTION II - RESULTS

The particle size required to break a wire was estimated to be one-half the size of the wire. Based on current estimates of the meteoroid influx rate, the required time for one break would be 24 days for the 2-mil wire cards and 120 days for the 3-mil cards. During the short life of the Explorer XIII, no hits were recorded in the $2\frac{1}{2}$ -day exposure to the space environment.

CHAPTER XI

CADMIUM-SULFIDE EXPERIMENT

By Luc Secretan
Goddard Space Flight Center

SECTION I - DESCRIPTION

The cadmium-sulfide sensors are designed to detect micrometeoroid particles too fine to damage heavy metallic hardware, but presumably present in sufficient numbers to damage sensitive surfaces. Cadmium-sulfide detectors of similar construction but of much smaller area have been used successfully on Vanguard satellites and on Explorer VII. On Explorer XIII, the useful area is 3.1 square inches or about 80 times that of the Vanguard cells.

Construction.- The construction shown in figure XI-1 is that of a mirrorized ellipsoidal flask; this geometrical body had two optical foci, so that a ray emanating from one focus would be concentrated at the second focus by the reflecting walls. To realize these conditions, the aluminized Mylar film was stretched in one of the focal planes while the cadmium-sulfide cell was mounted in the other. Should a micrometeoroid penetrate the opaque aluminized film, the rays from the sun would fall on the cell or be reflected on it from the mirrorized walls.

Calibration.- Each of the cells was calibrated as follows: The cell was covered by an opaque metallic cover provided with an elongated slot. The slot was then covered by a sliding blade pierced by a very small calibrated pinhole. Next, the assembly was mounted on a shaft actuated by a variable-speed motor and rotated in front of a Xenon-gas arc lamp to imitate the revolutions of the payload in the sun. A signal from the cadmium-sulfide cell, carried by collecting brushes and rings, indicated the response of the cell to the arc. (See fig. XI-2.) An investigation in sunlight verified the similarity between

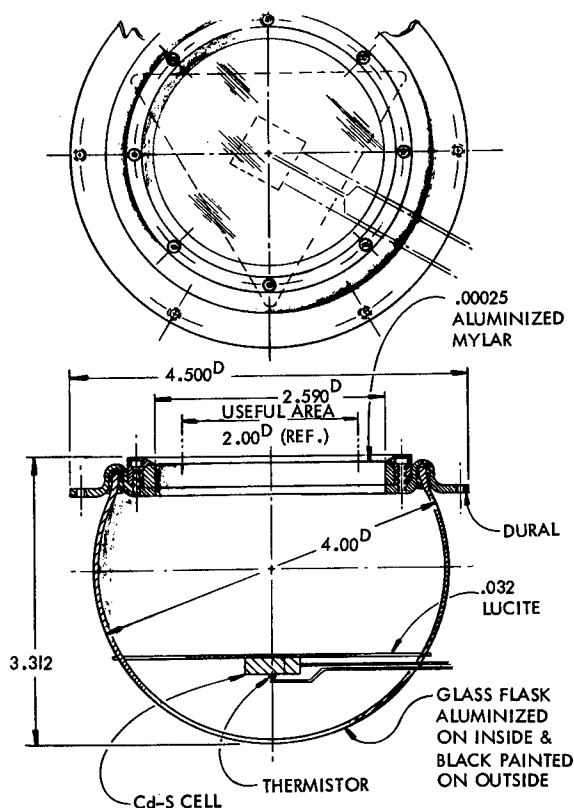


Figure XI-1.- Cadmium-sulfide-cell detector.
All dimensions are in inches.

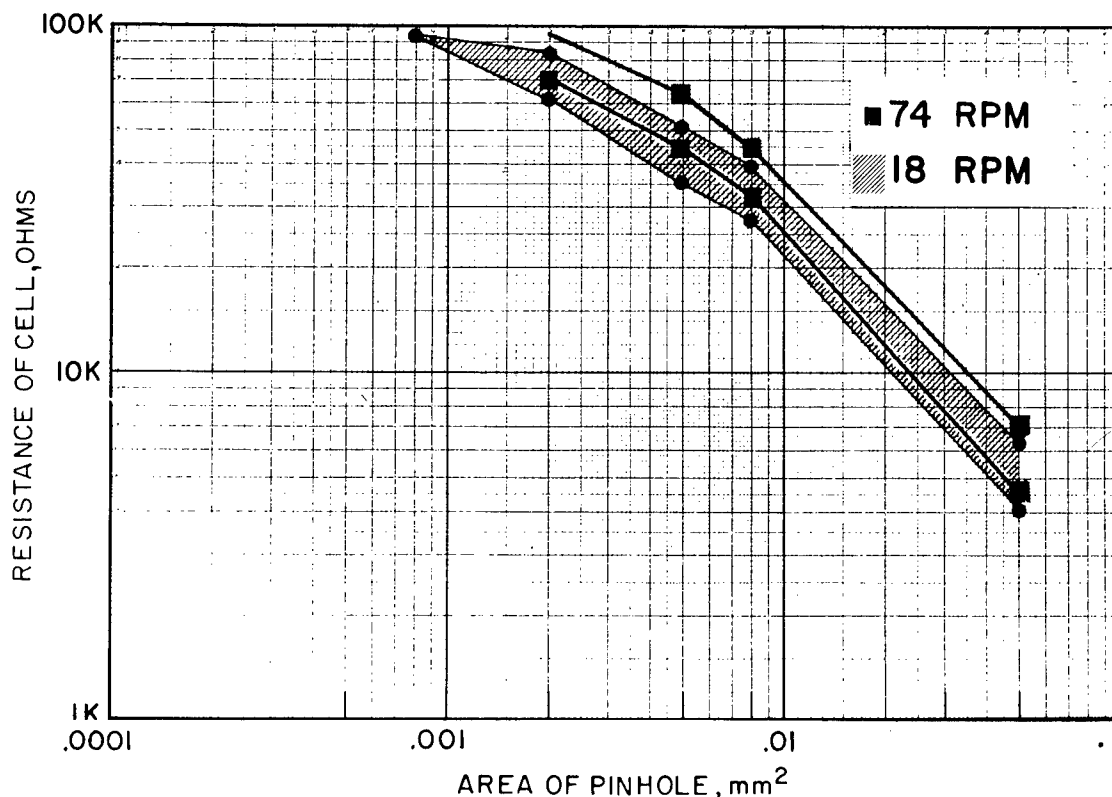


Figure XI-2.- Calibration of cadmium-sulfide cell.

the total radiant-energy input to the cell from the sun and from the arc. The slide with the pinhole was moved 1/4 inch at a time all the way across the diameter of the glass globe, and the response of the cell was noted at each stop. In order to diffuse the direct light from the pinhole to the cell and to equalize the sensitivity of the system from edge to edge, some white paint was applied to the front side of the cell.

SECTION II - RESULTS

The sensitivity of the cells was such that a particle about 1 mil (25 microns) in diameter could be detected. It was estimated that one hit by a particle this size would occur in about 20 days. As stated earlier in the report, the Mylar film ruptured during launch, and admitted a large amount of sunlight thus making the experiment inoperative. Postflight analysis and tests indicated that probable cause of failure was due to improper flask venting.

The glass flask described previously represents a volume of air that has to be evacuated as the satellite leaves the atmosphere. For this purpose a

vent hole had been provided through the rear of the flask into the large telemetry chamber. This, in turn, was vented to the outer space by series of large holes. Preliminary ground tests indicated that the aluminized Mylar film would not be torn by the expanding air, and that venting was adequate. A better plan has now been devised wherein the air is vented from the cell directly into the outer space. Ground tests have shown this new design to be adequate.

CHAPTER XII

IMPACT-DETECTION EXPERIMENT

By Alfred G. Beswick
Langley Research Center

SECTION I - INTRODUCTION

A meteoroid-particle impact-detection experiment was included as one of the secondary experiments of the Explorer XIII satellite. Its main purpose was to extend micrometeoroid measurements to a low population range where few data exist. An additional purpose was to correlate with and to augment the data amassed by previous satellites employing similar experimental technique. Impact detectors having three threshold levels of momentum sensitivity, nominally 0.01, 0.1, and 1.0 gram-centimeter per second, were provided to meet these objectives.

An impact detector consists of an impact-sensitive detecting surface with an attached transducer, and signal-conditioning, impact-event counting, and count-storage circuitry. Two physical configurations of detecting surface were used. One configuration was a pair of stainless-steel plates having total geometric area of 0.142 square meter mounted on the conical portion of the satellite forward shell and used for the high and the low sensitivity impact detection. The twenty 0.005-inch-thick pressurized-cell penetration detectors were also sensitized for impact detection and formed the second type of detecting surface. This configuration had a detecting surface area taken as 0.186 square meter and was used for intermediate sensitivity impact detection.

SECTION II - IMPACT-DETECTION-SYSTEMS OPERATION

The operation of the meteoroid-impact-detection systems depended upon the development of a propagating mechanical perturbation due to meteoroid particle impact upon a detecting surface. Figure XII-1 is a block diagram of the elements of the pressurized-cell impact-detection system, and figure XII-2 is a block diagram of the elements of the curved-plate system. The figures indicate the manner in which the transducer elements of the detecting surfaces were arrayed. The operations and functional elements of both systems are essentially the same. As indicated by figures XII-1 and XII-2, particle impact upon a detecting surface produces a propagating mechanical perturbation which is transduced to a representative electrical signal by the piezoelectric element attached to the underside of the surface. Figure XII-3 shows oscilloscope photographs of typical calibration impact signals. The transducer impact signal is routed to signal-conditioning circuitry and then to impact-event counting and count-storage circuitry.

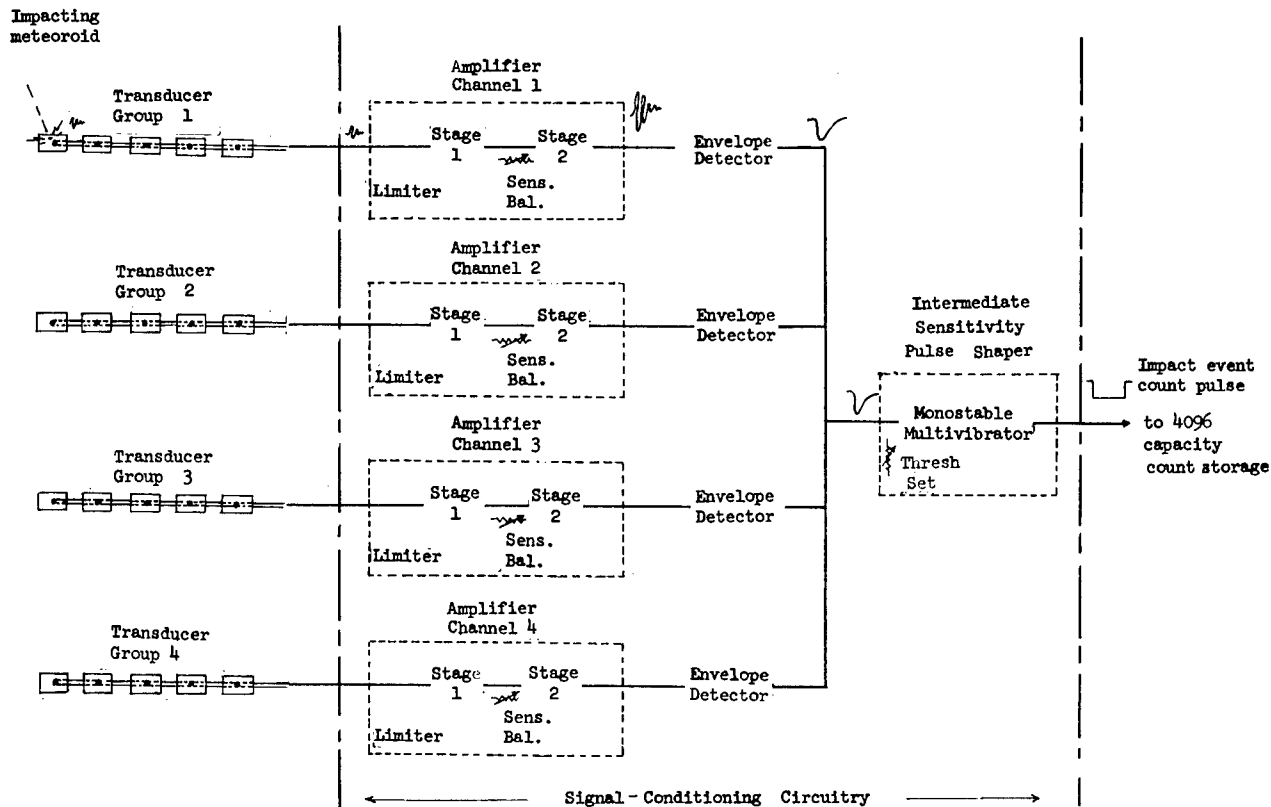


Figure XII-1.- Block diagram of pressurized-cell impact detection system.

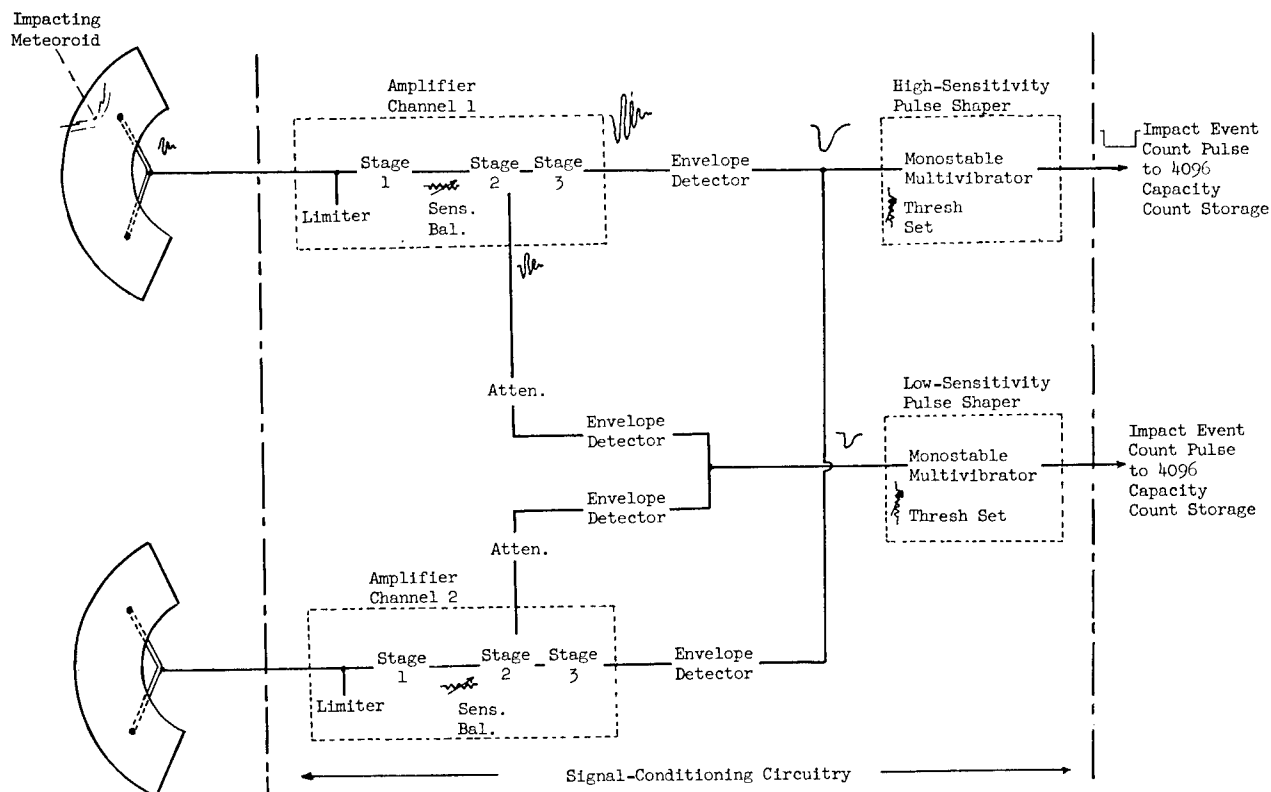


Figure XII-2.- Block diagram of curved-plate impact detection system.

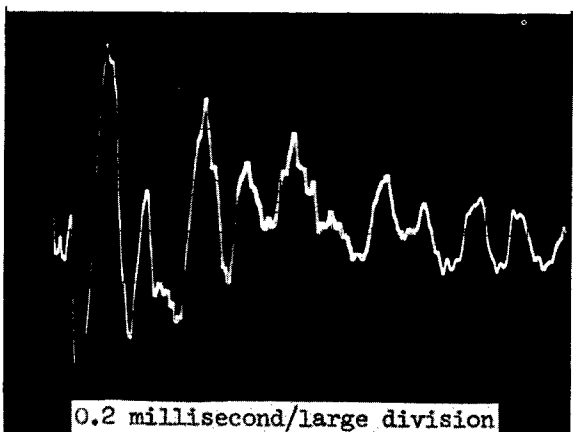
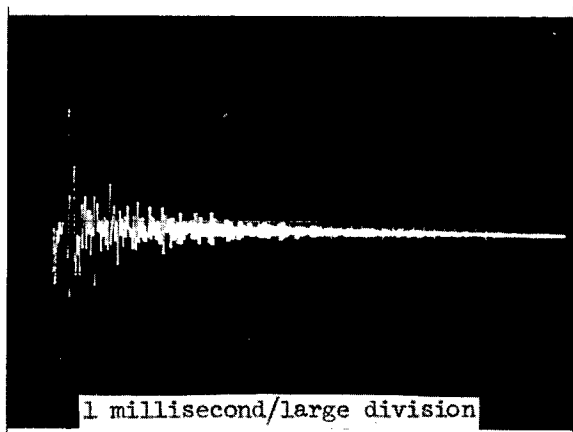
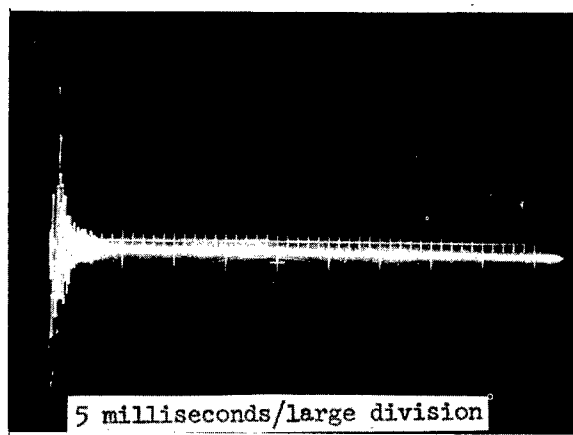


Figure XII-3.- Oscilloscope photographs of typical calibration impact signals.

The impact-detection-signal conditioning circuitry consists of a broadband amplifier and envelope detector, interconnection circuitry and a monostable multivibrator pulse shaper. Each transducer array has a separate amplifier and envelope detector channel.

The amplifier increased the transducer signal amplitude by a factor depending upon the required detection sensitivity. After amplification, the signal was applied to the envelope detector where it was rectified, and its high-frequency components filtered out. The impact signal at this point was then a replica of the negative half of the envelope of the signal originally developed by the piezoelectric element. The envelope detectors of each amplifier channel were paralleled by interconnection on their output side. Thus, a signal from any of the transducers of a given detecting-surface array could be treated by just one pulse-shaping circuit.

The signal was then applied to the input of the monostable multivibrator pulse-shaper circuit, the voltage bias level of which, in combination with the signal amplification factor, defined the detection-sensitivity threshold; sufficiently large signal amplitudes triggered the multivibrator which then executed its cyclic excursion; signal amplitudes below threshold level were not recognized.

The output signal of the multivibrator pulse-shaper circuit was the impact-event counting pulse. Its constant parameters provide a better form of input signal for the counting and storing circuitries than the originally transduced impact signal. The status of the impact event-counting and storage circuitries was telemetered whenever the satellite

transmitted its data. Thus, the number of impacts accumulated between data transmissions could be determined from the received data. Details of the circuitries which accomplished the impact event counting and count storage will be found in chapter IV of this compilation.

SECTION III - DESCRIPTION OF INSTRUMENTATION

Description of the instrumentation of the meteoroid-impact-detection experiment is divided into three parts: the impact-detecting surface arrays and their attached transducers, the associated electronic signal-conditioning circuitries, and the impact event-counting and count-storage circuitries.

Detecting Surfaces and Transducers.-- The impact-sensitized detecting surfaces were arrayed in two forms. Figure XII-4 is a photograph of the stainless-steel curved-plate detecting surfaces showing the location of a pair of electrically paralleled transducer assemblies on the undersurface. These detecting surfaces were fixed to the satellite forward shell by raised acoustic isolator stand-offs. Figure XII-5 is a photograph of one of the pressurized-cell

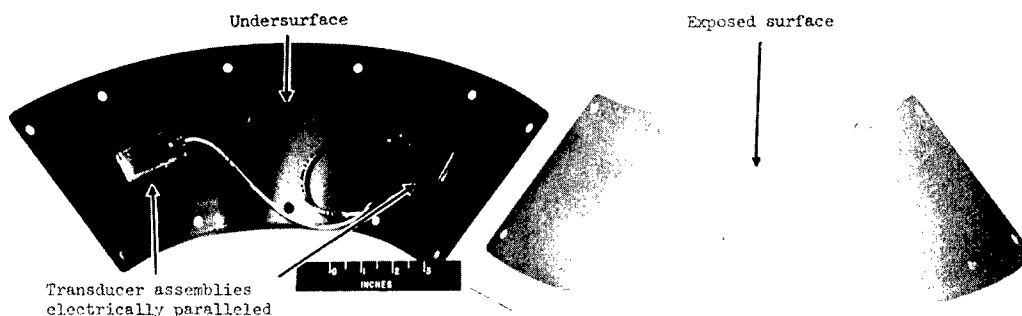


Figure XII-4.- Stainless-steel curved-plate detecting surfaces. L-62-8817.1

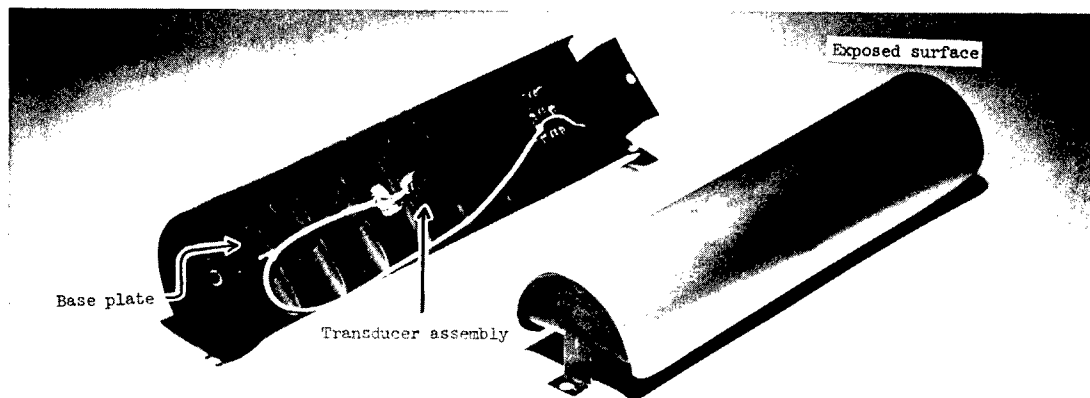


Figure XII-5.- Impact-sensitized pressurized cell. L-64-1980.1

detectors showing the location of the impact sensitizing transducer assembly on its base plate. The 20 impact sensitized pressurized-cell detectors were distributed on the satellite periphery as shown schematically in figure IV-22. Table XII-I lists the pertinent physical parameters of the two configurations of detecting surfaces.

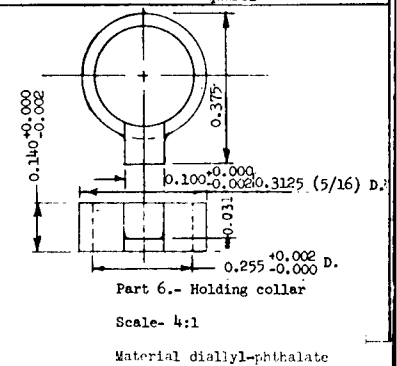
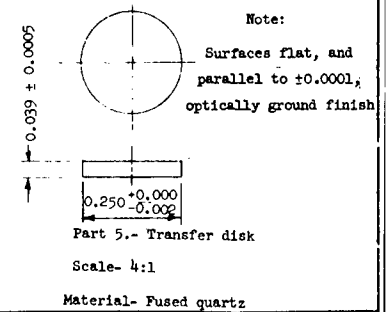
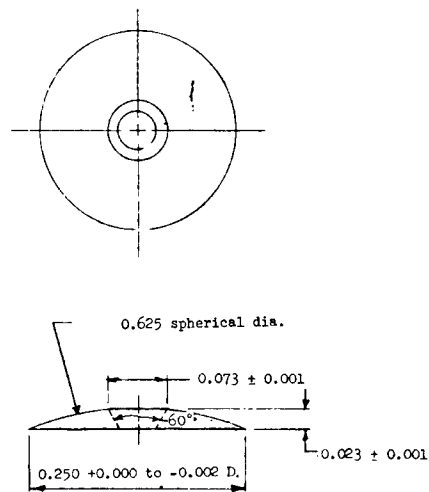
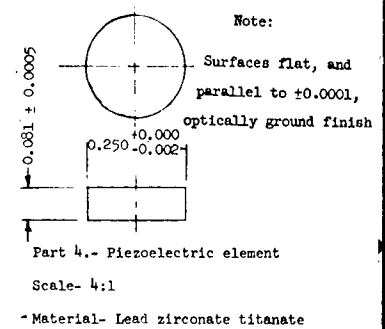
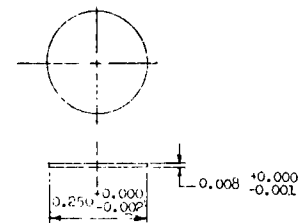
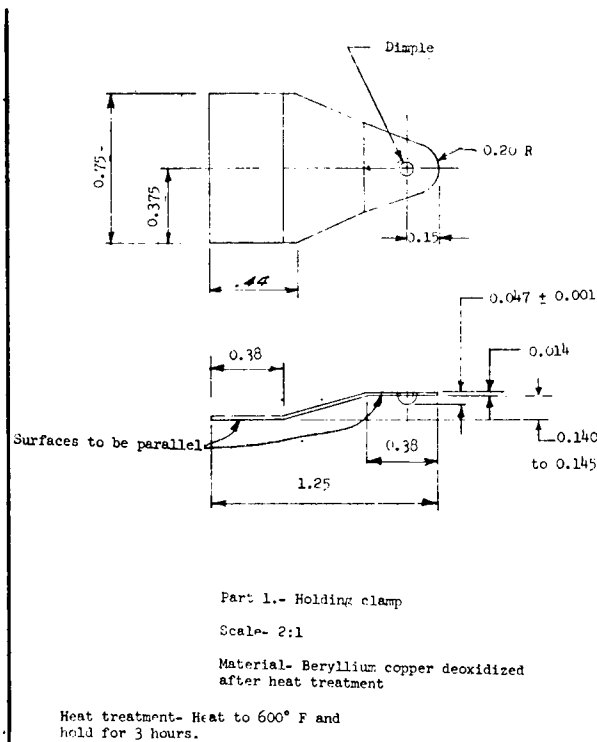
The impact-sensitizing transducer assembly was the same for both types of detecting surfaces. Figure XII-6 is a drawing of the components of the assembly. The sensitive element of the transducer assembly was the lead-zirconate titanate piezoelectric disk, part 4 of figure XII-6. This element was operated in a prestressed thickness expander mode, and the electrical signal resulting from particle impact was taken across the disk flats by the electrodes, part 7. The static loading was supplied by the cantilever spring, part 1, which also had the function of holding the assembly in place. The fused quartz transfer disk, part 5, coupled the impact perturbation signal to the piezoelectric disk, while maintaining electrical isolation from the satellite structure. The insulator disk, part 3, preserved electrical isolation and also served as a spacer. The transducer assembly was keyed in place by the dimple in the cantilever spring tip, which rested in the depression on the top of the domed brass locating disk, part 2. The thickness of part 2 was varied to adjust the static loading on the piezoelectric element to a desired value for each assembly. The assembly was prevented from gross lateral movement by the diallyl-phthalate holding collar, part 6, which had a slot for leadout of the electrodes. The curved-plate detecting surface transducer assemblies were covered by an electrical interference shield and dust cover.

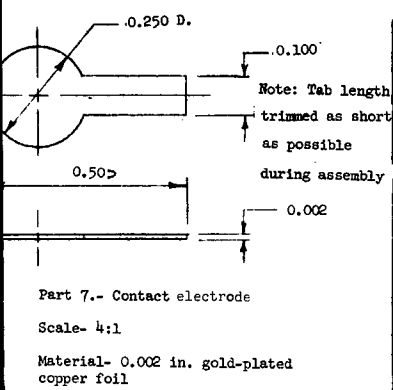
Tests showed that the transducer assemblies could be operated in electrically paralleled groups without significant detriment. Thus, the transducers of the 20 pressurized-cell detectors were interconnected in groups of five cells each. Each curved-plate detecting surface employed an electrically paralleled pair of transducers in order to improve its response uniformity.

Signal-Conditioning Circuitries.- The impact signals from the detecting surface transducers are sharply damping oscillations (fig. XII-3), and their predominant frequency components range from 5 to 40 kilocycles. Such signals required conditioning to become compatible with the data storage and telemetry systems of the satellite. The signal-conditioning circuitry consists of a broadband amplifier, an envelope detector, and a pulse shaper. Since the signal-conditioning circuitries are continuously powered in orbit, a minimum power-consumption design was required.

Each of the two detecting surface configurations has its signal-conditioning circuitry constructed in a separate modular package. Thus, there are four amplifier channels and envelope detectors in the impact-sensitized pressurized-cell signal-conditioning circuitry module, and two amplifier channels in the curved-plate detecting-surface signal-conditioning circuitry module. Figures XII-7 and XII-8 are photographs of the pressurized-cell and curved-plate signal-conditioning-circuitry modules, respectively.

Figure XII-9 is a schematic diagram of the signal-conditioning circuitry of the impact-sensitized pressurized-cell detectors. The four amplifier and envelope detector channels associated with the four transducer groups are shown





Part	No. req'd	Part description
1	1	Holding clamp
2	1	Dome
3	1	Insulator spacer, mica
4	1	Piezoelectric element
5	1	Transfer disc
6	1	Holding collar
7	2	Contact electrode

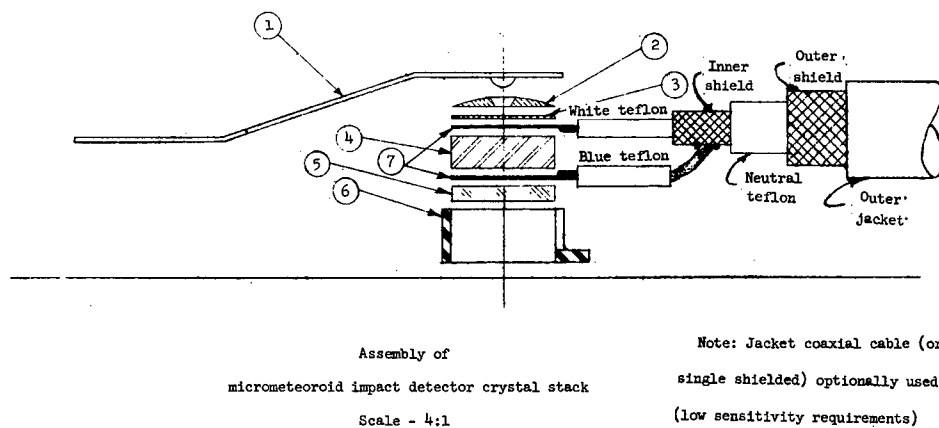
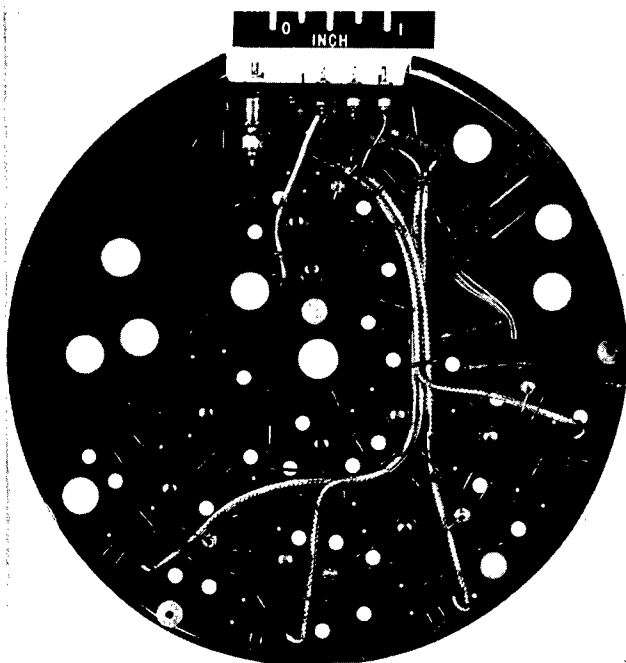
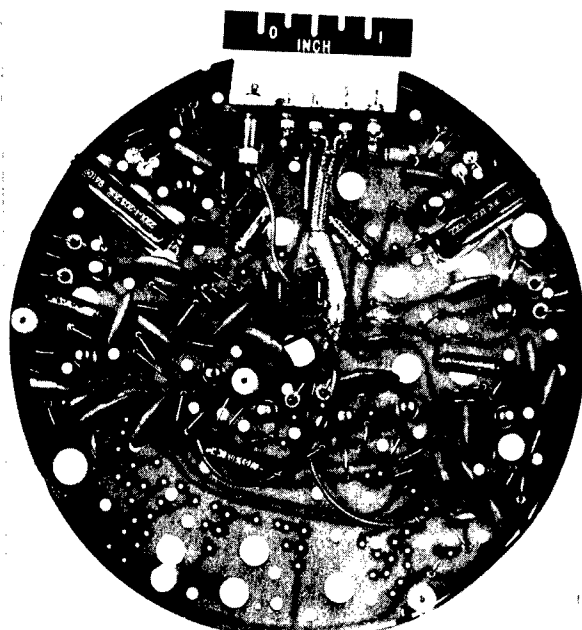


Figure XII-6.- Impactor detector transducer detail and assembly.



L-61-2022
Figure XII-7.- Signal-conditioning circuitry module for impact-sensitized pressurized cells.



L-61-2023
Figure XII-8.- Signal-conditioning circuitry module for curved-plate impact detecting system.

in figure XII-9. The input to the amplifier portion of each channel has a low pass filter to exclude radio-frequency signals and a shunt-diode limiter to prevent excessive transducer signals from possibly damaging the input transistor. The two amplifier stages are operated at fixed bias voltages, by-passed emitters, and very low quiescent collector currents. Equalization of transducer signal amplitude is provided by a variable resistance in the second amplifier stage. The amplifier section has a voltage amplification factor of about 900:1. Frequency-response and gain-linearity characteristics for this amplifier are shown in figures XII-10 and XII-11, respectively. A double-diode half-wave rectifier and shunt capacitor is used as an envelope detector to rectify and smooth the amplified signal at the output of each amplifier channel. The outputs of the four channels are interconnected following the envelope detectors, and signals from each channel are thus applied to the monostable multivibrator pulse shaper. The multivibrator will only respond to signals having amplitudes equal to or greater than the bias voltage level at its input, thus, a sensitivity threshold is established. When it is triggered, the multivibrator pulse shaper generates a signal of constant duration and amplitude, which has a short rise time. The duration of the multivibrator cycle is sufficient to prevent it triggering more than once by a single impact event. The constant parameters of the multivibrator output pulse, i.e., the impact events count pulse, provide uniform input signals to the counting and data storage circuitries which follow. Such uniformity does not exist in the normally variant parameters of transducer signals.

Figure XII-12 is a schematic diagram of the signal-conditioning

circuitry of the curved-plate impact-detecting surfaces. This circuitry employs two amplifier channels, one for each of the two curved-plate detecting surfaces. Each amplifier channel has three stages of gain and a voltage-amplification capability of about 20,000:1. The outputs of the third stages of the two amplifier channels are applied to envelope detectors. The envelope detector outputs are combined by interconnection and are applied to the threshold selection circuit at the input of the high-sensitivity monostable multivibrator impact-event-counting pulse generator. In addition, this signal-conditioning circuitry has provision for a second lower sensitivity threshold of impact detection. The lower sensitivity threshold is determined by applying the transducer signal from the second stage of each amplifier channel to a second low-sensitivity envelope detector. The output sides of the secondary low-sensitivity envelope detectors are also combined by interconnection, and signals at this point are applied to a second low-sensitivity monostable multivibrator pulse-shaper circuit. If the signal amplitude from the low-sensitivity envelope detectors is sufficient at the input to the second multivibrator, both the low- and high-sensitivity multivibrators will be triggered and cycle. Thus, a dual, high- and low-sensitivity threshold capability exists in the curved-plate impact-detection system signal-conditioning circuitry. The low-sensitivity threshold of impact detection was set to about 1/100th of the high-sensitivity threshold.

Both signal-conditioning circuitry modules provide test points at amplifier output stages and multivibrator input stages for monitoring of calibration signals during flight-qualification testing. The power-supply input is filtered and each amplifier stage is decoupled. Each circuitry module is entirely enclosed within a copper case, which is single-point connected to the satellite's power-supply ground-reference point. Each unit consumes less than 25 milliwatts of power.

Impact-Event-Counting and Count-Storage Circuitries.- The output of the signal-conditioning circuitry of each threshold level of sensitivity of the impact-detection experiment was applied to impact-event-counting and count-storage circuitries. There were three independent counting and storage circuitries, one for each of the three impact-detection sensitivity-threshold levels. Each count-storage circuit had a capacity of 4,096 counts before recycling. As previously mentioned, details of the impact-event-counting and count-storage circuitries are found in chapter IV.

SECTION IV - CALIBRATION

The calibration of the impact-detection experiments determined their response characteristics to impacts of known momenta. The average sensitivity of a detecting surface was determined by measuring its response to many impacts at various points on the surface. The appropriate correction to this average sensitivity was made by applying a correction factor derived from the restitution increment of the calibrating impact. Signal-conditioning-circuitry response to calibrating impacts was determined with respect to the varying supply voltages and circuitry temperatures anticipated in orbital flight.

From impact-sensitized pressurized-cell group

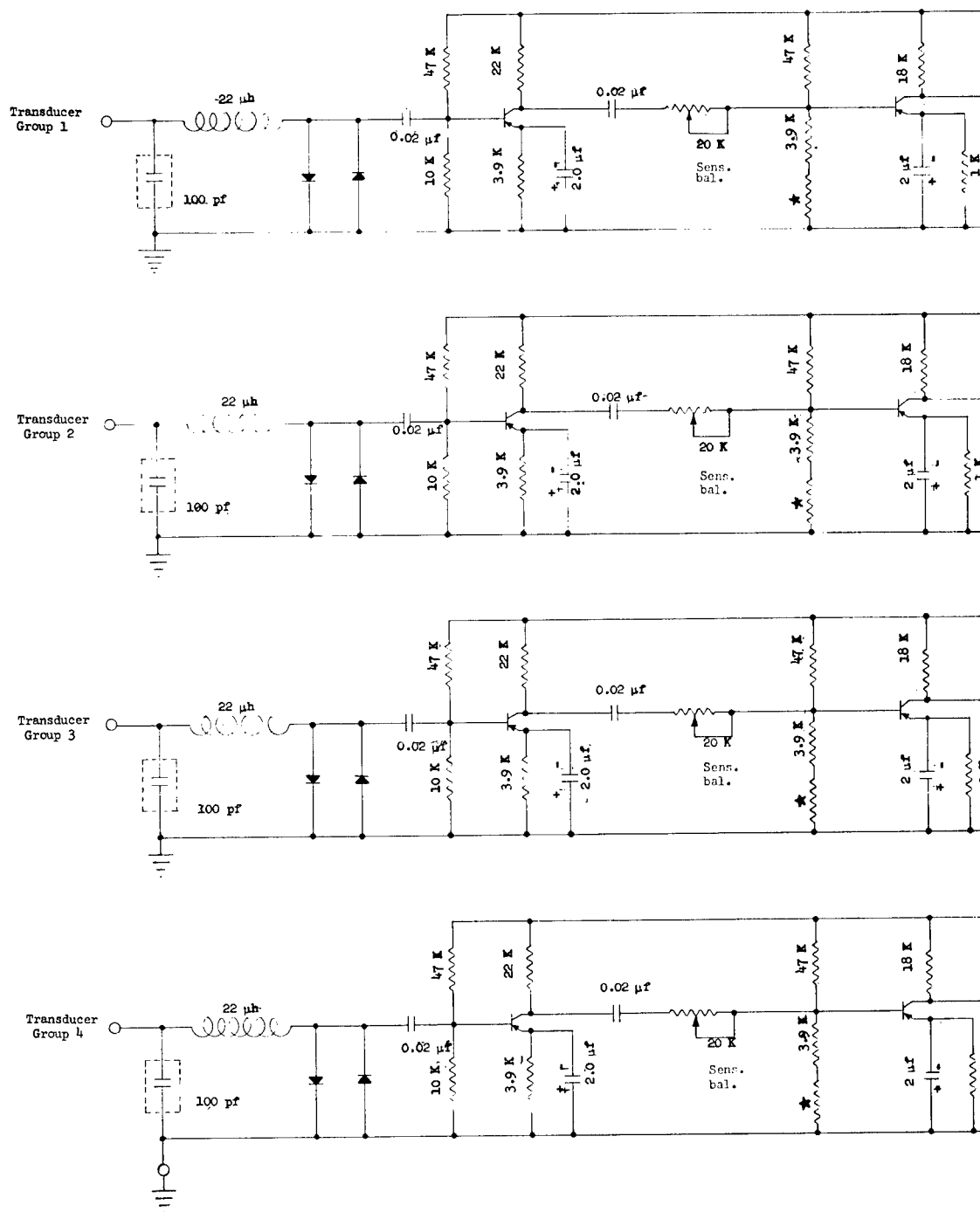
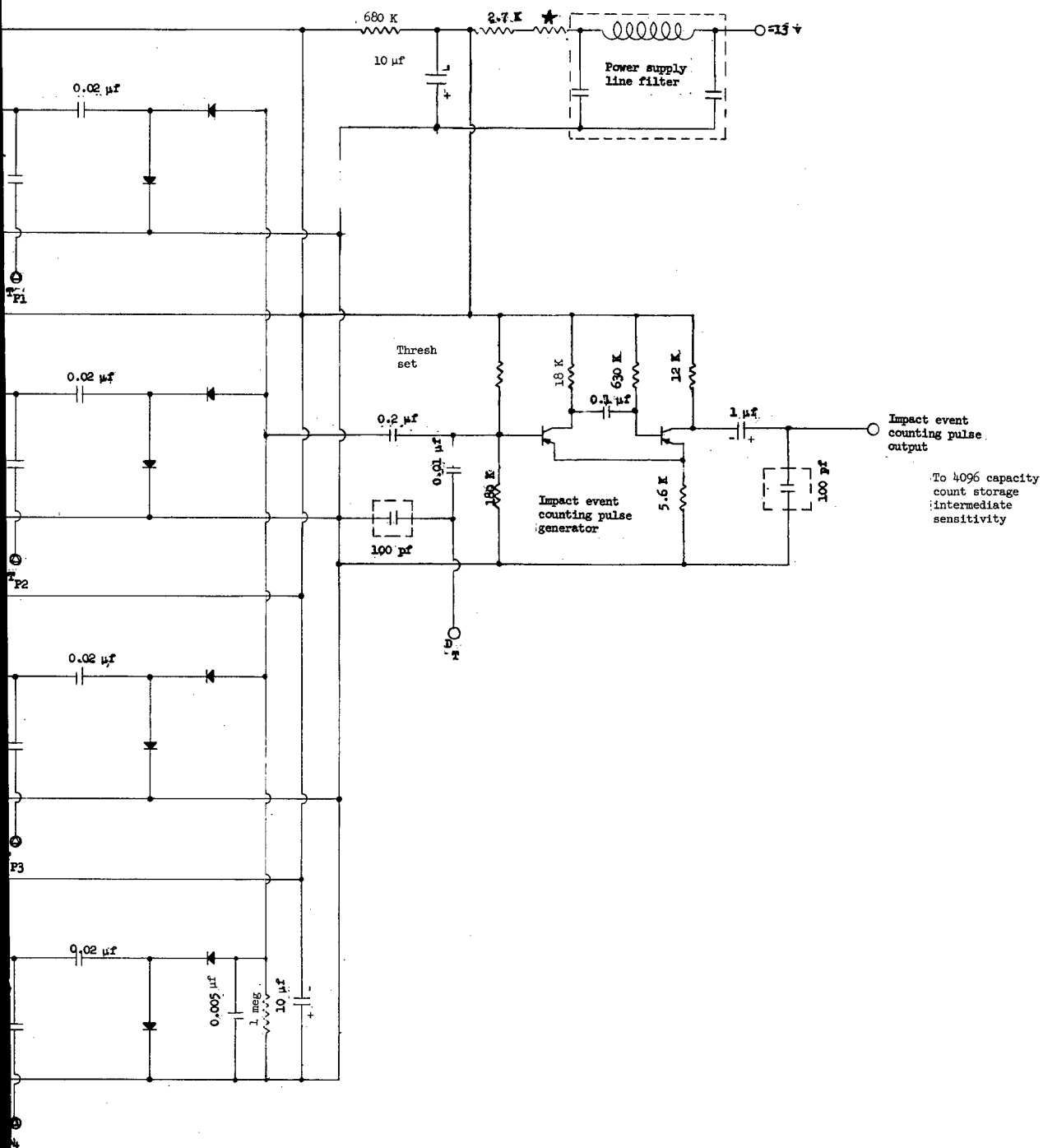


Figure XII-9.- Schematic diagram of signal-conditioning for impact sensitized pressurized cell.

starred resistance va



transistors type 2N393; all diodes type 1N626; TP1, TP2, TP3, TP4, leads removed after testing;
 selected during calibration.

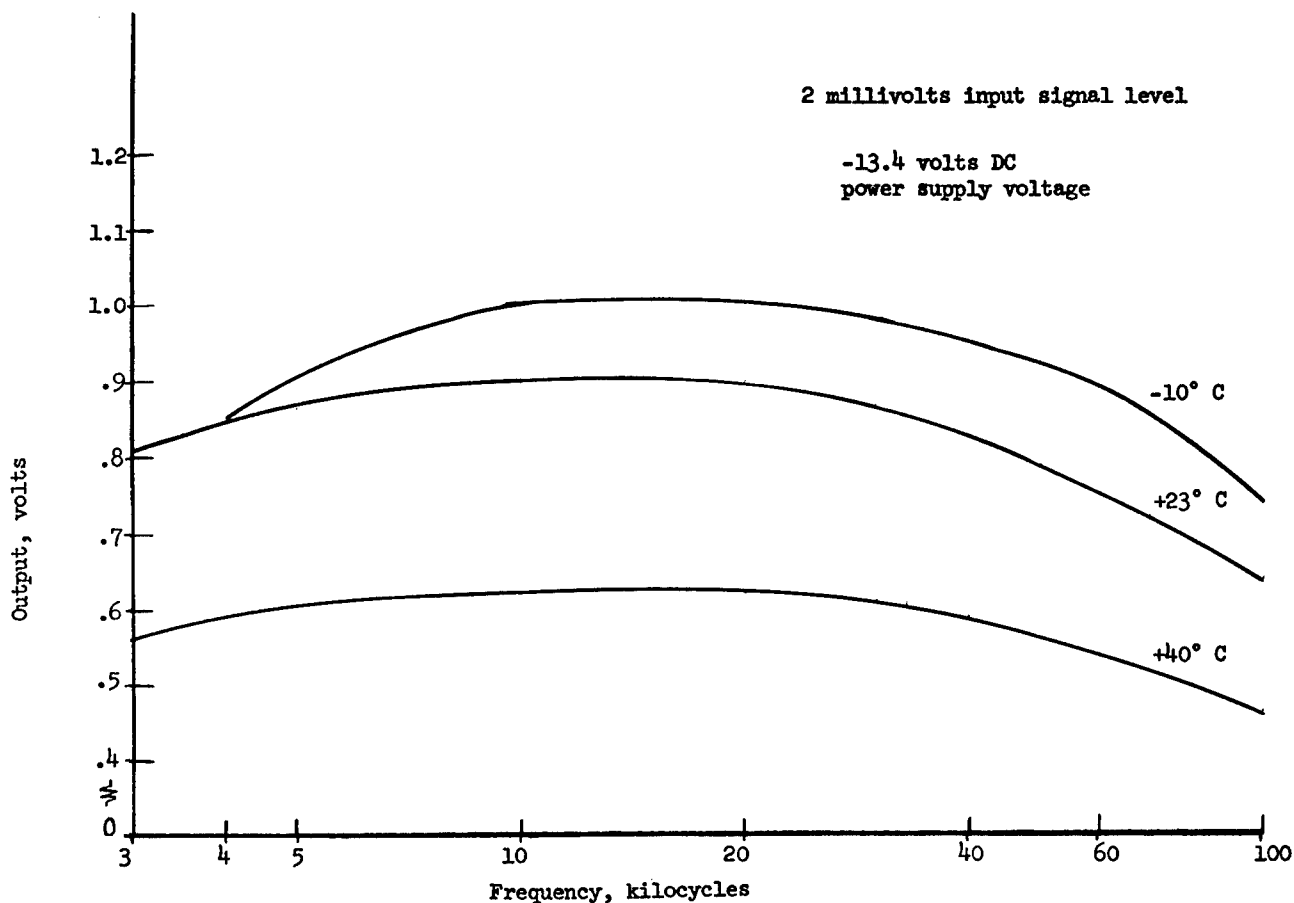


Figure XII-10.- Frequency-response characteristics of impact-sensitized pressurized-cell signal-conditioning circuitry.

The impact-calibration techniques employed particles of known mass falling upon detector surfaces through known heights, so that impact momenta were known. Linear response to impacting-particle momenta was assumed for this experiment. This assumption was in accordance with the practice of other United States experimenters performing similar experiments on satellites. The calibrating particles employed were spheres of aluminum oxide, of synthetic ruby and sapphire quality, ranging from 135 micrograms to 16.1 milligrams in mass. Dropping heights were accurately controlled, and were varied as required to obtain specific values of impact momenta. Drop heights were kept low, so that the effect of drag upon calculated momenta was negligible.

Figure XII-13 is a photograph of the manually operated calibrating mechanism employed in impact calibrations. The calibrating particles were positioned on the glass plate and gently pushed over its undercut beveled edge, designated by the arrow in the figure. The particles then fell through the known height onto the detecting surface positioned below. The manual-impact calibration technique produced consistently uniform transducer output provided the drop procedure was carefully controlled to minimize tangential and spin components of

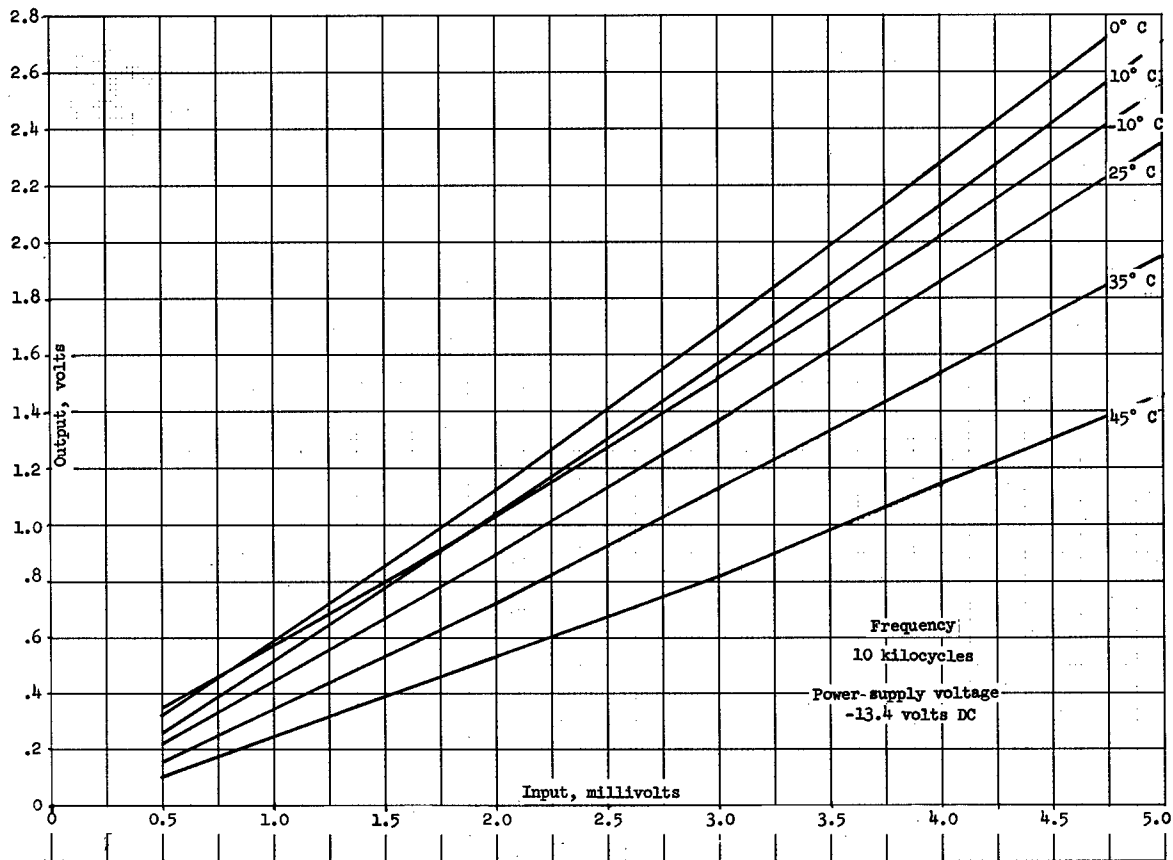


Figure XII-11.- Gain and linearity characteristics of impact-sensitized pressurized-cell signal-conditioning circuitry.

the impact-momentum vector. A very troublesome factor in the calibration of detecting surfaces was foreign matter in the path between the impact site and the piezoelectric element of the transducer assembly. Debris in this path produced unpredictable variations in transducer response to impact but was found to be avoidable by careful attention to cleanliness in both transducer assembly and calibration procedures.

A special test fixture was employed to measure the relative voltage sensitivities of the piezoelectric elements employed in transducer assemblies. The piezoelectric elements were then selected so that the electrically paralleled transducer assemblies in each transducer group were matched in impact sensitivity.

Special signal-conditioning circuitry was employed in the qualification and calibration of detector surfaces and transducers. The special circuitry was electrically identical to flight-model circuitries but provided additional test points for measuring impact-signal parameters and signal-conditioning-circuitry performance. The peak amplitude of the negative half of the amplified impact-signal envelope was monitored as the measure of the response of detecting surfaces and transducer assemblies to impact momenta.

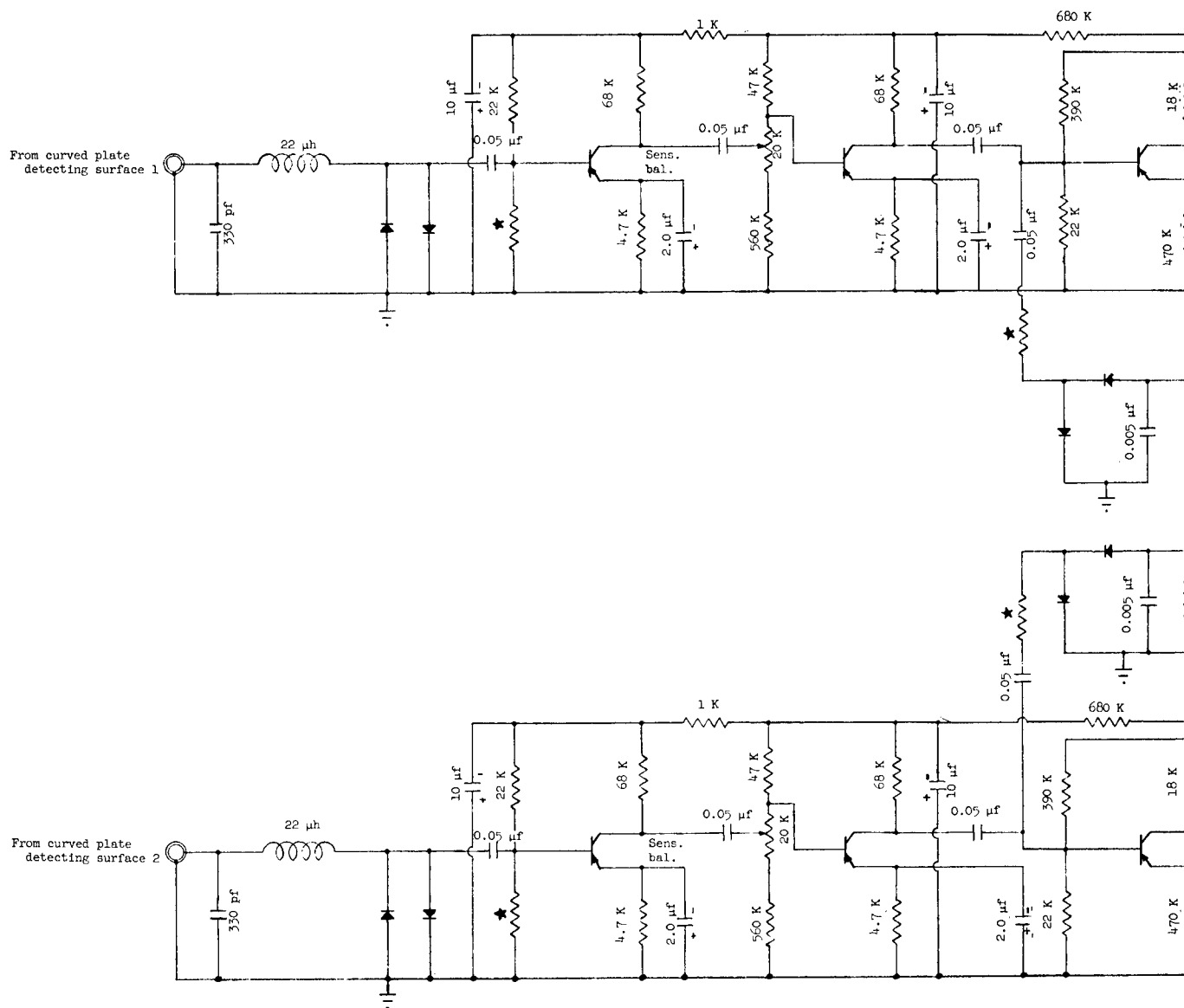
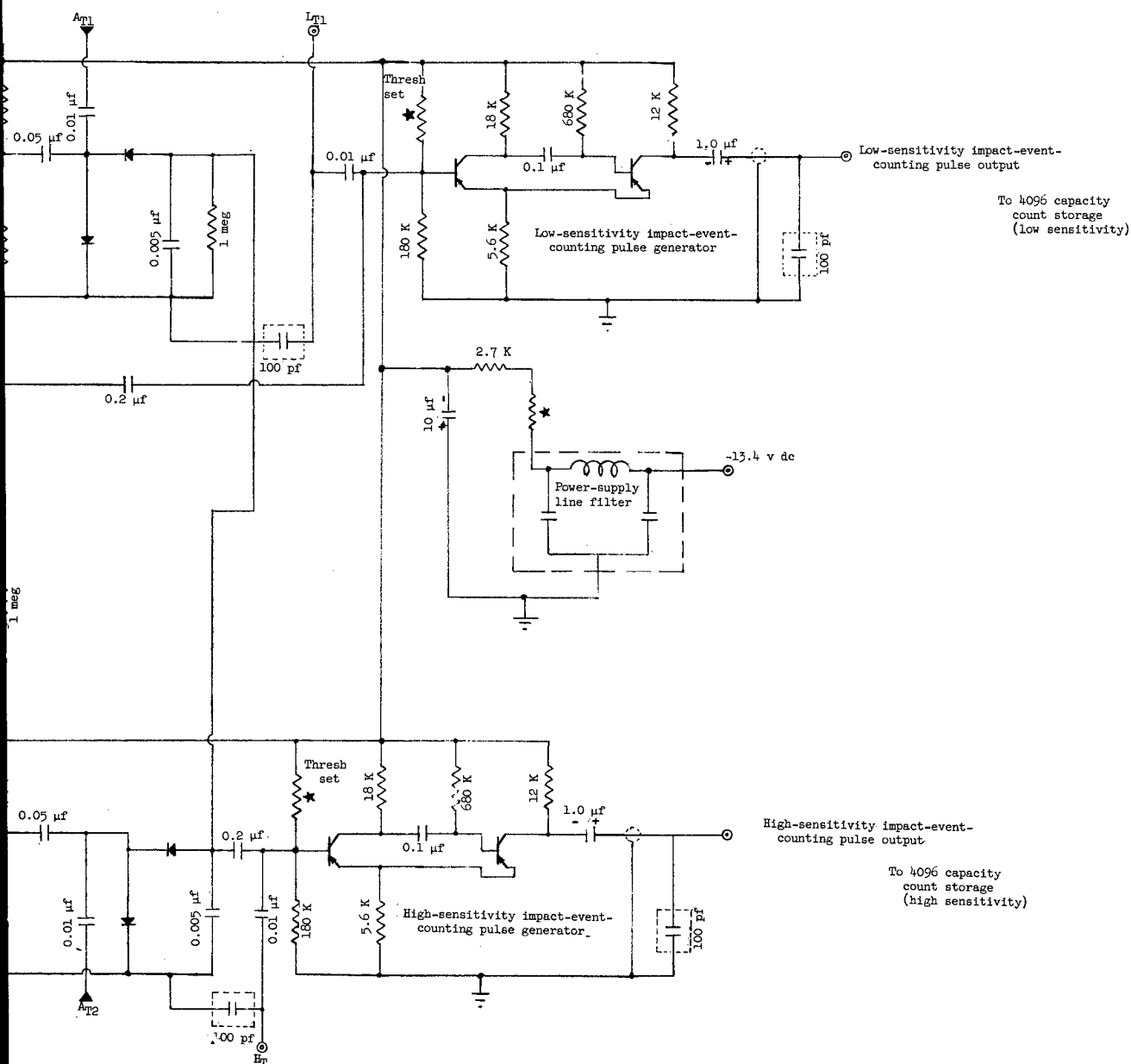
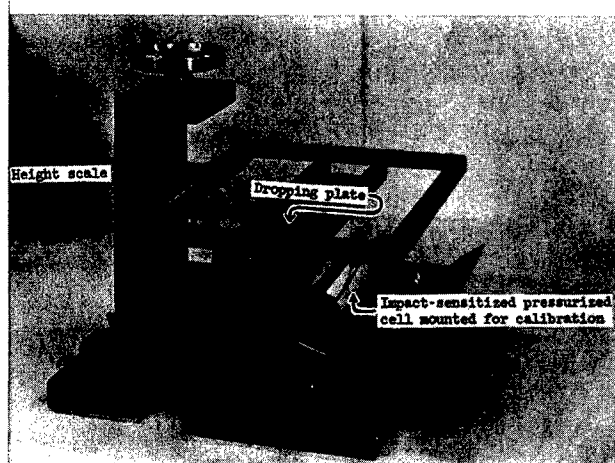


Figure XII-12.- Schematic diagram of signal-conditioning circuitry for curved-plate impact-detection
test point H_T grounded after testing; start



system. All transistors type 2N393; all diodes type 1N626; A_{T1} A_{T2} leads removed after testing;
 resistance values selected during calibrations.



L-62-7320.1

Figure XII-13.- Manually operated impact-calibrating test fixture.

Figures XII-14 and XII-15 show the variation of response of the detecting surface of an impact sensitized pressurized cell with impact site and incidence angle. The impact response calibration of detecting surfaces such as that illustrated by this figure was determined by averaging many impacts at each impact calibrating site. Figure XII-16 shows the change of impact sensitized pressurized cell response variation caused by depressurization. The characteristics of figure XII-16 include the effects of atmospheric coupling and damping, although these effects would not be present in orbit. However, these factors were considered to be small in comparison with tolerances of other meteoroid impact-detection-system parameters.

Figure XII-17 shows the variation of impact response with impact site of a curved-plate detecting surface. The figure also shows the effects upon impact-response variation resulting from operating a pair of electrically paralleled transducer assemblies matched in impact sensitivity, and appropriately positioned on the detecting surface underside.

Since it has been assumed that the response of the impact-detection experiment is to the momentum of the impacting particle, the impact momenta of calibrating particles must be corrected for the restitution increment of the essentially elastic collision of a calibrating impact. Photographic measurement of rebound heights of many impacts was employed in determining the coefficients of restitution for the impact-detecting surfaces of the Explorer XIII.

The measurements of detecting-surface response and transducer-assembly response to calibrating impacts and signal-conditioning-circuitry performance under various conditions of temperature and voltage permit the definition of the impact-detection-system performance. Figures XII-18, XII-19, and XII-20 are the impact-sensitivity characteristics of the 0.01, 0.1, and 1.0 gram-centimeter per second momentum threshold impact-detection systems, respectively. The momentum thresholds are plotted against signal-conditioning-circuitry temperature at three power-supply voltages. The characteristics shown on the figures include the effect of the coefficient of restitution.

For the Explorer XIII impact-detection experiment, it has been assumed that the momentum response of the impact-detection systems which is observed in calibration procedures remains valid for meteoroid particle encounters, even though meteoroid-particle impact velocities are enormously greater, and masses correspondingly smaller, than calibrating-particle velocities and masses. The assumption that impacting meteoroids can be assigned an average impact velocity derived from observations of other meteoroid monitoring techniques, permits the

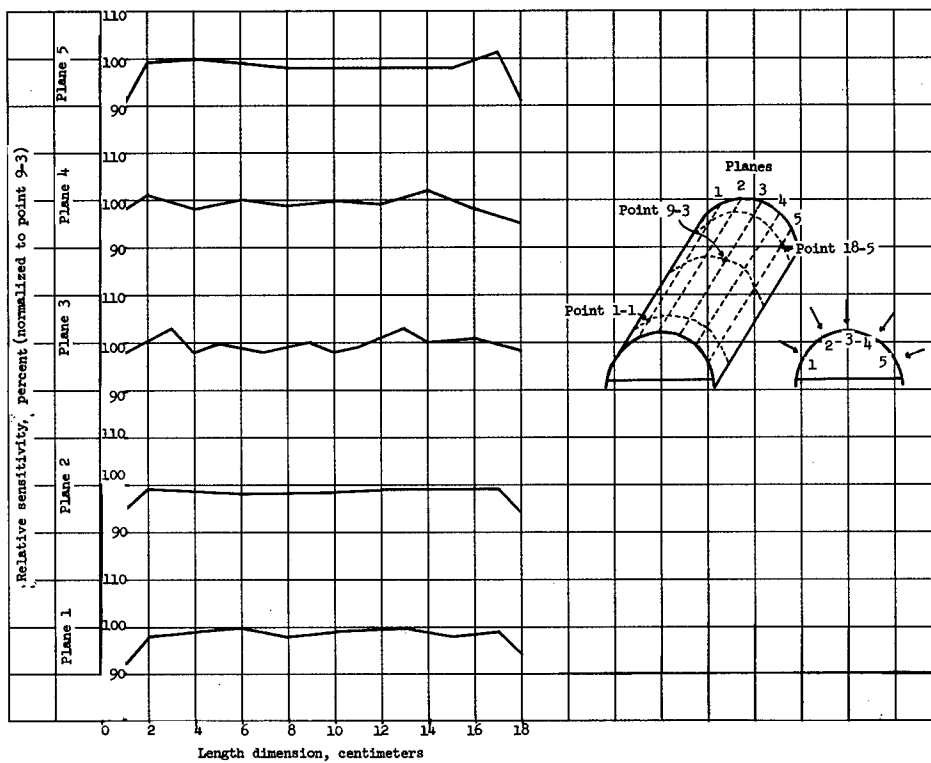


Figure XII-14.- Response variation of impact-sensitized pressurized cell with impact site.

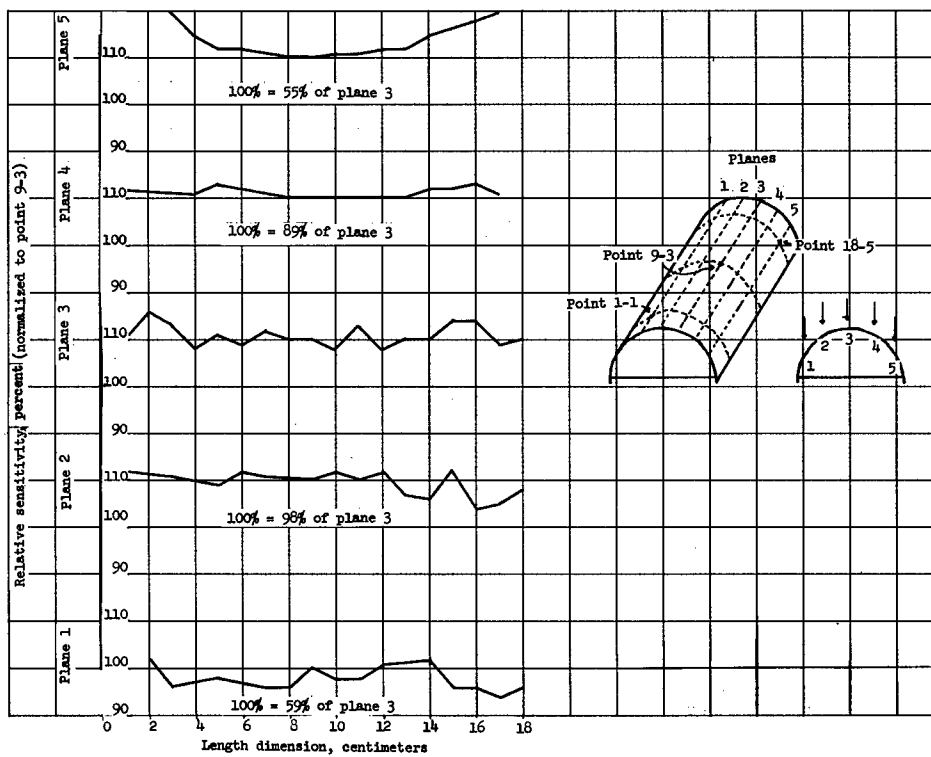


Figure XII-15.- Response variation of impact-sensitized pressurized cell with impact incidence angle.

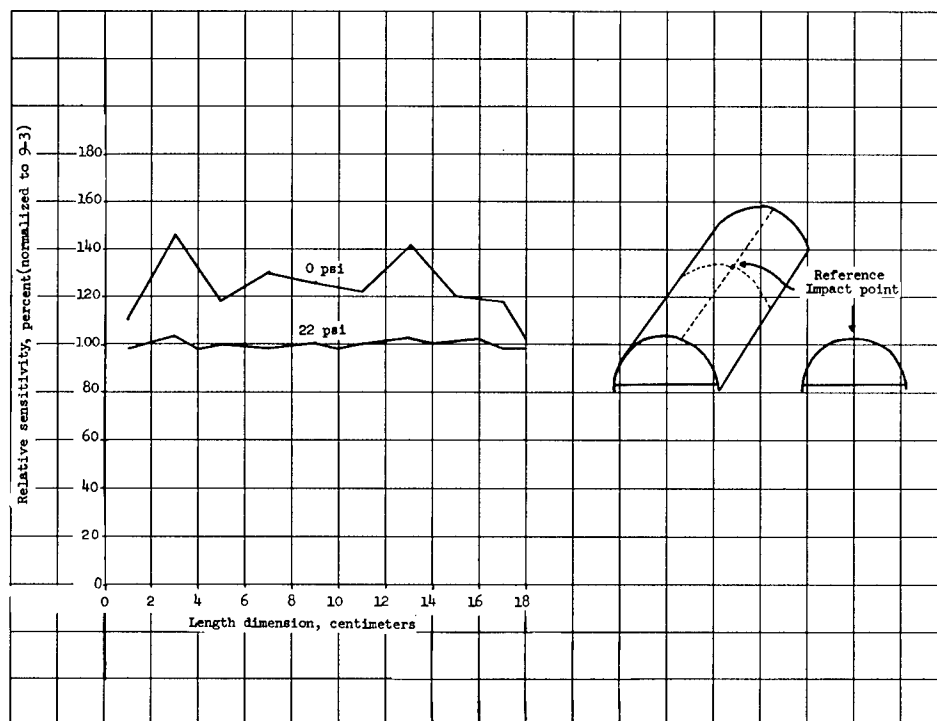


Figure XII-16.- Impact-sensitized pressurized-cell response variation with differential pressure.

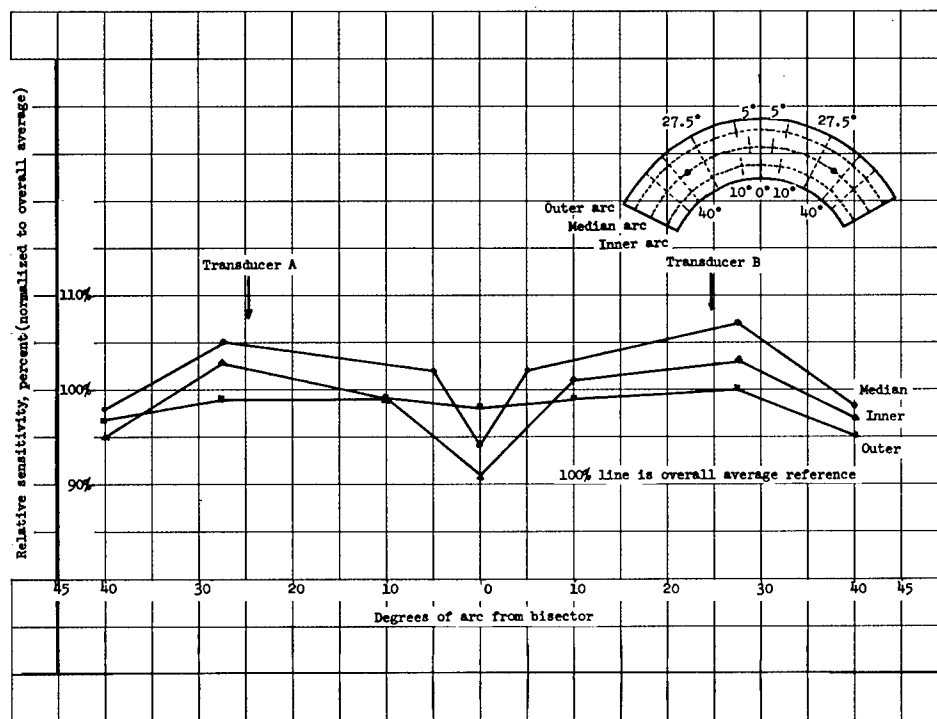


Figure XII-17.- Impact-response variation of curved-plate detecting surface with impact site.

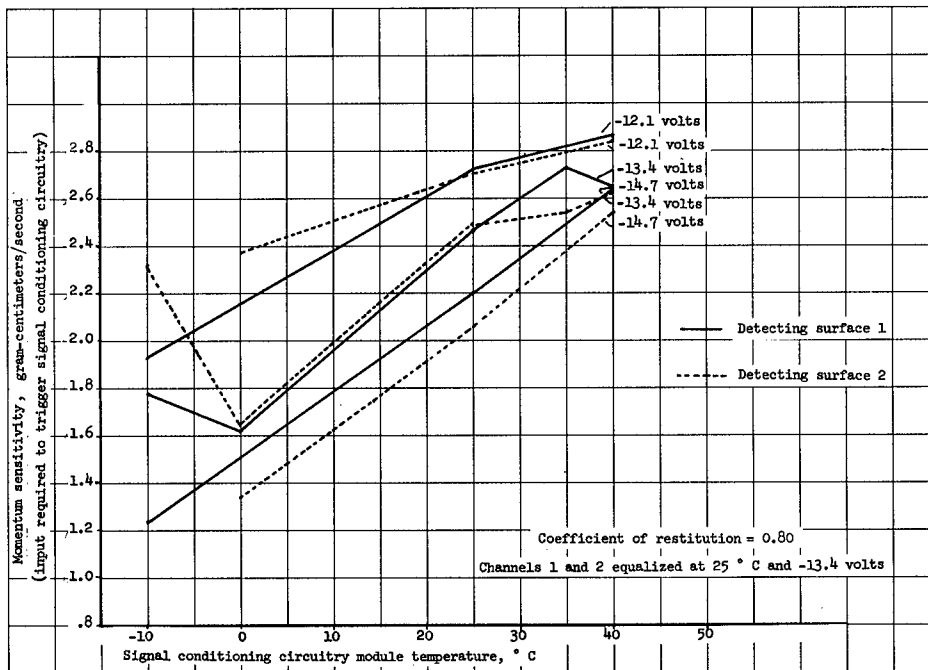


Figure XII-18.- Momentum-sensitivity threshold variation with signal-conditioning circuitry temperature and supply voltage for high-sensitivity curved-plate impact-detection system.

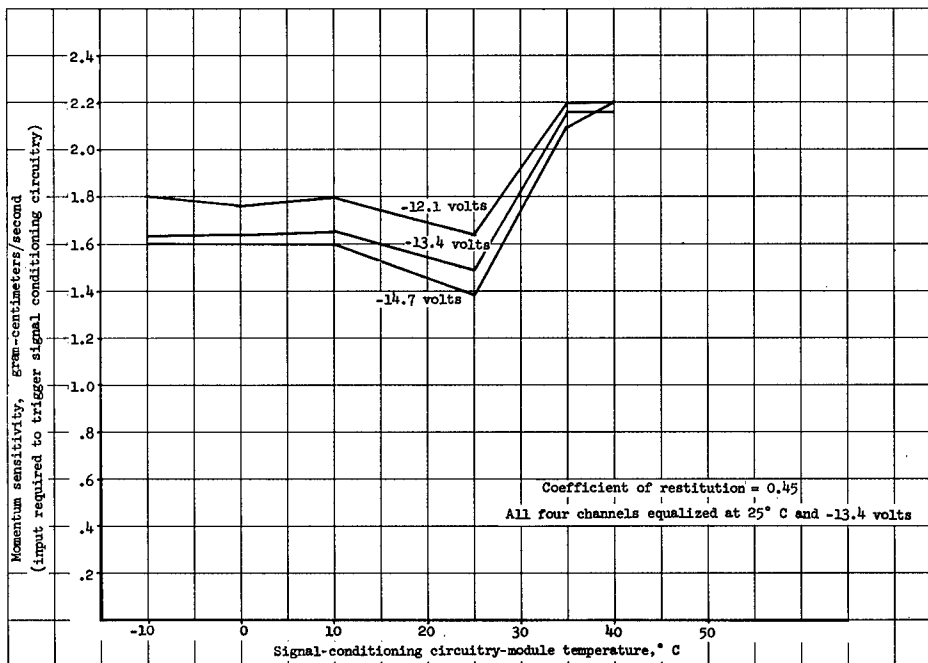


Figure XII-19.- Momentum-sensitivity threshold variation with signal-conditioning circuitry temperature and supply voltage for intermediate-sensitivity impact-sensitized pressurized-cell impact-detection system.

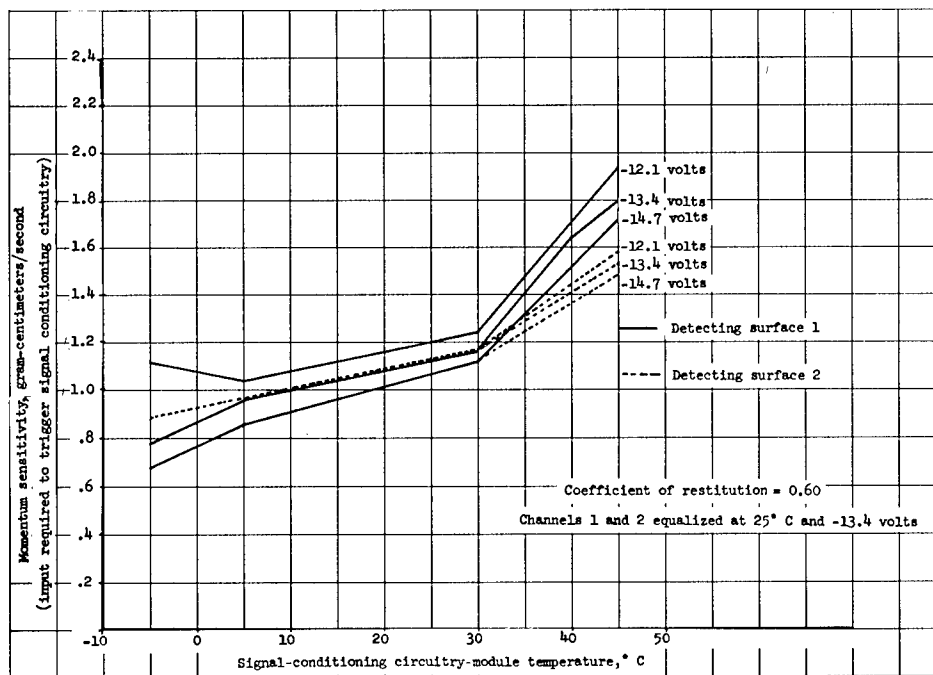


Figure XII-20.- Momentum-sensitivity threshold variation with signal-conditioning circuitry temperature and supply voltage for low-sensitivity curved-plate impact-detecting system.

assignment of an effective average-mass sensitivity threshold of the impact-detection systems. These two assumptions are in accordance with the practices of other United States experimenters (ref. 1).

Where the singularity of the Explorer XIII impact-detection systems precludes correlation with other similar experiments, as for example, in the case of the impact-sensitized detecting surfaces of the pressurized cells, an attempt has been made to provide sufficient calibration measurements so that the appropriate corrections can be applied when better knowledge of the proper way of doing so becomes available.

SECTION V - RESULTS AND CONCLUSIONS

The meteoroid-impact-detection experiment of the Explorer XIII operated normally for the majority of its brief orbital lifetime. The actual values of the counts registered by each of the three momentum-sensing levels are listed in table XII-II. This table lists the accumulated count readout of telemetered data. Certain applicable corrections such as the modification of the effective area of detecting surfaces due to the earth shielding factor, and signal-conditioning-circuitry power-supply voltage and temperature fluctuations due to orbital flight would produce minor modifications appropriate to rigorous analyses of these data. Figure XII-21 illustrates summaries of the Explorer XIII

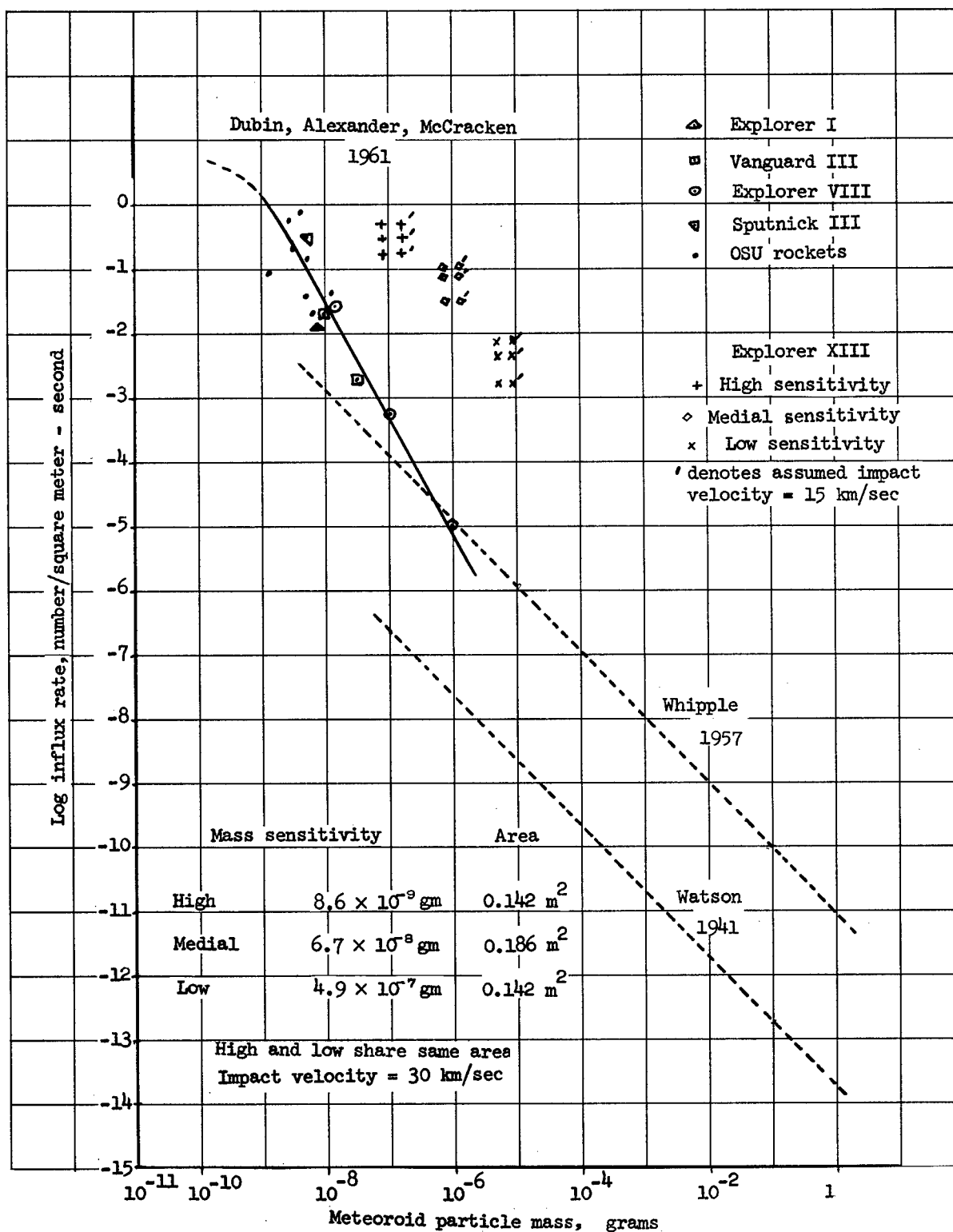


Figure XII-21.- Comparison of Explorer XIII impact-detection systems measured meteoroid influx with other meteoroid environment measurements. Vertical spread in Explorer XIII data points result from selecting orbital intervals; lower points are later intervals.

meteoroid-impact-detection-system counting rates of table XII-II compared with several models of the earth's meteoroid environment proposed by various observers. The figure shows that the measured impact flux rates are substantially higher than those measured by other similar satellite experiments represented by the curve of Dubin, Alexander, and McCracken, from reference 1, although these rates were decreasing with the satellite's time in orbit. No explanation is known for this circumstance, and better definition of the Explorer XIII meteoroid environment cannot be realized because of the lack of data.

It is possible that the orbit of Explorer XIII could have been a factor in producing the high counting rates of the meteoroid-impact-detecting systems. As has been described in previous sections of this compilation, the orbit had very low initial perigee (113.5 kilometers) which subsequently lowered progressively. Aerodynamic mechanical perturbances and temperature effects on the impact-sensing transducer elements might have caused the impact-detecting systems to register signals which were not meteoroid impacts.

Considering these factors, the meteoroid-impact data gathered by the flight of the Explorer XIII must be considered inconclusive. However, it is significant to point out that a valid experimental technique has been developed for the meteoroid hazard research satellite series. Indications are that more significant results would have been obtained from this experiment had the satellite remained aloft and performed satisfactorily for a longer period of time.

SECTION VI - REFERENCE

- XII-1 McCracken, C. W., Alexander, W. M., and Dubin, M.: Direct Measurements of Interplanetary Dust Particles in the Vicinity of Earth. NASA TN D-1174, 1961.

TABLE XII-I.- CHARACTERISTICS OF THE IMPACT DETECTING SURFACES

Shape	Size, cm	Weight, gm	Area, cm ²	Material	Coating
Forward shell curved plates (2)					
Conical section	12.5 width 59.2 outer circumference 32.8 inner circumference 0.079 thickness	430 ± 10	709 (each) 1418 (total)	410 stainless steel	Sandblasted surface; oxidized
Pressurized cells (20)					
Semi-cylindrical	18.8 length 4.93 diameter 0.0125 thickness	Part of pressurized-cell weight	92.8 (each)(projected) 1856 (total)	Beryllium-copper	Deposited aluminum surcoated with silicon monoxide

TABLE XII-II.- EXPLORER XIII METEOROID IMPACT DETECTION EXPERIMENT COUNT ACCUMULATION

Orbit	Minitrack recording station	Date/Time (Greenwich Mean Time)	Elapsed time from injection	Impact experiment count accumulation sensitivity threshold, gm-cm/sec		
				Low	Intermediate	High
Injection		25/1839	0	----	----	----
1	Blossom Point	25/2011	92	0	----	----
	Grand Forks	25/2011	92	0	----	----
9	Antofagasta	26/1002	923	124	----	----
10	Quito	26/1146	1027	132	----	----
13	Fort Myers	26/1513	1234	153	0	0
	Blossom Point	26/1515	1236	153	0	0
14	Blossom Point	26/1658	1339	156	157	538
15	Fort Myers	26/1840	1441	156	258	2400
21	Santiago	27/0445	2046	166	1425	3957
22	Santiago	27/0621	2141	171	1476	4214
23	Antofagasta	27/0803	2244	171	1506	4403
28	Woomera	27/1542	2699	172	----	----

An enlarged photograph (L-64-3017) of the component parts of the Explorer XIII spacecraft is available on request.

Requests for the copy should be addressed to:

Chief, Photographic Division
NASA Langley Research Center
Langley Station
Hampton, Virginia 23365

CUT

Date _____

Please send a copy of photograph L-64-3017 to TN D-2468.

Name of Organization

Street number

City and State

Zip code

Attention: Mr. _____

Title

Place
Stamp
Here

Chief, Photographic Division
NASA Langley Research Center
Langley Station
Hampton, Virginia 23365

<p>NASA TN D-2468 National Aeronautics and Space Administration. THE MICROMETEOROID SATELLITE EXPLORER XIII (1961 CHI) COLLECTED PAPERS ON DESIGN AND PERFORMANCE. Charles T. D'Aiutolo, Coordinator. November 1964. v, 198p. OTS price, \$3.50. (NASA TECHNICAL NOTE D-2468)</p> <p>Papers on the spacecraft, experiments, telemeter, and power supply systems, as well as the launch vehicle, for the Explorer XIII micrometeoroid satellite are presented. In addition to the major contributions from the Langley Research Center, two papers from the Goddard Space Flight Center are included. The preflight test program and re- sults are discussed. Ascent flight data and orbital performance are also presented. Finally, separate sections describe the aims of the experiments, discuss the design development, construction, and performance of the apparatus used, and report the results.</p>	<p>I. D'Aiutolo, Charles T. II. NASA TN D-2468</p>	<p>NASA TN D-2468 National Aeronautics and Space Administration. THE MICROMETEOROID SATELLITE EXPLORER XIII (1961 CHI) COLLECTED PAPERS ON DESIGN AND PERFORMANCE. Charles T. D'Aiutolo, Coordinator. November 1964. v, 198p. OTS price, \$3.50. (NASA TECHNICAL NOTE D-2468)</p> <p>Papers on the spacecraft, experiments, telemeter, and power supply systems, as well as the launch vehicle, for the Explorer XIII micrometeoroid satellite are presented. In addition to the major contributions from the Langley Research Center, two papers from the Goddard Space Flight Center are included. The preflight test program and re- sults are discussed. Ascent flight data and orbital performance are also presented. Finally, separate sections describe the aims of the experiments, discuss the design development, construction, and performance of the apparatus used, and report the results.</p>	<p>I. D'Aiutolo, Charles T. II. NASA TN D-2468</p>	<p>NASA TN D-2468 National Aeronautics and Space Administration. THE MICROMETEOROID SATELLITE EXPLORER XIII (1961 CHI) COLLECTED PAPERS ON DESIGN AND PERFORMANCE. Charles T. D'Aiutolo, Coordinator. November 1964. v, 198p. OTS price, \$3.50. (NASA TECHNICAL NOTE D-2468)</p> <p>Papers on the spacecraft, experiments, telemeter, and power supply systems, as well as the launch vehicle, for the Explorer XIII micrometeoroid satellite are presented. In addition to the major contributions from the Langley Research Center, two papers from the Goddard Space Flight Center are included. The preflight test program and re- sults are discussed. Ascent flight data and orbital performance are also presented. Finally, separate sections describe the aims of the experiments, discuss the design development, construction, and performance of the apparatus used, and report the results.</p>	<p>I. D'Aiutolo, Charles T. II. NASA TN D-2468</p>	<p>NASA TN D-2468 National Aeronautics and Space Administration. THE MICROMETEOROID SATELLITE EXPLORER XIII (1961 CHI) COLLECTED PAPERS ON DESIGN AND PERFORMANCE. Charles T. D'Aiutolo, Coordinator. November 1964. v, 198p. OTS price, \$3.50. (NASA TECHNICAL NOTE D-2468)</p> <p>Papers on the spacecraft, experiments, telemeter, and power supply systems, as well as the launch vehicle, for the Explorer XIII micrometeoroid satellite are presented. In addition to the major contributions from the Langley Research Center, two papers from the Goddard Space Flight Center are included. The preflight test program and re- sults are discussed. Ascent flight data and orbital performance are also presented. Finally, separate sections describe the aims of the experiments, discuss the design development, construction, and performance of the apparatus used, and report the results.</p>	<p>I. D'Aiutolo, Charles T. II. NASA TN D-2468</p>	<p>NASA TN D-2468 National Aeronautics and Space Administration. THE MICROMETEOROID SATELLITE EXPLORER XIII (1961 CHI) COLLECTED PAPERS ON DESIGN AND PERFORMANCE. Charles T. D'Aiutolo, Coordinator. November 1964. v, 198p. OTS price, \$3.50. (NASA TECHNICAL NOTE D-2468)</p> <p>Papers on the spacecraft, experiments, telemeter, and power supply systems, as well as the launch vehicle, for the Explorer XIII micrometeoroid satellite are presented. In addition to the major contributions from the Langley Research Center, two papers from the Goddard Space Flight Center are included. The preflight test program and re- sults are discussed. Ascent flight data and orbital performance are also presented. Finally, separate sections describe the aims of the experiments, discuss the design development, construction, and performance of the apparatus used, and report the results.</p>	<p>I. D'Aiutolo, Charles T. II. NASA TN D-2468</p>
---	--	---	--	---	--	---	--	---	--

"The aeronautical and space activities of the United States shall be conducted so as to contribute . . . to the expansion of human knowledge of phenomena in the atmosphere and space. The Administration shall provide for the widest practicable and appropriate dissemination of information concerning its activities and the results thereof."

—NATIONAL AERONAUTICS AND SPACE ACT OF 1958

NASA SCIENTIFIC AND TECHNICAL PUBLICATIONS

TECHNICAL REPORTS: Scientific and technical information considered important, complete, and a lasting contribution to existing knowledge.

TECHNICAL NOTES: Information less broad in scope but nevertheless of importance as a contribution to existing knowledge.

TECHNICAL MEMORANDUMS: Information receiving limited distribution because of preliminary data, security classification, or other reasons.

CONTRACTOR REPORTS: Technical information generated in connection with a NASA contract or grant and released under NASA auspices.

TECHNICAL TRANSLATIONS: Information published in a foreign language considered to merit NASA distribution in English.

TECHNICAL REPRINTS: Information derived from NASA activities and initially published in the form of journal articles.

SPECIAL PUBLICATIONS: Information derived from or of value to NASA activities but not necessarily reporting the results of individual NASA-programmed scientific efforts. Publications include conference proceedings, monographs, data compilations, handbooks, sourcebooks, and special bibliographies.

Details on the availability of these publications may be obtained from:

SCIENTIFIC AND TECHNICAL INFORMATION DIVISION
NATIONAL AERONAUTICS AND SPACE ADMINISTRATION
Washington, D.C. 20546